Microfluidic Synthesis of Block Copolymer Nanoparticles for Drug Delivery

by

Amandeep Singh Bains
B.Sc., Simon Fraser University, 2012

A Dissertation Submitted in Partial Fulfillment
of the Requirements for the Degree of

DOCTOR OF PHILOSOPHY

in the Department of Chemistry

Supervisory Committee

Microfluidic Synthesis of Block Copolymer Nanoparticles for Drug Delivery

by

Amandeep Singh Bains
B.Sc., Simon Fraser University, 2012

Supervisory Committee

Dr. Matthew G. Moffitt (Department of Chemistry)
Supervisor

Dr. Dennis K. Hore (Department of Chemistry)
Departmental Member

Dr. David Harrington (Department of Chemistry)
Departmental Member

Dr. Stephanie Willerth (Department of Mechanical Engineering)
Outside Member

Abstract

Supervisory Committee
Dr. Matthew G. Moffitt (Department of Chemistry)
Supervisor
Dr. Dennis K. Hore (Department of Chemistry)
Departmental Member
Dr. David Harrington (Department of Chemistry)
Departmental Member
Dr. Stephanie Willerth (Department of Mechanical Engineering)
Outside Member

In this dissertation, we studied two-phase microfluidics as a platform for the controlled synthesis of drug delivery polymeric nanoparticles (PNPs). The block copolymer we studied was poly(ε-caprolactone)-*block*-poly(ethylene oxide) (PCL-*b*-PEO). The anticancer drug we studied was paclitaxel (PAX). First, we explored microfluidic control of nanoparticle structure (size, morphology, and core crystallinity) on PCL-*b*-PEO PNPs without loaded PAX. We demonstrated the reproducible variability of PCL-*b*-PEO nanoparticle size and morphology. Microfluidic control of nanoparticle size and morphology was found to arise from the interplay of flow-induced particle coalescence and breakup. Next, we demonstrated the linear dependence of PCL core crystallization on flow-rate. We attributed this dependence of PCL core crystallization on flow-induced crystallization.

We then used our microfluidic device to control PAX-loaded PNP structure and function (small molecule loading efficiency, diffusional release kinetics, and cytotoxicity). At low drug loading ratios ($r < 0.1$), we demonstrated reproducible

variability of PAX-loaded PNP size and morphology. With increasing flow rate we were able to manufacture PNPs of high aggregation number. We were also able to reproducibly demonstrate the linear dependence of PCL core crystallinity on flow rate. Furthermore, PAX loading efficiency was dependent on PNP size and morphology. Formulations which consisted of cylindrical and lamellar type morphologies typically had higher PAX loading efficiencies, than formulations which consisted of spherical structures. Next, we studied diffusional PAX release, increasing core crystallinity correlated with slowing diffusional PAX release kinetics.

At high drug loading ratios ($r > 0.1$), we demonstrated reproducible control of PAX-loaded PNP structure and function. PCL core crystallinity was a major factor influencing PNP size and morphology. Samples with high core crystallinity formed PNP structures with low internal curvature. Furthermore, core crystallization had a large influence on PAX loading efficiency; as samples with high PAX loading efficiency correlated with low PCL core crystallinity. With respect to diffusional PAX release, we found that increasing PCL core crystallinity correlated with slowing diffusional PAX release kinetics. Next, we studied the cytotoxicity of our PAX-loaded PNPs using the MCF-7 cancer cell line. Due to the complex nature of the interactions between our PAX-loaded PNPs and the cancer cells, we were not able to elucidate the exact influence of flow rate on PNP cytotoxicity.

Table of Contents

List of Tables

List of Figures

Acknowledgments

First and foremost, I would like to express my most sincere gratitude to my supervisor, Dr. Matthew Moffitt, for the amazing opportunity to work on such a fascinating project. I am very grateful for your constant support and encouragement, endless patience, infectious enthusiasm and utmost optimism. I am truly thankful for all of the things you have taught me. Without your effort and understanding, this dissertation would not be possible.

Also, I would like to acknowledge Dr. Frank van Veggel, for his constant help and encouragement. Thank you for always having a '*few quick minutes*…' and our long discussions about politics and science.

In addition, I would like to thank:

The Moffitt group members past and present: Joe Wang, Abby Xu, Brian Coleman, Fraser Burns, Sun Kly, Alex Leung, Yimeng Cao, and Amy Chen.

The van Veggel group members past and present: Noah Johnson, Jothir Pichaandi, Armita Das, and Stephanie Bonvicini

Last and definitely not least, all the Chemistry faculty and staff - thank you for your help and continued support. These last four years of my PhD studies have truly been remarkable.

Dedication

To my family
Without you this would not have been possible.

Chapter 1

General Introduction

1.1 Background and Motivation

It is thought that almost half of potentially useful drug candidates fail to progress to formulation development because of their low aqueous solubility and associated poor or erratic cell uptake characteristics.[4-8] A response to this challenge has been the development of colloidal delivery systems, termed drug delivery vehicles, in which the therapeutic agent is encapsulated in micro- or nanosized particles, increasing their *in vivo* stability. A popular commercially available approach used to encapsulate hydrophobic drugs and increase their efficacy in aqueous environments is by way of lipid-based micellar systems.[4,5] However, compared to lipid-based systems, block copolymer based drug delivery systems are more robust, enjoy a greater ease of functionalization, and have broad diversity in terms of chemical and structural properties. Under the appropriate thermodynamic conditions, self-assembly of amphiphilic block copolymers into aqueous aggregates, termed polymeric nanoparticles (PNPs), results in a variety of morphologies such as spheres, cylinders and vesicles.[9-11] Due to the variety of morphologies and diversity in properties, block copolymer PNPs have been on the forefront of drug delivery formulation development for the last 15 – 20 years.

For amphiphilic block copolymers dissolved in solution, self-assembly into PNPs occurs upon the addition of water (a nonsolvent for the hydrophobic block) to a concentration above the critical water concentration (cwc). Amphiphilic block copolymer self-assembly in aqueous environments results in the formation of PNPs (sometimes called micelles or micellar aggregates) that are composed of relatively dense hydrophobic cores and solubilized hydrophilic coronae. Under equilibrium conditions, the morphologies of block copolymer PNPs are governed by a delicate balance of entropic and enthalpic contributions, including chain stretching within

the PNP core (entropic), repulsion between solubilized coronal chains (entropic and enthalpic), and interfacial tension between the core-forming block and the surrounding aqueous environment (enthalpic). Conventional or bulk experimental control of block copolymer PNP size and morphology involves variations in chemical conditions such as the choice of initial common solvent, water concentration, pH, ionic strength and block copolymer composition. Variations of these chemical conditions, also known as a "bottom-up" approach, can allow for the tuning of PNP size and morphology for increased drug efficacy in terms of drug loading and release.

Semicrystalline and biodegradable block copolymers such as poly(ε-caprolactone)-*block*-poly(ethylene oxide) (PCL-*b*-PEO), polylactic acid (PLLA), and poly(lactic-co-glycolic acid) (PLGA), are a class of block copolymers that have often been used in drug delivery formulation development.[12-22,5,6,23,7,8] Once these materials undergo self-assembly they form nanoparticles that have organization on multiple length scales (structural hierarchy), due to a combination of structural properties both on the colloidal (nanoparticle size and morphology) and nanoscale (crystallization of the hydrophobic polymeric chains within the PNP core).[7] The structural properties at both of these disparate length scales are of critical importance to drug delivery applications because of their complex influence on *in vivo* nanocarrier function (drug loading efficiency and diffusional release kinetics).[24-27,19,28,22] For example, on the colloidal scale (10 – 100 nm) nanoparticle size and morphology are distinctly designed with cellular uptake, *in vivo* fate, and hemorheological dynamics in mind.[19,22] On the molecular scale (1 – 10 nm), core crystallization will alter nanoparticle morphology and core microviscosity, influencing *in vivo* bioavailability and small molecule diffusional release kinetics, respectively.[15,17,29,30] These examples highlight a need for control of PNP multiscale structure in order to obtain drug

delivery vehicles with the desired physical, chemical, and biochemical properties for a specific therapeutic application.

Manufacturing of drug delivery vehicles using microfluidics has allowed for fast and efficient screening of process parameters and formulations. Microfluidics has also shown improvements in size control of PNPs.[32-34] Both of these improvements are possible due to the associated nanoscale volumes and laminar flow, enabling fine-tuning of local concentrations of reagents and mixing rates. Furthermore, fast and efficient screening of process parameters is critical for early stage manufacturing of drug delivery vehicles, allowing for rapid optimization of physical and chemical properties without the time inefficient "trial-and-error" approaches of conventional manufacturing strategies.

Over the last 7 years, our group has studied two-phase gas-liquid segmented microfluidic reactors for the manufacturing of block copolymer drug delivery vehicles.[63-65,52,23,31] In two-phase microfluidics, compartmentalization of liquid plugs occurs with a regular stream of argon gas bubbles that helps increase mixing rates due to chaotic advection. An important feature unique to gas-liquid segmented microfluidic reactors is the flow-variable high-shear[63] regions in the corners of the liquid plugs. Shear forces have been previously shown to exhibit control over block copolymer PNP size and morphology.[66] Gas-liquid segmented microfluidic reactors have high shear "hot-spots" in the corners of the gas-liquid plugs which exhibit shear levels that are five magnitudes higher[63] than what is achievable using conventional bench-top mixing techniques. Our group has been able to utilize the high shear available in two-phase microfluidics to control size and morphology in a model block copolymer system: polystyrene-*b*-poly(acrylic acid) (PS-*b*-PAA).[71,64] For example, in these studies Wang *et al.* were able to manufacture pure and relatively low-size dispersity vesicles under solvent conditions which

formed no vesicles using conventional manufacturing techniques.[71,64] Moving forward we use the garnered knowledge from this model system and apply this technology to a more therapeutically relevant formulation.

In this dissertation we present a new platform for the controlled synthesis of drug delivery nanoparticles. We apply two-phase microfluidics to reproducibly control structure (size, morphology and core crystallinity) and function (drug loading efficiency and release kinetics) of PCL-*b*-PEO PNPs loaded with the chemotherapeutic agent, paclitaxel (PAX). We use the block copolymer PCL-*b*-PEO because of its inherent biodegradable and semicrystalline properties, as well as, the considerable attention it has received as a potential commercial drug delivery system.[5-7] Furthermore, we use PAX in our drug delivery formulation because: 1. it is a well-known chemotherapeutic agent that has been used in many commercially available drug delivery formulations;[5,7] and, 2. it has a relatively high affinity for PCL. We intend to use microfluidics and systematically study the influence of flow-variable shear and a variety of chemical parameters (water content, copolymer composition and initial drug loading ratio) on multiscale structure of PAX-loaded PCL-*b*-PEO PNPs. We then intend to study the influence of multiscale structure on PAX-loaded PCL-*b*-PEO PNP function by monitoring drug loading efficiency, *in vitro* diffusional PAX release kinetics, and, cytotoxicity. Studying microfluidic control of PNP function by exploring PNP diffusional PAX release and cytotoxicity increases our understanding on how microfluidic-prepared PNPs behave within *in vitro* live biological environments (cell line studies); potentially setting the stage for future animal studies.

1.2 General Introduction to Polymers

1.2.1 Definition and Terminology

Polymers are large molecules, either synthetic or natural, constructed of smaller covalently bonded structural units called monomers.[72] Monomers covalently bonded together to form a polymer are called repeat units, and the average number of repeat units that construct a polymer is called the degree of polymerization. Based on how the monomers are connected to

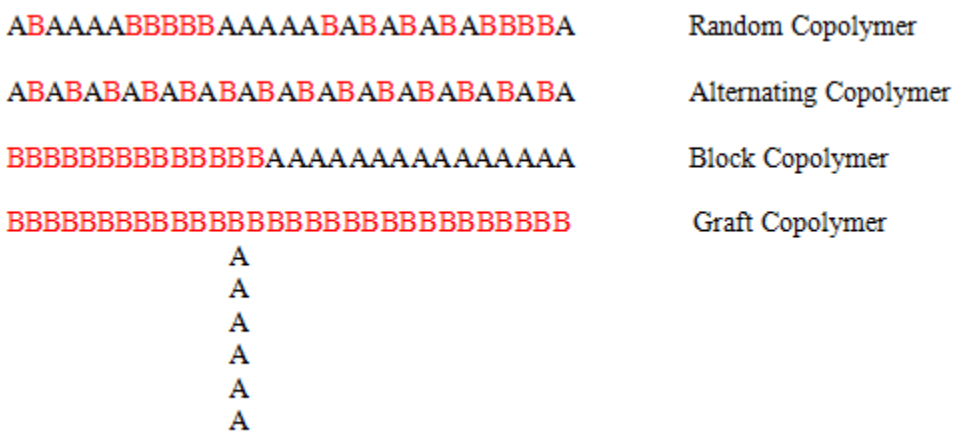

Figure 1.1. Different types of copolymers formed from A and B monomers

each other, polymers may be categorized as linear, branched or networks. More specifically, linear polymers have skeletal structures that are linear, whereas, branched polymers have side chains that extend from the main polymer backbone at different 'branch' points. Furthermore, branched polymers can form three dimensional networks called network polymers which are interconnected at junction points.[72]

Polymers constructed of one type of monomer repeat unit are called homopolymers. Accordingly, polymers constructed of more than one type of monomer are called copolymers.

Copolymers can be divided into four main categories depending on their specific sequential motifs: such as random copolymers, alternating copolymers, graft copolymers and block copolymers. Statistical or random copolymers have a random distribution of monomers along the polymer chain. Alternating copolymers have monomers that alternate along the polymer chain. Graft copolymers are a type of branched polymer in which the branches are structurally different monomer units when compared to the backbone. Block copolymers are a fascinating class of polymeric materials that are composed of two or more covalently bonded structurally distinct polymeric chains. In some cases the covalently bonded polymer chains are thermodynamically incompatible giving rise to a rich variety of microstructures in bulk and in solution.[72]

1.2.2 Molecular Weight Distribution

A distinct feature of polymers which distinguishes them from simple molecules is the inability to assign an exact molar mass to a polymer. In polymer samples, rarely do the individual polymer chains in the sample have the exact same degree of polymerization and

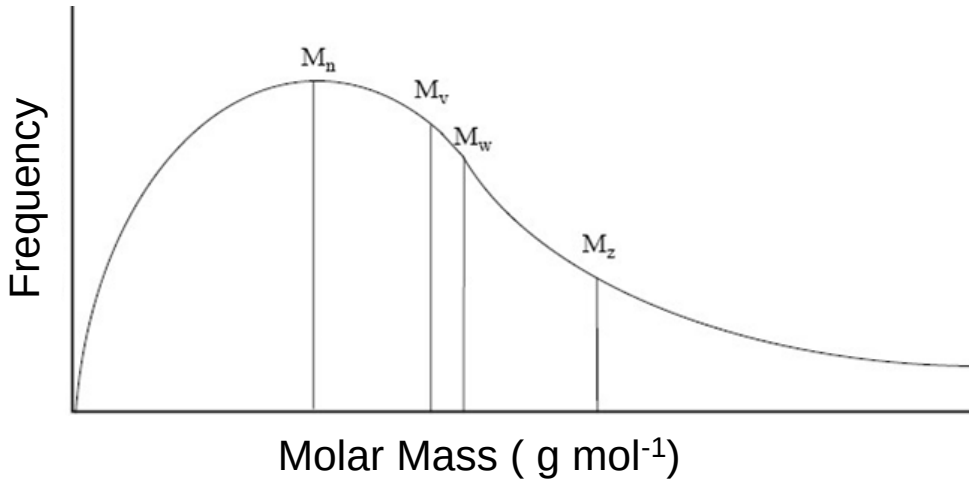

Figure 1.2. Theoretical molecular weight distribution of a polymer sample highlighting the positions of different molecular weight averages

molecular weight. There is always a distribution of repeat units and molecular weight around an average. The molar mass distribution of a polymer sample describes the number of molecules of each polymer species (N_i) and the molar mass of that species (M_i). Different average values can be applied using different statistical means of calculation. In practice there are four averages that can be calculated: number average molecular weight (M_n), weight average molecular weight (M_w), z-average molecular weight (M_z), and viscosity average molecular weight (M_v).

The number average molecular weight defines the total mass of the polymer sample over the total number of molecules of polymer present, and is defined by:

$$M_N = \frac{\sum_i N_i M_i}{\sum_i N_i}$$

where N_i is the number of molecules of species i with molecular weight M_i. The number average molecular weight can be measured using colligative methods such as osmotic pressure, boiling point elevation, freezing point depression, vapour pressure lowering.

The weight average molecular weight is defined by summing the total mass of polymer species multiplied by their molecular weight over the total mass of the polymer sample. The weight average molecular weight can be determined using light scattering measurements, a methodology which takes into account the species' size rather than the number of molecules. Statistically, the number average molecular weight is the first moment, and the weight average molecular weight is the ratio of the second to the first moment of the number distribution. M_w is defined by:

$$M_w = \frac{\sum_i N_i M_i^2}{\sum_i N_i M_i}$$

where w_i is the weight of all molecules of species i with molecular weight M_i.

Typically both the number average and weight average molecular weight are used to provide information on the distribution of polymer molecular weights. Furthermore, the polydispersity index (P.D.I.), the ratio of weight-average molecular weight and the number-average molecular weight, is used to describe the width of the molecular weight distribution for a polymer sample. Typically, polydispersity indices approaching unity are said to have low polymer dispersity whilst samples with P.D.I.s that are large are said to be highly polydisperse. In general terms it is said that synthetic polymer samples have a P.D.I. > 2 depending on the type of polymerization method. For example, step-growth polymerization techniques, such as condensation reactions, produce polymer samples with relatively broad size distributions, on the order of P.D.I. = 2.[72] On the other hand, polymerization techniques such as anionic polymerization produce polymer samples with lower polydispersities, values as low as 1.01.[73] However, monodisperse polymer samples (P.D.I. = 1) are not achievable for synthetic polymers.[72] P.D.I. is defined by:

$$P.D.I. = \frac{M_w}{M_n}$$

A method of describing the chain length of a polymer is by measuring the average degree of polymerization, x_n. In this dissertation x_n is defined by:

$$x_n = \frac{M_n}{M_o}$$

where M_o is the molecular weight of a single repeat unit.

1.3 Block Copolymer PNPs

1.3.1 Self-assembly of Block Copolymer PNPs

An intriguing property of block copolymers with two covalently attached thermodynamically incompatible blocks is their inherent ability to spontaneously self-assemble, upon addition of a selective solvent for one of the blocks, into colloidal nanostructures termed block copolymer micelles or PNPs.[9] This process is analogous to the well-known formation of micelles of relatively low-molecular weight surfactants (e.g. soap in water). Spontaneous formation of block copolymer PNPs has been extensively studied both theoretically as well as experimentally due to the plethora of available PNP morphologies such as spheres, cylinders and vesicles; as well as, applications in areas such as cosmetics, lubrication, and drug delivery of drugs that are insoluble under aqueous conditions.

Block copolymer self-assembly under aqueous conditions results in formation of PNPs with hydrophobic cores and solubilized hydrophilic coronae. In general, if self-assembly of PNPs occurs under aqueous conditions, the PNPs are referred to as regular PNPs. On the other hand, when self-assembly occurs in organic solvents, resulting in PNPs with hydrophilic cores and a hydrophobic coronae, the PNPs are referred to as reverse PNPs. For either reverse or regular PNPs, if the corona-forming block is short relative to the core-forming block, the PNPs are known as “crew-cut” PNPs, and if the reverse is true they are described as “star-like” PNPs. These classification schemes are represented pictorially in Figure 1.3.

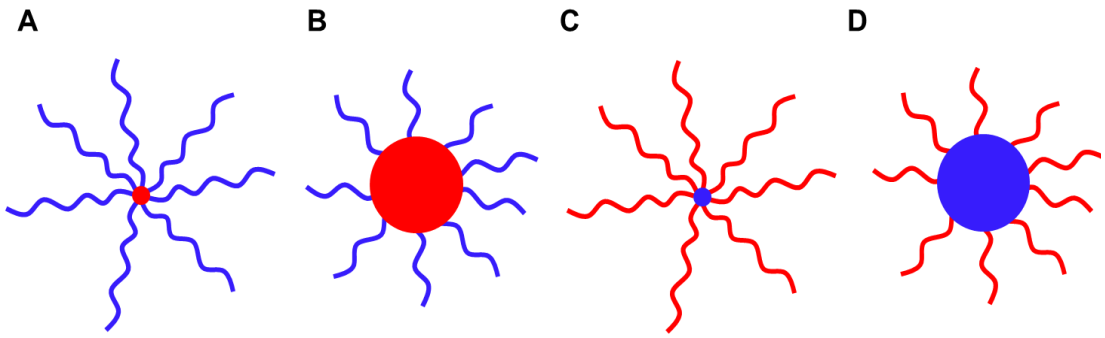

Figure 1.3. Schematic illustrations of the various types of amphiphilic block copolymer PNPs in aqueous solvent (A and B), and organic solvent (C, D). Blue indicates hydrophilic copolymer chains and red indicates hydrophobic chains.

1.3.2 Thermodynamics of Block Copolymer Self-assembly

Polymer-polymer and polymer-solvent interactions are important for the drug delivery field because depending on the magnitude and nature of these interactions, polymers can either exist as single chains or aggregates in solution. Block copolymers are especially interesting because they can either exist in solution as single chains, or under specific conditions they can aggregate and precipitate or stabilize in solution as nanosized colloids. Under appropriate solvent conditions, block copolymer self-assembly is a spontaneous process; microphase separation allows the system to achieve a minimum Gibbs free energy, *G*. The fundamental thermodynamic equation relating the change in G with the changes in enthalpy, *H*, and entropy, *S*, is:[72]

$$\Delta G = \Delta H - T\Delta S$$

The thermodynamics of micellization of block copolymers in organic solvents has been studied before.[74,75] Micellization of polystyrene based systems such as, polystyrene-*b*-polyisoprene (PS-*b*-PI) and polystyrene-*b*-poly(ethylene/propylene) (PS-*b*-PEP), in various

organic solvents have shown that micellization is an enthalpically-driven process. In organic media, micellization incurs a large entropic penalty due to the loss of both conformational entropy (chain stretching within the core- and corona-forming blocks) and translational entropy (localization of block junctions at the core/corona interface); however, due to favourable enthalpic contributions (transfer from high energy polymer/solvent interactions to low energy polymer/polymer interactions for the core forming block) micellization remains a spontaneous process.

Unlike micellization under organic conditions, the self-assembly of block copolymers into PNPs under aqueous conditions is an entropically driven process. Microphase separation of the block copolymer results in loss of entropy for the block copolymer chains; however, the greater increase in entropy of the surrounding water molecules (hydrophobic effect) drives the micellization process. More specifically, on the microscale, with the continued addition of water to a dissolved block copolymer system at a concentration below the critical water concentration, cwc, water molecules are forced into reconstructing their hydrogen bonds by building water "cages" around the hydrophobic block, leading to a reduction in entropy of the water molecules. However, as the continued addition of water occurs to a concentration above the cwc, aggregation of the hydrophobic block into PNP cores and stabilization of the aggregate by the solubilized hydrophilic corona allows the water molecules to move freely around the newly formed PNPs and thus increase their entropy providing the mechanism necessary to drive the micellization process spontaneously.

For the purposes of this dissertation, we will look at micellization of block copolymers in mixtures of polar organic solvents (e.g. DMF) and water. Using static light scattering experiments, Eisenberg *et al.* have studied the thermodynamics of PNP formation of polystyrene

based block copolymers polystyrene-*block*-poly(acrylic acid) (PS-*b*-PAA) in varying DMF and water mixtures.[9,10,76] Their results concluded that micellization of PS-*b*-PAA in DMF and water can be both an enthalpically and entropically driven process; the determining factor is the relative water concentration. For example, at low water contents (< 5 wt.% water) the exchange of unfavourable polymer/solvent interactions for the more favourable polymer/polymer and solvent/solvent interactions upon micellization result in a large negative enthalpy, driving micellization. However, at higher water contents (> 15 wt % water) there are stronger hydrophobic interactions between the polymer chains and the surrounding water molecules, which leads to a highly positive enthalpy term. On the other hand, micellization allows for large increases in entropy of the water molecules, outweighing the enthalpic penalty and driving the micellization process.

1.3.3 Block Copolymer Size and Morphology

Under the appropriate thermodynamic conditions, block copolymer chains will self-assemble into micellar aggregates, termed block copolymer PNPs. In 1995, Eisenberg *et al.* published the first report demonstrating control and production of PNPs of varying morphologies using the same family of copolymer, PS-*b*-PAA.[9] In the last 20 years, extensive research has been done to control block copolymer morphologies for various applications.[11] Block copolymers self-assemble in selective solvents to form a variety of morphologies such as: spheres, rods, vesicles, compound micelles, tubes, disks, and bowl- and needle- shaped micelles. The vast variety of morphologies available, their biocompatibility, and the near-endless potential applications are just a few of the motivating factors in studying block copolymer PNPs. Under equilibrium conditions block copolymer PNP size and morphology are governed by three

thermodynamic factors: 1. the interfacial tension between the PNP core and surrounding solvent; 2. the degree of chain stretching of the core-forming block; and, 3. the repulsive chain interactions of the corona forming blocks. These thermodynamic parameters are controlled by altering chemical parameters ("bottom-up" control) such as copolymer composition, copolymer concentration, the solution water concentration, and presence of additives such as ions or homopolymers. Thus, by varying and altering these chemical parameters it is possible to vary block copolymer PNP size and morphology.

1.3.5 Block Copolymer Crystallization

In materials science, significant crystallinity in a polymer is of interest.[72] The properties of the sample: density, optical clarity, modulus, and general mechanical response all change

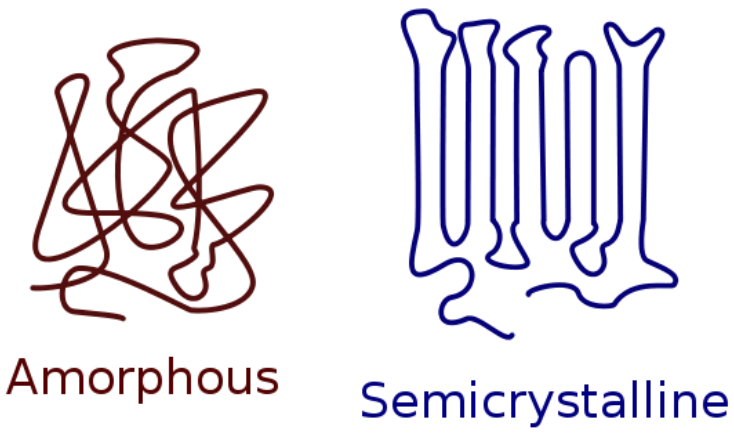

Figure 1.4. Schematic illustration of an amorphous *vs.* semicrystalline polymer[100]

dramatically when crystallites are present. However, a polymer sample is rarely completely crystalline, and their properties depend on the degree of crystallinity. Polymers are termed semicrystalline because below their melting temperature (T_m) they can have both crystallized and

amorphous regions. Whether a polymer is amorphous or semicrystalline depends on its structure and intermolecular forces. If the polymer has strong intermolecular forces and ordered structure it is more likely to be semicrystalline.

The creation of a crystalline state from a disordered state is a two-step process: 1. crystallite nucleation; and, 2. crystal growth. The first step in creating a stable nucleus is increasing order of copolymer chains through strong intra- and intermolecular forces. Increased order of copolymer chains is achieved by close-packing of chains in a highly extended, linear conformation. Packing of copolymer chains into an ordered structure is associated with large negative entropy of activation. To achieve crystallization, a favourable free-energy change has to occur, resulting in the offset of negative entropy by a large negative enthalpic contribution.

The second step is the growth of the crystalline region, the size of which is governed by the rate of addition of other chains to the nucleus. An optimum temperature of crystallization is restricted to a range between the melting temperature (T_m) and the glass transition temperature (T_g). At or above the T_m, the temperature is too high to allow for nucleation to occur at a significant rate, since random thermal motion of chain segments competes with formation of ordered, low-mobility regions. On the other hand, if the temperature is too low (near or below the T_g) chain mobility within the melt is too low to allow diffusion of chains and crystallite growth on experimental time scales.

1.3.5 Block Copolymers for Drug Delivery

The design and synthesis of novel biocompatible materials has driven the progress of drug delivery systems in the past few decades. Up till now, lipid-based drug delivery systems have enjoyed the greatest amount of success in terms of clinical applications and FDA approvals

of formulations. In contrast to their lipid-based counterparts, polymer based drug delivery systems allow for greater ease in functionalization, robustness, and a multitude of morphologies. Biodegradable polymers such as poly(lactic acid) (PLA) are widely used for drug delivery formulation development and in particular have been used to delivery various bioactive agents such as small molecule drugs,[77,25] peptides and proteins,[77] and plasmid DNA.[77]

In terms of block copolymer based drug delivery vehicles, many formulations have surpassed the development stage and have reached clinical trials and even commercial development. For example, in the late 80's and early 90's two independent groups worked on and developed a block copolymer based drug delivery formulation, with both reaching phase II clinical trials,[78,79] Kataoka[79] *et al.* used a PEG based A-B block copolymer system to delivery paclitaxel and doxorubicin, whilst Kabanov *et al.*[78] used a PEG based triblock system to deliver doxorubicin.

For cancer therapy, drug delivery vehicle localization within tumour sites is performed *in vivo* in one of two ways: 1. active-targeted delivery; or, 2. passive delivery.[5-7] The colloidal stability of copolymer based drug delivery systems is appealing for passive tumor targeting utilizing the enhanced permeation and retention (EPR) effect.[80,81] The EPR effect was first discovered by Maeda *et al.* in the mid-80s.[82] The general explanation the EPR effect is: due to the abnormal and leaky vasculature found within tumours, particles up to ~400 nm are known to passively accumulate within the tumour. The leaky vasculature is a result of the newly formed tumour blood vessels, which are usually structurally poor. These vessels will have misaligned defective endothelial cells with wide fenestrations that lead to abnormal molecular blood-flow dynamics. Blood will flow through this leaky tumour vasculature and any drug delivery nanoparticles within ~400 nm will permeate through the blood vessel and into the tumour,

accumulating over time. Then, upon localization within the tumour, the drug encapsulated nanoparticles can deliver their cargo either through diffusion, breakdown of the nanoparticle, or they may undergo endocytosis and then release their payload within tumour cells.[81]

Control of nanoparticle structural properties on the colloidal (100s of nm) and molecular (1 – 10 nm) scale have shown an influence on *in vivo* nanoparticle function. For example, on the colloidal length scale block copolymer nanocarrier size and morphology dictate tumour localization (*via* the EPR effect), biodistribution and blood circulation half-life.[24,18,26,27,19,84,28,22] With respect to nanoparticle biodistribution and blood half-life, Discher *et al. has* demonstrated how cylindrical block copolymer nanoparticle morphologies exhibit longer blood circulation half-lives (> 1 week), when compared to their spherical counterparts (2 – 3 days). Aside from morphological considerations, nanocarrier size influences *in vivo* biodistribution, blood half-life, and localization within tumours. For example, due to the large cell slit sizes of interendothelial cells, nanoparticles with diameters > 200 nm have shown increased blood clearance and accumulation within the spleen.[85,86] On the other hand, nanoparticles with diameters < 5 nm have been shown to undergo rapid renal clearance upon intravenous administration. Nevertheless, the intravenous administration of drug delivery nanoparticles that are between 50 – 150 nm in diameter have demonstrated an ability to exhibit longer blood half-lives.[87,88,86]

On the molecular scale, numerous studies have reported on the direct correlation between nanocarrier core crystallization and its effect on nanoparticle structure (particle morphology) and function (drug loading efficiency and release kinetics). For example, reports by Burt *et al.* have highlighted the influence of increasing core crystallization on local microviscosity within the hydrophobic core; thereby, changing the diffusion coefficient of entrapped small molecule cargo.[29,30] Aside from influencing diffusional release of encapsulated small molecule cargo,

reports by Winnik *et al*. show how PNP core crystallinity can influence PNP morphology. For example, semi-crystalline PNPs as a function of increasing core crystallinity will favour low internal curvature morphologies, such as lamellae, and filomicelles.[89] One explanation for this observation can be due to the tendency of crystallites to form at the solvent – polymer interface. Thus, increases in crystalline mass within the PNP core, lead to a greater density of crystallites at the interface, restricting PNP morphologies to those with lower internal curvatures.

1.3.6 Conventional Nanoparticle Formation

The most common methodology in used for conventional (bulk) block copolymer drug delivery nanoparticle fabrication is the nanoprecipiation method.[92,5-7] The nanoprecipitation method is performed by adding an organic solution, which contains the polymer and hydrophobic drug, to a stirring aqueous solution, either in a dropwise manner, or suddenly all at once. Once the organic media is introduced to the aqueous solution and the polymer solution diffuses into the aqueous phase, nanoparticles form instantaneously. Critical parameters that govern nanoparticle outcomes are the miscibility of the organic solvent with water, the rate of polymer addition and, the stirring speed during nanoparticle formation. All of these parameters influence nanoparticle size, morphology, and drug loading levels. The nanopercipitation method has been applied to a wide variety of polymers, peptides and amphiphilic cyclodextrins.[92]

Another method for PNP preparation is the emulsifaction-solvent evaporation method. Generally, emulsion based drug delivery nanoparticle fabrication methods involve two steps: 1. emulsified droplets of the organic phase in the aqueous phase are formed through sonication or vigorous agitation; and, 2. precipitation of the polymer to form dense drug-loaded nanoparticles. After emulsification, drug encapsulated nanoparticle formation is achieved through the evaporation of the volatile solvent under reduced pressure.

1.4 Microfluidics

1.4.1 Basic Concepts

Microfluidics is a discipline that deals with flow dynamics in small volumes and in confined spaces with one dimension that is at least < 1000 μm.[93] Microfluidics is a relatively new field that addresses many different areas of research such as, electronics, physics, biomedicine, analysis, and pharmaceuticals. The microfluidics research field is still in its infancy with the community still exploring and understanding basic principles, before applications to areas of research. The attraction to microfluidics lies in its microdimensions, where fluid dynamics are vastly different from the macroscale. Fluid dynamics on the microscale differ from their macroscale counterparts by offering 1. small reagent volumes; 2. improved heat and mass transfer due to increased surface area-to-volume ratios; 3. precise control over flow dynamics (laminar flow); 4. continuous flow operation where residence time distributions can be easily tuned by simply adjusting flow rates; 5. increased control over mixing and local reagent volumes; and, 6. facile production of material libraries by changing flow-rate or chemical parameters.

Flow dynamics on the microscale can be assessed by the dimensionless Reynolds number (*Re*). The Reynolds number is a measure of the ratio of inertial forces to viscous forces and can be defined as:

$$Re = \frac{\rho U d_H}{\mu}$$

where ρ is the fluid density, U is the characteristic fluid velocity, d_H is the characteristic channel diameter, and μ is the dynamic viscosity of the fluid. For flow dynamics to be characterized as laminar flow, Reynolds numbers are typically on the order of ≤ 1. In the laminar flow regime,

fluid flow is predictable and flows in parallel layers with no lateral mixing. In contrast to the laminar flow regime, fluid dynamics on the macroscale are at high Reynolds numbers and flow characteristics are described as turbulent and unpredictable.

Microscale flow is usually achieved by means of mechanical pumping (pressure-driven flow). Pressure-driven flow, or Poiseuille flow (Figure 1.5), is well understood and is generally characterized by a parabolic flow velocity profile, with the maximum flow velocity in the center of the channel and zero velocity near the walls (no-slip boundary condition). The reason why fluid flow velocity near the channel walls is zero when compared to the center of the channel is due to the interaction between the liquid and microchannel wall. The microchannel walls exert a uniform force over the cross-sectional area of the channel. Fluid momentum is lost at the walls due the greater attractive forces between fluid and wall particles (adhesive forces) than the cohesive forces between the fluid particles. This contrast in flow-velocity results in the parabolic flow velocity described earlier and represented pictorially in Figure 1.5.

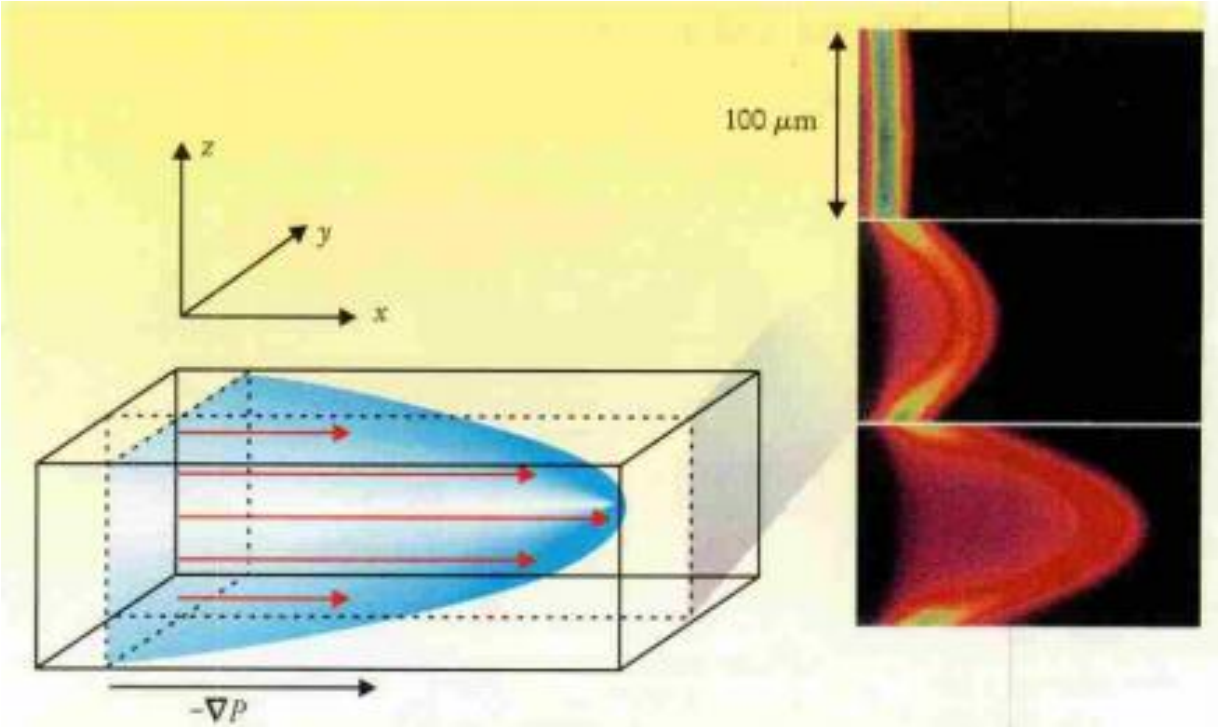

Figure 1.5. Flow profiles in microchannels. A pressure gradient - ∇ *P*, along a channel generates a parabolic or Poiseuille flow profile in the channel. The velocity of the flow varies across the entire cross-sectional area of the channel. On the right is an experimental measurement of the distortion of a volume of fluid in a Poiseuille flow. The frames show the state of the volume of fluid 0, 66, and 165 ms after the creation of a fluorescent molecule.[3]

1.4.2 Single- vs. Multiphase Microfluidic Reactors

Single phase microfluidic reactors are a popular platform for drug delivery formulation development because of their simple and easy operation.[3,94,95,1,96] A major drawback of single-phase reactors is their slow mixing which is dominated by diffusion. Diffusion dominated mixing is due to the lack of turbulent flow within the microchannels. Generating turbulence within the microchannels in an effort to increase mixing would require extremely high flow-rates. Ultimately, high flow-rates are undesirable because of their associated high reagent consumption

and high pressure. Another drawback with single-phase microfluidic reactors stems from their characteristic Poiseuille flow. Due to the no-slip boundary condition, nanoparticles flowing along the microchannel walls have broader residence time distributions compared to particles flowing through the center of the channel. For nanoparticles such as vesicles, broader nanoparticle residence time distributions result in greater polydispersities of fabricated materials, due to collision-induced coalescence occurring along the microchannel walls.[42] One way to circumvent these problems is by introducing a second immiscible stream of fluid (gas or liquid) into the system, resulting in the generation of a succession of immiscible fluid segments.

Multiphase microfluidic devices can generally be divided into two main types: gas-liquid segmented reactors (Figure 1.6A) and droplet reactors (liquid-liquid; Figure 1.6B). In droplet reactors, liquid droplets flow through the reactor encapsulated in a carrier phase, which wets the microchannel. The relative interfacial tension between the channel surface and fluid will determine which liquid is the carrier phase and which liquid is the droplet phase. The fluid with the relatively higher interfacial tension with the channel wall will form the liquid droplets; whereas, the fluid with the relatively low interfacial tension will form the carrier phase. Sizes of encapsulated liquid droplets within the carrier phase are a function of flow-rate. For nanoparticle synthesis using droplet reactors, the reagents are compartmentalized within the encapsulated droplets and do not come into contact with the microchannel surface. On the other hand, in gas-liquid segmented microfluidic reactors, the liquid “plugs” are the carrier phase and are segmented by gas bubbles. For nanoparticle synthesis using gas-liquid reactors, the reagents are contained in the carrier phase and are compartmentalized by the gas bubbles.

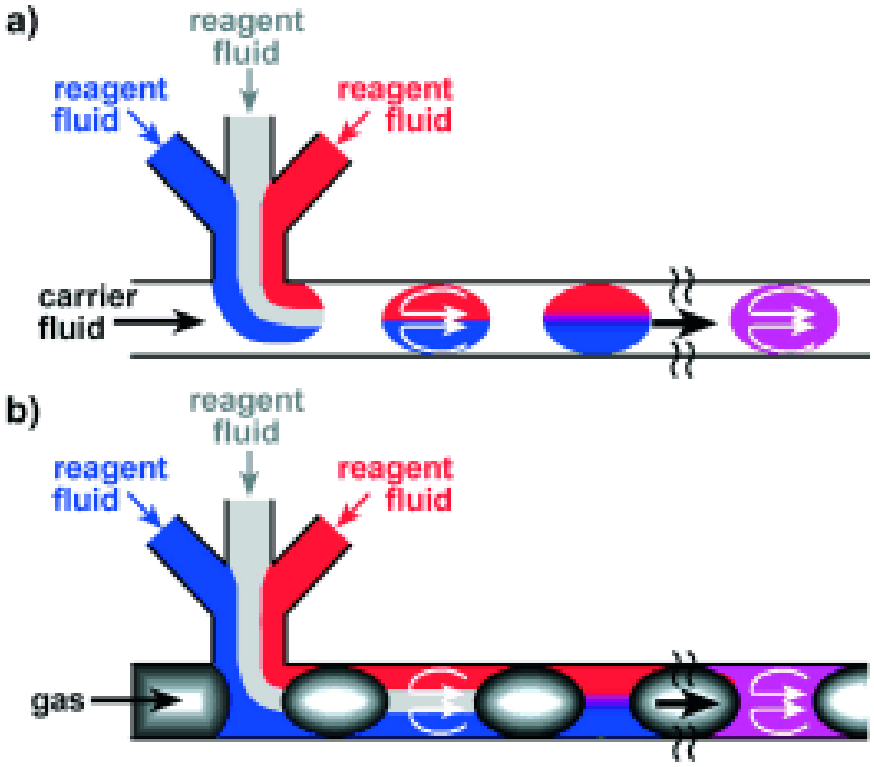

Figure 1.6. Reactions can be studied in two types of segmented flows in microfluidic channels. A) Discrete liquid plugs are encapsulated by an immiscible continuous phase (for example, a fluorocarbon-based carrier fluid). Reactions occur within the dispersed phase (within the plugs). Owing to the surface properties of the microchannel walls, these walls are preferentially wet by the continuous phase. B) Aqueous slugs are separated by another immiscible phase (for example, discrete gas bubbles). Reactions occur within the continuous phase (i.e., within the slugs).[1]

In contrast to single-phase microfluidic reactors, an appealing characteristic of multiphase microfluidic reactors is the recirculating flow that is induced in droplets travelling through the microfluidic channels. This recirculation is in the form of a pair of counter-rotating vortices in the top and bottom halves of the droplets or liquid "plugs". The counter-rotating vortices greatly enhance mixing *via* chaotic advection when compared to the diffusional mixing available in single-phase reactors (Figure 1.7). Another advantage that is unique to two-phase gas-liquid microfluidic reactors is the high shear 'hot-spots' in the corners of the gas-liquid interface. The shear available in these 'hot-spots' is ~ 5 orders of magnitude higher than what can be achieved using a conventional bench top stir plate setup. Within the last 5 years, our

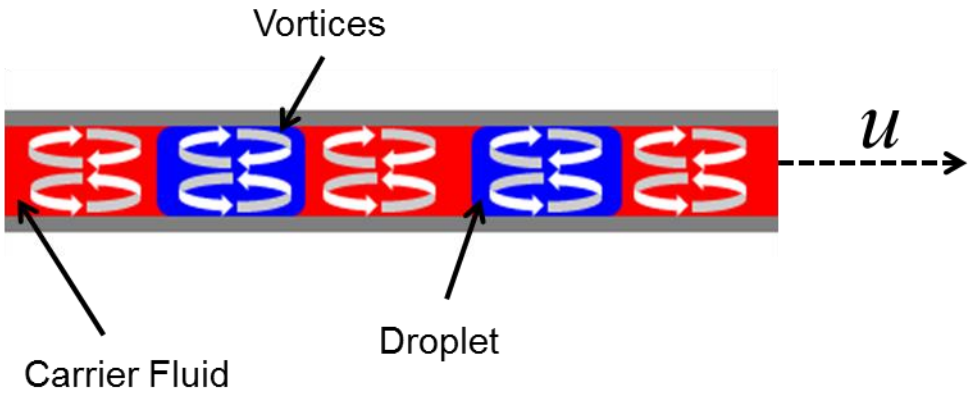

Figure 1.7. Schematic showing mixing patterns inside droplets/plugs moving downstream with velocity *u*.

group has utilized these gas-liquid reactors and has used the available high shear as a ‘top-down’ control handle on nanoparticle fabrication and drug delivery formulation development.

1.4.3 Microfabrication

Microfluidics first started to garner interest in the 1970s, and the first devices were made at Stanford University using silicon and glass.[97] Most of the early systems were fabricated used highly developed and available technologies such as photolithography, micromachining and etching in silicon and glass. Silicon and glass are both not ideal materials for microfluidic device fabrication. Silicon is a relatively expensive material that is also opaque in the visible/UV region, making it unsuitable for systems that use optical detection. On the other hand, glass is transparent, however due to its amorphous properties vertical side walls are difficult to etch, compared to silicon. Another drawback for both silicon- and glass-based materials is the sealing process requires each device to be made in a cleanroom environment. Furthermore, along with the cleanroom, the sealing process also requires high voltages and/or temperatures. These early methods were time-consuming and expensive, and the mechanical properties of the materials imposed challenges during the fabrication process and limited the range of geometries that could be made. Therefore, for the next generation of microfluidic devices, there was a need for new materials and fabrication methods.

Promising alternatives to glass and silicon materials for microfluidic device fabrication are soft polymeric materials. Soft polymers have been used as new microfluidic fabrication materials due to their relatively low cost, potential for mass fabrication, and tunable physical and chemical properties. Soft lithography is a technique that is used to fabricate microfluidic devices

relatively quickly (< 1 day) and without the use of a clean room. Success of soft lithography depends on the ability to produce masters without any surface defects, as any defects on the master will be passed on to the soft polymer molds. Soft lithography is a suite of nonphotolithographic methods for replicating a pattern, which is done in two stages: rapid prototyping and replica molding.

1.4.5 Rapid Prototyping and Replica Molding

Rapid prototyping begins with the creation of a design for a device using a computer-aided design (CAD) program.[97] Then, a high resolution image of the device design is printed onto a transparency, serving as the photomask. With respect to the devices produced for this dissertation, the photomask is typically black (in order to block UV exposure) with the desired microchannel pattern transparent. After the photomask has been prepared, a negative master of the microchannels is fabricated using photolithography (Figure 1.8). Photolithography is a process whereby the 2-dimensional features of the channel are transferred onto a photoresist though light exposure. A photoresist, in this case SU-8 (a photocurable epoxy), is a light sensitive material whose physical properties can be altered when exposed to light of a specific wavelength. To prepare the microchannel master, the photoresist is spin coated onto a silicon wafer and then allowed to harden. The photomask is then placed on top of the photoresist and then exposed to UV light. After the exposure to UV light, the photoresist will polymerize during a post-exposure bake. The photoresist is then cooled to room temperature before it is placed in a developer solution. A developer solution is used to wash away the unexposed area on the photoresist, rendering a completed microfluidic master on a silicon wafer. The size of the

features obtainable with rapid prototyping is between 50-100 μm, which fits most microfluidic applications. The height of the microchannel can be adjusted by choosing SU-8 with appropriate viscosity.

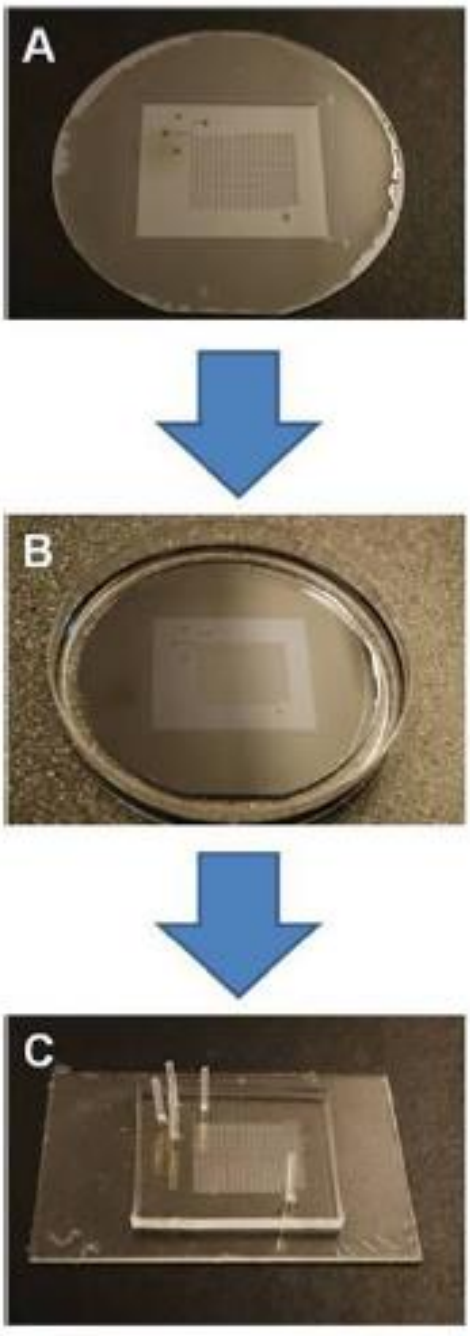

Figure 1.8. Images of microchip fabrication at different times: a) finished SU-8 master on a silicon wafer; b) master chip submerged in cured PDMS in a Petri dish; and, c) cut-out and sealed PDMS microchip, ready for use.[2]

Once a master is fabricated, the channels are printed onto polydimethyl siloxane (PDMS) by replica molding. PDMS has garnered interest as a microfluidic material as it is relatively inexpensive and micron scale features can be reproduced well with replica molding. Replica molding is simply the casting of a prepolymer against a master and generating a negative replica of the master in PDMS.

Once molded and cured, the PDMS is removed from the master. Since most microfluidic applications require materials to withstand pressures $\geq$ 5 psi, the PDMS is treated with oxygen plasma in order to irreversibly seal the negative mold with a PDMS coated glass substrate. The plasma treatment oxidizes the PDMS surface methyl groups (Si-CH_3) and generates silanol groups (Si-OH). The plasma treated mold is then placed onto a PDMS coated glass substrate and irreversibly sealed using heat.

1.5 Characterization Tools

1.5.1 Transmission Electron Spectroscopy

For this dissertation, PNP sizes and morphologies were routinely characterized using transmission electron microscopy (TEM). TEM is possible because of the work of de Broglie. We are able to use electrons for imaging of nanoparticles, due to the fact that an accelerated electron beam has an effective wavelength that is ~10^5 times shorter than visible light. Nanoparticle images are generated when an accelerated electron beam hits the specimen, scattering electrons at different angles. Depending on the electron density of the specimen, the electrons from the electron beam can either be: 1. undeflected; 2. deflected without loss of energy (elastic scattering); or, 3. deflected with significant loss of energy (inelastic scattering). The relative brightness of the image depends on the number of unscattered electrons that pass

through the objective aperture. Furthermore, regions of the specimen composed of light atoms (carbon) will scatter relatively fewer electrons appearing bright; whereas, heavy atoms (iron) will

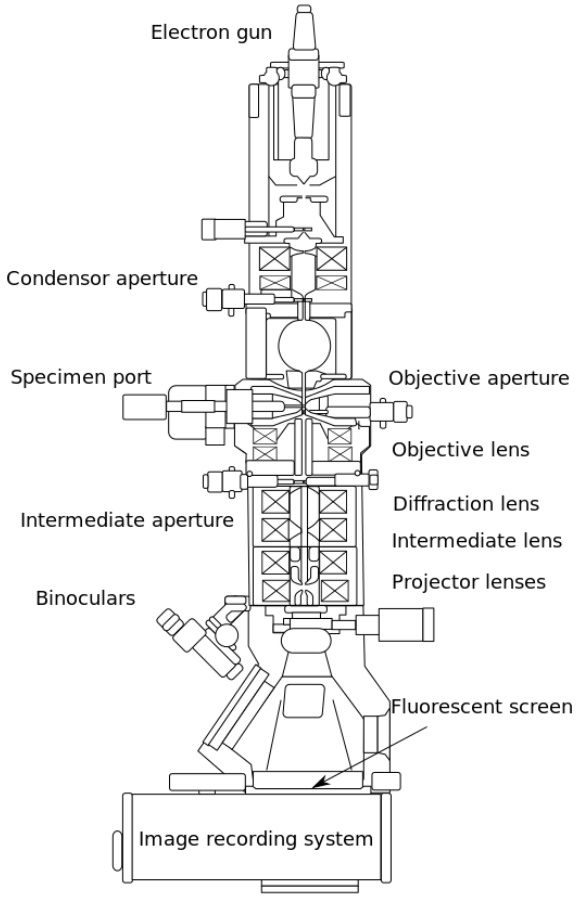

Figure 1.9 Schematic illustration of a transmission electron microscope[101]

scatter greater amounts of electrons, and appear dark.

In this dissertation, we regularly use uranyl acetate to negatively stain our images, providing contrast for our PCL-*b*-PEO PNPs. Since the PNPs used in this dissertation are composed mostly of carbon atoms, they do not provide enough contrast to allow for effective imaging. Uranyl acetate selectively binds to the PEO block of our PNPs, providing negative

contrast by deflecting greater amounts of electrons than the PCL core. Due to this negative staining, our TEM images appear dark, with light regions representing PCL-*b*-PEO PNPs.

1.5.2 Dynamic Light Scattering (DLS)

Dynamic light scattering (DLS) is a technique that is used in this dissertation to determine *in situ* size distributions of drug loaded PNPs. DLS characterizes fluctuations in the intensity of scattered light, which is due to the Brownian motion of the particles. These movements change the interparticle distances and consequently the intensity of the scattered light. Since particles of different sizes will diffuse at different rates, the intensity changes can be related to the size of the particles.

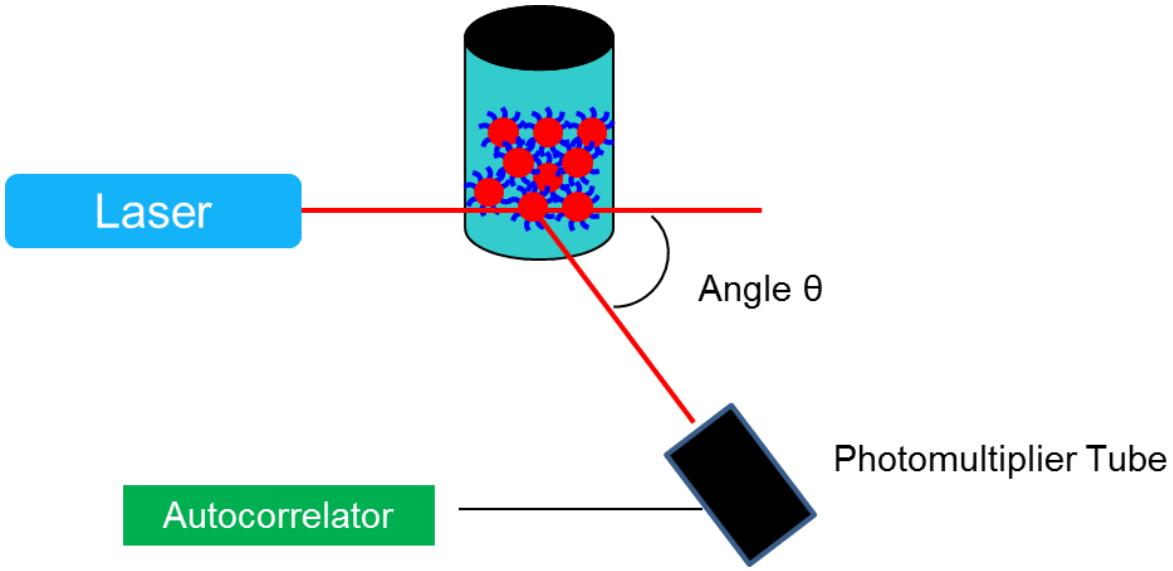

Figure 1.10 Schematic illustration of a typical DLS experimental setup

In a typical DLS experiment, particle sizes are measured by analyzing time dependent fluctuations in scattered light intensity to determine the diffusion coefficient, D_0. The Stokes-Einstein equation is then applied to determine the hydrodynamic radius, r_h, of the particles:

$$r_h = \frac{k_B T}{6\pi\eta D_0}$$

where k_B is the Boltzmann constant, T is temperature and, η is the viscosity of the solvent.

1.5.3 X-Ray Diffraction (XRD)

A particularly effective method to analyze semicrystalline polymers is by X-ray diffraction (XRD). In a polymer sample, the crystallites regions will diffract X-ray beams from parallel planes for incident angles, θ, which are determined from the Bragg equation:

$$n\lambda = 2d \sin\theta$$

where n is an integer, λ is the wavelength of the incident beam and, d is the distance between parallel crystallite planes.

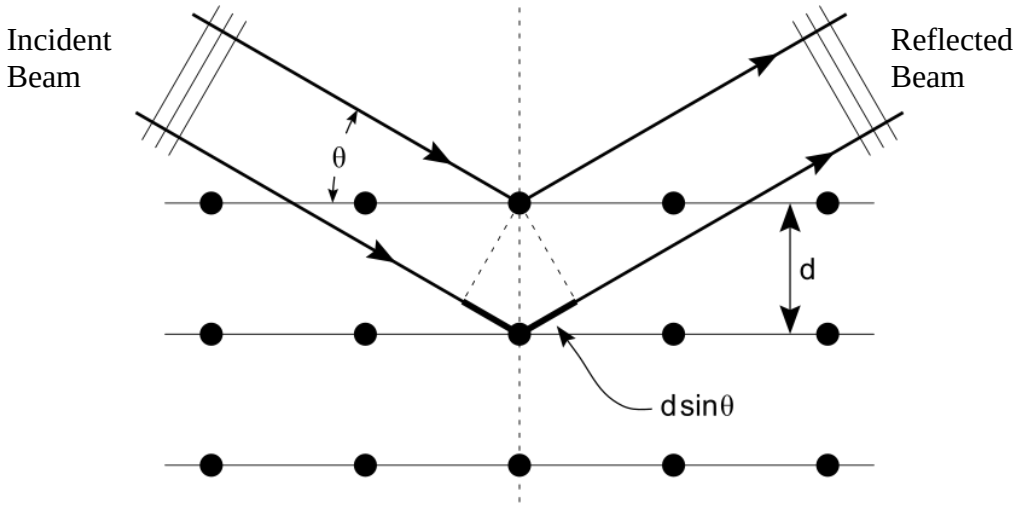

Figure 1.11 Schematic illustration of incident X-rays elastically scattering off of atoms in a crystal lattice.[102]

When the incident beam interacts with crystallite regions within the polymer sample diffraction rings are produced. These diffraction rings will be sharply defined for highly crystalline materials and become increasingly diffuse when the amorphous content is high. Each semicrystalline polymer sample will have a characteristic diffraction pattern. To obtain an X-ray

diffraction spectrum, a Fourier transform is applied to the X-ray diffraction pattern. An example of an XRD spectrum is presented in Figure 8.3 (Appendix II). Weight percentage of polymer crystallinity can be calculated by accounting for the relative areas under crystallite peaks and amorphous halos. This procedure is described in detail in the experimental of chapters 2 – 5.

1.5.4 Liquid Chromatography – Mass Spectrometry (LCMS)

Liquid chromatography – mass spectrometry is an analytical technique that combines the separation capabilities of liquid chromatography with the analytical capabilities of mass spectrometry. In this dissertation, LCMS was used to quantify PAX encapsulation or release from PCL-*b*-PEO PNP samples. LCMS is a very sensitive technique, with limits of detection approaching the 100s – 1000s of parts per billion. In general, the application of LCMS is oriented towards the separation, general detection and, potential identification of solutes in solution.

In a typical LCMS experiment, sample is carried through a packed column (stationary phase) by a liquid at high pressure (mobile phase). As the sample moves through the column it is separated based on interactions between the sample and the stationary phase. For example, if the stationary phase is hydrophobic, hydrophobic sample molecules in the mobile phase tend to adsorb to the stationary phase, and the hydrophilic sample molecules will pass through the column and are eluted first. After separation, the sample then flows into the mass spectrometer. The mass spectrometer can then detect and quantify the particular sample.

LCMS methods are historically divided into two different sub-classes based on stationary phases and the corresponding required polarity of the mobile phase. In the context of this dissertation, we use octadecylsilyl (C18) as our stationary phase and a pH-adjusted water-organic

mixture (water – acetonitrile) as our mobile phase. Due to the hydrophobic nature of the stationary phase, this particular type of setup is called reversed phase liquid chromatography.

1.6 Content of This Dissertation

The remainder of this dissertation consists of four experimental chapters and one conclusion and future directions chapter. Each experimental chapter provides insights into the microfluidic fabrication of small molecule loaded PCL-*b*-PEO polymeric nanoparticles and their characterizations. Specific content for each chapter is summarized below:

Chapter 2 provides insight into drug delivery vehicle formulation development in an early stage. In this chapter, PCL-*b*-PEO polymer nanoparticles were fabricated using a two-phase gas-liquid segmented microfluidic platform with and without the encapsulation of paclitaxel (PAX). Two sets of experiments were conducted in this chapter: 1. the study of PCL-*b*-PEO PNP structure without PAX; and, 2. the study of PCL-*b*-PEO PNP structure with PAX. For the work done without PAX encapsulation, we were able to demonstrate reproducible variability of PNP size, morphology, and core crystallinity. For the work done with PAX encapsulation, we were able to reproducibly vary PNP structure as well as function (PAX loading efficiency and release kinetics). This work serves as a proof of concept for two-phase microfluidic self-assembly of PAX encapsulated PCL-*b*-PEO nanoparticles and on-chip variability of PNP structure and function. This work has previously been published as a communication.[23]

Chapter 3 looks into the two-phase microfluidic system as a platform for drug delivery formulation development. In this chapter, the drug surrogate, DiI (1,1′-dioctadecyl-3,3,3′,3′-tetramethylindocarbocyanine perchlorate), is used as the lipophilic encapsulant, and self-assembly of DiI encapsulated PCL-*b*-PEO nanoparticles is carried out on-chip using two water

concentrations. In this chapter we expanded our chemical parameters relevant to control of PNP structure and function. We studied two water contents (cwc + 10 and 75 %) and results indicated that higher water contents resulted in higher core crystallization and lower DiI loading efficiency. We also studied the influence of temperature and release media on DiI diffusional release by monitoring release kinetics in pure water, 1 % phosphate buffered saline (PBS), and 1 % PBS and albumin (45 g / L). This chapter gave insight into the influence of small molecule loading in PCL-*b*-PEO nanoparticles and the influence of release media on diffusional release kinetics. This knowledge was applied to chapter 4 where we moved back from DiI to PAX encapsulation. This chapter has been submitted to be published as an article.

Chapter 4 provides a systematic study in which a whole range of drug delivery system formulation parameters are screened. Self-assembly of the PAX encapsulated PCL-*b*-PEO nanoparticles is conducted on-chip using three different copolymer compositions, two water contents, and four initial drug-to-copolymer ratios. *In vitro* drug release into 1% PBS and albumin (45 g/L) at physiological temperature (37 °C) for all PAX loaded drug delivery systems was monitored. This chapter gave insight into the influence of PAX on PCL-*b*-PEO structure at the limit of small free volume perturbations within the micellar core by loading low initial PAX concentrations. This insight from this work setup the investigation conducted in chapter 5 where PAX concentrations that are therapeutically relevant were explored ($r >> 0.01$).

Chapter 5 looks into the fabrication of PAX-loaded PCL-*b*-PEO nanoparticles at high initial drug-to-copolymer ratios ($r > 0.1$). Self-assembly was conducted on-chip using three flow-rates, three copolymer compositions, and four initial drug-to-copolymer ratios. For five formulations *in vitro* diffusional release and cytotoxicity using the MCF-7 cancer cell lines were also studied. We were able to demonstrate variability of PCL-*b*-PEO PNP structure at high drug

loading ratios. We were also able to demonstrate how microfluidic assembly of these drug loaded PNPs can result in variations of PNP function, such as: drug loading efficiency, *in vitro* diffusional release kinetics, and cytotoxicity. The results from this chapter pave the way for further cytotoxicity studies and eventually *in vivo* studies.

Chapter 6 contains concluding remarks and describes some directions for future work.

1.7 References

(1) Song, H.; Chen, D. L.; Ismagilov, R. F. Reactions in droplets in microflulidic channels. *Angew. Chem.-Int. Edit.* **2006**, *45*, 7336-7356.

(2) Wang, C. W., University of Victoria, 2012.

(3) Stroock, A. D. W., G. *Physics Today* **2001**, 42-49.

(4) Savic, R.; Eisenberg, A.; Maysinger, D. Block copolymer micelles as delivery vehicles of hydrophobic drugs: micelle-cell interactions. *Journal of drug targeting* **2006**, *14*, 343-355.

(5) Zhang, Y.; Chan, H. F.; Leong, K. W. Advanced materials and processing for drug delivery: The past and the future. *Adv. Drug Deliv. Rev.* **2013**, *65*, 104-120.

(6) Ahmad, Z.; Shah, A.; Siddiq, M.; Kraatz, H.-B. Polymeric micelles as drug delivery vehicles. *RSC Advances* **2014**, *4*, 17028-17038.

(7) Eetezadi, S.; Ekdawi, S. N.; Allen, C. The challenges facing block copolymer micelles for cancer therapy: In vivo barriers and clinical translation. *Adv. Drug Deliv. Rev.* **2015**, *91*, 7-22.

(8) Hickey, J. W.; Santos, J. L.; Williford, J. M.; Mao, H. Q. Control of polymeric nanoparticle size to improve therapeutic delivery. *J. Controlled Release* **2015**, *219*, 536-547.

(9) Zhang, L. E., A. *Science* **1995**, *268*, 1728-1731.

(10) Zhang, L. E., A. *J. Am. Chem. Soc.* **1996**, *118*, 3168-3181.

(11) Mai, Y. Y.; Eisenberg, A. Self-assembly of block copolymers. *Chem. Soc. Rev.* **2012**, *41*, 5969-5985.

(12) Allen, C.; Yu, Y.; Maysinger, D.; Eisenberg, A. Polycaprolactone-*b*-poly(ethylene Oxide) Block Copolymer Micelles as a Novel Drug Delivery Vehicle for Neurotrophic Agents FK506 and L-685,818. *Bioconjugate Chem.* **1998**, *9*, 564-572.

(13) Miyata, T.; Masuko, T. Crystallization behaviour of poly(L-lactide). *Polymer* **1998**, *39*, 5515-5521.

(14) Allen, C. E., A.; Maysinger, D. PCL-*b*-PEO Micelles as a Delivery Vehicle for FK506: Assessment of a Functional Recovery of Crushed Peripheral Nerve. *Drug Delivery* **2000**, *7*, 139-145.

(15) Liggins, R. T.; Burt, H. M. Paclitaxel loaded poly(L-lactic acid) microspheres: properties of microspheres made with low molecular weight polymers. *Int. J. Pharm.* **2001**, *222*, 19-33.

(16) Lavasanifar, A.; Samuel, J.; Kwon, G. S. Poly(ethylene oxide)-*block*-poly(l-amino acid) micelles for drug delivery. *Adv. Drug Deliv. Rev.* **2002**, *54*, 169-190.

(17) Liggins, R. T.; Burt, H. M. Paclitaxel loaded poly(l-lactic acid) (PLLA) microspheres: II. The effect of processing parameters on microsphere morphology and drug release kinetics. *Int. J. Pharm.* **2004**, *281*, 103-106.

(18) Geng, Y.; Discher, D. E. Hydrolytic Degradation of Poly(ethylene oxide)-*block*-Polycaprolactone Worm Micelles. *J. Am. Chem. Soc.* **2005**, *127*, 12780-12781.

(19) Cai, S.; Vijayan, K.; Cheng, D.; Lima, E.; Discher, D. E. Micelles of Different Morphologies—Advantages of Worm-like Filomicelles of PEO-PCL in Paclitaxel Delivery. *Pharm. Res.* **2007**, *24*, 2099-2109.

(20) Khan, I. U.; Serra, C. A.; Anton, N.; Vandamme, T. Microfluidics: A focus on improved cancer targeted drug delivery systems. *J. Controlled Release* **2013**, *172*, 1065-1074.

(21) Nicolas, J.; Mura, S.; Brambilla, D.; Mackiewicz, N.; Couvreur, P. Design, functionalization strategies and biomedical applications of targeted biodegradable/biocompatible polymer-based nanocarriers for drug delivery. *Chem. Soc. Rev.* **2013**, *42*, 1147-1235.

(22) Oltra, N. S.; Swift, J.; Mahmud, A.; Rajagopal, K.; Loverde, S. M.; Discher, D. E. Filomicelles in nanomedicine - from flexible, fragmentable, and ligand-targetable drug carrier designs to combination therapy for brain tumors. *J. Mater. Chem. B.* **2013**, *1*, 5177-5185.

(23) Bains, A.; Cao, Y.; Moffitt, M. G. Multiscale Control of Hierarchical Structure in Crystalline Block Copolymer Nanoparticles Using Microfluidics. *Macromol. Rapid Commun.* **2015**, n/a-n/a.

(24) Discher, B. M.; Won, Y.-Y.; Ege, D. S.; Lee, J. C.-M.; Bates, F. S.; Discher, D. E.; Hammer, D. A. Polymersomes: Tough Vesicles Made from Diblock Copolymers. *Science* **1999**, *284*, 1143-1146.

(25) Ahmed, F.; Discher, D. E. Self-porating polymersomes of PEG–PLA and PEG–PCL: hydrolysis-triggered controlled release vesicles. *J. Controlled Release* **2004**, *96*, 37-53.

(26) Kim, Y.; Dalhaimer, P.; Christian, D. A.; Discher, D. E. Polymeric worm micelles as nano-carriers for drug delivery. *Nanotechnology* **2005**, *16*, S484-S491.

(27) Ahmed, F.; Pakunlu, R. I.; Brannan, A.; Bates, F.; Minko, T.; Discher, D. E. Biodegradable polymersomes loaded with both paclitaxel and doxorubicin permeate and shrink tumors, inducing apoptosis in proportion to accumulated drug. *J. Controlled Release* **2006**, *116*, 150-158.

(28) Geng, Y. D., P.; Cai, S.; Tsai, R.; Tewari, M.; Minko, T.; Discher, D.E. Shape effects of filaments versus spherical particles in flow and drug delivery. *Nat. Nanotechnol.* **2007**, *2*, 249-255.

(29) Letchford, K.; Burt, H. A review of the formation and classification of amphiphilic block copolymer nanoparticulate structures: micelles, nanospheres, nanocapsules and polymersomes. *Eur. J. Pharm. Biopharm.* **2007**, *65*, 259-269.

(30) Letchford, K.; Liggins, R.; Wasan, K. M.; Burt, H. In vitro human plasma distribution of nanoparticulate paclitaxel is dependent on the physicochemical properties of poly(ethylene glycol)-*block*-poly(caprolactone) nanoparticles. *Eur. J. Pharm. Biopharm.* **2009**, *71*, 196-206.

(31) Xu, Z.; Yan, B.; Riordon, J.; Zhao, Y.; Sinton, D.; Moffitt, M. G. Microfluidic Synthesis of Photoresponsive Spool-Like Block Copolymer Nanoparticles: Flow-Directed Formation and Light-Triggered Dissociation. *Chem. Mater.* **2015**, *27*, 8094-8104.

(32) Ali, H. S. M. Y., P.; Ali, A. M. A.; Blagden, N. *J. Control. Rel* **2011**, *149*, 175.

(33) Zhang, Q.-X. X., L.-M.; Zhou, Y. *Ind. Eng. Chem.* **2011**, *50*, 13805.

(34) Tran, T. H. N., C. T.; Kim, D.-P.; Lee, Y.-K.; Huh, K. M. *Lab Chip* **2012**, *12*, 589.

(35) Andar, A. U.; Hood, R. R.; Vreeland, W. N.; Devoe, D. L.; Swaan, P. W. Microfluidic Preparation of Liposomes to Determine Particle Size Influence on Cellular Uptake Mechanisms. *Pharm. Res.* **2014**, *31*, 401-413.

(36) Kong, F.; Zhang, X.; Hai, M. T. Microfluidics Fabrication of Monodisperse Biocompatible Phospholipid Vesicles for Encapsulation and Delivery of Hydrophilic Drug or Active Compound. *Langmuir* **2014**, *30*, 3905-3912.

(37) Lim, J.-M.; Swami, A.; Gilson, L. M.; Chopra, S.; Choi, S.; Wu, J.; Langer, R.; Karnik, R.; Farokhzad, O. C. Ultra-High Throughput Synthesis of Nanoparticles with Homogeneous Size Distribution Using a Coaxial Turbulent Jet Mixer. *ACS Nano* **2014**, *8*, 6056-6065.

(38) Shih, R.; Bardin, D.; Martz, T. D.; Sheeran, P. S.; Dayton, P. A.; Lee, A. P. Flow-focusing regimes for accelerated production of monodisperse drug-loadable microbubbles toward clinical-scale applications. *Lab Chip* **2013**, *13*, 4816-4826.

(39) Eyer, K.; Paech, F.; Schuler, F.; Kuhn, P.; Kissner, R.; Belli, S.; Dittrich, P. S.; Kramer, S. D. A liposomal fluorescence assay to study permeation kinetics of drug-like weak bases across the lipid bilayer. *J. Controlled Release* **2014**, *173*, 102-109.

(40) Abbaspourrad, A.; Carroll, N. J.; Kim, S. H.; Weitz, D. A. Polymer Microcapsules with Programmable Active Release. *J. Am. Chem. Soc.* **2013**, *135*, 7744-7750.

(41) He, J.; Wang, L.; Wei, Z. J.; Yang, Y. L.; Wang, C. Y.; Han, X. J.; Nie, Z. H. Vesicular Self-Assembly of Colloidal Amphiphiles in Microfluidics. *ACS Appl. Mater. Interfaces* **2013**, *5*, 9746-9751.

(42) Kang, X. J.; Luo, C. X.; Wei, Q.; Xiong, C. Y.; Chen, Q.; Chen, Y.; Ouyang, Q. Mass production of highly monodisperse polymeric nanoparticles by parallel flow focusing system. *Microfluid. Nanofluid.* **2013**, *15*, 337-345.

(43) Sui, X. F.; Shui, L. L.; Cui, J.; Xie, Y. B.; Song, J.; van den Berg, A.; Hempenius, M. A.; Vancso, G. J. Redox-responsive organometallic microgel particles prepared from poly(ferrocenylsilane)s generated using microfluidics. *Chem. Commun.* **2014**, *50*, 3058-3060.

(44) Thiele, J.; Steinhauser, D.; Pfohl, T.; Forster, S. Preparation of Monodisperse Block Copolymer Vesicles via Flow Focusing in Microfluidics. *Langmuir* **2010**, *26*, 6860-6863.

(45) Khan, W.; Choi, J. H.; Kim, G. M.; Park, S. Y. Microfluidic formation of pH responsive 5CB droplets decorated with PAA-*b*-LCP. *Lab Chip* **2011**, *11*, 3493-3498.

(46) Foster, T.; Dorfman, K. D.; Davis, H. T. Giant biocompatible and biodegradable PEG-PMCL vesicles and microcapsules by solvent evaporation from double emulsion droplets. *J. Colloid Interface Sci.* **2010**, *351*, 140-150.

(47) Ivorra, B.; Redondo, J. L.; Santiago, J. G.; Ortigosa, P. M.; Ramos, A. M. Two- and three-dimensional modeling and optimization applied to the design of a fast hydrodynamic focusing microfluidic mixer for protein folding. *Phys. Fluids* **2013**, *25*, 17.

(48) Kathuria, S. V.; Chan, A.; Graceffa, R.; Nobrega, R. P.; Matthews, C. R.; Irving, T. C.; Perot, B.; Bilsel, O. Advances in turbulent mixing techniques to study microsecond protein folding reactions. *Biopolymers* **2013**, *99*, 888-896.

(49) Capretto, L.; Mazzitelli, S.; Colombo, G.; Piva, R.; Penolazzi, L.; Vecchiatini, R.; Zhang, X.; Nastruzzi, C. Production of polymeric micelles by microfluidic technology for combined drug delivery: Application to osteogenic differentiation of human periodontal ligament mesenchymal stem cells (hPDLSCs). *Int. J. Pharm.* **2013**, *440*, 195-206.

(50) Hung, L. Y.; Chuang, Y. H.; Kuo, H. T.; Wang, C. H.; Hsu, K. F.; Chou, C. Y.; Lee, G. B. An integrated microfluidic platform for rapid tumor cell isolation, counting and molecular diagnosis. *Biomed. Microdevices* **2013**, *15*, 339-352.

(51) Velasco, D.; Tumarkin, E.; Kumacheva, E. Microfluidic Encapsulation of Cells in Polymer Microgels. *Small* **2012**, *8*, 1633-1642.

(52) Wang, C.-W.; Bains, A.; Sinton, D.; Moffitt, M. G. Flow-Directed Loading of Block Copolymer Micelles with Hydrophobic Probes in a Gas–Liquid Microreactor. *Langmuir* **2013**, *29*, 8385-8394.

(53) Kamholz, A. E.; Yager, P. Molecular diffusive scaling laws in pressure-driven microfluidic channels: deviation from one-dimensional Einstein approximations. *Sensors and Actuators B: Chemical* **2002**, *82*, 117-121.

(54) Floyd, T. M.; Schmidt, M. A.; Jensen, K. F. Silicon Micromixers with Infrared Detection for Studies of Liquid-Phase Reactions. *Industrial & Engineering Chemistry Research* **2004**, *44*, 2351-2358.

(55) Knight, J. B.; Vishwanath, A.; Brody, J. P.; Austin, R. H. Hydrodynamic Focusing on a Silicon Chip: Mixing Nanoliters in Microseconds. *Phys. Rev. Lett.* **1998**, *80*, 3863-3866.

(56) Johnson, T. J.; Ross, D.; Locascio, L. E. Rapid Microfluidic Mixing. *Anal. Chem.* **2001**, *74*, 45-51.

(57) Stroock, A. D.; Dertinger, S. K. W.; Ajdari, A.; Mezić, I.; Stone, H. A.; Whitesides, G. M. Chaotic Mixer for Microchannels. *Science* **2002**, *295*, 647-651.

(58) Nanosystems, P. 2014; Vol. 2014.

(59) Leung, A. K.; Hafez, I. M.; Baoukina, S.; Belliveau, N. M.; Zhigaltsev, I. V.; Afshinmanesh, E.; Tieleman, D. P.; Hansen, C. L.; Hope, M. J.; Cullis, P. R. Lipid Nanoparticles Containing siRNA Synthesized by Microfluidic Mixing Exhibit an Electron-Dense Nanostructured Core. *The journal of physical chemistry. C, Nanomaterials and interfaces* **2012**, *116*, 18440-18450.

(60) Zhigaltsev, I. V.; Belliveau, N.; Hafez, I.; Leung, A. K.; Huft, J.; Hansen, C.; Cullis, P. R. Bottom-up design and synthesis of limit size lipid nanoparticle systems with aqueous and triglyceride cores using millisecond microfluidic mixing. *Langmuir* **2012**, *28*, 3633-3640.

(61) Song, H.; Tice, J. D.; Ismagilov, R. F. A Microfluidic System for Controlling Reaction Networks in Time. *Angew. Chem.* **2003**, *115*, 792-796.

(62) Günther, A.; Jhunjhunwala, M.; Thalmann, M.; Schmidt, M. A.; Jensen, K. F. Micromixing of Miscible Liquids in Segmented Gas−Liquid Flow. *Langmuir* **2005**, *21*, 1547-1555.

(63) Schabas, G.; Yusuf, H.; Moffitt, M. G.; Sinton, D. Controlled self-assembly of quantum dots and block copolymers in a microfluidic device. *Langmuir* **2008**, *24*, 637-643.

(64) Wang, C.-W.; Sinton, D.; Moffitt, M. G. Flow-Directed Block Copolymer Micelle Morphologies via Microfluidic Self-Assembly. *J. Am. Chem. Soc.* **2011**, *133*, 18853-18864.

(65) Wang, C.-W.; Bains, A.; Sinton, D.; Moffitt, M. G. Flow-Directed Assembly of Block Copolymer Vesicles in the Lab-on-a-Chip. *Langmuir* **2012**, *28*, 15756-15761.

(66) Chen, Q.; Zhao, H.; Ming, T.; Wang, J.; Wu, C. Nanopore Extrusion-Induced Transition from Spherical to Cylindrical Block Copolymer Micelles. *J. Am. Chem. Soc.* **2009**, *131*, 16650-16651.

(67) Kumaraswamy, G.; Issaian, A. M.; Kornfield, J. A. Shear-Enhanced Crystallization in Isotactic Polypropylene. 1. Correspondence between in Situ Rheo-Optics and ex Situ Structure Determination. *Macromolecules* **1999**, *32*, 7537-7547.

(68) Zhou, W.-J.; Kornfield, J. A.; Ugaz, V. M.; Burghardt, W. R.; Link, D. R.; Clark, N. A. Dynamics and Shear Orientation Behavior of a Main-Chain Thermotropic Liquid Crystalline Polymer. *Macromolecules* **1999**, *32*, 5581-5593.

(69) Kumaraswamy, G.; Verma, R. K.; Issaian, A. M.; Wang, P.; Kornfield, J. A.; Yeh, F.; Hsiao, B. S.; Olley, R. H. Shear-enhanced crystallization in isotactic polypropylenePart 2. Analysis of the formation of the oriented "skin". *Polymer* **2000**, *41*, 8931-8940.

(70) Kumaraswamy, G.; Kornfield, J. A.; Yeh, F.; Hsiao, B. S. Shear-Enhanced Crystallization in Isotactic Polypropylene. 3. Evidence for a Kinetic Pathway to Nucleation. *Macromolecules* **2002**, *35*, 1762-1769.

(71) Wang, C.-W.; Sinton, D.; Moffitt, M. G. *ACS Nano* **2013**, *7*, 1424-1436.

(72) Cowie, J. W. G. V., A. *Polymers: Chemistry and Physics of Modern Materials*; 3 ed.; Taylor & Francis Group: Boca Raton, Florida, 2007.

(73) Riess, G. *Prog. Polym. Sci.* **2003**, *28*, 1107-1170.

(74) Price, C. *Pure Appl. Chem* **1983**, *55*, 1563-1572.

(75) Price, C. C., E. K. M.; Pilcher, G.; Stubberfield, R. B. *Eur. Polym. J.* **1985**, *21*, 627-628.

(76) Zhang, L. Y., K.; Eisenberg, A. *Science* **1996**, *272*, 1777-1779.

(77) Garlotta, D. A literature review of poly(lactic acid). *J. Polym. Environ.* **2001**, *9*, 63-84.

(78) Vinogradov, S. V.; Bronich, T. K.; Kabanov, A. V. Self-assembly of polyamine-poly(ethylene glycol) copolymers with phosphorothioate oligonucleotides. *Bioconjug Chem* **1998**, *9*, 805-812.

(79) Matsumura, Y.; Kataoka, K. Preclinical and clinical studies of anticancer agent-incorporating polymer micelles. *Cancer science* **2009**, *100*, 572-579.

(80) Maeda, H.; Wu, J.; Sawa, T.; Matsumura, Y.; Hori, K. Tumor vascular permeability and the EPR effect in macromolecular therapeutics: a review. *J. Controlled Release* **2000**, *65*, 271-284.

(81) Fang, J.; Nakamura, H.; Maeda, H. The EPR effect: Unique features of tumor blood vessels for drug delivery, factors involved, and limitations and augmentation of the effect. *Adv. Drug Deliv. Rev.* **2011**, *63*, 136-151.

(82) Matsumura, Y.; Maeda, H. A New Concept For Macromolecular Therapeutics In Cancer-Chemotherapy - Mechanism Of Tumoritropic Accumulation Of Proteins And The Antitumor Agent Smancs. *Cancer Res.* **1986**, *46*, 6387-6392.

(83) Wang, W.; Zhang, M. J.; Chu, L. Y. Functional Polymeric Microparticles Engineered from Controllable Microfluidic Emulsions. *Acc. Chem. Res.* **2014**, *47*, 373-384.

(84) Discher, D. E.; Ortiz, V.; Srinivas, G.; Klein, M. L.; Kim, Y.; Christian, D.; Cai, S.; Photos, P.; Ahmed, F. Emerging applications of polymersomes in delivery: From molecular dynamics to shrinkage of tumors. *Prog. Polym. Sci.* **2007**, *32*, 838-857.

(85) Chen, L.-T.; Weiss, L. The Role of the Sinus Wall in the Passage of Erythrocytes Through the Spleen. *Blood* **1973**, *41*, 529-537.

(86) CabralH; MatsumotoY; MizunoK; ChenQ; MurakamiM; KimuraM; TeradaY; Kano, M. R.; MiyazonoK; UesakaM; NishiyamaN; KataokaK. Accumulation of sub-100 nm polymeric micelles in poorly permeable tumours depends on size. *Nat Nano* **2011**, *6*, 815-823.

(87) Braet, F.; Wisse, E.; Bomans, P.; Frederik, P.; Geerts, W.; Koster, A.; Soon, L.; Ringer, S. Contribution of high-resolution correlative imaging techniques in the study of the liver sieve in three-dimensions. *Microsc. Res. Tech.* **2007**, *70*, 230-242.

(88) Soo Choi, H.; Liu, W.; Misra, P.; Tanaka, E.; Zimmer, J. P.; Itty Ipe, B.; Bawendi, M. G.; Frangioni, J. V. Renal clearance of quantum dots. *Nat Biotech* **2007**, *25*, 1165-1170.

(89) Massey, J. A.; Temple, K.; Cao, L.; Rharbi, Y.; Raez, J.; Winnik, M. A.; Manners, I. Self-assembly of organometallic block copolymers: The role of crystallinity of the core-forming polyferrocene block in the micellar morphologies formed by poly(ferrocenylsilane-*b*-dimethylsiloxane) in n-alkane solvents. *J. Am. Chem. Soc.* **2000**, *122*, 11577-11584.

(90) Kim, K. T. M., S. A.; Roeland, J. M.; van Hest, J.C.M. Smart nanocontainers and nanoreactors. *Nanoscale* **2010**, *2*, 844-858.

(91) Cabane, E.; Malinova, V.; Menon, S.; Palivan, C. G.; Meier, W. Photoresponsive polymersomes as smart, triggerable nanocarriers. *Soft Matter* **2011**, *7*, 9167-9176.

(92) Elsabahy, M.; Wooley, K. L. Design of polymeric nanoparticles for biomedical delivery applications. *Chem. Soc. Rev.* **2012**, *41*, 2545-2561.

(93) Renolds, O. *Philos. Trans. R. Soc.* **1883**, *174*, 935-982.

(94) Stone, H. A.; Stroock, A. D.; Ajdari, A. Engineering flows in small devices: Microfluidics toward a lab-on-a-chip. *Annu. Rev. Fluid Mech.* **2004**, *36*, 381-411.

(95) Squires, T. M.; Quake, S. R. Microfluidics: Fluid physics at the nanoliter scale. *Rev. Mod. Phys.* **2005**, *77*, 977-1026.

(96) Teh, S. Y.; Lin, R.; Hung, L. H.; Lee, A. P. Droplet microfluidics. *Lab Chip* **2008**, *8*, 198-220.

(97) Duffy, D. C.; McDonald, J. C.; Schueller, O. J. A.; Whitesides, G. M. Rapid Prototyping of Microfluidic Systems in Poly(dimethylsiloxane). *Anal. Chem.* **1998**, *70*, 4974-4984.

(98) Geng, y. D., D.E. *Polymer* **2006**, *47*, 2519-2525.

(99) Cuong, N.-V.; Li, Y.-L.; Hsieh, M.-F. Targeted delivery of doxorubicin to human breast cancers by folate-decorated star-shaped PEG-PCL micelle. *J. Mater. Chem.* **2012**, *22*, 1006-1020.

(100) https://en.wikipedia.org/wiki/Crystallization_of_polymers. Updated 30 May 2010. Access 26 Feburary 2016.

(101) http://en.wikipedia.org/wiki/Transmission_electron_microscope. Updated 17 June 2009. Access 26 Feburary 2016.

(102) http://en.wikipedia.org/wiki/X-ray_crystallography. Updated 1 December 2011. Access 26 Feburary 2016.

Chapter 2

Multiscale Control of Hierarchical Structure in Crystalline Block Copolymer Nanoparticles using Microfludics

This chapter was reproduced with permission from Aman Bains, Yimeng Cao, and Matthew G. Moffitt *Macro. Molecular Rapid Comm.* **2015**, 36, 2000-2005

2.1 Introduction

The solution self-assembly of amphiphilic block copolymers to form micellar nanoparticles has become one of the most broadly researched topics of colloidal nanoscience.[1-9] A growing number of potential applications, including drug delivery,[10-17] sensing,[18] and medical imaging,[4] highlights the need for methods of generating block copolymer nanoparticles with controlled structural parameters (e.g., size and shape). The vast majority of research efforts have applied variation in chemical conditions (e.g., copolymer composition, concentration, and solvent) to change the nature and strength of intermolecular forces and thus the structural products of self-assembly ("bottom-up" control).[1-9] More recently, a small number of studies have applied forces external to the molecular system (e.g., shear or confinement) to direct the structural outcome of self-assembly ("top–down" control);[22,23] such strategies offer the potential for "dialing in" specific nanostructures through simple changes in processing conditions without the need to alter chemical formulations. For example, recent work from our group has shown that localized high-shear "hot spots" within segmented gas–liquid microfluidic reactors enable flow-directed self-assembly of polystyrene-*block*-poly(acrylic acid) (PS-*b*-PAA), providing "top–down" control of nanoparticle morphologies and sizes via flow rate under constant chemical conditions.[24-27]

Micellar nanoparticles formed from semicrystalline block copolymers, including poly(l-lactide)-*block*-poly(ethylene oxide) (PLLA-*b*-PEO) and polycaprolactone-*block*-poly(ethylene oxide) (PCL-*b*-PEO), have recently garnered increased attention, due in part to the importance of such materials for drug delivery applications.[28] Such nanoparticles exhibit multiscale organization, or structural hierarchy, due to a combination of structural features at the colloidal length scale (≈10–100 nm), characterized by the size and morphology of the nanoparticles, and at

the nanoscale (≈1–10 nm), characterized by the ordering of chain segments within crystallites in the nanoparticle cores. For drug delivery, organization on both of these disparate length scales is critical to the functions of selected targeting and drug release.[29-33] For example, nanoparticle size and morphology are found to strongly influence biodistribution (e.g., via the enhanced permeability and retention effect in tumors) and circulation time,[29-32] while internal crystallinity is a critical factor of particle stability, flexibility, and release rate.[29-33]

The recent interest in microfluidics for preparing drug delivery nanoparticles has been spurred by the potential for fast and efficient on-chip screening and fine control of reagent concentrations.[34,35] However, a microfluidic approach offering continuous variability of structure on *both* critical length scales has not been previously demonstrated; such a platform would greatly enhance opportunities for tailoring nanomedicine function for specific treatments and optimum patient outcomes. In this chapter, we apply a segmented microfluidic reactor to the generation of semicrystalline and biocompatible PCL-*b*-PEO micellar nanoparticles, demonstrating that structural features on multiple length scales, including nanoparticle sizes, morphologies, and internal crystallinities, can be tuned via flow rate under constant chemical conditions. The application of unique flow fields[24-27] within the reactor to direct multiple levels of organization simultaneously through a single control variable highlights the general utility of this microfluidic reactor for the controlled manufacturing of hierarchical polymeric nanoparticles. Next, we demonstrate a proof-of-concept application of the microfluidic platform to the production of PCL-*b*-PEO drug delivery nanoparticles containing the anticancer agent paclitaxel (PAX); we show that flow-directed control of multiscale structure enables optimization of PAX loading and top–down variability of drug release kinetics.

2.2 Experimental Procedure

2.2.1 Materials.

Poly(caprolactone)-*block*-poly(ethylene oxide) (PCL_{105}-*b*-PEO_{114}, where numbers in subscripts denote number-average degrees of polymerization for the respective blocks) was purchased from Advanced Polymer Inc. and used as received. *N*,*N*-dimethylformamide (DMF) (Aldrich, 99.9+%, HPLC grade, H_2O < 0.03%) was used as received without further purification. Paclitaxel from Polymed Therapeutics, Inc. was used as received. All quantitative stock solutions of PCL-*b*-PEO in DMF or PCL-*b*-PEO/PAX in DMF were prepared gravimetrically by accurately weighing the solid(s) into a glass vial followed by gravimetric addition of a known quantity of DMF; stock solutions were equilibrated overnight with stirring before further use.

2.2.2 Critical Water Content Determination.

Static light scattering (SLS) measurements were carried out to accurately determine the critical water content (cwc) of 0.33 wt % DMF solutions of PCL-*b*-PEO, which was the initial condition for all self-assembly experiments in this study. SLS measurements were carried out using a Brookhaven Instruments photon correlation spectrometer equipped with a BI-200SM goniometer, a BI-9000AT digital autocorrelator, and a Melles Griot He-Ne Laser (633 nm) with a maximum power output of 75 mW.

A 1.0 wt % stock solution of PCL-*b*-PEO in DMF was filtered through a Teflon syringe membrane filter with a nominal pore size of 0.45 μm (VWR) into precleaned scintillation vials. The filtered stock was then diluted to 0.33 wt % by gravimetric addition of the required quantity of DMF. To the resulting ~6 g of solution, deionized water was added in successive 0.03-0.06 g quantities *via* a microsyringe equipped with two membrane filters (VWR) with nominal pore size

of 0.20 μm connected in series. After each addition of water, the solution was agitated using a vortexer to aid in mixing. The solution was then allowed to equilibrate for 15 min before measuring the scattered light intensity. All measurements were carried out at a scattering angle of 90° and a temperature of 23 °C. From the resulting plot of scattered light intensity versus weight percentage of added water (Table 7.1), the cwc was determined from the intercept of linear fits to the baseline and the region of the plot showing a sharp increase in scattered light intensity. Determination of the cwc was carried out in triplicate from the same stock solution and the mean value and standard deviation of the three measurements were used to calculate the reported cwc and experimental error: cwc = 5.5 ± 0.4 wt %.

2.2.3 Microfluidic Chip Fabrication

Negative masters were fabricated on high quality silicon wafers (Silicon Quest International, Santa Clara, CA) using the negative photoresist SU-8 100 (Microchem Inc.) in the following manner. Immediately prior to use, the wafer was heated on a hot plate at 200 °C for 20 minutes to remove moisture. A 150 μm-thick SU-8 film was spin-coated onto the wafer and then heated to 95 °C for 60 minutes to remove residual SU-8 solvent. A photomask was then placed over the SU-8 film and exposed to UV light for 180 s. Finally, the UV-treated film was heated at 95 °C for 20 min before submersion in SU-8 developer (Microchem) until all unexposed photoresist was removed.

Poly(dimethylsiloxane) (PDMS) microfluidics chips were fabricated from the negative masters using a SYLGARD 184 silicon elastomer kit (Dow Corning, Midland, MI). For chips used in the preparation of nanoparticles without PAX, an elastomer base-to-curing agent ratio of 10:1 was employed as recommended by the kit. However, improved adhesion between the

channel and substrate PDMS layers was later found when base-to-curing agent ratios were adjusted to 7:1 and 20:1 for the two layers, respectively; these ratios were employed for the PAX-encapsulation experiments described the text. For fabrication of all PDMS chips, the elastomer and curing agent were mixed together and degassed in a vacuum chamber. The degassed PDMS was then poured over a negative master in a Petri dish and further degassed until all remaining air bubbles were removed. The PDMS was then heated at 85 °C for ~60 min until cured. The microfluidic chip was then peeled off of the negative master and holes were punched through its reservoirs to allow for the insertion of tubing. A thin PDMS film (substrate layer) was also formed on a glass slide by spin-coating and was permanently bonded to the base of the microfluidic reactor (channel layer) after both components were exposed to oxygen plasma for 60 s. The resulting microfluidic reactors have a set channel depth of 150 μm and consist of a sinusoidal mixing channel 100 μm wide and 18 mm in length and a sinusoidal processing channel 200 μm wide and 740 mm in length.

For further stabilization of the bubble generation process, an external resistor chip was used between the Ar gas tank and the microfluidic chip. The resistor chips served as high pressure drop systems to efficiently dampen the pressure fluctuations caused by the Ar gas tank and the bubble generation process. The total pressure drop in the external resistor chip was at least one order of magnitude higher than the pressure drop in the reaction channel. The resistor chip channels were 1000 mm long, 150 μm deep and 400 μm wide.

2.2.4 Flow Delivery and Control

Pressure-driven flow of liquids to the reactor inlet was provided using 1 mL gastight syringes (Hamilton, Reno, NV) mounted on syringe pumps (Harvard Apparatus, Holliston, MA). The

microfluidic chip was connected to the liquid syringes *via* 1/ 16th-inch (OD) Teflon tubing (Scientific Products and Equipment, ON). Gas flow was introduced to the chip *via* an Ar tank regulator and a downstream regulator (Johnston Controls) for fine adjustments. The chip was connected to the downstream regulator through a 1/16th-inch (OD) / 100-μm (ID) Teflon tube (Upchurch Scientific, Oak Harbor, WA). The liquid flow rate (Q_{liq}) was programmed *via* the syringe pumps and the gas flow rate (Q_{gas}) was fine-tuned *via* the downstream pressure regulator in order to dial in the nominal total flow rates of 5, 25, 50 and 100 μL/min described in the main text. Due to the compressible nature of the gas and the high gas/liquid interfacial tension, discrepancies arise between the nominal (programmed) and actual values of Q_{gas}, Q_{gas}/Q_{liq}, and the total flow rate (Q_{total}). Therefore, actual gas flow rates were calculated from the frequency of bubble formation and the average volume of gas bubbles, determined from image analysis of the mean lengths of liquid and gas plugs, L_{liq} and L_{gas}, respectively, under a given set of flow conditions. This method of flow calculation has been previously employed in the context of gas-liquid segmented flow in the microfluidic device. Actual flow parameters pertaining to each microfluidic experiment described in the chapter are listed in

Table 7.3 and Table 7.4. For all experiments, the relative gas-to-liquid flow ratio, Q_{gas}/Q_{liq} ~1 and all actual Q_{total} values are within 10% of nominal values reported in the main text.

Visualization of the gas bubbles and liquid plugs within the microfluidic reactor was achieved using an upright optical microscope (Omax) with a 10x-objective lens. Images were captured using a 2.07 megapixel PupilCam (Ken-A-Vision) and mean lengths of liquid and gas plugs were determined from the images using image analysis software (ImageJ).

2.2.5 Microfluidic Preparation of PCL-*b*-PEO Nanoparticles

For microfluidic preparation of nanoparticles without loaded drug, the following three fluid streams were combined at equal flow rate to form gas-segmented liquid plugs within the reactor: (1) 1.0 wt % solution of PCL-*b*-PEO in DMF, (2) a separator stream containing DMF only, and (3) a DMF solution containing either 22.5, 31.5, or 46.5 wt % deionized water. Combination of the three liquid streams yielded steady-state on-chip concentrations of 0.33 wt % copolymer and either 7.5, 10.5, or 15.5 wt % water, corresponding to 2.0, 5.0, and 10.0 wt % above the cwc (5.5 wt %), respectively. Microfluidic flow conditions were selected and controlled as described in the previous section.

Nanoparticle samples without loaded drug were collected from the reactor into empty vials for immediate analysis by TEM, XRD, and DSC as described in the corresponding sections below. All samples were prepared in triplicate under the specified chemical and flow conditions.

2.2.6 Microfluidic Preparation of PAX-Loaded PCL-*b*-PEO Nanoparticles

For microfluidic preparation of nanoparticles loaded with drug, similar streams to the preparation of nanoparticles without drug were combined at equal flow rate, except that PAX was codissolved in the copolymer stream. Thus, the following three fluid streams were combined at equal flow rate to form gas-segmented liquid plugs within the reactor: (1) 1.0 wt % solution of PCL-*b*-PEO in DMF with codissolved PAX in a drug : copolymer ratio of 0.01 (w/w), (2) a separator stream containing DMF only, and (3) a DMF solution containing 31.5 wt % deionized water. Combination of the three liquid streams yielded steady-state on-chip concentrations of 0.33 wt % copolymer and 10.5 wt % water, corresponding to 5.0 wt % above the cwc (5.5 wt %). Microfluidic flow conditions were selected and controlled as described in the previous section.

Nanoparticle samples with loaded drug were collected from the reactor into vials containing a 10x-excess volume of deionized water, followed by 12 h dialysis against deionized water (with changing of water every hour for the first 4 h of dialysis) to remove residual DMF and unencapsulated PAX. The resulting aqueous dispersions of PAX-loaded nanoparticles were analyzed by TEM, XRD, and fluorescence anisotropy, and also used for studies of PAX loading efficiencies and release kinetics, as described in the corresponding sections below. All samples were prepared in triplicate under the specified chemical and flow conditions.

2.2.7 Bulk Preparation of PAX-Loaded PCL-*b*-PEO Nanoparticles.

PAX-loaded nanoparticles were also prepared by a conventional drop-wise water addition method described elsewhere in the literature for comparison with microfluidic preparations. Initial conditions for self-assembly were kept identical to the on-chip formulations. Thus, to ~5 mL of a 0.33 wt % copolymer solution in DMF with codissolved PAX at a drug : copolymer ratio of 0.01 (w/w), water was added drop-wise using a micropipette at a constant rate of 20 μL every 10 s with moderate magnetic stirring (600 RPM). Drop-wise water addition at constant rate was continued to a water content of 80 wt %, then the nanoparticles were quenched immediately into 10x-volume excess of deionized water, followed by 12 h dialysis against deionized water (with changing of water every hour for the first 4 h of dialysis) to remove residual DMF and unencapsulated PAX. The resulting aqueous dispersion of PAX-loaded nanoparticles was analyzed by TEM, XRD, and fluorescence anisotropy, and also used for studies of PAX loading efficiencies and release kinetics, as described in the corresponding sections below. The sample was prepared in triplicate under the specified conditions.

2.2.8 Transmission Electron Microscopy

Transmission electron microscopy (TEM) was performed using a JEOL JEM-1400 TEM, operating at an accelerating voltage of 65 kV and equipped with a Gatan Orius SC1000 CCD camera. TEM images were obtained by depositing diluted dispersions (~0.03 wt % copolymer) consisting of either PCL-*b*-PEO nanoparticles in DMF/water or PAX-loaded PCL-*b*-PEO nanoparticles in water onto carbon-coated 300 mesh copper TEM grids as described below.

Uranyl acetate is a negative stain that selectively binds to the PEO coronal chains, providing reverse contrast for the PCL cores, which appear white in TEM images of stained samples. For reverse staining experiments, nanoparticle dispersions were mixed with 1 wt. % aqueous solution of uranyl acetate in a 1:1 ratio (v/v) and one drop of the resulting mixture was deposited onto a TEM grid. Excess liquid was immediately removed using lens paper, followed by drying of remaining liquid under ambient conditions.

Due to the high electron density of uranyl acetate, negative staining generally impedes visualization of the internal lumen of vesicle structures, such that vesicles and spheres cannot be readily distinguished from stained samples. Therefore, all samples revealing aggregates of spherical shape in negative contrast TEM images were also imaged without staining. In unstained images, contrast is provided by high density PCL crystallites which appear dark relative to both the background and the internal lumen of vesicles, such that vesicles appear hollow in unstained images. We find that one complication of imaging PCL-*b*-PEO nanoparticles without staining is that upon drying under ambient conditions, deposited dispersions form large crystallites of PEO which are prominent “drying artifacts” in the resulting TEM images, obscuring identification of micellar PCL cores. To avoid this problem, micellar dispersions deposited without reverse staining were freeze-dried on TEM grids using the following method.

First, one drop of the micellar dispersion was deposited onto a TEM grid and excess liquid was immediately removed using lens paper. The remaining liquid was then vitrified by submerging the TEM grid into liquid ethane. The resulting vitrified sample was then freeze-dried under vacuum. Finally, for the morphological identification of lamellar aggregates, Pt/Pd shadowing of unstained aggregates following freeze-drying was carried out at a shadowing angle of 45°; aggregate heights were then calculated from shadow lengths on the resulting TEM images.

For each set of conditions (water content and flow rate), reported prominent morphologies and mean dimensions from TEM of nanoparticle aggregates without (Table 7.1, Appendix I) and with (Table 7.2, Appendix I) loaded PAX were determined from TEM analysis of three separate preparations starting with three individually-prepared stock solutions. For each sample preparation and TEM grid deposition method (unstained, stained, and shadowed), at least 2-3 TEM images taken in different regions of the grid were evaluated. Prominent morphologies for each condition were assigned based on the following definitions with associated evaluation methods in brackets. Spheres were defined as aggregates with circular projections (TEM with staining) but without internal lumen (TEM without staining). Vesicles were defined as aggregates with circular projections (TEM with staining) with internal lumen (TEM without staining). Cylinders were defined as high aspect-ratio filaments of approximately regular width (TEM with staining). Lamellae were defined as irregularly-shaped aggregates (TEM with staining) with heights significantly smaller than their lateral dimensions (TEM with shadowing); from cases where aggregate shadowing was carried out, lamellae heights were determined to be ~7 nm. For each preparation, mean dimensions were determined from ~400 particles; therefore, for each of the mean dimensions in Tables 7.1 and 7.2, N = 400 x 3 preparations = ~1200, such that the reported errors (~5-25%) reflect reproducibility of the microfluidic preparation method.

Sizing errors associated with TEM instrumental fluctuations were determined to be ~5%. Mean sphere diameters and cylinder widths were determined exclusively from TEM images with staining. For determination of mean vesicle wall thicknesses, mean vesicle radii were determined from TEM images with staining and mean lumen radii were determined from TEM images without negative staining and the difference of these two values was taken as the mean wall thickness. Averaging and statistical analysis of dimensions from TEM images was conducted using Image J software.

To confirm that nanoparticle morphologies were not significantly affected by solvent removal in the TEM preparations described above, we also performed cryogenic transmission electron microscopy (cryo-TEM) on selected samples in the Bioimaging Facility at the University of British Columbia. For these experiments, one drop of micellar dispersion was deposited onto a TEM grid. The sample was then vitrified in liquid ethane using an FEI Vitrobot Mark 4 before being inserted into the FEI Tecnai G2 200kV TEM operating at an accelerating voltage of 75 kV. Images were taken using a high-resolution FEI Eagle 4K bottom mount CCD camera.

2.2.9 Dynamic Light Scattering

Effective hydrodynamic diameters of PAX-loaded PCL-*b*-PEO nanoparticles were determined using dynamic light scattering (DLS). DLS measurements were carried out using a Brookhaven Instruments photon correlation spectrometer equipped with a BI-200SM goniometer, a BI-9000AT digital autocorrelator, and a Melles Griot He-Ne Laser (633 nm) with a maximum power output of 75 mW. All DLS measurements of PAX-loaded nanoparticles were

performed in pure water and an experimental temperature of 23˚C and at a scattering angle of 90˚.

After overnight dialysis against deionized water to remove residual DMF and unencapsulated PAX, PAX-loaded nanoparticles were transferred to pre-cleaned scintillation vials then diluted 5x using deionized water filtered through two nylon syringe filters in series with nominal pore sizes of 0.2 μm (National Scientific Company) to give a final copolymer concentration of ~0.07 mg/mL. For each nanoparticle preparation, mean effective hydrodynamic sizes were determined from three measurements of the autocorrelation function using cumulent analysis. Reported mean effective hydrodynamic diameters (Figure S7) are averages determined from triplicate nanoparticle preparations under the specified conditions.

2.2.10 X-Ray Diffraction.

X-ray diffraction measurements were performed on a Rigaku Miniflex diffractometer with a Cr source (KR radiation, λ = 2.2890 Å) operating at 30 kV and 15 mA with a resolution of 0.05° (2θ) and a scan speed of 1°/min. X-ray diffraction profiles were collected for 2θ ranging from 10-80°.

For XRD sample preparation, solvent was removed from nanoparticles in water/DMF or PAX-loaded nanoparticles in water by rotory evaporation at 25 °C until solid films were obtained (~ 1 hour rotary evaporation time). The resulting films were then scraped as a powder into the XRD specimen holder with no subsequent drying step to remove residual solvent. We note that this preparation method will significantly increase the crystallinity of coronal PEO blocks relative to their colloidal state, as removal of water from the nanoparticle coronae will allow initially-solubilized PEO chains to pack together. However, the crystallinity of the core-

forming PCL blocks is not expected to be strongly affected when nanoparticle powders are recovered by rotory evaporation of the colloid, according to the following considerations: In the case of the purely-aqueous PAX-loaded nanoparticles, the hydrophobic nanoparticle cores will contain no water and so removal of water will have no significant effect on the microphase-separated cores. In the case of nanoparticles in DMF/water, the semicrystalline nanoparticle cores will be highly swollen with DMF; during rotory evaporation at 25 °C, bulk DMF/water will evaporate first, leaving plasticizing DMF solubilized within the nanoparticle cores such that core crystallinity within the resulting nanoparticle powders should not be significantly different from that in the colloid state. Therefore, our XRD experiments should provide a reasonable probe of nanoparticle core crystallinity in the colloidal state; this conclusion is supported by the observed flow-dependence of PCL crystallinity, and corroborated by fluorescence anisotropy experiments described in the following section.

Peak deconvolution was done using Origin Pro Version 8.1. Two characteristic reflections for each of crystalline PCL and crystalline PEO were identified from the literature and these were used to fix the positions of four Lorentzian peak contributions to the fit; another small Lorentzian peak contribution was used to account for a small shoulder on the more intense PCL peak in order to obtain a good fit. Thus, XRD data were fit to a sum of 6 Lorentzian functions: 3 peaks assigned to crystalline PCL (2θ = 32.5, 32.7, and 35.7), 2 peaks assigned to crystalline PEO (2θ = 29.2 and 35.4), and 1 peak (no fixed position) assigned to incoherent scattering from amorphous copolymer (amorphous halo). Areal peak contributions from the three components (crystalline PCL, crystalline PEO, and amorphous copolymer) were then determined by integration and percentages of crystalline PCL and PEO were calculated using:

$$\% \textit{ Crystalline } \text{PCL} = A_{\text{PCL}}/A_{\text{total}}$$

$$\% \textit{ Crystalline } \text{PEO} = A_{\text{PEO}}/A_{\text{total}},$$

where $A_{\text{total}} = A_{\text{PCL}} + A_{\text{PEO}} + A_{\text{amorph.}}$ Also, for the copolymer:

$$\% \textit{ Crystalline Total} = \% \textit{ Crystalline } \text{PCL} + \% \textit{ Crystalline } \text{PEO}.$$

Reported *% Crystalline* PCL, *% Crystalline* PEO, and *% Crystalline Total* values from XRD are averages determined from triplicate nanoparticle preparations under the specified conditions.

2.2.11 Differential Scanning Calorimetry

To confirm the reported flow-dependence of copolymer crystallinity determined from XRD results, we also determined *% Crystalline Total* for PCL-*b*-PEO nanoparticles prepared under various flow conditions using differential scanning calorimetry (DSC). DSC measurements were performed using a SDT Q600 DSC instrument over a temperature range of 25 – 100 °C (Figure 7.16; Appendix I). For DSC sample preparation, solvent was removed from nanoparticles in water/DMF by rotory evaporation at 25 °C until solid films were obtained. The resulting films were then scraped as a powder onto an alumina crucible for analysis. DSC traces were analyzed using TA Instruments Universal Analysis software to determine the total specific enthalpy of the overlapping endothermic melting transitions for crystalline PEO and crystalline PCL. The total melting enthalpy was calibrated using a known mass of PCL-*b*-PEO nanoparticles for which XRD data indicated *% Crystalline Total* = 100% (prepared on-chip at cwc + 75 wt % and Q_{total} = 100 μL/min); measured specific enthalpies were then converted into *% Crystalline Total* values for the various samples prepared at different flow rates (Figure 3).

Reported *% Crystalline Total* values from DSC are averages determined from triplicate nanoparticle preparations under the specified conditions.

2.2.12 Fluorescence Anisotropy

Fluorescence anisotropy was used to investigate the core microviscosity of PAX-loaded nanoparticles in order to corroborate the flow-dependence of core crystallinity determined using XRD. Unlike XRD, fluorescence measurements are done in the colloidal state and thus allow the core environment to be probed *in situ*, without removal of solvent. The depolarization of the fluorescent probe 1,6-diphenyl-1,3,5-hexatriene (DPH) is sensitive to the microviscosity of its surroundings,[30] with higher probe anisotropies indicating higher microviscosities within the core. Therefore, the DPH probe was loaded into the hydrophobic cores of PAX-loaded nanoparticles in the following manner. Approximately 1 g of a ~0.04 wt % DPH solution in chloroform was added to ~5 g of an aqueous dispersion of PAX-loaded nanoparticles to generate a liquid-liquid two-phase mixture. The mixture was stirred vigorously for 12 hours under ambient conditions allowing the chloroform to evaporate and the DPH to partition into the nanoparticle cores.

Fluorescence measurements were carried out using an Edinburgh Instruments FLS 820 fluorimeter equipped with a Xe 450 W arc lamp and a red-sensitive PMT (R928-P). DPH fluorescence intensity was measured using excitation and emission wavelengths of 365 and 428 nm, respectively. For each PAX-loaded nanoparticle sample, fluorescence intensity of DPH was measured with relative polarizer orientations parallel (I_{vv}) and perpendicular (I_{vh}) with respect to the vertically-polarized excitation light. The fluorescence anisotropy (r) was then calculated using:

$$r = \frac{I_{vv} - I_{vh}}{I_{vv} + 2I_{vh}}$$

To rule out experimental artifacts, two control experiments were conducted. First, the anisotropy of the DPH probe in chloroform solution was measured under identical conditions, resulting in $r = 0$ as expected. Then, the fluorescence intensities I_{vv} and I_{vh} were measured for the PAX-loaded nanoparticles without DPH probe and both signals were found to be negligible. Reported fluorescence anisotropies are averages determined from triplicate nanoparticle preparations under the specified conditions.

2.2.13 PAX Loading Efficiency Determination.

To determine PAX loading efficiencies, PAX-loaded nanoparticles were dissolved in acetonitrile (ACN): first, water was removed from a known mass (~1 g) of an aqueous dispersion of PAX-loaded nanoparticles of known copolymer concentration by rotary evaporation at 25 °C; then a known mass (~0.5 g) of ACN was added to the resulting solid and the solution was stirred for 4 h. High performance liquid chromotography-mass spectrometry (HPLC-MS, Ultimate 3000, Thermo Scientific) was then used with a C18 column (Phenomenex Luna 5u C18) and a constant eluent composition of 65/35 acetonitrile/water (v/v) with 1 vol % formic acid to quantify the concentration of drug in the resulting solutions. Sample injection volumes were 50 μL and the HPLC-MS flow rate was set to 1 mL/min. For loading efficiency determinations, PAX solution concentrations were sufficiently high such that they could be detected and quantified using the diode array detector (DAD) by monitoring the elution of PAX at a characteristic absorption wavelength of 227 nm. A calibration curve for the DAD was generated by analysis of 5 stock solutions containing different known PAX concentrations in ACN. Quantities of PAX in the various dissolved nanoparticle solutions were determined and loading efficiencies calculated for each sample using the following expression:

$$loading\ efficiency\ (\%) = \frac{PAX\ in\ micelles\ (g)}{total\ PAX\ used\ (g)} \times 100\%$$

Reported loading efficiencies are averages determined from triplicate nanoparticle preparations under the specified conditions.

2.2.14 *In Vitro* PAX Release Kinetics.

Experiments were carried out to monitor the *in vitro* release of PAX from PAX-loaded nanoparticles using HPLC-MS (see previous section for instrument specifications). In a typical experiment, ~10 g of aqueous dispersion of PAX-loaded nanoparticles were transferred to a 10 mL-dialysis bag (SpectrumLabs, MWCO 100 kDa) which was placed in a 4 L-beaker of the release medium, consisting of ~2.5 L of a 1% phosphate buffer saline (PBS, pH = 7.4) solution containing albumin (Sigma Aldrich) at a concentration of 45 g/L; throughout release experiments, the release medium was constantly stirred using magnetic stirring and maintained at physiological temperature (37°C) in an incubator. At each predetermined time, an aliquot of known mass (~1 g) was removed from the dialysis bag to which a known mass (~150 mg) of a deuterated PAX internal standard (d5-PAX, ~1 mg/mL, Toronto Research Chemicals) in ACN was added. A liquid-liquid extraction was conducted using methyl *tert*-butyl ether (Sigma Aldrich). The top organic liquid phase containing PAX and internal standard was decanted from the lower aqueous phase containing albumin. The methyl *tert*-butyl ether was then removed by rotary evaporation at 25 °C then a known quantity of ACN (0.1-0.5 g depending on release time) was added. The resulting solution was injected into the HPLC-MS and PAX and d5-PAX were detected and quantified using the MS detector by single ion monitoring (SIM) of the m/z = 286 and m/z = 291 peaks, respectively. Separate calibration curves for SIM detection of PAX and the internal standard were generated by analysis of five known stock solutions of both analytes. The

internal standard (d5-PAX) was used to determine the efficiency of each liquid-liquid PAX extraction, which was found to vary from 60-80%. These extraction efficiencies were used to calculate PAX concentrations in each aliquot before liquid-liquid extraction from PAX concentrations determined by HPLC-MS. From determined masses of PAX in aliquots obtained at different release times, percentages of PAX released were calculated relative to the determined mass of nanoparticle-encapsulated PAX at the $t = 0$ release time. Reported release percentages at each release time are averages determined from triplicate nanoparticle preparations under the specified conditions. Although release kinetics in such *in vitro* experiments have been shown to be very different from *in vivo* pharmakinetics,[5] they provide useful information on drug diffusion and nanoparticle breakup that may contribute to drug release in pharmaceutical applications.

2.2.15 Monitoring Hydrolytic Degradation of PAX-Loaded PCL-*b*-PEO Nanoparticles

During the *in vitro* release of PAX into PBS and albumin (pH = 7.4, 37°C), aliquots of PAX-loaded nanoparticles were removed at four different release times (t = 0, 6, 12, and 24 h) for analysis by TEM and DLS, in order to monitor hydrolytic degradation of the nanoparticles. Aliquots taken at t = 0 and 6 h were analyzed immediately after removal from the release medium; aliquots taken at t = 12 and 24 h were first dialyzed against pure water overnight at 4 °C to remove accumulated albumin and then analyzed. For TEM analysis, aliquots were directly deposited onto TEM grids with reverse staining (as previously described) for analysis of nanoparticle morphologies; for DLS analysis, aliquots were diluted 10x with deionized water and then analyzed for effective hydrodynamic sizes and size distributions.

2.3 Results and Discussion

The specific polymer used in this work is PCL_{105}-*b*-PEO_{114}, where numbers in subscripts denote number-average degrees of polymerization for the respective blocks. The gas–liquid segmented microfluidic system (Figure 2.1) is described in our previous papers.[24-27] For all microfluidic and bulk (control) self-assembly experiments, the starting condition was 0.33 wt% copolymer in *N*,*N*-dimethylformamide (DMF) with micellization induced by the addition of water above the critical water concentration (cwc = 5.5 wt%). Increasing the total flow rate (gas + liquid) increases linearly the maximum shear rate in the hot spots; therefore, multiple flow rates and water contents were investigated in order to vary both chemical and shear forces during self-assembly. For preliminary PAX loading experiments reported here, a drug:copolymer ratio of 0.01 (w/w) was employed.

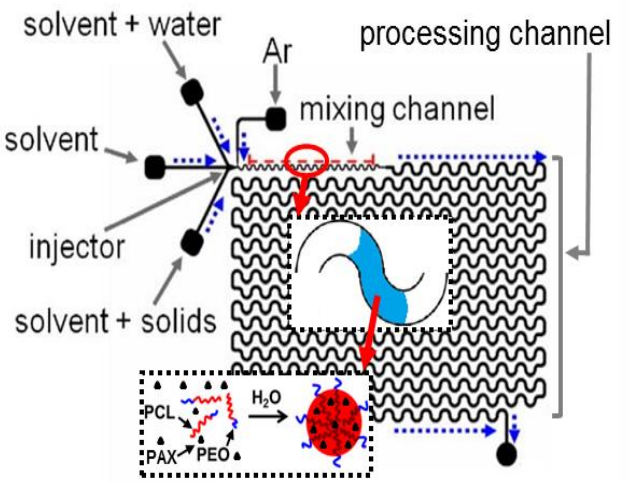

Figure 2.1 Schematic of the gas-liquid segmented reactor and on-chip formation of PAX-loaded PCL-*b*-PEO PNPs.

Microfluidic self-assembly (Figure 2.1) was initiated by combining three liquid streams at the reactor inlet: DMF/PCL-*b*-PEO (or DMF/PCL-*b*-PEO/PAX for drug loading), DMF (separator stream), and DMF/water. The streams were joined with argon gas, which

compartmentalized the liquid plugs and induced chaotic advection, enabling fast mixing and triggering nanoparticles formation. PCL-*b*-PEO nanoparticles then proceeded through the processing channel where they were exposed to high-shear hot spots. Unless otherwise stated, nanoparticles without PAX were collected from the reactor into empty vials for immediate characterization by transmission electron microscopy (TEM), X-ray powder diffraction (XRD), and differential scanning calorimetry (DSC); PAX-loaded PCL-*b*-PEO nanoparticles were collected into a 10-times excess volume of water and then dialyzed overnight to remove residual DMF and unencapsulated PAX, followed by characterization and release studies. For comparison with on-chip results, a conventional bulk PAX-loading experiment was carried out in which water was added dropwise to the copolymer/PAX solution to 80 wt% followed by overnight dialysis.[10]

We first investigated the on-chip self-assembly of PCL-*b*-PEO without PAX. Figure 2.2 shows TEM images of the plethora of nanoparticle morphologies obtained at three water contents (cwc + 2 wt%, cwc + 5 wt%, and cwc + 10 wt %) and four flow rates (Q = 5, 25, 50, and 100 μL/min) from a single PCL-*b*-PEO block copolymer. At each water content, all major nanoparticle morphologies—spheres, cylinders (filomicelles), lamellae, and vesicles (polymersomes)—are formed on-chip by changing flow rate between Q = 5 and 100 μL/min. This demonstrates top–down control of PCL-*b*-PEO morphologies via flow rate under constant chemical conditions. At each water content, the observed morphologies change nonmonotonically, going through a minimum in interfacial curvature with increasing flow rate. For example, at cwc + 10 wt% (Figure 2.2 I–L), high-curvature spheres are generated at Q = 5 μL/min, with lower-curvature cylinders and lamellae, and then vesicles, appearing as the flow rate increases to Q = 25 and 50 μL/min, respectively; finally, high-curvature spheres reappear at

Q = 100 μL/min. Prominent morphologies and their mean dimensions for each set of conditions are reported in Table 7.1 (Appendix I) with excellent reproducibility observed over multiple preparations (Figures 7.2–7.4; Appendix I).

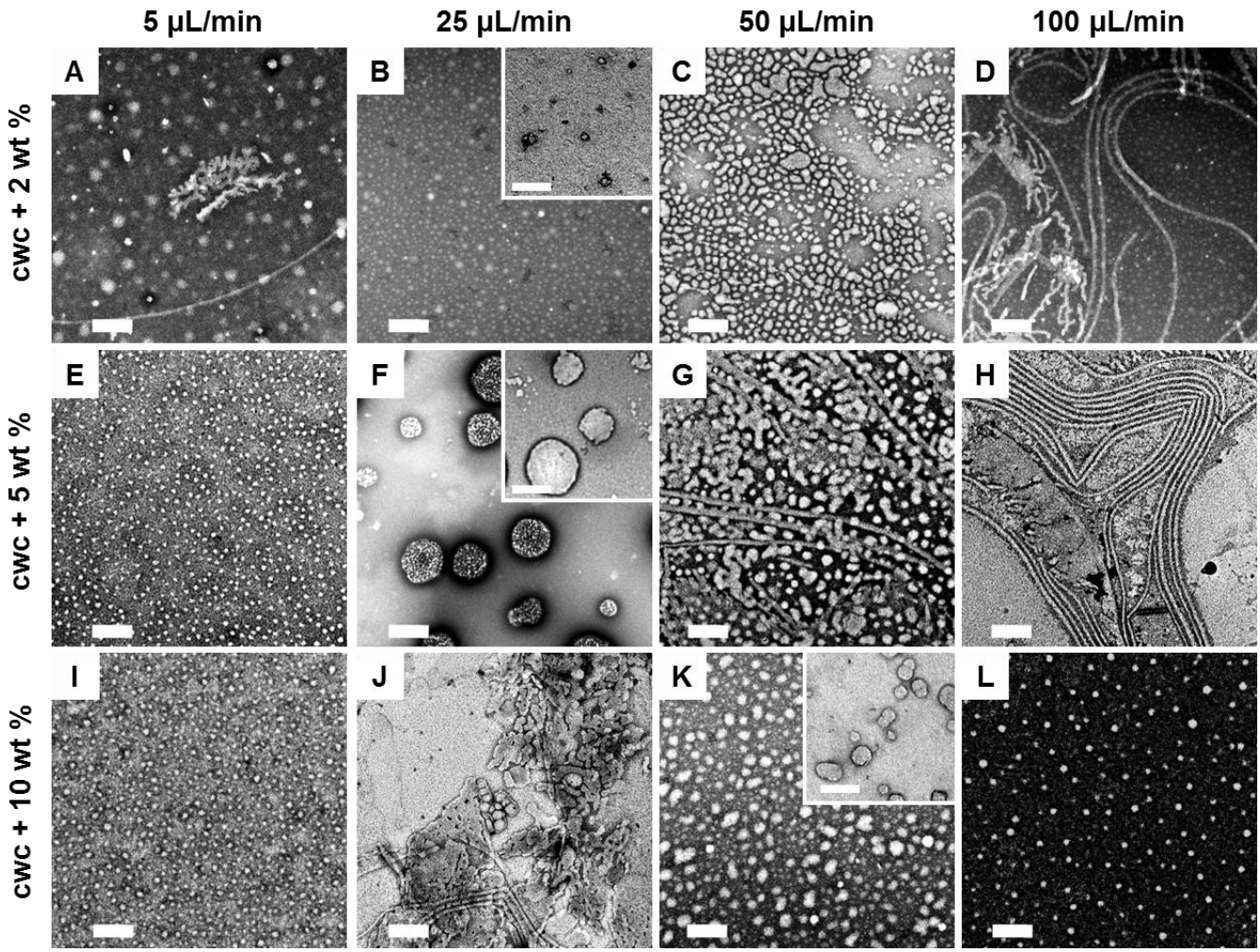

Figure 2.2 TEM images of multiple flow-directed morphologies of PCL-*b*-PEO PNPs formed on-chip at various water contents and flow rates. Main images were produced with negative staining with uranyl acetate; insets are unstained images allowing visualization of the internal lumen of vesicles. Main image scale bars are 200 nm and inset scale bars are 100 nm.

These flow-directed morphologies reflect a complex interplay of chemical and shear forces operating in the channels. Similar to PS-*b*-PAA self-assembly within an identical

reactor[6], shear-induced coalescence and breakup mechanisms are expected to strongly influence morphologies formed on-chip. As described in our previous publications,[6] the vast majority of nanoparticles (≈98 % v/v) form outside the highly localized, high-shear hot spots. Following their initial formation upon mixing with water near the injector, nanoparticles circulate through

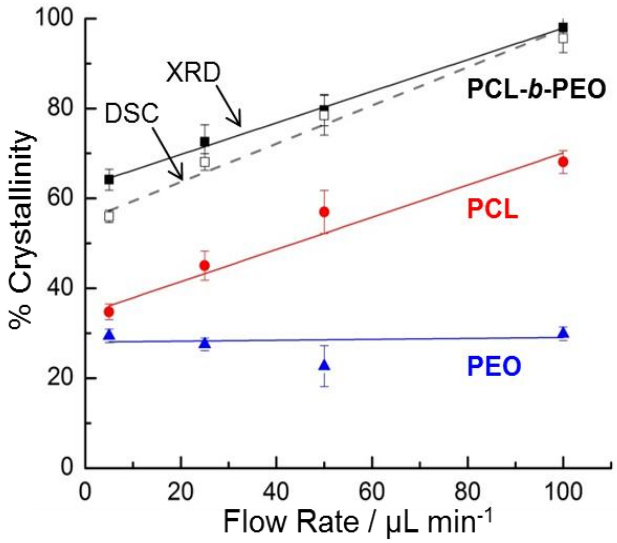

Figure 2.3 Percentages of crystallinity relative to the total copolymer mass for PCL-*b*-PEO PNPs formed on-chip at cwc + 10 wt % and various flow rates.

the hot spots where high shear can increase the rate of coalescence, leading to larger, nonequilibrium aggregates; due to kinetic constraints, these aggregates relax via intramicellar rearrangements to form various nonergotic morphologies. Another possibility worthy of consideration is that under certain conditions the directionality of shear forces may facilitate the formation of cylinders via 1D assembly of spheres[36] along the direction of shear; however, we point out that the formation of lamellae and vesicles under certain chemical and shear conditions indicates that such shear-templated 1D assembly is not operative in all cases.

Crystallization of PCL blocks has been shown to have a strong effect on PCL-*b*-PEO morphologies,[28,37,38] and so the occurrence of flow-induced crystallization could also contribute

to the observed flow dependence. Although flow-induced polymer crystallization from melt and solution states has been widely studied,[39] flow effects on block copolymer crystallization during solution self-assembly and nanoparticle formation have not been previously reported to our knowledge. XRD data for PCL-*b*-PEO nanoparticles collected at different flow rates show identical sharp reflections, suggesting flow rate does not affect the crystalline PCL and PEO unit cells (Figure 7.8, Appendix I); however, the incoherent scattering halo decreases markedly with increasing flow rate. To quantify this effect, PCL crystalline, PEO crystalline, and amorphous contributions were deconvoluted from XRD data and resulting peak areas were used to calculate percentages of crystalline PCL and PEO relative to the total copolymer mass (Figure 2.3, cwc + 10 wt%). The percentage of crystalline PEO shows no significant flow rate dependence, since PEO blocks are solubilized on-chip and crystallized during solvent evaporation after collection. By contrast, PCL crystallinity shows a marked linear dependence on flow rate, suggesting flow-induced crystallization within the hydrophobic nanoparticle cores. Total copolymer crystallinities from XRD and DSC give good agreement for the two methods Figure 2.3). For the two lower on-chip water contents (cwc + 5 wt% and cwc + 2 wt%), similar linear increases in PCL crystallinity with increasing flow rate were obtained, with the slopes of the resulting plots decreasing with decreasing water content (Figure 7.8; Appendix I).

To understand the increase in internal nanoparticle crystallinity with increasing flow rate, we consider two related and well-studied phenomena: flow-induced crystallization of polymers from solution and flow-induced crystallization of polymers from the melt state.[39] Polymer crystallization from solution is induced primarily by extensional components of flow (and not by shear), whereas shear components are found to induce polymer crystallization from the melt state[13]. For the present case, we consider that PCL blocks begin in the solution state, but upon

mixing with water are transferred via self-assembly to the melt state within the nanoparticle cores. As indicated above, almost all high-shear exposure occurs after nanoparticle formation has taken place, such that flow-induced PCL crystallization should most closely resemble the shear dependence of polymer crystallization from the melt state. This explains why increasing the maximum shear rate within the hot spots by increasing the flow rate increases the internal crystallinity of the micellar nanoparticles. Although we do not know the exact mechanism by which shear affects PCL crystallinity, we propose that transient and elastic nanoparticle deformations within the hot spots could result in elongation of internal PCL chains along the shear direction thus promoting nucleation of crystallites.

A particularly intriguing feature of these results is the contrast between the monotonic and linear increase in PCL crystallinity with increasing flow rate at all water contents and the corresponding nonmonotonic changes in internal nanoparticle curvature. For quiescent self-assembly of PCL-*b*-PEO in aqueous media, nanoparticle morphologies are found to be strongly coupled to PCL crystallinity.[28,37,38] For example, Du *et al.* have demonstrated a strong correspondence between PCL-*b*-PEO nanoparticle morphologies and PCL crystallization temperatures;[38] in addition, Eisenberg and co-workers have described crystallinity-driven transitions from spheres to rods on timescales from hours to weeks and from rods to ribbons and small lamellae on timescales of weeks to months.[38] Both of these studies suggest that PCL crystallization favors particle morphologies with low internal curvature such as rods and platelets (lamellae). In contrast, our results demonstrate that in the unique flow environment of the reactor, morphology and crystallinity can be partly decoupled, due to additional and independent flow-directed mechanisms operating simultaneously with PCL crystallization (e.g., particle breakup). As a result, on-chip combinations of multiscale structural features are generated at

high flow rate (e.g., highly crystalline spheres generated at cwc + 10 wt% and Q = 100 μL/min, Figure 2.2L and Figure 2.3) that would not normally form under bulk self-assembly conditions.

The morphological stability of selected PCL-*b*-PEO nanoparticles under quiecent conditions at 4 °C after collection from the chip was investigated for short-term (24 h, Figure 7.5; Appendix I) and long-term (4 weeks, Figure 7.6; Appendix I) ageing periods. For these experiments, the nanoparticles were *not* quenched into excess water upon collection (unlike PAX loading experiments) and so the water content of the solution was the same during ageing as it was during on-chip nanoparticle formation.

For short-term ageing, we investigatedthe stability of nanoparticles formed at the lowest (cwc + 2 wt %) and highest (cwc + 10 wt %) water contents at all four flow rates (Q = 5, 25, 50, and 100 μL/min). After 24 h, the morphologies of nanoparticles formed at the lowest water content and the two lower flow rates (Figure 7.5, A and B; Appendix I) did not change significantly from immediately following collection (Figure 2.2, A and B); however, nanoparticles formed at the same water content at the two higher flow rates (Figure 7.5, C and D) showed changes in morphology over the 24 h ageing process. Specifically, primarily spheres initially formed at Q = 50 μL/min (Figure 2.2C) evolved to a mixture of spheres and large lamellae (Figure S5C) and long cylinders (filomicelles) initially formed at Q = 100 μL/min (Figure 2.2C) broke down into much shorter, irregular cylinders (Figure 7.5D; Appendix I). In contrast, nanoparticles formed at the highest water content showed morphological stability over 24 h for all four flow rates (Figure 7.5, E-H; Appendix I), when compared with morphologies immediately following collection (Figure 2.2, I-L).

Since nanoparticles formed on-chip are non-equilibrium structures, their off-chip morphological stability is entirely dependent on kinetic factors, specifically chain dynamics

within the nanoparticle cores. For PCL cores, slow chain dynmaics giving rise to kinetic stability is attributed to crystallites, which act as physical crosslinks between viscoelastic amorphous regions. Our XRD data shows that, shortly after collection, the core crystallinity of cwc + 2 wt % nanoparticles is actually higher over the range of flow rates than the cwc + 10 wt % nanoparticles (Figure 7.8E; Appendix I), suggesting that the former nanoparticles should initially have slower chain dynamics. However, nanoparticles formed at cwc + 2 wt % are aged in a higher DMF-content mixture than those formed at cwc + 10 wt %, leading to greater solvent-swelling of the PCL cores, more extensive crystallite melting over 24 h, and therefore lower kinetic stability. Since the initial PCL crystallinity at cwc + 2 wt % is lower at the two lower flow rates (Figure 7.8E; Appendix I), we speculate that subsequent melting of crystallites over 24 h leads to a weaker thermodynamic perturbation, explaining the higher morphological stability in those two cases.

Finally, nanoparticles formed at the intermediate water content, cwc + 5 wt %, were investigated 4 weeks after collection from the chip. Even after a month, the observed morphologies (Figure 7.6; Appendix I) showed excellent agreement with those observed immediately after collection (Figure 2.2, E-H). These data suggest that, except for nanoparticles prepared at the lowest water content (cwc + 2 wt %), PCL-*b*-PEO morphologies formed on-chip show excellent short- and long-term stabilities under quienscent conditions, even without quenching and dialysis to remove organic solvent. Of course, long term stabilities of PAX-loaded PNPs that have been quenched and dialyzed to remove DMF should be even higher at 4 °C (although hydrolytic degradation can occur at physiological temperature as discussed below).

We next demonstrated the applicability of on-chip multiscale structure control to tailoring function for drug delivery, by preparing PAX-loaded PCL-*b*-PEO nanoparticles on-chip at cwc + 5 wt% and three different flow rates (Q = 25, 50, and 100 μL/min), and via conventional (bulk) dropwise water addition. Similar to nanoparticles without PAX, drug-loaded nanocarriers show flow-tunable morphologies and sizes, starting with spheres, and then filomicelles, and then filomicelles and lamellae, as flow rate increases (Figure 2.4A and Table 7.2; Appendix I), with a corresponding increase in mean effective hydrodynamic diameters from 47 to 1030 nm by dynamic light scattering (Figure 7.9, Appendix I). The PAX-loaded filomicelles, "dialed-in" via flow rate under constant chemical conditions, are particularly intriguing, due to demonstrated advantages over spheres of these flexible, fragmentable, and longer-circulating drug delivery vehicles[8]. Next, the structure and dynamics of the PAX-loaded nanoparticle cores were investigated, with XRD indicating an increase in core crystallinity with flow rate (Figure 2.4B, "zero-flow" represents bulk-prepared nanoparticles). The flow-dependence of the core environment was corroborated by fluorescence anisotropy of a hydrophobic probe (DPH) dissolved in the core. The increase in fluorescence anisotropy with flow rate indicates that as PCL crystallinity increases, so does the microviscosity within the core (Figure 2.4B).[33] Thus flow rate provides simultaneous multiscale control of the size and shape of polymer nanocarriers, as well as the internal diffusion environment of their hydrophobic cargo.

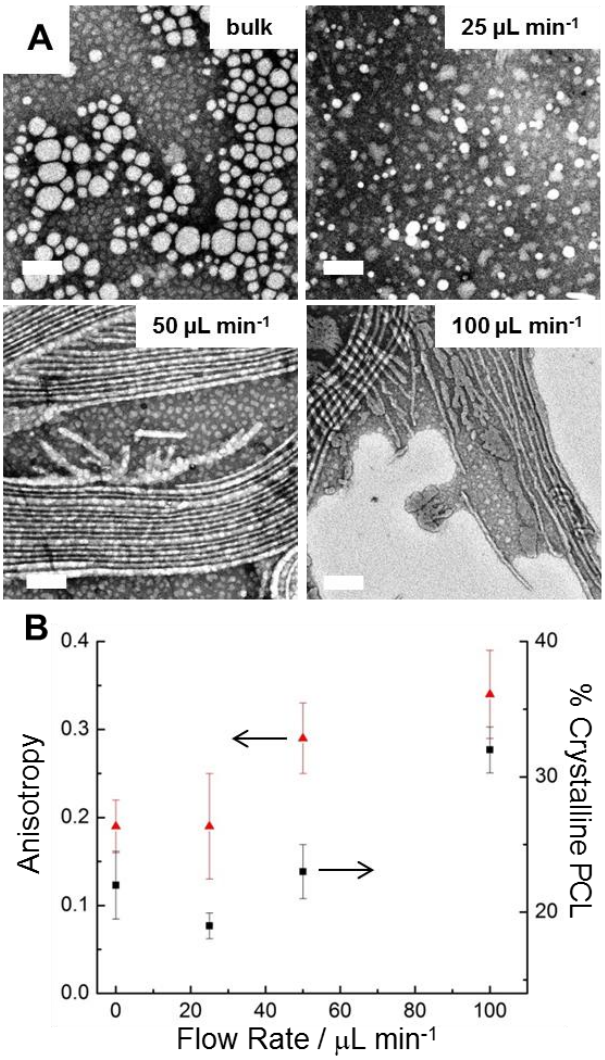

Figure 2.4 (A) TEM images of PAX-loaded PNPs formed on-chip at cwc + 5 wt % and various flow rates. Images were produced with negative staining and all scale bars are 200 nm. (B) Percentages of crystalline PCL (■) and fluorescence anisotropies (▲) of DPH probe revealing the core environments within the associated PNPs.

Finally, loading and release properties of the PAX-loaded nanoparticles were studied using high performance liquid chromatography-mass spectrometry for PAX quantification (Figure 2.5). PAX loading efficiencies, defined as: loading efficiency (%) = [PAX in nanoparticles(g)/total PAX used(g)] × 100%, show marked improvements with increasing flow rate, with an on-chip loading efficiency of ≈90 % at Q = 100 μL/min compared to ≈45 % for the

bulk-prepared control (Figure 2.5A). We attribute the increase in loading efficiency with flow rate to the corresponding evolution of filomicelles and lamellae from significantly smaller spheres (Figure 2.4A), since polymer nanoparticles with higher aggregation numbers generally lead to higher solubilities of hydrophobic drugs.[15,32] On the other hand, the increase in PCL crystallinity with flow rate (Figure 2.4B) should impede PAX encapsulation and so is not expected to contribute positively to the increased drug loading.

In vitro release profiles of PAX-loaded PCL-*b*-PEO nanoparticles under model physiological conditions (37 °C, PBS buffer: pH = 7.4, 45 g/L albumin) show slower release for all on-chip samples compared to the bulk-prepared sample (Figure 2.5B). Moreover, we find that on-chip flow rate provides a direct handle on release times. For the bulk-prepared nanocarriers, PAX is completely released after ≈1 d; by contrast, for the Q = 25 and 50 μL/min on-chip samples, complete release occurs over a total of ≈5 and ≈9 days, respectively. Finally, for the Q = 100 μL/min sample, PAX release plateaus at ≈85% after ≈5 days, suggesting the remaining ≈15% PAX is "trapped" in the higher-crystallinity cores (Figure 2.4B) formed at this flow rate. We note that such "dial-in" control of release times offers immense potential for tunable timed release of specific drugs for desired treatments. Flow-controlled PAX release times can be explained by the corresponding flow dependence of multiscale nanoparticle structure. As flow rate increases, both the core size (Figure 2.4A) and the crystallinity (Figure 2.4B) increase; the corresponding increase in diffusion distance and decrease in diffusion coefficient, respectively, will both contribute to the observed increase in release time. Another consideration is that the effects of morphology and crystallinity on nanoparticle hydrolytic degradation (Figures 7.11–7.15, Appendix I) may contribute to further flow dependences of drug release.[40]

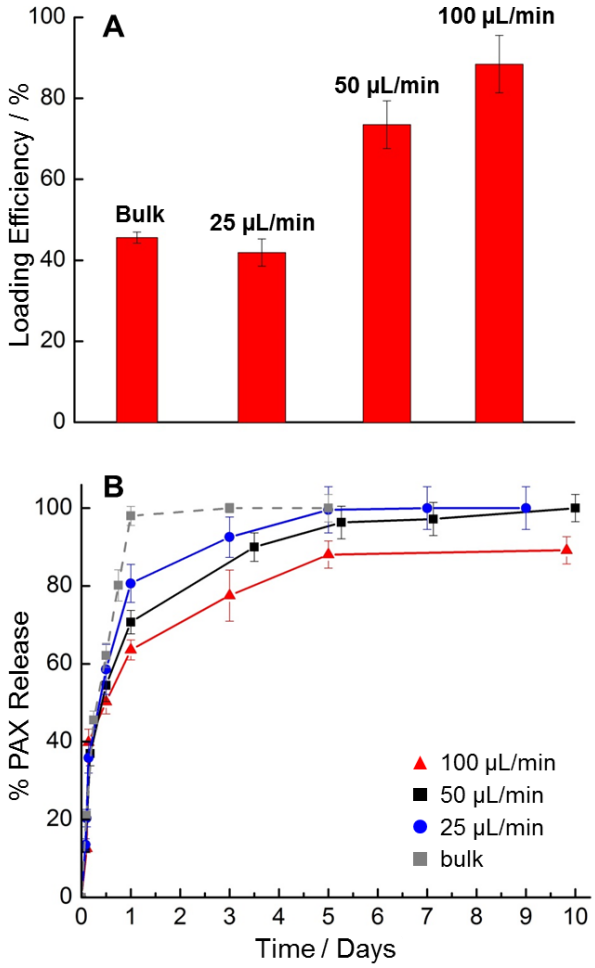

Figure 2.5 PAX loading efficiencies (A) and release kinetics (B) for PAX-loaded PNPs formed on-chip at cwc + 5 wt % and various flow rates, and a bulk-prepared control sample.

The breakdown of polyester-based block copolymer nanoparticles *via* hydrolysis of the polyester block has been studied previously.[24-36] Two main hydrolysis mechanisms have been proposed: random scission at acidic pH and sequential cleavage from the polymer chain end at alkaline pH, with higher temperature leading to accelerated degradation in both cases.[6] Discher *et al.* have reported hydrolytic degradation as a mechanism for release of hydrophilic and hydrophobic small molecule cargo from PCL-*b*-PEO aggregates.[9] On the time scale of days, they studied the effect of temperature and pH on hydrolytic degradation of the PCL core

(temperature = 4°C or 37°C; pH = 7.4 or 9.0). Under various conditions, they observed the spontaneous shortening of cylindrical nanoparticles *via* concomitant formation of spherical nanoparticles which pinch off from the cylinder ends.[33,34] The rate of this hydrolysis-driven breakdown of cylinders into spheres increased as either temperature increased or pH decreased.[9]

Our study of the *in vitro* release of PAX from PAX-loaded PCL-*b*-PEO nanoparticles reveal that times for complete PAX release under model physiological conditions (37 °C, PBS buffer: pH = 7.4, 45 g/L albumin) vary from ~4-10 days (Figure 2.5B) depending on flow rate and nanoparticle preparation method. All four release profiles show similar fast and approximately linear release kinetics for release times t < ~12 h (Figure 2.5B). For longer release times, the four samples show different, non-linear release profiles, which we fit to a diffusive model[11] by plotting *% PAX Release* vs. $t^{1/2}$ and performing linear regression on release times $t \geq$ 12 h (Figure 7.8; Appendix I). The resulting slopes confirm flow-directed release rates in the order: bulk-prepared > Q = 25 μL/min > Q = 50 μL/min > Q = 100 μL/min.

The imperfect fits to the diffusive model for the microfluidic preparations (R^2 = 0.80 – 0.87) are explained by nanoparticle breakdown over the release period, which along with simple diffusion contributes another mechanism of PAX release. Within the first 12 hours of release, TEM images reveal a decrease in the PCL core sizes of spherical nanoparticles formed in the bulk (Figure 7.9; Appendix I) and Q = 25 μL / min (Figure 7.10; Appendix I) cases, and to a breakdown of non-spherical nanoparticles (filomicelles and lamellae) in the Q = 50 μL / min (Figure 7.11; Appendix I) and Q = 100 μL/min (Figure 7.12; Appendix I) cases. This decrease in nanoparticle sizes *via* hydrolytic degradation was also confirmed by DLS (Figure 7.13; Appendix I). These results suggest that hydrolytic degradation of the PCL cores will be a significant factor in PAX release of all four samples in the first 12 hours. Between 12 and 24 h,

we find that the sizes of degraded nanoparticles continue to decrease somewhat until by the 24 h release time all samples have reached a nearly identical effective hydrodynamic size of ~18 nm (Figure 7.13; Appendix I). We note that even after the nanoparticles have degraded to similar sizes, such that diffusion distances within the cores will be similar, the release rates continue to show significant differences, which we attribute to the flow-directed differences in the microviscosity of the hydrophobic cores, as discussed previously.

We note that on the basis of simple diffusion and assuming equivalent PAX distributions within the cores, the significantly faster release time for the bulk sample compared to the on-chip 25 μL/min sample is not consistent with their relative nanoparticle sizes and crystallinities; this suggests an additional factor distinguishing PAX-loaded nanoparticles prepared on-chip from those prepared in the bulk. One possibility is that faster mixing (≈1 s) within the reactor results in a more uniform distribution of PAX throughout the PCL cores, whereas relatively slow water addition during bulk preparations (including drop wise or dialysis addition)[10] allows PAX to migrate to the core–coronae interface, significantly accelerating its release.

2.4 Conclusions

In summary, semicrystalline PCL-*b*-PEO nanoparticles were produced in a segmented gas–liquid microfluidic reactor with unprecedented top–down control of disparate levels of multiscale structural features, including nanoparticle morphologies, sizes, and internal crystallinities. Using the same microfluidic platform, PAX-loaded PCL-*b*-PEO nanoparticles were also produced with improved PAX loading efficiencies (up to 90%) and slower in vitro release kinetics compared to a conventional bulk preparation. Control of multiscale structure enabled tailoring of drug delivery nanoparticle function, as demonstrated by tuning of PAX

release rates via on-chip flow rate. A comprehensive investigation of the effects of multiple chemical and flow variables on drug delivery PNPs prepared using microfluidics will be described in Chapters 3 and 4. Investigations of the therapeutic applications of flow-directed polymeric nanocarriers, including cell viability studies, will be described in Chapter 5.

2.5 References

1. Zhang, L.; Eisenberg, A. *Science* **1995**, *268*, 1728.
2. Zhang, L.; Eisenberg, A. *J. Am. Chem. Soc.* **1996**, *118*, 3168.
3. Mai, Y.; Eisenberg, A. *Chem. Soc. Rev.* **2012**, *41*, 5969.
4. Discher, B. M.; Won, Y.-Y.; Ege, D. S.; Lee, J. C.-M.; Bates, F. S.; Discher, D. E.; Hammer, D. A. *Science* **1999**, *284*, 1143.
5. Jain, S.; Bates, F. S. *Science* **2003**, *300*, 460.
6. Cui, H.; Chen, Z.; Zhong, S.; Wooley, K. L.; Pochan, D. J. *Science* **2007**, *317*, 647.
7. Wang, X. S.; Guerin, G.; Wang, H.; Wang, Y. S.; Manners, I.; Winnik, M. A. *Science* **2007**, *317*, 644.
8. Forster, S.; Plantenberg, T. *Angew. Chem., Int. Ed.* **2002**, *41*, 688.
9. Li, Z.; Kesselman, E.; Talmon, Y.; Hillmyer, M. A.; Lodge, T. P. *Science* **2004**, *306*, 98.
10. Allen, C.; Maysinger, D.; Eisenberg, *A. Coll. Surf. B: Biointerf.* **1999**, *16*, 3.
11. Discher, D. E.; Ortiz, V.; Srinivas, G.; Klein, M. L.; Kim, Y.; Christian, D.; Cai, S.; Photos, P.; Ahmed, F. *Prog. Polym. Sci.* **2007**, *32*, 838.
12. Tyrrell, Z. L.; Shen, Y.; Radosz, M. *Prog. Polym. Sci.* **2010**, *35*, 1128.
13. Parveen, S.; Misra, R.; Sahoo, S. K. *Nanomed.: NBM* **2012**, *8*, 147.

14. Gong, J.; Chen, M.; Zheng, Y.; Wang, S.; Wang, Y. *J. Control. Release* **2012**, *159*, 312.

15. Ahmad, Z.; Shah, A.; Siddiq, M.; Kraatz, H.-B. *RSC Adv.* **2014**, *4*, 17028.

16. Oltra, N. S.; Nair, P.; Discher, D. E. *Annu. Rev. Chem. Biomol. Eng.* **2014**, *5*, 281.

17. Yokoyama, M. *J. Drug Target.* **2014**, *22*, 576.

18. Gonzalez, D.C.; Savariar, E. N.; Thayumanavan, S. *J. Am. Chem. Soc.* **2009**, *131*, 7708.

19. Torchilin, V. P. *Adv. Drug Delivery Rev.* **2002**, *54*, 235.

20. Nasongkla, N.; Bey, E.; Ren, J. M.; Ai, H.; Khemtong, C.; Guthi, J. S.; Chin, S. F.; D., S. A.; Boothman, D. A.; Gao, J. M. *Nano Lett.* **2006**, *6*, 2427.

21. Wu, W. C.; Chen, C. Y.; Tian, Y. Q.; Jang, S. H.; Hong, Y. N.; Liu, Y.; Hu, R. R.; Tang, B. Z.; Lee, Y. T.; Chen, C. T.; C., C. W.; Jen, A. K. Y. *Adv. Funct. Mater.* **2010**, *20*, 1413.

22. Wang, J. F.; Chen, Q. J.; Zhao, H.; Ming, T.; Wu, C. *J. Am. Chem. Soc.* **2009**, *131*, 16650.

23. Zhang, M.; Wang, M. F.; He, S.; Qian, J. S.; Saffari, A.; Lee, A.; Kumar, S.; Hassan, Y.; Guenther, A.; Scholes, G.; Winnik, M. A. *Macromolecules* **2010**, *43*, 5066.

24. Wang, C.-W.; Sinton, D.; Moffitt, M. G. *J. Amer. Chem Soc.* **2011**, *133*, 18853.

25. Wang, C.-W.; Bains, A.; Sinton, D.; Moffitt, M. G. *Langmuir*. **2012**, *28*, 15756.

26. Wang, C.-W.; Sinton, D.; Moffitt, M. G. *ACS Nano.* **2013**, *7*, 1424.

27. Wang, C.-W.; Bains, A.; Sinton, D.; Moffitt, M. G. *Langmuir.* **2013**, *29*, 8385.

28. He, W.-N.; Xu, J.-T. *Prog. Polym. Sci.* **2012**, *37*, 1350.

29. Cai, S.; Vijayan, K.; Chen, D.; Lima, E. M.; Discher, D. E. *Pharmaceut. Res.* **2007**, *24*, 2099.

30. Geng, Y.; Dalhaimer, P.; Cai, S.; Tsai, R.; Tewari, M.; Minko. T.; Discher, D. E. *Nature Nanotech.* **2007**, *2*, 249.

31. Venkataraman, S.; Hedrick J. L.; Ong, Z. Y.; Yang, C.; Ee, P. L. R.; Hammond, P. T.; Yang, Y. Y. *Adv. Drug Deliv. Rev.* **2011**, *63*, 1228.

32. Oltra, N. S.; Swift, F.; Mahmud, A.; Rajagopal, K.; Lovede, S. M.; Discher, D. E. *J. Mater. Chem. B* **2013**, *1*, 5177.

33. Letchford, K.; Liggins, R.; Burt, H. *Eur. J. Pharm. Biopharm.* **2009**, *71*, 196.

34. Glover, A. L.; Nikles, S. M.; Nikles, J. A.; Brazel, C. F.; Nikles, D. E. *Langmuir* **2012**, *28*, 10653.

35. Karnik, R.; Gu, F.; Basto, P.; Cannizzaro, C.; Dean, L.; Kyei-Manu, W.; Langer, R.; Farokhzad, O. C. *Nano Lett.* **2008**, *8*, 2906.

36. Capretto, L.; Carugo, D.; Mazzitelli, S.; Nastruzzi, C.; Zhang, X. *Adv. Drug Deliv. Rev.* **2013**, *65*, 1496.

37. He, W.-N.; Xu, J.-T.; Du, B.-Y.; Fan, Z.-Q. *Macromolecules* **2012**, *45*, 9768.

38. Du, Z.-X.; Xu, J.-T. Xu; Fan, Z.-Q. *Macromol. Rapid Commun.* **2008**, *29*, 467.

39. Rizis, G.; van de Ven, Th. G. M.; Eisenberg, A. *Soft Matter* **2014**, *10*, 2825.

40. Lamberti, G. *Chem. Soc. Rev.* **2014**, *43*, 2240.

41. Geng, Y.; Discher, D. E. *J. Amer. Chem. Soc.* **2005**, *127*, 12780.

Chapter 3

Microfluidic Synthesis of Dye-Loaded Polycaprolactone-*block*-poly(ethylene oxide) Nanoparticles: Insights into Flow-Directed Loading and In Vitro Release for Drug Delivery

3.1 Introduction

Block copolymer-based drug delivery nanoparticles have a number of potential advantages over more conventional lipid-based systems, including increased morphological variability, robustness, and ease of functionalization.[1-4] In aqueous media, amphiphilic block copolymers form micellar nanoparticles of various morphologies, including nanoscale spheres, cylinders (filomicelles), lamellae, and vesicles (polymersomes), consisting of cores of aggregated hydrophobic blocks capable of solubilizing lipophilic drug molecules, surrounded by a soluble coronal layer of hydrophilic blocks.[5-11] Biocompatible and semicrystalline block copolymers, such poly(L-lactide)-*block*-poly(ethylene oxide) (PLLA-*b*-PEO)[12-15] and polycaprolactone-*block*-poly (ethylene oxide) (PCL-*b*-PEO)[7,16-20] are often applied to drug delivery applications. Such materials self-assemble to form nanoparticles with structural hierarchy or multiscale organization, due to a combination of features at the colloidal length scale (~10-100 nm; e.g. nanoparticle size and morphology) and at the nanoscale (~1-10 nm; e.g. crystallization of hydrophobic segments within nanoparticle cores). For drug delivery applications, structural features on both disparate length scales strongly affect the function of block copolymer nanocarriers.[21,22,19,23-25] For example, at the colloidal scale, the sizes of nanoparticles carrying anticancer agents will influence their localization within tumours *via* the enhanced permeability and retention effect (EPR),[26] whereas nanoparticle morphologies have been shown to significantly affect *in vivo* circulation times:[21,22,19,23,25] at the nanoscale, the internal crystallinity of semicrystalline nanoparticles is an important factor in such important figures of merit as stability, flexibility, and release kinetics.[21,22,19,23-25] These examples highlight a critical need for controlling all levels of multiscale structure in order to obtain hierarchical

nanoparticles with the desired physical, chemical, and biochemical properties for a specific therapeutic application.

Our group has recently developed a microfluidic platform consisting of a segmented gas-liquid microreactor for the generation of block copolymer nanoparticles offering continuous variability of structure *via* the convenient "top-down" variable of on-chip flow rate.[27-30,20] For the amorphous block copolymer polystyrene-*block*-poly(acrylic acid), PS-*b*-PAA, it was shown that flow-directed self-assembly enables control over the sizes and morphologies of the resulting nanoparticles as a result of shear effects on particle coalescence and breakup.[27,28,30] More recently, as described in Chapter 2, we demonstrated that for the semicrystalline copolymer PCL-*b*-PEO, flow rate provides a top-down experimental handle on structure at *both* critical length scales, including nanoparticle size, morphology, *and* internal crystallinity;[20] we further showed that such multiscale structure control allows the function of drug delivery nanoparticles, in particular release rates of the encapsulated drug paclitaxel (PAX), to be tuned via flow rate.[20] In addition, it was found that at a given flow rate the on-chip chemical environment (i.e. water content) also strongly influences the structural products of self-assembly and the function of the resulting nanoparticles (i.e. PAX loading efficiencies and release rates).[20] In order to develop this microfluidic reactor as a general platform for the controlled manufacturing of polymeric drug delivery nanoparticles, we consider that each hydrophobic drug will interact differently with the solvent and polymer environments, thus affecting self-assembly and loading in different ways.[31-35] Optimal on-chip chemical and flow conditions will therefore need to be tailored for specific drug cargos, requiring an increased understanding of the effects of flow rate on nanoparticle structure and function under a wide range of on-chip chemical conditions (e.g. solvent, water content, polymer concentration, drug-to-polymer ratio).

Fluorescent dyes are often used as model hydrophobic probes or "drug surrogates" for the development of block copolymer- and lipid-based nanocarriers.[31-35,29] Although the refinement of on-chip conditions for a given application will inevitably require experimentation with the specific target drug, initial investigations using a hydrophobic probe with a size and solubility representative of a range of hydrophobic drugs can provide insight into general trends and establish important *a priori* information for subsequent studies. This approach increases both the time and cost efficiency of formulation development, as model probes are available at a fraction of the cost of some therapeutics identified for drug delivery applications. In addition, the high sensitivity of fluorescence measurements allows probe dyes to be quantified from much smaller sample aliquots than are required for non-fluorescent drug molecules (including PAX). This makes probe dyes particularly well suited for the investigation of microfluidic systems, where continuous variability of flow and chemical parameters allows a large number of small-volume samples to be collected within a short timeframe.

For example, our group has recently utilized the dyes pyrene and naphthalene as model probes with high and low chemical affinities, respectively, for the PS cores of PS-*b*-PAA nanoparticles formed in a segmented gas-liquid microfluidic reactor under various chemical conditions and two different on-chip flow rates (Q = 5 and 50 μL/min).[29] In that study, it was shown that loading efficiencies first increased and then decreased with increasing water content at a constant flow rate as a result of competing thermodynamic and kinetic factors. It was also found that the effect of flow rate on dye loading was generally small, except at an intermediate water content where a higher particle aggregation number at the lower flow rate corresponded to a higher loading efficiency. Maximum on-chip loading efficiencies measured for the pyrene and naphthalene probes were ~73 % and ~11% respectively, reflecting the higher solubility of the

former molecule in the PS cores of the nanoparticles. For nanoparticles prepared at the intermediate water content and at two different flow rates, *in vitro* release kinetics of the pyrene probe were compared, revealing that greater burst release followed by longer overall release times were associated with nanoparticles formed at the higher flow rate.

Compared to amorphous nanoparticles such as PS-*b*-PAA, the structural hierarchy of semicrystalline PCL-*b*-PEO nanoparticles should give rise to even more complex flow effects on the loading and release of hydrophobic molecules, due to the interplay of flow-induced structure formation processes operating on multiple length scales, including particle coalescence, particle breakup, and crystallization within particle cores. This is supported by our preliminary loading and release data for the specific drug PAX in PCL-*b*-PEO nanoparticles formed on-chip at three different flow rates and at a single water content, which suggest that flow-directed particle size, internal crystallinity, and mixing all influence loading and release of PAX from the nanocarriers.[20] An appropriate dye with high affinity for PCL should enable studies providing a greater understanding of flow effects on loading efficiencies for various hydrophobic drugs under a broad range of chemical conditions.

A specific characteristic of drug delivery nanoparticles that is widely studied is the *in vitro* release of the encapsulated drug into an aqueous reservoir.[36,37,33,38,39,34,40-50,29,20] Although the chemical and physical characteristics of the reservoir are often set to mimic physiological conditions, it has been shown that *in vitro* experiments fall short of recreating the dynamic release mechanisms that exist *in vivo*, such that *in vitro* and *in vivo* release kinetics are often drastically different.[51,18,19] Nonetheless, the ease of carrying out *in vitro* experiments compared to the financial and practical challenges of *in vivo* testing make the former an important tool in the development of chemistry and methods for nanocarrier formulations, providing a baseline and

point of comparison for more advanced testing. The comparison of *in vitro* results from different studies is often complicated by the range of different experimental conditions that are applied..[34] Other studies have instead mimicked perfect sink conditions using a large volume differential (≥ 250×) between the release medium and the sample. Within the latter group, the release medium can vary from pure (deionized) water,[37,34,29] to phosphate buffered saline (PBS),[36,38,40,43] to PBS containing dissolved albumin,[1,39,42,44,46] to cell lysate,[52,53] representing increasing similarity with the chemical complexity of physiological environments. An additional complication is the demonstrated effect of temperature and pH on the *in vitro* hydrolytic breakdown of PCL and similar degradable polymers which provides an additional mechanism for release.[54,55] To our knowledge, a systematic comparison of *in vitro* release have the strongest influence on the release kinetics of polymeric nanocarriers. *in vitro* release kinetics into a variety of release media, representing a wide range of physical and chemical characteristics, has not yet appeared in the literature. Such a study should prove immensely useful for establishing which experimental features of *in vitro* release have the strongest influence on the release kinetics of polymeric nanocarriers.

In this chapter, we apply the hydrophobic dye 1,1′-dioctadecyl-3,3,3′,3′-tetramethylindocarbocyanine perchlorate (DiI) as a fluorescent probe to study on-chip loading into PCL-*b*-PEO nanocarriers under various chemical and flow conditions within a segmented gas-liquid microfluidic reactor, followed by *in vitro* release from the resulting nanoparticle formulations. DiI is a well-known biological probe commonly applied to labeling cells and tissues[56,57], and has been shown to have a high affinity for the PCL cores of PCL-*b*-PEO nanoparticles in aqueous and polar mixed solvent media.[34,35] The results of this study provide important insights into the effects of on-chip flow rate and water content on loading efficiencies

and release kinetics of nanocarriers synthesized in our segmented microfluidic reactor, while also developing a general strategy for establishing process-structure-function relations for nanocarriers manufactured using microfluidics. Furthermore, we describe a systematic study of the dependence of nanoparticle degradation and *in vitro* release of hydrophobic probe on the chemical and physical characteristics of the release medium, comparing effects of temperature, static medium vs. constant flow, and various release media including PBS buffer, albumin solution, and cell lysate.

3.2 Experimental

3.2.1 Materials.

Poly(caprolactone)-*block*-poly(ethylene oxide) (PCL_{105}-*b*-PEO_{114}, where numbers in subscripts denote number-average degrees of polymerization for the respective blocks) was purchased from Advanced Polymer Inc. and used as received. *N*,*N*-Dimethylformamide (DMF) (Aldrich, 99.9+%, HPLC grade, H_2O < 0.03%) was used as received without further purification. 1,1′-Dioctadecyl-3,3,3′,3′-tetramethylindocarbocyanine perchlorate (DiI) (Aldrich) was used as received. The Bio-Rad protein assay (Bradford assay) was used as received without further modifications. All quantitative stock solutions of PCL-*b*-PEO/DiI in DMF were prepared gravimetrically by accurately weighing the solids into a glass vial followed by gravimetric addition of a known quantity of DMF; stock solutions were then equilibrated overnight with stirring before further use. All experiments, unless otherwise noted, were run in triplicate from separately prepared stock solutions.

3.2.2 Critical Water Content Determination

Static light scattering (SLS) measurements were carried out to accurately determine the critical water content (cwc) of 0.33 wt % DMF solutions of PCL-*b*-PEO, which was the initial condition for all self-assembly experiments in this study. SLS measurements were carried out using a Brookhaven Instruments photon correlation spectrometer equipped with a BI-200SM goniometer, a BI-9000AT digital autocorrelator, and a Melles Griot He-Ne Laser (633 nm) with a maximum power output of 75 mW.

A 1.0 wt % stock solution of PCL-*b*-PEO in DMF was filtered through a Teflon syringe membrane filter with a nominal pore size of 0.45 μm (VWR) into precleaned scintillation vials. The filtered stock was then diluted to 0.33 wt % by gravimetric addition of the required quantity of DMF. To the resulting ~6 g of solution, deionized water was added in successive 0.03-0.06 g quantities via a microsyringe equipped with two membrane filters (VWR) with nominal pore size of 0.20 μm connected in series. After each addition of water, the solution was agitated using a vortexer to aid in mixing. The solution was then allowed to equilibrate for 15 min before measuring the scattered light intensity. All measurements were carried out at a scattering angle of 90° and a temperature of 23 °C. From the resulting plot of scattered light intensity versus weight percentage of added water (Figure 8.1; Appendix II), the cwc was determined from the intercept of linear fits to the baseline and the region of the plot in which scattered light intensity increased sharply (above the cwc). Determinations of cwc were carried out three times from the same stock solution and the mean value and standard deviation of the three measurements were used to calculate the reported cwc and experimental error: cwc = 5.5 ± 0.4 wt %.

3.2.3 Microfluidic Chip Fabrication

Negative masters were fabricated on high quality silicon wafers (Silicon Quest International, Santa Clara, CA) using the negative photoresist SU-8 100 (Microchem Inc.). Immediately prior to use, the wafers were heated on a hot plate at 200 °C for 20 minutes to remove moisture. A 150 μm-thick SU-8 film was spin-coated onto the silicon and then heated to 95 °C for 60 minutes to remove residual SU-8 solvent. A photomask was then placed over the SU-8 film and exposed to UV light for 180 s. Then, the UV-treated film was heated at 95 °C for 20 min before submersion in SU-8 developer (Microchem) until all unexposed photoresist was removed.

Microfluidics chips were fabricated from poly(dimethylsiloxane) (PDMS) using a SYLGARD 184 silicon elastomer kit (Dow Corning, Midland, MI). For chips used in the preparation of nanoparticles without PAX, an elastomer base-to-curing agent ratio of 10:1 was employed as recommended by the kit. However, improved adhesion between the channel and substrate PDMS layers was later found when base-to-curing agent ratios were adjusted to 7:1 and 20:1 for the two layers, respectively, and these ratios were employed for the PAX-encapsulation experiments described the text. For fabrication of all PDMS chips, the elastomer and curing agent were mixed together and degassed in a vacuum chamber. The degassed PDMS was then poured over the negative master in a Petri dish and further degassed until all remaining air bubbles were removed. The PDMS was then heated at 85 °C for ~60 min until cured. The microfluidic chip was then peeled off of the negative master and holes were punched through its reservoirs to allow for the insertion of tubing. A thin PDMS film (substrate layer) was also formed on a glass slide by spin-coating and was permanently bonded to the base of the microfluidic reactor (channel layer) after both components were exposed to oxygen plasma for

60 s. The reactor has a set channel depth of 150 μm and consists of a sinusoidal mixing channel 100 μm wide and 18 mm in length and a sinusoidal processing channel 200 μm wide and 740 mm in length.

For further stabilization of the bubble generation process, an external resistor chip was used between the Ar gas tank and the microfluidic chip. The resistor chips served as high pressure drop systems to efficiently dampen the pressure fluctuations caused by the Ar gas tank and the bubble generation process. The total pressure drop in the external resistor chip was at least one order of magnitude higher than the pressure drop in the reaction channel. The resistor chip channels were 1000 mm long, 150 μm deep and 400 μm wide.

3.2.4 Flow Delivery and Control

Pressure-driven flow of liquids to the reactor inlet was provided using 1 mL gastight syringes (Hamilton, Reno, NV) mounted on syringe pumps (Harvard Apparatus, Holliston, MA). The microchip was connected to the liquid syringes via 1/16th-inch (OD) Teflon tubing (Scientific Products and Equipment, ON). Gas flow was introduced to the microchip via an Ar tank regulator and a downstream regulator (Johnston Controls) for fine adjustments. The microchip was connected to the downstream regulator through a 1/16th-inch (OD) / 100-μm (ID) Teflon tube (Upchurch Scientific, Oak Harbor, WA). The liquid flow rate (Q_{liq}) was programmed via the syringe pumps and the gas flow rate (Q_{gas}) was fine-tuned via the downstream pressure regulator in order to dial in the nominal total flow rates described in the main text. Due to the compressible nature of the gas and the high gas/liquid interfacial tension, discrepancies arise between the nominal (programmed) and actual values of Q_{gas}, Q_{gas}/Q_{liq}, and the total flow rate (Q_{total}). Therefore, actual gas flow rates were calculated from the frequency of bubble formation

and the average volume of gas bubbles, determined from image analysis of the mean lengths of liquid and gas plugs, L_{liq} and L_{gas}, respectively, under a given set of flow conditions. This method of flow calculation has been previously employed in the context of gas-liquid segmented flow in the microfluidic device.[27] Actual flow parameters pertaining to each microfluidic experiment described in the chapter are listed in Table 8.1 (Appendix II). For all experiments, the relative gas-to-liquid flow ratio, Q_{gas}/Q_{liq} ~1 and all actual Q_{total} values are within 10% of nominal values reported in the main text.

Visualization of the gas bubbles and liquid plugs within the microfluidic reactor was achieved using an upright optical microscope (Omax) with a 10x-objective lens. Images were captured using a 2.07 megapixel PupilCam (Ken-A-Vision) and mean lengths of liquid and gas plugs were determined from the images using image analysis software (ImageJ).

3.2.5 Microfluidic Preparation of DiI-Loaded PCL-*b*-PEO Nanoparticles

For microfluidic preparation of nanoparticles loaded with dye, three different streams were combined with an Ar gas stream to form gas-segmented liquid plugs. The following three fluid streams were combined at equal flow rate to form gas-segmented liquid plugs within the reactor: (1) 1.0 wt % solution of PCL-*b*-PEO in DMF with DiI codissolved at a dye:copolymer ratio of 0.02; (2) a separator stream containing DMF only; and (3) a water-containing stream consisting of either a DMF solution containing 46.5 wt % deionized water or pure deionized water. Combination of the three liquid streams yielded a steady-state on-chip copolymer concentration of 0.33 wt % and a steady-state water concentration of either 15.5 or 80.5 wt %. These two on-chip water concentrations corresponded to cwc + 10 wt % and cwc + 75 wt %,

respectively, where the measured cwc of the copolymer solution was determined to be 5.5 wt %. Microfluidic flow conditions were selected and controlled as described in the previous section.

Nanoparticle samples with loaded dye were collected from the reactor into vials containing a 10×-excess volume of deionized water, followed by 12 h dialysis (overnight dialysis) against deionized water (with changing of water every hour for the first 4 h of dialysis) to remove residual DMF and unencapsulated DiI. The resulting aqueous dispersions of DiI-loaded nanoparticles were analyzed by TEM, XRD, and DLS, and loading efficiencies and release kinetics were determined using fluorescence spectroscopy.

3.2.6 Transmission Electron Microscopy

Transmission electron microscopy (TEM) was performed using a JEOL JEM-1400 TEM, operating at an accelerating voltage of 65 kV and equipped with a Gatan Orius SC1000 CCD camera. TEM images were obtained by depositing diluted dispersions (~0.03 wt % copolymer) consisting of DiI-loaded PCL-*b*-PEO nanoparticles in water onto carbon-coated 300 mesh copper TEM grids as described below.

To improve contrast, uranyl acetate was used to negatively stain the PCL-*b*-PEO nanoparticles. Uranyl acetate selectively binds to the PEO coronal chains, providing reverse contrast for the PCL cores, which appear white in TEM images of stained samples. For reverse staining experiments, nanoparticle dispersions were mixed with 1 wt % aqueous solution of uranyl acetate in a 1:1 ratio (v/v) and one drop of the resulting mixture was deposited onto a TEM grid. Excess liquid was immediately removed using lens paper, followed by drying of remaining liquid under ambient conditions.

Due to the high electron density of uranyl acetate, negative staining generally impedes visualization of internal lumen of vesicle structures, such that vesicles and spheres cannot be readily distinguished from stained samples. Therefore, all samples revealing aggregates of spherical shape in negative contrast TEM images were also imaged without staining. In unstained images, contrast is provided by high density PCL crystallites which appear dark relative to both the background and the internal lumen of vesicles, such that vesicles appear hollow in unstained images and so can be differentiated from spheres. We find that one complication of imaging PCL-*b*-PEO nanoparticles without staining is that upon drying under ambient conditions, deposited dispersions form large crystallites of PEO which obscure identification of micellar PCL cores. To avoid this problem, micellar dispersions deposited without reverse staining were freeze-dried on TEM grids using the following method. First, one drop of the micellar dispersion was deposited onto a TEM grid and excess liquid was immediately removed using lens paper. The remaining liquid was then vitrified by submerging the TEM grid into liquid ethane. The resulting vitrified sample was then freeze-dried under vacuum. As discussed below, the morphological identification of some aggregates required the evaluation of their heights. For these experiments, Pt/Pd shadowing of unstained aggregates following freeze-drying on the grid was carried out at a shadowing angle of 45°.

For each set of conditions (water content and flow rate), reported prominent morphologies and mean dimensions from TEM of nanoparticles with loaded DiI (Table 3.1) were determined from TEM analysis of three separate preparations starting with three individually-prepared stock solutions. For each sample preparation and TEM grid deposition method (unstained, stained, and shadowed), at least 2-3 TEM images taken in different regions of the grid were evaluated. Prominent morphologies for each condition were assigned based on

the following definitions with associated evaluation methods in brackets. Spheres were defined as aggregates with circular projections (TEM with staining) but without internal lumen (TEM without staining). Cylinders were defined as high aspect-ratio filaments of approximately regular width (TEM with staining). Lamellae were defined as irregularly-shaped aggregates (TEM with staining) with heights significantly smaller than their lateral dimensions (TEM with shadowing); from cases where aggregate shadowing was carried out, lamellae heights were determined to be 9 nm (Figure 8.2; Appendix II). For each preparation, mean dimensions were determined from ~400 particles; therefore, for each of the mean dimensions in Table 3.1, $N = 400 \times 3$ preparations = ~1200, such that the reported errors reflect reproducibility of the preparation method. Mean sphere diameters and cylinder widths were determined exclusively from TEM images with staining. Averaging and statistical analysis of dimensions from TEM images was conducted using Image J software.

3.2.7 Dynamic Light Scattering

Effective hydrodynamic diameters of DiI-loaded PCL-*b*-PEO nanoparticles were determined using dynamic light scattering (DLS). DLS measurements were carried out using a Brookhaven Instruments photon correlation spectrometer equipped with a BI-200SM goniometer, a BI-9000AT digital autocorrelator, and a Melles Griot He-Ne Laser (633 nm) with a maximum power output of 75 mW. All DLS measurements of DiI-loaded nanoparticles were performed in pure water and an experimental temperature of 23˚C and at a scattering angle of 90˚.

After overnight dialysis against deionized water to remove residual DMF and unencapsulated DiI, the DiI-loaded nanoparticles were transferred to pre-cleaned scintillation

vials then diluted 5× using deionized water, filtered through two nylon syringe filters in series with nominal pore sizes of 0.2 m (National Scientific Company) to give a final copolymer concentration of ~0.07 mg/mL. For each nanoparticle preparation, mean effective hydrodynamic sizes were determined from three measurements of the autocorrelation function using cumulent analysis. Mean effective hydrodynamic diameters were determined from three separate data collections corresponding to one individually-prepared stock solution, such that reported errors reflect the error in data collection.

3.2.8 X-Ray Diffraction

X-ray diffraction measurements were performed on a Rigaku Miniflex diffractometer with a Cr source (kR radiation, λ = 2.2890 Å) operating at 30 kV and 15 mA with a resolution of 0.05° (2θ) and a scan speed of 1°/min. X-ray diffraction profiles were collected for 2θ ranging from 10-80 degrees.

For XRD sample preparation, water was removed from suspensions of DiI-loaded nanoparticles by rotory evaporation at 25 °C until solid films were obtained. The resulting films were then scraped as a powder into the XRD specimen holder with no subsequent drying step to remove residual solvent. We note that this preparation method will significantly increase the crystallinity of coronal PEO blocks relative to their colloidal state, as removal of water from the nanoparticle coronae will allow initially-solubilized PEO chains to pack together. However, since the hydrophobic cores will contain no water in the purely aqueous suspensions, we do not expect the crystallinity of the core-forming PCL blocks to be strongly affected when water is removed by rotory evaporation. Therefore, our XRD experiments should provide a reasonable probe of nanoparticle core crystallinity in the colloidal state.

Peak deconvolution of XRD data was done using Origin Pro Version 8.1. Two characteristic reflections for each of crystalline PCL and crystalline PEO were identified from the literature and these were used to fix the positions of four Lorentzian peak contributions to the fit;[58,20] another small Lorentzian peak contribution was used to account for a small shoulder on the more intense PCL peak in order to obtain a good fit (Figure 8.3; Appendix II). Thus, XRD data were fit to a sum of 6 Lorentzian functions: 3 peaks assigned to crystalline PCL (2θ = 32.5, 32.7, and 35.7), 2 peaks assigned to crystalline PEO (2θ = 29.2 , 35.4), and 1 peak (no fixed position) assigned to incoherent scattering from amorphous copolymer (amorphous halo). Areal peak contributions from the three components (crystalline PCL, crystalline PEO, and amorphous copolymer) were then determined by integration and percentages of crystalline PCL and PEO were calculated using:

$$\%\ Crystalline\ \text{PCL} = A_{\text{PCL}}/A_{\text{total}},\ \text{and}\ \%\ Crystalline\ \text{PEO} = A_{\text{PEO}}/A_{\text{total}},$$

$$\text{where } A_{\text{total}} = A_{\text{PCL}} + A_{\text{PEO}} + A_{\text{amorph.}}$$

3.2.9 DiI Loading Efficiency Determination

To determine the dye loading efficiency, DiI-loaded nanoparticles were dissolved by adding a small weighed aliquot of the nanoparticle dispersion (1 – 2 drops) to a known quantity of DMF (selected so that maximum absorbance values were ≤ 0.1) and stirring for 4 h in the dark. Fluorescence intensity – concentration calibration curves for DiI at the emission maximum (λ_{ex} = 549 nm; λ_{em} = 565 nm, Figure S4) in DMF solutions were determined in the linear range; fluorescence intensities of dissolved nanoparticle solutions were measured at the same wavelengths and under identical conditions to those of the calibration standards, and within 5 min of obtaining the calibration curves. Before calculating integrated photoluminescence

intensities, a solvent background was subtracted and a correction for the detector response was applied to each sample and standard measurement. The dye concentrations were then determined from the calibration curves. After correcting for dilution factors, the loading efficiency was determined using the following expression:

$$\text{loading efficiency (\%)} = \frac{\text{DiI in PNPs (g)}}{\text{total DiI used (g)}} \times 100\%$$

Errors on loading efficiencies were calculated from standard deviations of values for three repeat preparations of DiI-loaded nanoparticles under the same chemical and flow conditions.

3.2.10 Determination of DiI Release Kinetics Under Perfect Sink Conditions

Dye release kinetics for nanoparticles prepared at various flow rates and two different water contents were determined under perfect sink conditions. For these experiments, a dialysis bag (MWCO: 50 kDa, Spectrum Labs) containing a 1.5 g suspension of DiI-loaded nanoparticles was placed in a 250 mL beaker filled with tap water. The beaker was then placed in a crystallization dish (190 x 100) equipped with a valve for out-flowing water. Tap water (4 ˚C, pH = 5.4) was allowed to flow into the beaker at ~480 mL/min via a Tygon tube. The beaker was allowed to overflow into the crystallization dish and subsequently flow out into the sink. At various times, *t*, aliquots of the dye-loaded nanoparticles were taken out of the dialysis bag. The sample was then put into a quartz microcuvette and subsequently analyzed using fluorescence spectroscopy (λ_{ex} = 549 nm; λ_{em} = 565 nm) to determine I(t). After analysis, the aliquot of dye-loaded nanoparticles was returned to the dialysis bag and perfect sink conditions.

3.2.11 Release Experiments into Various Media.

In order to determine the effect of the release medium on the release kinetics of the dye, release experiments for a single sample of DiI-loaded nanoparticles prepared at a water content of cwc + 10 wt % and a flow rate of 100 μL/min were carried out into the following media at the indicated temperatures: 1. perfect sink conditions, 4 ˚C, pH = 5.4; 2. deionized water, 23 ˚C, pH = 6.7; 3. 1% PBS, 23 ˚C, pH = 7.4; 4. 1% PBS + albumin (Sigma Aldrich) (45 g / L), 23 ˚C, pH = 7.4; 5. 1% PBS + albumin (Sigma Aldrich) (45 g / L), 37 ˚C, pH = 7.4; 6. 1% PBS + albumin (Sigma Aldrich) (45 g / L), 37 ˚C, pH = 4.0; and 7. 1% PBS + cell lysate (protein concentration = 0.38 g / L), 37 ˚C, pH = 7.4. The pH of all PBS-containing solutions was adjusted to either 7.4 or 4.0 using either HCl or NaOH before the release was started.

For all release experiments except those under perfect sink conditions, which are described in the previous section, the following procedures were applied. DiI-loaded nanoparticle dispersions (~10 mL) were transferred to a dialysis bag (SpectrumLabs, MWCO 100 kDa) which was placed into a reservoir containing 250× volume excess of a particular release medium compared to the DiI-loaded nanoparticle dispersions. Throughout the release experiments, the release medium was constantly stirred using magnetic stirring and maintained at experimental temperature using a hot plate in conjunction with a thermocouple. At predetermined times, aliquots of the sample were removed from the dialysis bag, air dried, and dissolved into DMF followed by DiI quantification using fluorescence spectroscopy (λ_{ex} = 549 nm; λ_{em} = 565 nm). For aliquots containing albumin or PBS, a liquid- liquid extraction using methyl *tert*-butyl ether (Sigma Aldrich) was conducted to extract DiI from the media solution. Prior to quantifying the amount of DiI obtained from liquid-liquid extraction, triplicate control experiments were conducted to determine the efficiency of the liquid-liquid extraction: known

amounts of DiI were mixed in with a solution containing both albumin and PBS, then a liquid-liquid extraction was conducted using methyl tert-butyl ether: the amount of DiI recovered was calculated to be >95% (w/w).

To prepare the cell lysate, the MCF-7 human adenocarcinoma breast cancer cell line was obtained as a generous gift from the BC Cancer agency. Cells were grown in Dulbecco's Modified Eagle's Medium (DMEM) supplemented with 10% fetal bovine serum in a 175 cm^2 culture flask and maintained at 37 °C with 5% CO_2 in a tissue culture incubator. To lyse the cells, the cells were exposed to lysis buffer (0.5% Triton X- 100, 0.5% NP-40, 0.15 M NaCl, 0.05 M Tris pH 8, and 0.001 M EDTA) and supplemented with a protease inhibitor cocktail set III (Millipore). The lysate protein concentration was quantified using the Bradford assay (Bio-Rad), using bovine serum albumin (BSA) as a standard. In brief, the cell lysate (5 μL) was combined with the Bradford assay reagent (1 mL) and then analyzed for the protein concentration by monitoring absorbance at 595 nm.

3.3 Results and Discussion

3.3.1 Effect of Flow Rate on Multiscale Structure of DiI-Loaded Nanoparticles.

Figure 3.2 presents the influence of on-chip flow rate on nanoparticle morphologies from TEM images and corresponding hydrodynamic size distributions from CONTIN analysis of DLS data. For two different water contents, both nanoparticle morphologies and hydrodynamic sizes show very similar trends with increasing flow rate. Starting with nanoparticles prepared at an on-chip flow rate of Q = 25 μL/min, TEM shows a combination of small spheres, lamellae and long filaments (Figure 3.2, A and D); the corresponding DLS size distributions show three distinct populations at ~70 nm, ~800 nm, and ~2000 nm, which we attribute to spheres, lamellae, and filaments, respectively, based on their lateral dimensions from TEM. When the flow rate is increased to Q = 50 μL/min, we find that long filaments are no longer present in the TEM images (Figure 3.2, B and E) but that spheres and lamellae persist; this is also supported by the DLS

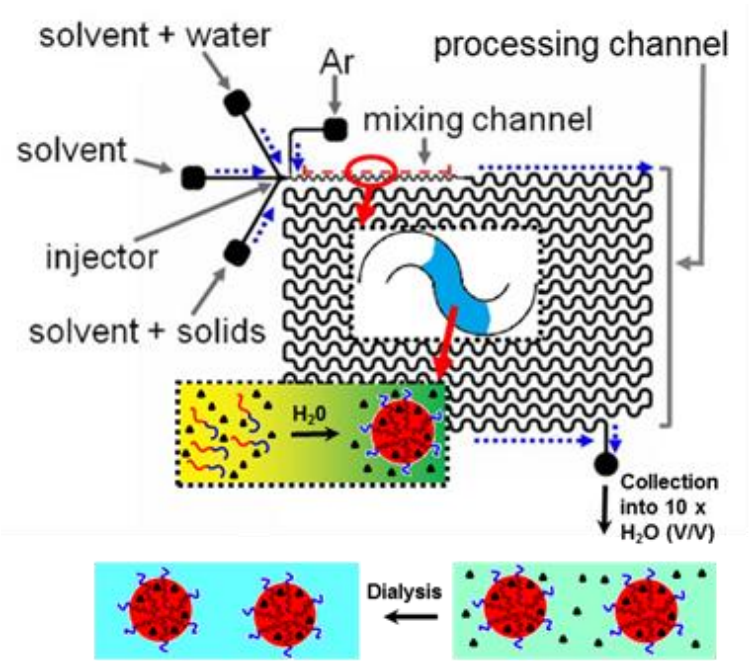

Figure 3.1 Schematic of the gas-liquid segmented reactor and on-chip formation of DiI-loaded PCL-*b*-PEO nanoparticles.

results, which show only two particle populations at ~70 nm and ~1000 nm. Finally, at a flow rate of Q = 100 μL/min (Figure 3.2,C and F), the long filaments return and all three morphologies (spheres, lamellae and filaments) are again present in the TEM images with three distinct populations observed by DLS. Table 3.1 lists morphologies and mean dimensions for each set of conditions, with excellent reproducibility observed over multiple preparations (Figures 8.5 and 8.6; Appendix II).

The nonmonotonic trend in nanoparticle morphologies on the colloidal length scale, with long filaments first disappearing and then reappearing with increasing on-chip flow rate, is in contrast to the corresponding linear behaviour of the internal crystallinity of nanoparticles at the nanoscale. Figure 3.3 shows a clear linear increase in PCL crystallinity versus flow rate for both water contents. These data include the three flow rates discussed in Figure 3.2 along with additional flow rates to confirm the linear trend.

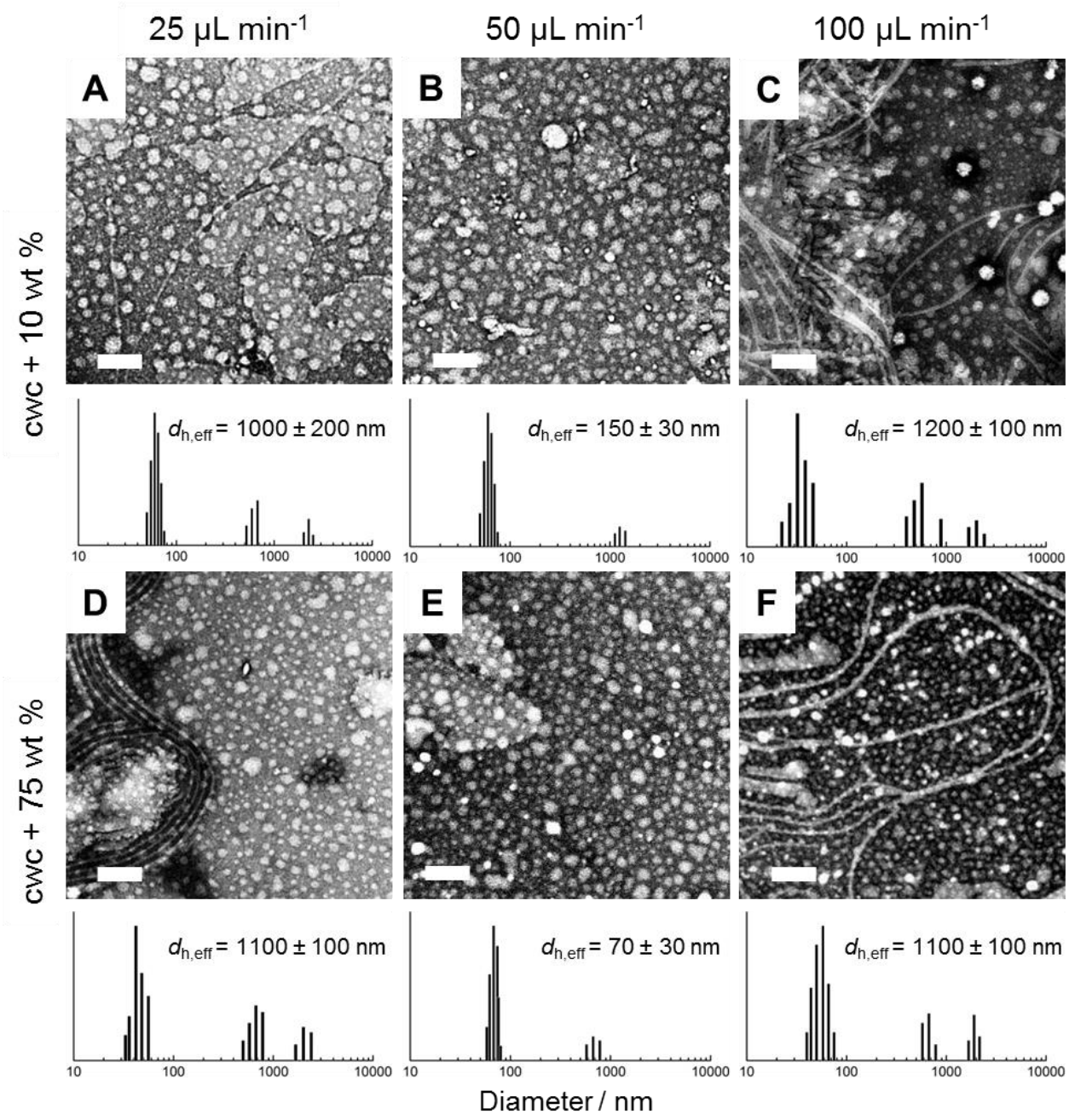

Figure 3.2 Effect of flow rate and water content on morphology and hydrodynamic size of DiI-loaded PCL-*b*-PEO nanoparticles. TEM images were produced by negative staining with uranyl acetate. All scale bars are 200 nm. Below each TEM image is a representative size distribution obtained from CONTIN analysis of DLS autocorrelation functions, along with the mean effective hydrodynamic diameter determined from CUMULENT analysis.

3.3.2 Effect of Water Content on Multiscale Structure of DiI-Loaded Nanoparticles.

Considering the effect of on-chip water content during nanoparticle formation, Figure 3.2 shows very similar nanoparticle morphologies and sizes for two vastly different water contents, cwc + 10 wt % and cwc + 75 wt %, at each of the three on-chip flow rates. This indicates a minimal influence of water content on the size and structure of DiI-loaded nanoparticles on the colloidal length scale. However, at the nanoscale, Figure 3.3 show that mass of crystalline PCL within the PNPs is 15-30 % higher at lower water content compared to higher water content over the range of investigated flow rates.

3.3.3 Discussion of Effects of Flow Rate and Water Content on Multiscale Structure of DiI-Loaded Nanoparticles.

The effects of on-chip flow rate on the size, morphology and internal crystallinity of block copolymer nanoparticles formed in segmented gas-liquid microfluidic reactors have been described in our previous publications.[27,30,20] Flow effects are attributed to the influence of high-shear "hot spots" on the evolution of polymeric nanoparticles as they progress through the processing channel (Figure 3.1) following their initial formation due to water mixing in the mixing channel. Three main mechanisms have been described by which hot spots can affect the final size and structure of polymeric nanoparticles: 1. shear-induced breakup of larger particles followed by intraparticle chain rearrangements; 2. shear-induced coalescence of smaller particles followed by intraparticle chain rearrangements; and 3. shear-induced crystallization. The first mechanism favours lower aggregation numbers with increasing flow rate, whereas the last two mechanisms favour higher aggregation numbers with increasing flow rate. The relative importance of these three mechanisms depends on a number of factors, including the maximum

shear rate and the sizes, morphologies, and internal viscosities of the initially-formed nanoparticles.[20,27,30]

Table 3.1 Morphologies[a] and Mean Dimensions[b] for PCL-*b*-PEO Nanoparticles Prepared in the Segmented Microfluidic Reactor at Various Water Contents and Flow Rates.

Water Content (cwc + *x* wt %)	25 μL/min	50 μL/min	100 μL/min
10	S (48 ± 4 nm) + C (15 ± 3 nm) + L	S (51 ± 5 nm) + L	S (47 ± 4 nm)+ C (16 ± 4 nm) + L
75	S (46 ± 5 nm) + C (15 ± 3 nm) + L	S (49 ± 4 nm) + L	S (49 ± 4 nm)+ C (14 ± 3 nm) + L

a) Prominent morphologies are indicated as S (spheres), C (cylinders or filomicelles), and L (lamellae).

b) Numbers refer to mean sphere diameters and cylinder widths. Reported errors are standard deviations of mean values determined for three replicate preparations.

Our previous work on PCL-*b*-PEO nanoparticles without hydrophobic molecules loaded in the cores showed nonmonotonic trends in morphology and size with respect to on-chip flow rate which were attributed to the competition between these flow-directed mechanisms.[20] In the present case, the disappearance of long filaments between Q = 25 μL/min (Figure 3.2, A and D) and Q = 50 μL/min (Figure 3.2, B and E), and the corresponding decrease in hydrodynamic size, is explained by the increased importance of shear-induced breakup of filaments in this range of flow rates. Then, when the flow rate is increased to Q = 100 μL/min (Figure 3.2, C and F), the reappearance of filaments and increase in hydrodynamic size can be explained by an increased rate of either shear-induced coalescence or shear-induced crystallization or a combination of both mechanisms. In contrast, our work on microfluidic-prepared PAX-loaded PCL-*b*-PEO nanoparticles showed a monotonic trend of increasing nanoparticle hydrodynamic size with increasing flow rate, although the both the water content (cwc + 5 wt %) and loading ratio (r = 0.01) during nanoparticle formation were both lower than in the present case.[20] However, this difference does highlight potential differences between results obtained using dye surrogates and

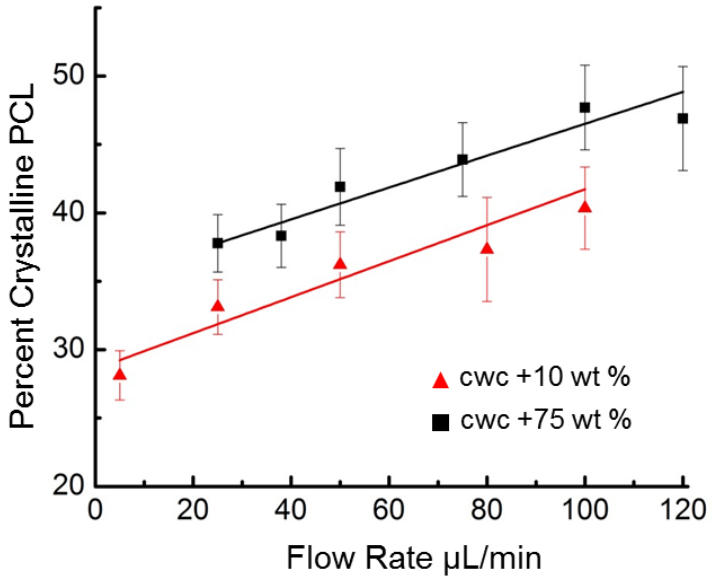

Figure 3.3 Effect of flow rate and water content on PCL crystallinity within the cores of DiI-loaded PCL-*b*-PEO nanoparticles

those obtained for specific drug targets; it also emphasizes that although dyes such as DiI may be useful for preliminary screening of on-chip manufacturing conditions, they will not eliminate the need for optimization experiments employing the specific molecule of interest.

We have previously reported a linear increase in the crystallinity of PCL cores with on-chip flow rate for both nanoparticles formed without hydrophobic cargo and with PAX loaded in the cores.[20] This was explained by shear-induced crystallization in the processing channel as PNPs formed in the mixing channel are exposed to the high-shear hot spots, where transient and elastic nanoparticle deformations may increase the orientation and crystallization of PCL chains. Here we find that a similar linear trend exists for DiI-loaded nanoparticles formed at both low (cwc + 10 wt %) and high (cwc + 75 wt %) water contents (Figure 3.3). Moreover, the overall higher PCL crystallinities for nanoparticles formed at the higher water content can be explained by the lower DMF solvent in the PCL phase under these conditions, allowing the less plasticized PCL to crystallize more readily. These results indicate that for the microfluidic

formation of PCL-*b*-PEO nanoparticles containing various hydrophobic cargo molecules, both the water content and flow rate will be critical manufacturing parameters.

3.3.4 Effect of Flow Rate and Water Content on DiI Loading Efficiency.

Loading efficiencies of DiI within nanoparticles prepared at three different flow rates (Q = 25, 50, and 100 μL/min) and two different water contents (cwc + 10 wt % and cwc + 75 wt %) are shown in Figure 3.4. Loading efficiency data obtained for nanoparticles prepared at additional flow rates between Q = 5 and 120 μL/min are shown in Figure 7.7. At the lower water content (cwc + 10 wt %), loading efficiencies increase monotonically with increaseing on-chip flow rate, starting at 76 % at 25 μL/min, then jumping to 90 % at 50 μL/min, then further increasing slightly to 94 % at 100 μL/min. Interestingly, we previously reported a similar trend of increasing loading efficiency with increasing on-chip flow rate for the drug PAX at a similarly-low water content (cwc + 5 wt %), despite differences in flow dependencies of size and morphology for PAX- and DiI-loaded nanoparticles.[20] At the high water content (cwc + 75 wt %), loading efficiencies are significantly lower than at the low water content, and also show a nonmonotomic trend with increasing flow rate, starting at 52 % at Q = 25 μL/min, then dropping to 43% at Q = 50 μL/min, then jumping back to 53 % at Q = 100 μL/min.

Based on thermodynamics alone, the higher water content should lead to a higher interfacial tension between the PCL core and the surrounding aqueous environment, and therefore a stronger partitioning of hydrophobic DiI into the core. However, we find instead that the lower water content leads to consistently higher loading efficiencies (Figure 3.4). This can be partially explained by the role of kinetics in the partitioning of the dye into the nanoparticle cores: at lower water content, the cores are more highly swollen with DMF, which lowers their

viscosities and facilitates the diffusion of dye into the cores. Also, the ordered PCL chains within crystallites will exclude guest dye molecules; therefore the higher PCL crystallinities at higher water content (Figure 3.3) could contribute to the lower DiI solubilities within the cores.

The effect of on-chip flow rate on loading efficiency is found to be different at the lower and higher water contents. At the higher water content (cwc + 75 wt %), the loading efficiency tracks with the mean size of nanoparticles (Figure 3.2, D-F), first decreasing and then increasing with increasing flow rate (Figure 3.4). Larger hydrophobic cores are known to show higher solubility for hydrophobic molecules,[25,61] which can explain this tracking of loading efficiency with nanoparticle size. In contrast, at the lower water content (cwc + 10 wt %), where the loading efficiencies are generally much higher, loading efficiencies are found to increase steadily with flow rate rate, despite a similar nonmonotonic trend in nanoparticle size as the the cwc + 75 wt % case (Figure 3.2, A-C). This suggests that DiI solubility is not strongly tied to nanoparticle size at the lower water content, probably due to the strong swelling of PCL cores with DMF in this case. Our understanding of the increase in loading efficiency with flow rate in the cwc + 10 wt % case (Figure 3.4) is unclear, although this trend may be due in part to a positive effect of increased mixing rate under higher shear conditions on dye loading.

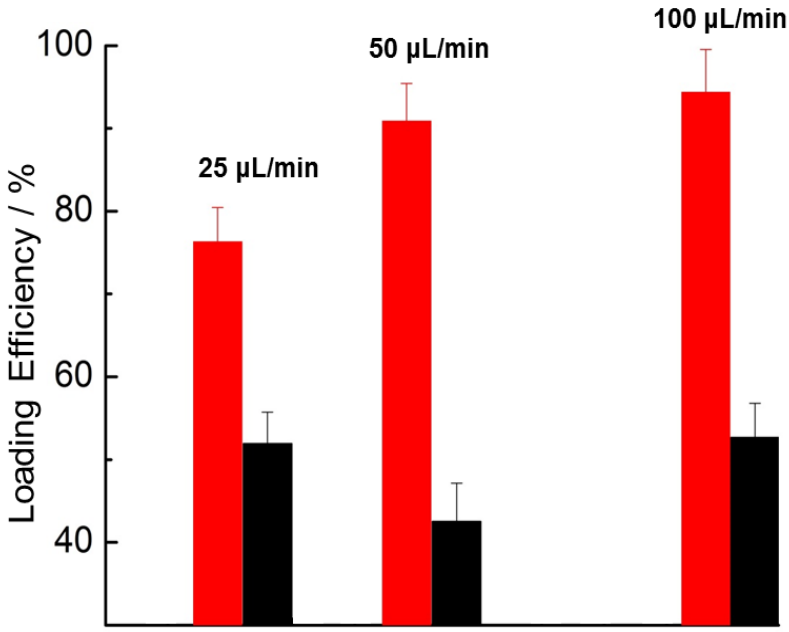

Figure 3.4 Effect of flow rate and water content on the loading efficiency of DiI-loaded PCL-*b*-PEO nanoparticles. Red bars: nanoparticles prepared at cwc + 10 wt %; black bars: nanoparticles prepared at

3.3.5 Effect of Flow Rate and Water Content on DiI Release Kinetics.

Similar to loading efficiencies, DiI release kinetics under perfect sink conditions show different on-chip flow rate dependencies at the high and low water contents. DiI release profiles at three different flow rates and at two different water contents are shown in Figure 3.5. Nanoparticles formed at the lower water content (cwc + 10 wt %) show generally faster release kinetics, with complete DiI release occurring in the range of ~2-4 days (Figure 3.5A). This is in contrast to nanoparticles formed at the higher water content (cwc + 75 wt %), which required a minimum of 15 days for dye release and some cases showing incomplete release even after 20 days (Figure 3.5B).

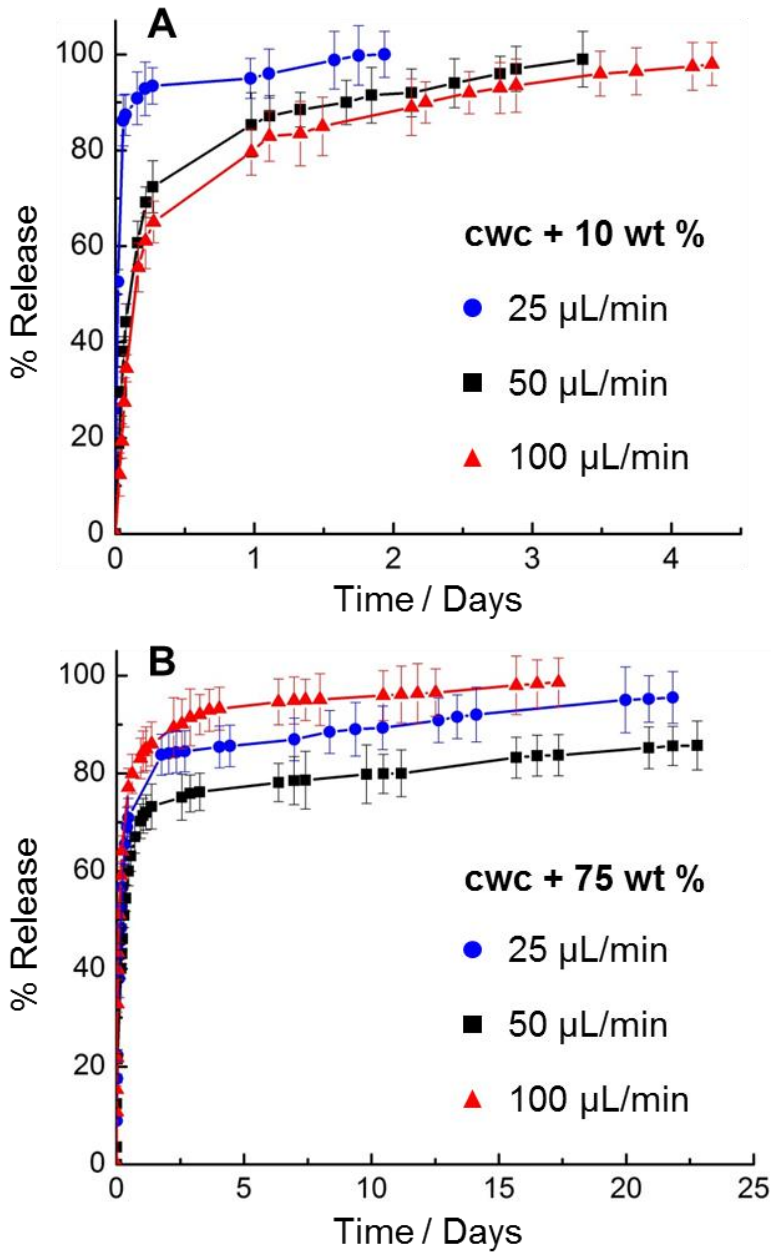

Figure 3.5 Effect of flow rate and water content on the release of DiI from DiI-loaded PCL-*b*-PEO nanoparticles. (A) Release profiles for nanoparticles prepared at cwc + 10 wt % and various flow rates. (B) Release profiles for nanoparticles prepared at cwc + 75 wt % and various flow rates. All release experiments carried out under perfect sink conditions as described in the text.

For the cwc + 10 wt % nanoparticles (Figure 3.5A), dye release becomes progressively slower with increasing flow rate of on-chip manufacturing. Nanoparticles formed at the lowest flow rate (Q = 25 µL/min) show the fastest dye release, with $t_{1/2}$ = 30 min and 100 % release

after ~2 days. For the intermediate flow rate of Q = 50 μL/min, the release is significantly slower, with $t_{1/2}$ = 3 h and ~3.5 days required for complete release. Finally, at the highest flow rate of Q = 100 μL/min, dye release is slower still, with $t_{1/2}$ = 4 h and 100 % release achieved after ~4 days.

On the other hand, nanoparticles formed at cwc + 75 wt % (Figure 3.5B) show release kinetics that first decrease and then increase with increasing flow rate. Nanoparticles formed at Q = 25 μL/min show release of DiI with $t_{1/2}$ = 5 h and a maximum of ~95 % dye released after 22 days. When the flow rate is increased to Q = 50 μL/min, a decrease in dye release rate is observed, with $t_{1/2}$ = 7 h and a maximum of ~85 % dye released after 22 days. However, when the flow rate is further increased to Q = 100 μL/min, the resulting nanoparticles show a sharp increase in release kinetics and the fastest dye release at this water content, with $t_{1/2}$ = 2 hrs and 100 % release achieved after ~17 days (Figure 3.5B).

3.3.6 Discussion of the Relationship Between Multiscale Structure and DiI Release Kinetics.

The described trends in release kinetics with respect to both the flow rate and water content of nanoparticle formation should be directly tied to the multiscale structure of the nanoparticles. Based on previous observations from our group and elsewhere in the literature,[12,13,55,18,19,61,20] three specific aspects of nanoparticle structure will influence the release kinetics of hydrophobic molecules from the core: 1. core volume; 2. core morphology; and 3. internal core crystallinity. For diffusional release, both core volume and morphology (through the surface-to-volume ratio) will influence diffusional distances of molecules to escape the hydrophobic cores. Core crystallinity has been shown to have a direct correlation with internal core viscosity, which will influence diffusion coefficients within the cores. In addition, all three

structural factors (volume, morphology and crystallinity) will affect the kinetics of hydrolytic nanoparticle degradation which, along with simple diffusion, provides another mechanism of release.[16,20]

First considering the effect of water content on release kinetics, the significantly faster release at the lower water content (cwc + 10 wt %, Figure 3.5A) compared to the higher water content (cwc + 75 wt %, Figure 5B) is explained by the corresponding lower PCL crystallinities in the former case (Figure 3.3). Higher PCL crystallinity has been previously shown to increase the microviscosity of the nanoparticle core, leading to slower diffusion of encapsulated molecules and correspondingly slower release kinetics.[12,13,19,20] In addition to slower release, the high PCL crystallinity appears to result in the kinetic trapping of DiI molecules within the cores of two of the three cwc + 75 wt % samples, as evinced by the leveling off of release levels at ~95 % and ~85 % after ~20 days for the Q = 25 μL/min and 50 μL/min nanoparticles, respectively (Figure 3.5B).

We next consider the effect of on-chip flow rate on release kinetics at a water content of cwc + 10 wt % (Figure 3.5A). The observed monotonic slowing down of release kinetics with increasing flow rate can be explained by the concomitant increase in core crystallinity (Figure 3.3), which will lead to a corresponding increase in core viscosity and decrease in the diffusion coefficient of DiI within the cores. Since neither nanoparticle size nor morphology track with the DiI release rates at this water content, it appears that, of the three structural parameters listed above, the role of core crystallinity is most important in determining the flow dependence of release kinetics under these conditions. We find that this monotonic trend of slower release kinetics with increasing on-chip flow rate agrees with results obtained previously for PAX-

loaded nanoparticles prepared in an identical microfluidic reactor at a low but slightly different water content (cwc + 5 wt %).[20]

Finally, we consider the nonmonotonic effect of on-chip flow rate on the release kinetics of nanoparticles prepared at a water content of cwc + 75 wt % (Figure 3.5B). Interestingly, the slowest release kinetics at this water content are shown by nanoparticles prepared at the intermediate flow rate (Q = 50 μL/min), which is the one flow rate that does not produce a significant number of filaments, as discussed previously (Figure 3.2E). In previous work, the hydrolytic degradation of filaments has been shown to occur more rapidly than other morphologies, providing an additional pathway for faster release of DiI. The tracking of the availability of this pathway with the presence of filament nanoparticles thus explains the observed flow dependence of release kinetics.

3.3.7 Effect of Release Media on DiI Release Kinetics

Along with release kinetics under perfect sink conditions described above (flowing tap water, 4 °C, pH = 5.4), for a single DiI-loaded nanoparticle sample we also investigated release into a variety of media at different temperatures meant to mimic physiological conditions to various extents. For all release media except perfect sink conditions, the aqueous reservoir was static (i.e. not continually replenished) although a strong concentration gradient was maintained through a large volume differential (250×) in favour of the release medium compared to the dialyzing sample.

First, release kinetics under perfect sink conditions were compared with release into various aqueous reservoirs at room temperature (deionized water, pH = 6.7; PBS buffer only, pH = 7.4; and PBS buffer + albumin, pH = 7.4). The resulting four release profiles are shown in

Figure 3.6A. Due to the importance of hydrolytic nanoparticle degradation to release kinetics, the hydrodynamic nanoparticle sizes under the various conditions were also tracked by DLS for the first 24 h of release and the corresponding plots are shown in Figure 3.6B. Of the four release

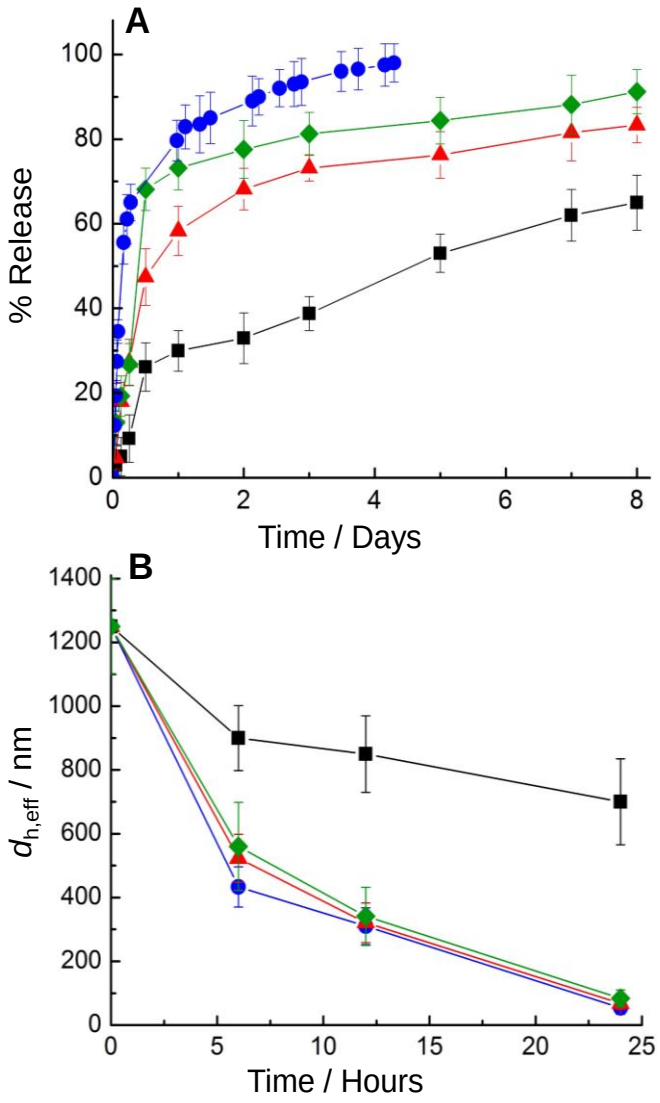

Figure 3.6 Effect of different chemical and physical characteristics of release media on DiI release profiles (A) and decay of nanoparticle hydrodynamic size (B) for DiI-loaded PCL-*b*-PEO nanoparticles assembled on-chip at a flow rate of 100 µL/min and a water content of cwc + 10 wt %. In both (A) and (B), the release media are as follows: 1. perfect sink conditions, 4 ˚C, pH = 5.4 (●); 2. deionized water, 23 ˚C, pH = 6.7 (■); 3. PBS buffer, 23 ˚C, pH = 7.4 (▲); and 4. PBS buffer + albumin, 23 ˚C, pH = 7.4 (◆).

profiles (Figure 3.6A), perfect sink conditions at pH = 5.4 show fastest release (blue curve, $t_{1/2}$ = 4 h), followed by PBS buffer + albumin at pH = 7.4 (green curve, $t_{1/2}$ = 10 h), then PBS only at pH = 7.4 (red curve, $t_{1/2}$ = 13 h), and finally deionized water at pH = 6.7, which shows significantly slower release than the other four conditions (black curve, $t_{1/2}$ = 5 days). From the corresponding plots of nanoparticle size (Figure 3.6B), we find that deionized water also leads to the slowest rate of size decrease, suggesting slowest hydrolytic degradation of the nanoparticles, with the other three conditions showing similar rates of nanoparticle degradation within experimental error.

From these results, we conclude that the main bottleneck for the significantly slower release into deionized water is the correspondingly slow rate of nanoparticle degradation under these conditions. This underlines the importance of hydrolytic degradation to the release of hydrophobic molecules from PCL-*b*-PEO nanoparticles. It also suggests that the presence of ions in the aqueous media, such as are present in tap water and all solutions containing PBS but not in deionized water, play an important catalytic role in the hydrolysis reaction. The significant but more subtle differences in the other three conditions, which show essentially identical degradation rates in the first 24 h, indicate that other aspects of the release media also play a role in influencing the release. For example, the fastest release rate occurring for perfect sink conditions is attributed to the continual replenishing of the release media and the maintenance of an infinite chemical potential gradient in that experiment. The slightly higher release rate into PBS + albumin compared to PBS alone is ascribed to the hydrophobic surface of the albumin protein allowing adhesion of the hydrophobic dye and facilitating transport through the aqueous medium.

Next, release kinetics were compared for various aqueous reservoirs at physiological temperature (37°C, PBS + albumin, pH = 4.0; PBS + albumin, pH = 7.4; and PBS + cell lysate, pH = 7.4), along with room temperature release into PBS + albumin at pH = 7.4. The resulting four release profiles are shown in Figure 3.7A with corresponding plots of nanoparticle size in Figure 7B. Of the three release profiles obtained at 37°C (Figure 3.7A, solid curves), PBS + albumin at pH = 4.0 showed the fastest release (purple curve, $t_{1/2}$ = 8 h), followed by PBS + albumin at pH = 7.4 (orange curve, $t_{1/2}$ = 9 h), then PBS + cell lysate at pH = 7.4 (gray curve, $t_{1/2}$ = 12 h). Comparing identical chemical conditions at two different temperatures, DiI release into PBS + albumin at pH = 7.4 and room temperature (dashed green curve, $t_{1/2}$ = 10 h) is slightly slower than release into the same medium at physiological temperature (orange curve, $t_{1/2}$ = 9 h); this can be attributed to a marginally faster rate of hydrolytic degradation at the more elevated temperature, as indicated by the corresponding plots of nanoparticle size in Figure 3.7B.

We note that the effect of acidic pH into otherwise equivalent solutions of PBS + albumin is a slight increase in release rate (Figure 3.7A, purple and orange curves, pH = 4.0 and 7.4, respectively) which can be attributed to an increased rate of PCL hydrolysis under acidic conditions. However, if the rate of hydrolysis is faster at pH = 4.0 than at 7.4 under these conditions, this is not reflected in the corresponding plots in Figure 3.7B, which show similar rates of decreasing nanoparticle size in these two cases; one possibility is that pathways of PCL hydrolytic degradation that contribute to DiI release but do not significantly affect hydrodynamic diameter, such as poration, are selectively accelerated at decreased pH. Finally, the relatively slow rate of release into PBS + cell lysate at pH = 7.4 compared to PBS + albumin at pH = 7.4 (Figure 3.7A, gray and orange curves) can be explained by the relatively low protein concentration in the cell lysate compared to the prepared albumin solution leading to slower

transport of hydrophobic dye through the aqueous phase. We note that although the lysate will also contain trypsin and related enzymes, which could accelerate release by providing enzymatic pathways for PCL hydrolysis, in the present experiment these pathways were blocked by the

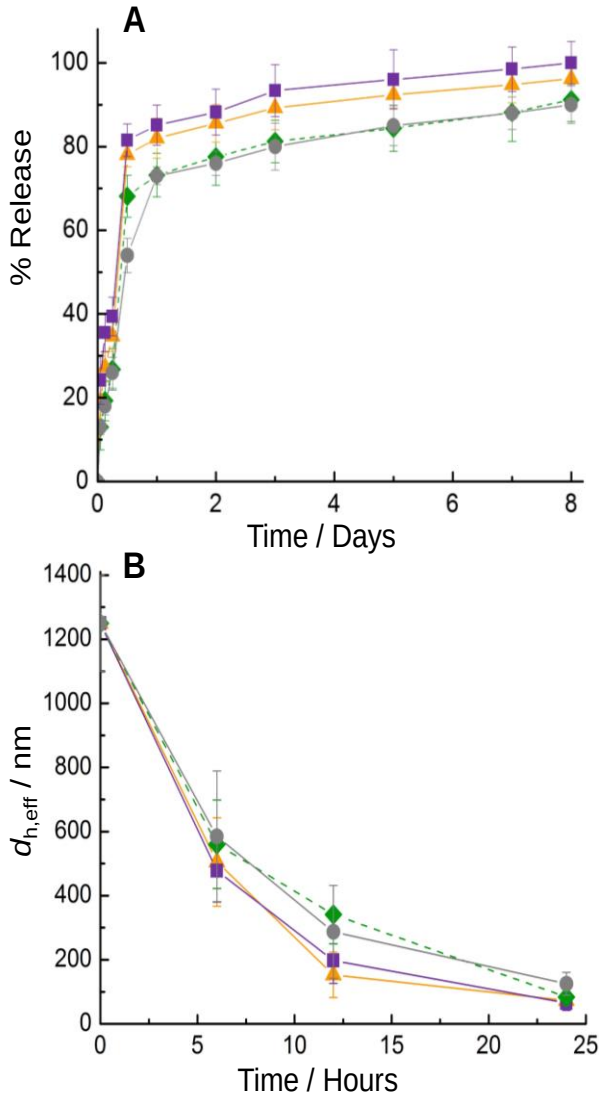

Figure 3.7 Effect of different chemical and physical characteristics of release media on DiI release profiles (A) and decay of nanoparticle hydrodynamic size (B) for DiI-loaded PCL-*b*-PEO nanoparticles assembled on-chip at a flow rate of 100 μL/min and a water content of cwc + 10 wt %. In both (A) and (B), the release media are as follows: 1. PBS buffer + albumin, 23 ˚C, pH = 7.4 (◆); 2. PBS buffer + albumin, 37 ˚C, pH = 7.4 (▲); 3. PBS buffer + albumin, 37 ˚C, pH = 4.0 (■); 4. PBS buffer + cell lysate, 37 ˚C, pH = 7.4 (●).

protease inhibitor cocktail. An interesting and somewhat puzzling observation is that the relative rates of decreasing nanoparticle size (Figure 3.7B, gray and orange curves) also suggest slightly slower PCL degradation in the cell lysate compared to the albumin solution, despite the two

aqueous media being at the same temperature and pH. Although this could suggest a catalytic role of albumin in PCL degradation at physiological temperature, we note that the difference in the rates of size decrease is small compared to experimental error and further investigation is required to confirm this effect.

3.4 Conclusions

We have studied the effects on-chip manufacturing conditions (water content and flow rate) on the multiscale structure (hydrodynamic size, morphology, and internal crystallinity) and function (loading efficiency and release rate) of DiI-loaded PCL-*b*-PEO nanoparticles produced in a gas-liquid segmented microfluidic device. Consistent with previous results for PAX-loaded and "empty" nanoparticles, we find a linear increase in PCL crystallinity in the nanoparticle cores with increasing flow rate. The relationships between flow rate and nanoparticle size and morphology are more complex; for both high and low water contents, we find first a decrease and then an increase in nanoparticle size (coincident with the disappearance and reappearance of long filament nanoparticles) with increasing flow rate. We show that chemical and flow control of multiscale structure provides tunable loading and release of the DiI probe dye. Specifically, loading efficiencies at the lower water content (cwc + 10 wt %) were generally higher (up to 94%) compared to the higher water content (cwc + 75 wt %, up to 53%) and also showed significant and different flow rate dependencies at the two water contents. Kinetic release profiles revealed DiI release times between ~2-4 days for nanoparticles produced at the lower water content but >15 days for nanoparticles produced at the higher water content. At the lower water content, the flow dependence of release rates tracked with the crystallinity within the nanoparticle core, whereas at the higher water content, the flow rate dependence of release rates

tracked with the presence of long filament nanoparticles within the samples. These results highlight some useful general information on the importance of both flow rate and the chemical environment for the microfluidic production of PCL-*b*-PEO nanoparticles containing hydrophobic cargo, and provide valuable guidelines for producing specific delivery formulations using this platform. This work also demonstrates that while specific flow rate-structure trends (morphology and hydrodynamic size) for DiI-loaded nanoparticles differed from those found previously for PAX-loaded nanoparticles manufactured in an identical microfluidic reactor (Chapter 2), pertinent flow rate-function trends (loading efficiency and release rate) were similar at a similarly low water content. This highlights the general utility of DiI as a hydrophobic probe for screening on-chip manufacturing conditions for drug-loaded nanoparticles.

Finally, we use a single DiI-loaded PCL-*b*-PEO nanoparticle formulation to determine the effect of chemical and physical characteristics of the release medium on the kinetics of dye release and nanoparticle degradation. Although subtle differences in release kinetics were observed depending on temperature, pH, and the presence of albumin or cell lysate, the most important factor appeared to be the presence (or absence) of ions in the aqueous reservoir, with release into deionized water being markedly slower than other experiments. Since such *in vitro* release experiments are ubiquitous in the literature, and often employ different chemical and physical conditions, we conclude that meaningful comparison of these results requires careful consideration of any differences in the release media and in specific experimental conditions.

3.5 References

(1) Kataoka, K.; Harada, A.; Nagasaki, Y. Block Copolymer Micelles for Drug Delivery: Design, Characterization and Biological Significance. *Adv. Drug Deliv. Rev.* **2001**, *47*, 113-131.

(2) O'Reilly, R. K.; Hawker, C. J.; Wooley, K. L. Cross-Linked Block Copolymer Micelles: Functional Nanostructures of Great Potential and Versatility. *Chem. Soc. Rev.* **2006**, *35*, 1068-1083.

(3) Sutton, D.; Nasongkla, N.; Blanco, E.; Gao, J. M. Functionalized Micellar Systems for Cancer Targeted Drug Delivery. *Pharm. Res.* **2007**, *24*, 1029-1046.

(4) Elsabahy, M.; Wooley, K. L. Design of Polymeric Nanoparticles for Biomedical Delivery Applications. *Chem. Soc. Rev.* **2012**, *41*, 2545-2561.

(5) Zhang, L. Eisenberg, A. Multiple Morphologies of "Crew-Cut" Aggregates of Polystyrene-*b*-Poly(acrylic acid) Block Copolymers. *Science* **1995**, *268*, 1728-1731.

(6**)** Zhang, L. Eisenberg, A. Multiple Morphologies and Characteristics of "Crew-Cut" Micelle-like Aggregates of Polystyrene-*b*-Poly(acrylic acid) Diblock Copolymers in Aqueous Solutions *J. Am. Chem. Soc.* 1996, *118*, 3168-3181.

(7) Discher, B. M.; Won, Y.-Y.; Ege, D. S.; Lee, J. C.-M.; Bates, F. S.; Discher, D. E.; Hammer, D. A. Polymersomes: Tough Vesicles Made from Diblock Copolymers. *Science* **1999**, *284*, 1143-1146.

(8) Förster, S.; Plantenberg, T. From Self-Organizing Polymers to Nanohybrid and Biomaterials. *Angew. Chem. Int. Ed.* **2002**, *41*, 688-714.

(9) Jain, S.; Bates, F. S. On the Origins of Morphological Complexity in Block Copolymer Surfactants. *Science* **2003**, *300*, 460-464.

(10) Cui, H.; Chen, Z.; Zhong, S.; Wooley, K. L.; Pochan, D. J. Block Copolymer Assembly via Kinetic Control. *Science* **2007**, *317*, 647-650.

(11) Wang, X.; Guerin, G.; Wang, H.; Wang, Y.; Manners, I.; Winnik, M. A. Cylindrical Block Copolymer Micelles and Co-Micelles of Controlled Length and Architecture. *Science* **2007**, *317*, 644-647.

(12) Liggins, R. T.; Burt, H. M. Paclitaxel Loaded Poly(L-lactic acid) Microspheres: Properties of Microspheres Made With Low Molecular Weight Polymers. *Int. J. Pharm.* **2001**, *222*, 19-33.

(13) Liggins, R. T.; Burt, H. M. Paclitaxel Loaded Poly(L-lactic acid) (PLLA) Microspheres: II. The Effect of Processing Parameters on Microsphere Morphology and Drug Release Kinetics. *Int. J. Pharm.* **2004**, *281*, 103-106.

(14) Yang, X. Q.; Zhu, B.; Dong, T. A.; Pan, P. J.; Shuai, X. T.; Inoue, Y. S. Interactions Between an Anticancer Drug and Polymeric Micelles Based on Biodegradable Polyesters. *Macromol. Biosci.* **2008**, *8*, 1116-1125.

(15) He, W.-N.; Xu, J.-T. Crystallization Assisted Self-assembly of Semicrystalline Block Copolymers. *Prog. Polym. Sci.* **2012**, *37*, 1350-1400.

(16) Geng, Y.; Discher, D. E. Hydrolytic Degradation of Poly(ethylene oxide)-*block*-Polycaprolactone Worm Micelles. *J. Am. Chem. Soc.* **2005**, *127*, 12780-12781.

(17) Discher, D. E.; Ortiz, V.; Srinivas, G.; Klein, M. L.; Kim, Y.; Christian, D.; Cai, S.; Photos, P.; Ahmed, F. Emerging Applications of Polymersomes in Delivery: From Molecular Dynamics to Shrinkage of Tumors. *Prog. Polym. Sci.* **2007**, *32*, 838-857.

(18) Letchford, K.; Burt, H. A Review of the Formation and Classification of Amphiphilic Block Copolymer Nanoparticulate Structures: Micelles, Nanospheres, Nanocapsules and Polymersomes. *Eur. J. Pharm. Biopharm.* **2007**, *65*, 259-269.

(19) Letchford, K.; Liggins, R.; Wasan, K. M.; Burt, H. In Vitro Human Plasma Distribution of Nanoparticulate Paclitaxel is Dependent on the Physicochemical Properties of Poly(ethylene glycol)-*block*-Poly(caprolactone) Nanoparticles. *Eur. J. Pharm. Biopharm.* **2009**, *71*, 196-206.

(20) Bains, A.; Cao, Y.; Moffitt, M. G. Multiscale Control of Hierarchical Structure in Crystalline Block Copolymer Nanoparticles Using Microfluidics. *Macromol. Rapid Commun.* **2015**, DOI: 10.1002/marc.201500359

(21) Cai, S.; Vijayan, K.; Cheng, D.; Lima, E.; Discher, D. Micelles of Different Morphologies—Advantages of Worm-like Filomicelles of PEO-PCL in Paclitaxel Delivery. *Pharm. Res.* **2007**, *24*, 2099-2109.

(22) Geng, Y.; Dalhaimer, P.; Cai, S.; Tsai, R.; Tewari, M.; Minko, T.; Discher, D. E. Shape Effects of Filaments Versus Spherical Particles in Flow and Drug Delivery. *Nat Nano* **2007**, *2*, 249-255.

(23) Venkataraman, S.; Hedrick, J. L.; Ong, Z. Y.; Yang, C.; Ee, P. L. R.; Hammond, P. T.; Yang, Y. Y. The Effects of Polymeric Nanostructure Shape on Drug Delivery. *Adv. Drug Deliv. Rev.* **2011**, *63*, 1228-1246.

(24) Glover, A. L.; Nikles, S. M.; Nikles, J. A.; Brazel, C. S.; Nikles, D. E. Polymer Micelles with Crystalline Cores for Thermally Triggered Release. *Langmuir* **2012**, *28*, 10653-10660.

(25) Oltra, N. S.; Swift, J.; Mahmud, A.; Rajagopal, K.; Loverde, S. M.; Discher, D. E. Filomicelles in Nanomedicine - From Flexible, Fragmentable, and Ligand-Targetable Drug Carrier Designs to Combination Therapy for Brain Tumors. *J. Mater. Chem. B.* **2013**, *1*, 5177-5185.

(26) Fang, J.; Nakamura, H.; Maeda, H. The EPR effect: Unique Features of Tumor Blood Vessels for Drug Delivery, Factors Involved, and Limitations and Augmentation of the Effect. *Adv. Drug Deliv. Rev.* **2011**, *63*, 136-151.

(27) Wang, C.-W.; Sinton, D.; Moffitt, M. G. Flow-Directed Block Copolymer Micelle Morphologies via Microfluidic Self-Assembly. *J. Am. Chem. Soc.* **2011**, *133*, 18853-18864.

(28) Wang, C.-W.; Bains, A.; Sinton, D.; Moffitt, M. G. Flow-Directed Assembly of Block Copolymer Vesicles in the Lab-on-a-Chip. *Langmuir* **2012**, *28*, 15756-15761.

(29) Wang, C.-W.; Bains, A.; Sinton, D.; Moffitt, M. G. Flow-Directed Loading of Block Copolymer Micelles with Hydrophobic Probes in a Gas–Liquid Microreactor. *Langmuir* **2013**, *29*, 8385-8394.

(30) Wang, C.-W.; Sinton, D.; Moffitt, M. G. Morphological Control via Chemical and Shear Forces in Block Copolymer Self-Assembly in the Lab-on-Chip. *ACS Nano* **2013**, *7*, 1424-1436.

(31) Alexandridis, P.; Athanassiou, V.; Fukuda, S.; Hatton, T. A. Surface-Activity of Poly(ethylene oxide)-*block*-Poly(propylene oxide)-*block*-Poly(Ethylene oxide) Copolymers. *Langmuir* **1994**, *10*, 2604-2612.

(32) Inoue, T.; Chen, G. H.; Nakamae, K.; Hoffman, A. S. An AB Block Copolymer of Oligo(methyl methacrylate) and Poly(acrylic acid) for Micellar Delivery of Hydrophobic Drugs. *J. Controlled Release* **1998**, *51*, 221-229.

(33) Allen, C.; Han, J. N.; Yu, Y. S.; Maysinger, D.; Eisenberg, A. Polycaprolactone-*b*-Poly(ethylene oxide) Copolymer Micelles as a Delivery Vehicle for Dihydrotestosterone. *J. Controlled Release* **2000**, *63*, 275-286.

(34) Soo, P. L.; Luo, L. B.; Maysinger, D.; Eisenberg, A. Incorporation and Release of Hydrophobic Probes in Biocompatible Polycaprolactone-*block*-Poly(ethylene oxide) Micelles: Implications for Drug Delivery. *Langmuir* **2002**, *18*, 9996-10004.

(35) Mahmud, A.; Lavasanifar, A. The Effect of Block Copolymer Structure on the Internalization of Polymeric Micelles by Human Breast Cancer cells. *Colloid Surf. B-Biointerfaces* **2005**, *45*, 82-89.

(36) Kim, S. Y.; Shin, I. L. G.; Lee, Y. M.; Cho, C. S.; Sung, Y. K. Methoxy Poly(ethylene glycol) and ϵ-Caprolactone Amphiphilic Block Copolymeric Micelle Containing Indomethacin.: II. Micelle Formation and Drug Release Behaviours. *J. Controlled Release* **1998**, *51*, 13-22.

(37) Teng, Y.; Morrison, M. E.; Munk, P.; Webber, S. E.; Procházka, K. Release Kinetics Studies of Aromatic Molecules into Water from Block Polymer Micelles. *Macromolecules* **1998**, *31*, 3578-3587.

(38) Liu, M.; Kono, K.; Fréchet, J. M. J. Water-Soluble Dendritic Unimolecular Micelles:: Their Potential as Drug Delivery Agents. *J. Controlled Release* **2000**, *65*, 121-131.

(39) Lavasanifar, A.; Samuel, J.; Kwon, G. S. Poly(ethylene oxide)-*block*-Poly(l-amino acid) Micelles for Drug Delivery. *Adv. Drug Deliv. Rev.* **2002**, *54*, 169-190.

(40) Cho, Y. W.; Lee, J.; Lee, S. C.; Huh, K. M.; Park, K. Hydrotropic Agents for Study of In Vitro Paclitaxel Release from Polymeric Micelles. *J. Controlled Release* **2004**, *97*, 249-257.

(41) Shuai, X.; Ai, H.; Nasongkla, N.; Kim, S.; Gao, J. Micellar Carriers Based on Block Copolymers of Poly(ε-caprolactone) and Poly(ethylene glycol) for Doxorubicin Delivery. *J. Controlled Release* **2004**, *98*, 415-426.

(42) Liu, J.; Zeng, F.; Allen, C. Influence of Serum Protein on Polycarbonate-Based Copolymer Micelles as a Delivery System for a Hydrophobic Anti-Cancer Agent. *J. Controlled Release* **2005**, *103*, 481-497.

(43) Liu, S. Q.; Tong, Y. W.; Yang, Y.-Y. Incorporation and In Vitro Release of Doxorubicin in Thermally Sensitive Micelles Made From Poly(N-isopropylacrylamide-co-N,N-dimethylacrylamide)-*b*-Poly(d,l-lactide-co-glycolide) With Varying Compositions. *Biomaterials* **2005**, *26*, 5064-5074.

(44) Zeng, F. Q.; Lee, H.; Allen, C. Epidermal Growth Factor-Conjugated Poly(ethylene glycol)-*block*-Poly(delta-valerolactone) Copolymer Micelles for Targeted Delivery of Chemotherapeutics. *Bioconjugate Chem.* **2006**, *17*, 399-409.

(45) Aliabadi, H. M.; Brocks, D. R.; Mahdipoor, P.; Lavasanifar, A. A Novel Use of an In Vitro method to Predict the In Vivo Stability of Block Copolymer Based Nano-Containers. *J. Controlled Release* **2007**, *122*, 63-70.

(46) Liu, J.; Zahedi, P.; Zeng, F.; Allen, C. Nano-Sized Assemblies of a PEG-Docetaxel Conjugate as a Formulation Strategy for Docetaxel. *J. Pharm. Sci.* **2008**, *97*, 3274-3290.

(47) Upadhyay, K. K.; Bhatt, A. N.; Mishra, A. K.; Dwarakanath, B. S.; Jain, S.; Schatz, C.; Le Meins, J. F.; Farooque, A.; Chandraiah, G.; Jain, A. K.; Misra, A.; Lecommandoux, S. The Intracellular Drug Delivery and Anti Tumor Activity of Doxorubicin Loaded Poly(gamma-benzyl L-glutamate)-*b*-Hyaluronan Polymersomes. *Biomaterials* **2010**, *31*, 2882-2892.

(48) Cheng, Y. X.; Hao, J.; Lee, L. A.; Biewer, M. C.; Wang, Q.; Stefan, M. C. Thermally Controlled Release of Anticancer Drug from Self-Assembled Gamma-Substituted Amphiphilic Poly(ε-caprolactone) Micellar Nanoparticles. *Biomacromolecules* **2012**, *13*, 2163-2173.

(49) Gong, J.; Chen, M. W.; Zheng, Y.; Wang, S. P.; Wang, Y. T. Polymeric Micelles Drug Delivery System in Oncology. *J. Controlled Release* **2012**, *159*, 312-323.

(50) Liu, Z. H.; Wang, Y. T.; Zhang, N. Micelle-Like Nanoassemblies Based on Polymer-Drug Conjugates as an Emerging Platform for Drug Delivery. *Expert Opinion on Drug Delivery* **2012**, *9*, 805-822.

(51) Zhang, X. C.; Burt, H. M.; VonHoff, D.; Dexter, D.; Mangold, G.; Degen, D.; Oktaba, A. M.; Hunter, W. L. An Investigation of the Antitumour Activity and Biodistribution of Polymeric Micellar Paclitaxel. *Cancer Chem. Pharmacol.* **1997**, *40*, 81-86.

(52) Kannan, S.; Kolhe, P.; Raykova, V.; Glibatec, M.; Kannan, R. M.; Lieh-Lai, M.; Bassett, D. Dynamics of Cellular Entry and Drug Delivery by Dendritic Polymers into Human Lung Epithelial Carcinoma Cells. *J. Biomater. Sci., Polym. Ed.* **2004**, *15*, 311-330.

(53) Sahu, A.; Bora, U.; Kasoju, N.; Goswami, P. Synthesis of Novel Biodegradable and Self-Assembling Methoxy Poly(ethylene glycol)–Palmitate Nanocarrier for Curcumin Delivery to Cancer Cells. *Acta Biomaterialia* **2008**, *4*, 1752-1761.

(54) Geng, Y. D., D.E. Visualization of Degradable Worm Micelle Breakdown in Relation to Drug Release. *Polymer* **2006**, *47*, 2519-2525.

(55) Geng, Y. D., P.; Cai, S.; Tsai, R.; Tewari, M.; Minko, T.; Discher, D.E. Shape Effects of Filaments Versus Spherical Particles in Flow and Drug Delivery. *Nat. Nanotechnol.* **2007**, *2*, 249-255.

(56) Vidal-Sanz, M.; Villegas-Pérez, M. P.; Bray, G. M.; Aguayo, A. J. Persistent Retrograde Labeling of Adult Rat Retinal Ganglion Cells With the Carbocyanine Dye DiI. *Exp. Neurol.* **1988**, *102*, 92-101.

(57) Asahara, T.; Murohara, T.; Sullivan, A.; Silver, M.; van der Zee, R.; Li, T.; Witzenbichler, B.; Schatteman, G.; Isner, J. M. Isolation of Putative Progenitor Endothelial Cells for Angiogenesis. *Science* **1997**, *275*, 964-966.

(58) Cuong, N.-V.; Li, Y.-L.; Hsieh, M.-F. Targeted Delivery of Doxorubicin to Human Breast Cancers by Folate-Decorated Star-Shaped PEG-PCL Micelle. *J. Mater. Chem.* **2012**, *22*, 1006-1020.

(59) Spector, T. Refinement Of Coomassie Blue Method Of Protein Quantitative - Simple and Linear Spectrophotometric Assay For Less-Than-Or-Equal-To 0.5 To 50 Mu-g Of Protein. *Anal. Biochem.* **1978**, *86*, 142-146.

(60) Sapan, C. V.; Lundblad, R. L.; Price, N. C. Colorimetric Protein Assay Techniques. *Biotechnol. Appl. Biochem.* **1999**, *29*, 99-108.

(61) Ahmad, Z.; Shah, A.; Siddiq, M.; Kraatz, H.-B. Polymeric Micelles as Drug Delivery Vehicles. *RSC Advances* **2014**, *4*, 17028-17038.

Chapter 4

Effect of Initial Drug Loading Ratio and Copolymer Composition on On-Chip Assembled Paclitaxel Loaded PCL-*b*-PEO Nanoparticles

4.1 Introduction

In Chapters 2 and 3, we have used the semicrystalline and biodegradable block copolymer poly(ε-caprolactone)-*block*-poly(ethylene oxide) (PCL-*b*-PEO) to investigate our microfluidic platform as a tool to control polymeric nanoparticle (PNP) structure (size, morphology and core crystallinity) and function (drug loading efficiency and release profiles). Materials such as PCL-*b*-PEO self-assemble to form PNPs with structural organization over multiple length scales. PNP hierarchical organization is a result of structural properties on the nano- (crystallization of hydrophobic cores) and colloidal- (size and morphology) scale.[2,4] Properties on both length scales are of importance to PNP function. Compared to conventional preparatory methods, microfluidics allows for fast and efficient screening of multiple chemical parameters influencing PNP drug loading and release. A microfluidic approach offering continuous variability of PNP structure and function on multiple length scales would greatly enhance efficacy of polymeric nanomedicine formulations for optimum patient outcomes.

In Chapter 2, we demonstrated flow-variable multiscale structure and function of PCL-*b*-PEO PNPs loaded with the anticancer drug paclitaxel (PAX) manufactured in segmented gas-liquid microfluidic channels.[11] On the colloidal scale, reproducible, flow-directed control of PNP morphology (spheres, cylinders and lamellae) and hydrodynamic diameter (10s – 1000s nm) was demonstrated. On the molecular scale, linear variability of PCL crystallinity versus flow rate was demonstrated. The work in this chapter suggested that this microfluidic platform holds promise for dial-in control of the structure, drug loading, and drug release, of PAX-loaded PCL-*b*-PEO NPs.

In Chapter 3, flow-directed control of the structure and function of polymeric nanocarriers manufactured using the same microfluidic platform was explored over a range of

variables (water concentration and flow-rate), using the fluorescent dye DiI as a drug surrogate. The investigation of PNP multiscale structure revealed a dependence of colloidal and nanoscale structure on water concentration and flow-rate, similar to chapter 2. In the same chapter, we also explored how the nature of the release media affects release kinetics in the context of *in vitro* release experiments, which are typical early-stage experiments for testing polymer drug delivery particles. For example, release experiments conducted at 37 °C increased release rates relative to room temperature experiments, while the presence of phosphate buffered saline (PBS) and albumin increased release rates relative to a release medium of deionized water.

In this chapter, we return to the anticancer drug PAX as a cargo molecule for PCL-*b*-PEO NPs manufactured in the gas-liquid microfluidic reactor, and expand the range of variables by investigating the effects of block copolymer composition, drug-to-polymer loading ratio, and flow rate on the structure and function of PAX-loaded block copolymer NPs. The PAX loading ratios investigated in this chapter are equal to or lower than loading ratios in Chapter 2 ($r \leq 0.01$); therefore these experiments probe the effects of PAX concentration on NP structure and function in the limit of small free volume perturbations within the PNP core, by loading with small amounts of small-molecule cargo. We find significant differences in morphology and size, moderate differences in crystallinity and loading ratio, and insignificant differences in release rates, for different loading ratios of PAX in this range. We also show that block copolymer composition (in particular the length of the PCL block) and flow rate provide complementary chemical and mechanical handles, respectively, on reproducible variation of structure and function of PAX-loaded NPs. Therefore, this work provides critical insights that set up the capstone investigation of PAX-loaded NPs with medically-relevant loading levels ($r >> 0.01$) in Chapter 5.

4.2 Experimental

4.2.1 Materials

Three different poly(ε-caprolactone)-*block*-poly(ethylene oxide) (PCL-*b*-PEO) copolymers with constant PEO block length and variable PCL block lengths were purchased from Advanced Polymer Inc. and used as received: PCL_{12k}-*b*-PEO_{5k}; $PCL_{6.4k}$-*b*-PEO_{5k}; $PCL_{2.1k}$-*b*-PEO*5k*, where numbers in subscripts refer to number-average molecular weights of the respective blocks; these three copolymers are referred to simply as PCL(12k), PCL(6.4k) and PCL(2.1k) elsewhere in the chapter. N,N-dimethylformamide (DMF) (Aldrich, 99.9+%, HPLC grade, H2O < 0.03%), paclitaxel (PAX, Polymed Therapeutics, Inc.), methyl tert-butyl ether (Sigma-Aldrich) and bovine serum albumin (Sigma Aldrich), were used as received without further purification.

All quantitative stock solutions of PCL-*b*-PEO and PAX in DMF were prepared gravimetrically by accurately weighing the solid(s) into clean glass vials followed by gravimetric addition of a known quantity of DMF; all stock solutions were equilibrated overnight with stirring before further use.

4.2.2 Critical Water Content Determination

Static light scattering (SLS) measurements were carried out to determine the critical water content (cwc) of 0.33 wt % DMF solutions of PCL-*b*-PEO, which was the initial condition for all self-assembly experiments in this study. SLS measurements were carried out using a Brookhaven Instruments photon correlation spectrometer equipped with a BI-200SM goniometer, a BI-9000AT digital autocorrelator, and a Melles Griot He-Ne Laser (633 nm) with a maximum power output of 75 mW.

A 1.0 wt % stock solution of PCL-*b*-PEO in DMF was filtered through a Teflon syringe membrane filter with a nominal pore size of 0.45 μm (VWR) into precleaned scintillation vials. The filtered stock was then diluted to 0.33 wt % by gravimetric addition of the required quantity of DMF. To the resulting ~6 g of solution, deionized water was added in successive 0.03-0.06 g quantities via a microsyringe equipped with two membrane filters (VWR) with nominal pore size of 0.20 μm connected in series. After each addition of water, the solution was agitated using a vortexer to aid in mixing. The solution was then allowed to equilibrate for 15 min before measuring the scattered light intensity. All measurements were carried out at a scattering angle of 90° and a temperature of 23 °C. From the resulting plot of scattered light intensity versus weight percentage of added water, the cwc was determined from the intercept of linear fits to the baseline and the region of the plot in which scattered light intensity increased sharply (above the cwc). Determinations of cwc were carried out three times from the same stock solution and the mean value and standard deviation of the three measurements were used to calculate the reported cwc and experimental error. The cwc for the PCL(12k) sample in DMF is = 5.5 ± 0.4 wt %; the cwc for the PCL(6.4k) sample in DMF is = 6.3 ± 0.2 wt %; and, the cwc for the PCL(2.1k) sample in DMF is = 13.1 ± 0.2 wt %.

4.2.3 Microfluidic Chip Fabrication

Negative masters were fabricated on high quality silicon wafers (Silicon Quest International, Santa Clara, CA) using the negative photoresist SU-8 100 (Microchem Inc.). Immediately prior to use, the wafers were heated on a hot plate at 200 °C for 20 minutes to remove moisture. A 150 μm-thick SU-8 film was spin-coated onto the silicon and then heated to 95 °C for 60 minutes to remove residual SU-8 solvent. A photomask was then placed over the

SU-8 film and exposed to UV light for 180 s. Then, the UV-treated film was heated at 95 °C for 20 min before submersion in SU-8 developer (Microchem) until all unexposed photoresist was removed.

Microfluidics chips were fabricated from poly(dimethylsiloxane) (PDMS) using a SYLGARD 184 silicon elastomer kit (Dow Corning, Midland, MI). For chips used in the preparation of PAX-loaded PNPs, an elastomer base-to-curing agent ratio of 10:1 was employed as recommended by the kit. However, improved adhesion between the channel and substrate PDMS layers was later found when base-to-curing agent ratios were adjusted to 7:1 and 20:1 for the two layers, respectively, and these ratios were employed for the PAX-encapsulation experiments described the text. For fabrication of all PDMS chips, the elastomer and curing agent were mixed together and degassed in a vacuum chamber. The degassed PDMS was then poured over the negative master in a Petri dish and further degassed until all remaining air bubbles were removed. The PDMS was then heated at 85 °C for ~60 min until cured. The microfluidic chip was then peeled off of the negative master and holes were punched through its reservoirs to allow for the insertion of tubing. A thin PDMS film (substrate layer) was also formed on a glass slide by spin-coating and was permanently bonded to the base of the microfluidic reactor (channel layer) after both components were exposed to oxygen plasma for 60 s. The reactor has a set channel depth of 150 μm and consists of a sinusoidal mixing channel 100 μm wide and 18 mm in length and a sinusoidal processing channel 200 μm wide and 740 mm in length.

For further stabilization of the bubble generation process, an external resistor chip was used between the Ar gas tank and the microfluidic chip. The resistor chips served as high pressure drop systems to efficiently dampen the pressure fluctuations caused by the Ar gas tank

and the bubble generation process. The total pressure drop in the external resistor chip was at least one order of magnitude higher than the pressure drop in the reaction channel. The resistor chip channels were 1000 mm long, 150 μm deep and 400 μm wide.

4.2.4 Flow Delivery and Control

Pressure-driven flow of liquids to the reactor inlet was provided using 1 mL gastight syringes (Hamilton, Reno, NV) mounted on syringe pumps (Harvard Apparatus, Holliston, MA). The microchip was connected to the liquid syringes via 1/16th-inch (OD) Teflon tubing (Scientific Products and Equipment, ON). Gas flow was introduced to the microchip via an Ar tank regulator and a downstream regulator (Johnston Controls) for fine adjustments. The microchip was connected to the downstream regulator through a 1/16th-inch (OD) / 100-μm (ID) Teflon tube (Upchurch Scientific, Oak Harbor, WA). The liquid flow rate (Q_{liq}) was programmed via the syringe pumps and the gas flow rate (Q_{gas}) was fine-tuned via the downstream pressure regulator in order to dial in the nominal total flow rates described in the main text. Due to the compressible nature of the gas and the high gas/liquid interfacial tension, discrepancies arise between the nominal (programmed) and actual values of Q_{gas}, Q_{gas}/Q_{liq}, and the total flow rate (Q_{total}). Therefore, actual gas flow rates were calculated from the frequency of bubble formation and the average volume of gas bubbles, determined from image analysis of the mean lengths of liquid and gas plugs, L_{liq} and L_{gas}, respectively, under a given set of flow conditions. This method of flow calculation has been previously employed in the context of gas-liquid segmented flow in the microfluidic device.[27] For all experiments, the relative gas-to-liquid flow ratio, Q_{gas}/Q_{liq} ~1 and all actual Q_{total} values are within 10% of nominal values reported in the main text.

Visualization of the gas bubbles and liquid plugs within the microfluidic reactor was achieved using an upright optical microscope (Omax) with a 10x-objective lens. Images were captured using a 2.07 megapixel PupilCam (Ken-A-Vision) and mean lengths of liquid and gas plugs were determined from the images using image analysis software (ImageJ).

4.2.5 Microfluidic Preparation of PAX-Loaded PCL-*b*-PEO PNPs

For experiments probing the effect of copolymer composition and drug concentration on microfluidic assembly of PAX-loaded PCL-*b*-PEO nanoparticles, three fluid streams were combined at equal flow rate to form gas-segmented liquid plugs within the reactor: (1) for copolymer composition experiments: 1.0 wt % solution of PCL-*b*-PEO (PCL(12k), PCL (6.4k), and PCL(2.1k)) in DMF with codissolved PAX in drug : copolymer ratio, *r*, of 0.01 (w/w); for drug concentration experiments: 1.0 wt % solution of PCL-*b*-PEO (PCL(12k)) in DMF with codissolved PAX in drug : copolymer ratios of *r* = 0.001, 0.005, 0.0001, and 0.0005 (w/w), (2) a separator stream containing DMF only, and (3) a DMF solution containing deionized water (water concentration was cwc + 5 wt % x 3). Combination of the three liquid streams yielded steady-state on-chip concentrations of 0.33 wt % copolymer cwc + 5 wt% deionized water. Microfluidic flow conditions were selected and controlled as described in the previous section.

The PAX-loaded nanoparticle samples were collected from the reactor into vials containing a 10x-excess volume of deionized water, followed by 12 h dialysis against deionized water (with changing of water every hour for the first 4 h of dialysis) to remove residual DMF and unencapsulated PAX. The resulting aqueous dispersions of PAX-loaded nanoparticles were analyzed by TEM, XRD, and also used for studies of PAX loading efficiencies and release

kinetics, as described in the corresponding sections below. All samples were prepared in triplicate under the specified chemical and flow conditions.

4.2.6 Bulk Preparation of PAX-Loaded PCL-*b*-PEO PNPs

Off-chip PAX-loaded PCL-*b*-PEO nanoparticles were prepared by a conventional drop-wise water addition method described elsewhere in literature12. Initial conditions for self-assembly were kept identical to the on-chip formulations. Approximately 5 mL of 0.33 wt % copolymer solution was prepared in DMF at a drug : copolymer ratio of 0.01 (w/w) and water was added drop-wise using a micropipette at a constant rate of 20 μL every 10 s with moderate magnetic stirring (600 RPM). Drop-wise water addition at constant rate was continued to a water content of cwc + 5 wt %, then the drug-loaded nanoparticles were quenched immediately into 10x-volume excess of deionized water, followed by 12 h dialysis against deionized water (250 x excess; with changing of water every hour for the first 4 h of dialysis) to remove residual DMF and unencapsulated PAX. The resulting aqueous dispersions of PAX-loaded nanoparticles were analyzed by TEM, XRD, and also used for studies of PAX loading efficiencies and release kinetics, as described in the corresponding sections below. All samples were prepared in triplicate under the specified chemical and flow conditions.

4.2.7 Transmission Electron Microscopy

Transmission electron microscopy (TEM) was performed using a JEOL JEM-1400 TEM, operating at an accelerating voltage of 65 kV and equipped with a Gatan Orius SC1000 CCD camera. TEM images were obtained by depositing diluted dispersions (~0.03 wt % copolymer)

consisting of PAX-loaded PCL-*b*-PEO nanoparticles in water onto carbon-coated 300 mesh copper TEM grids as described below.

To improve contrast, uranyl acetate was used to negatively stain the PCL-*b*-PEO nanoparticles. Uranyl acetate selectively binds to the PEO coronal chains, providing reverse contrast for the PCL cores, which appear white in TEM images of stained samples. For reverse staining experiments, nanoparticle dispersions were mixed with 1 wt % aqueous solution of uranyl acetate in a 1:1 ratio (v/v) and one drop of the resulting mixture was deposited onto a TEM grid. Excess liquid was immediately removed using lens paper, followed by drying of remaining liquid under ambient conditions.

Due to the high electron density of uranyl acetate, negative staining generally impedes visualization of internal lumen of vesicle structures, such that vesicles and spheres cannot be readily distinguished from stained samples. Therefore, all samples revealing aggregates of spherical shape in negative contrast TEM images were also imaged without staining. In unstained images, contrast is provided by high density PCL crystallites which appear dark relative to both the background and the internal lumen of vesicles, such that vesicles appear hollow in unstained images and so can be differentiated from spheres. We find that one complication of imaging PCL-*b*-PEO nanoparticles without staining is that upon drying under ambient conditions, deposited dispersions form large crystallites of PEO which obscure identification of micellar PCL cores. To avoid this problem, micellar dispersions deposited without reverse staining were freeze-dried on TEM grids using the following method. First, one drop of the micellar dispersion was deposited onto a TEM grid and excess liquid was immediately removed using lens paper. The remaining liquid was then vitrified by submerging the TEM grid into liquid ethane. The resulting vitrified sample was then freeze-dried under

vacuum. As discussed below, the morphological identification of some aggregates required the evaluation of their heights. For these experiments, Pt/Pd shadowing of unstained aggregates following freeze-drying on the grid was carried out at a shadowing angle of 45°.

For each set of conditions (water content and flow rate), reported prominent morphologies and mean dimensions from TEM of nanoparticles with loaded PAX were determined from TEM analysis of three separate preparations starting with three individually-prepared stock solutions. For each sample preparation and TEM grid deposition method (unstained, stained, and shadowed), at least 2-3 TEM images taken in different regions of the grid were evaluated. Prominent morphologies for each condition were assigned based on the following definitions with associated evaluation methods in brackets. Spheres were defined as aggregates with circular projections (TEM with staining) but without internal lumen (TEM without staining). Cylinders were defined as high aspect-ratio filaments of approximately regular width (TEM with staining). Lamellae were defined as irregularly-shaped aggregates (TEM with staining) with heights significantly smaller than their lateral dimensions (TEM with shadowing). For each preparation, mean dimensions were determined from ~400 particles; therefore, for each of the mean dimensions in Table 1, N = 400 x 3 preparations = ~1200, such that the reported errors reflect reproducibility of the preparation method. Mean sphere diameters and cylinder widths were determined exclusively from TEM images with staining. Averaging and statistical analysis of dimensions from TEM images was conducted using Image J software.

4.2.8 Dynamic Light Scattering

Effective hydrodynamic diameters of DiI-loaded PCL-*b*-PEO nanoparticles were determined using dynamic light scattering (DLS). DLS measurements were carried out using a

Brookhaven Instruments photon correlation spectrometer equipped with a BI-200SM goniometer, a BI-9000AT digital autocorrelator, and a Melles Griot He-Ne Laser (633 nm) with a maximum power output of 75 mW. All DLS measurements of DiI-loaded nanoparticles were performed in pure water and an experimental temperature of 23˚C and at a scattering angle of 90˚.

After overnight dialysis against deionized water to remove residual DMF and unencapsulated DiI, the DiI-loaded nanoparticles were transferred to pre-cleaned scintillation vials then diluted 5x using deionized water, filtered through two nylon syringe filters in series with nominal pore sizes of 0.2 m (National Scientific Company) to give a final copolymer concentration of ~0.07 mg/mL. For each nanoparticle preparation, mean effective hydrodynamic sizes were determined from three measurements of the autocorrelation function using cumulent analysis. Mean effective hydrodynamic diameters were determined from three separate data collections corresponding to one individually-prepared stock solution, such that reported errors reflect the error in data collection.

4.2.9 X-Ray Diffraction

X-ray diffraction measurements were performed on a Rigaku Miniflex diffractometer with a Cr source (kR radiation, λ = 2.2890 Å) operating at 30 kV and 15 mA with a resolution of 0.05° (2θ) and a scan speed of 1°/min. X-ray diffraction profiles were collected for 2θ ranging from 10-80 degrees.

For XRD sample preparation, water was removed from suspensions of DiI-loaded nanoparticles by rotory evaporation at 25 °C until solid films were obtained. The resulting films were then scraped as a powder into the XRD specimen holder with no subsequent drying step to remove residual solvent. We note that this preparation method will significantly increase the crystallinity of coronal PEO blocks relative to their colloidal state, as removal of water from the nanoparticle coronae will allow initially-solubilized PEO chains to pack together. However, since the hydrophobic cores will contain no water in the purely aqueous suspensions, we do not expect the crystallinity of the core-forming PCL blocks to be strongly affected when water is removed by rotory evaporation. Therefore, our XRD experiments should provide a reasonable probe of nanoparticle core crystallinity in the colloidal state.

Peak deconvolution of XRD data was done using Origin Pro Version 8.1. Two characteristic reflections for each of crystalline PCL and crystalline PEO were identified from the literature and these were used to fix the positions of four Lorentzian peak contributions to the fit;[99,23] another small Lorentzian peak contribution was used to account for a small shoulder on the more intense PCL peak in order to obtain a good fit (Figure 8.3). Thus, XRD data were fit to a sum of 6 Lorentzian functions: 3 peaks assigned to crystalline PCL (2θ = 32.5, 32.7, and 35.7), 2 peaks assigned to crystalline PEO (2θ = 29.2 , 35.4), and 1 peak (no fixed position) assigned to

incoherent scattering from amorphous copolymer (amorphous halo). Areal peak contributions from the three components (crystalline PCL, crystalline PEO, and amorphous copolymer) were then determined by integration and percentages of crystalline PCL and PEO were calculated using:

$$\% \textit{ Crystalline } \text{PCL} = A_{\text{PCL}}/A_{\text{total,}} \text{ and } \% \textit{ Crystalline } \text{PEO} = A_{\text{PEO}}/A_{\text{total}},$$

where $A_{\text{total}} = A_{\text{PCL}} + A_{\text{PEO}} + A_{\text{amorph.}}$

4.2.10 PAX Loading Efficiency Determination

To determine PAX loading efficiencies, PAX-loaded nanoparticles were dissolved in acetonitrile (ACN): First, water was removed from a known mass (~1 g) of an aqueous dispersion of PAX-loaded nanoparticles of known copolymer concentration by rotary evaporation at 25 °C; 2. Then a known amount (~0.5 g) of ACN was added to break up the PAX-loaded nanoparticles by stirring in ACN for 4 h. PAX quantification was conducted using high performance liquid chromotography-mass spectrometry (HPLC-MS, Ultimate 3000, Thermo Scientific) with a C18 column (Phenomenex Luna 5u C18) and a mobile phase composition of 65/35 acetonitrile/water (v/v) and 1 vol % formic acid using the diode array detector (DAD). Sample injection volumes were 50 μL and the HPLC-MS flow rate was set to 1 mL/min. For loading efficiency determinations, PAX solution concentrations were sufficiently high such that they could be detected and quantified using the diode array detector (DAD) by monitoring the elution of PAX at a characteristic absorption wavelength of 227 nm. A calibration curve for the DAD was generated by analysis of 5 stock solutions containing different known PAX concentrations in ACN. Quantities of PAX in the various dissolved PNP solutions were determined and loading efficiencies calculated for each sample using the following expression:

$$loading\ efficiency\ (\%) = \frac{PAX\ in\ micelles\ (g)}{total\ PAX\ used\ (g)} \times 100\%$$

Reported loading efficiencies are averages determined from triplicate nanoparticle preparations under the specified conditions.

4.2.11 *In Vitro* PAX Release Kinetics

Experiments were carried out to monitor the *in vitro* release of PAX from PAX-loaded PNPs using HPLC-MS (see previous section for instrument specifications). A detailed experimental has been reported previously[11].

In a typical experiment, an aqueous dispersion of PAX-loaded nanoparticles (~10 g) were transferred to a 10 mL-dialysis bag (SpectrumLabs, MWCO 100 kDa), which was placed in a 4 L-beaker containg the release medium. The release media consisted of ~2.5 L of a 1% phosphate buffer saline (PBS, pH = 7.4) solution containing albumin (Sigma Aldrich) at a concentration of 45 g/L; throughout release experiments, the release medium was constantly stirred using magnetic stirring and maintained at physiological temperature (37 °C) in an incubator. At predetermined times, aliquots of known mass (~1 g) were removed from the dialysis bag to which a known mass (~150 mg) of a deuterated PAX internal standard (d5-PAX, ~1 mg/mL, Toronto Research Chemicals) in ACN was added. A liquid-liquid extraction was conducted using methyl tert-butyl ether (Sigma Aldrich) to extract PAX from the aqueous solution. Methyl tert-butyl ether was then removed by rotary evaporation at 25 °C. Acetonitrile was then added to solubilized PAX before injection into the HPLC-MS.

The amount of PAX released was quantified using HPLC-MS on single ion monitoring (SIM) mode. Separate calibration curves for SIM detection of PAX and the internal standard were generated by analysis of five known stock solutions of both analytes. The internal standard

(d_5-PAX) was used to determine the efficiency of each liquid-liquid PAX extraction, which was found to vary from 60-80%. From determined masses of PAX in aliquots obtained at different release times, percentages of PAX released were calculated relative to the determined mass of nanoparticle-encapsulated PAX at the t = 0 release time. Reported release percentages at each release time are averages determined from triplicate PNP preparations under the specified conditions.

4.3 Results and Discussion

Effect of Flow Rate and Block Copolymer Composition on the Multiscale Structure of PAX-Loaded Nanoparticles. We first explored how both copolymer composition and flow-rate influence PAX-loaded PCL-*b*-PEO nanoparticle multiscale structure (size, morphology and core crystallinity). Self-assembly and PAX encapsulation was conducted at constant PAX loading ratio and water content (r = 0.01 and cwc + 5 wt %, respectively) for three different block copolymers (PCL(2.1k), PCL(6.4k) and PCL(12k)) and five different flow rates (Q = 0, 25, 50, 100 and 200 μL/min), where Q = 0 designates the bulk NP preparation. Three samples from the PCL(12k) formulation (Q = 25 – 100 μL/min) are previously reported in chapter 2 and are included in Figure 4.1 for completeness.

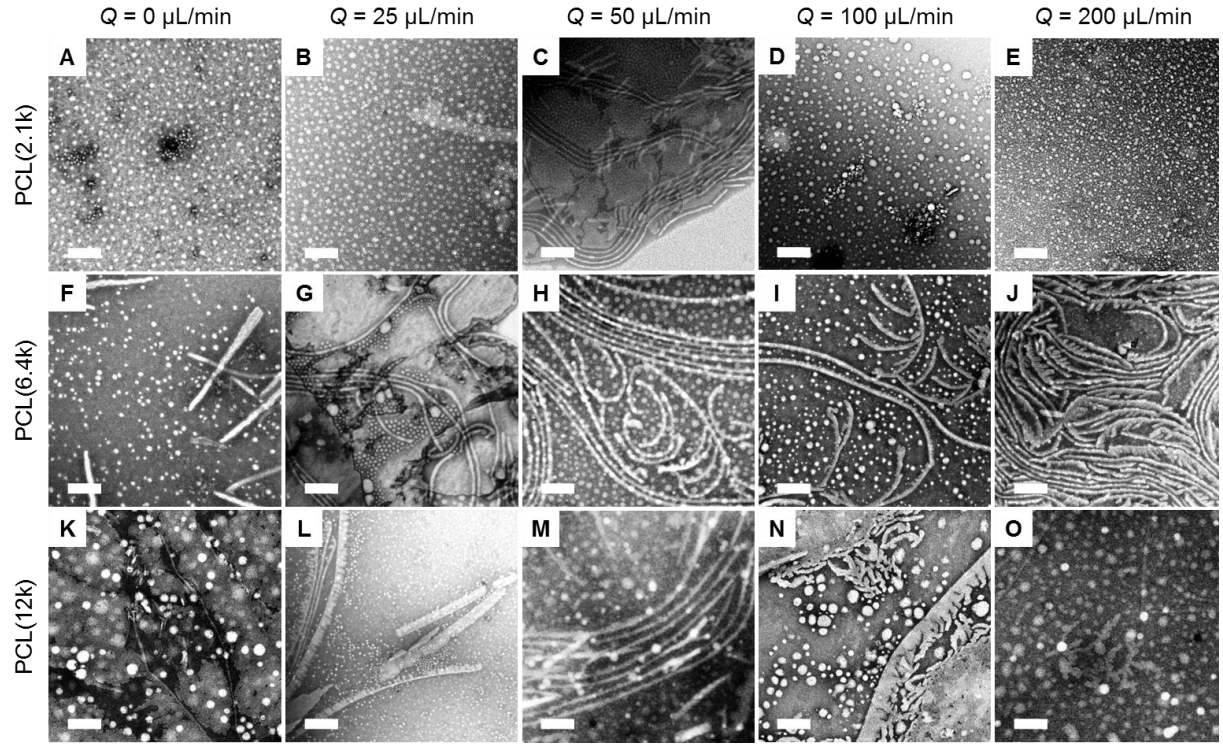

Figure 4.1 Effect of flow rate and copolymer composition on morphology and hydrodynamic size of PAX-loaded PCL-*b*-PEO nanoparticles. TEM images were produced by negative staining with uranyl acetate. All scale bars are 200 nm.

Figure 4.1 shows the resulting TEM data for the PAX-loaded PCP-*b*-PEO PNPs prepared from three block copolymers and five flow rates. In general, both the PCL(2.1k) and PCL(12k) samples yield increasing numbers of cylinders with increasing flow rate (Q < 200 µL/min), shifting to mostly spherical morphologies at high flow rate (Q = 200 µL/min); whereas, the PCL(6.4k) sample continues to yield increasing numbers of cylinders with increasing flow rate. For example, the PCL(2.1k) formulation is composed of PNPs with spherical morphologies for the Q = 0, 25, 100 and 200 µL/min formulations; whereas, the Q = 100 µL/min condition yields spheres, cylinders and lamellae. The PCL(6.4k) formulation is composed of spheres, cylinders and lamellae for flow conditions where Q < 200 µL/min; for the Q = 200 µL/min condition only cylinders are observed. The PCL(12k) formulation had two distinct changes in morphology: 1.

between the Q = 25 μL/min spheres and lamellae) and Q = 50 μL/min (spheres, cylinders and lamallae) flow conditions; and, 2. between the Q = 100 μL/min (spheres, cylinders and lamellae) and Q = 200 μL/min (spheres and lamellae) flow conditions.

Next we will discuss the trends reported in the previous section regarding PNP size and morphology with respect to flow rate (Figure 4.1). For the PCL(2.1k) formulation, the morphological shift from mostly spheres at Q = 25 μL/min (Figure 4.1 B), to spheres, cylinders and lamellae at Q = 50 μL/min (Figure 4.1 C) is attributed to flow-induced particle coalescence. As flow rate is further increased to Q = 100 μL/min (Figure 4.1 D), only spheres are present; a demonstration of flow-induced particle breakup. On the other hand, the PCL(6.4k) composition has an increasing number of cylinders with increasing flow rate. This change in morphology is also attributed to flow-induced particle coalescence. As for the PCL(12k) composition, the change in morphology between Q = 25 μL/min (Figure 4.1 L) and Q = 50 μL/min (Figure 4.1 M) is an example of flow-induced particle coalescence. Furthermore, the disappearance of cylinders with increasing flow rate between Q = 100 (Figure 4.1 N) and 200 μL/min (Figure 4.1 O), is another demonstration of flow-induced particle breakup. Furthermore, we note that the three different PCL block lengths have different morphological trends with respect to flow rate. The different trends in morphology can be attributed to the influence of core crystallization and PAX loading efficiently. These factors are discussed in detail in the upcoming sections.

The influence of copolymer composition on PNP size and morphology is stronger for bulk preparation compared to microfluidic preparations (Figure 4.1; Q = 0 μL/min). In general, with increasing PCL block length, PNP morphologies trend towards low internal curvature structures. Typically, as the molecular weight of the core forming block is increased, there is a

tendency for PNPs to favour morphologies with high aggregation numbers and low core curvatures.[11]

Figure 4.2 shows how PCL core crystallinity is influenced by block copolymer molecular weight and flow rate. The data in Figure 4.2 present two main trends: 1. at constant flow rate, PCL crystallinity increases with increasing PCL block length; 2. for a given block copolymer, PCL crystallinity for microfluidic-prepared PNPs ($Q > 0$) mainly increases with flow rate, except at the highest flow rate for the PCL(2.1k) and PCL(12k) copolymers where a decrease in crystallinity is observed. We note that these trends in core crystallinity correlate with trends in

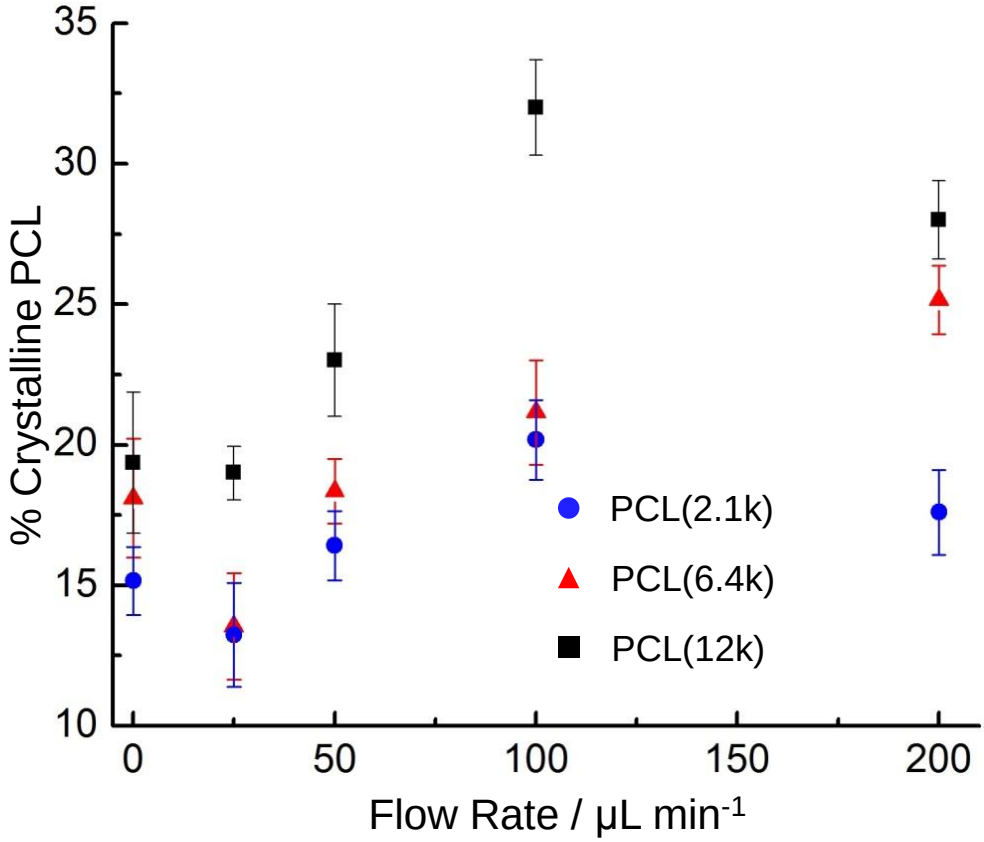

Figure 4.2 Effect of flow rate and water content on PCL crystallinity within the cores of PAX-loaded PCL-*b*-PEO nanoparticles.

PNP morphology. For example, for the bulk formulations, increasing crystallinity is mirrored with increasing numbers of low curvature morphologies (Figure 4.1 A, K and F). As for the microfluidic-prepared PNPs, increasing core crystallinity for the PCL(6.4k) formulation trends with increasing numbers of cylindrical PNPs (Figure 4.1 G-J). On the other hand, for the extreme block lengths, increasing core crystallinity trends with formation of low curvature morphologies; except for the Q = 200 μL/min condition, where a drop in core crystallinity is mirrored with the disappearance of cylindrical PNPs (Figure 4.1 E and O).

With respect to the first trend, higher molecular weight polymers are known to correlate with increasing core crystallinity.[17-21] With respect to the second trend, the dependence of core crystallinity on flow-rate is a result of shear-induced crystallization. In chapters 2 and 3, we reported that core crystallinity of PAX-loaded PCL-*b*-PEO PNPs increased linearly with increasing flow rate. This increase in core crystallinity coincided with the formation of low curvature PNP morphologies, such as: cylinders and lamellae. A similar result is observed for the PCL(6.4k) formulation (Figure 4.2). Higher core crystallinity is matched with low curvature PNPs (Figure 4.1 G-J). For the two extreme block lengths, high flow rate (Q = 200 μL/min) results in a drop in core crystallinity; mirrored with the disappearance of cylindrical PNPs (Figure 4.1 E and O). This result suggests that increasing PCL crystallization favours particle morphologies with low internal curvature such as cylinders and lamellae.

Effect of Flow Rate and Block Copolymer Composition on PAX Loading Efficiencies. For the 15 PNP preparations described in the previous section (three different block copolymers and five different flow rates), PAX loading efficiencies were determined and those data are presented in Figure 4.3. For the bulk preparations (Figure 4.3, bulk), loading efficiency

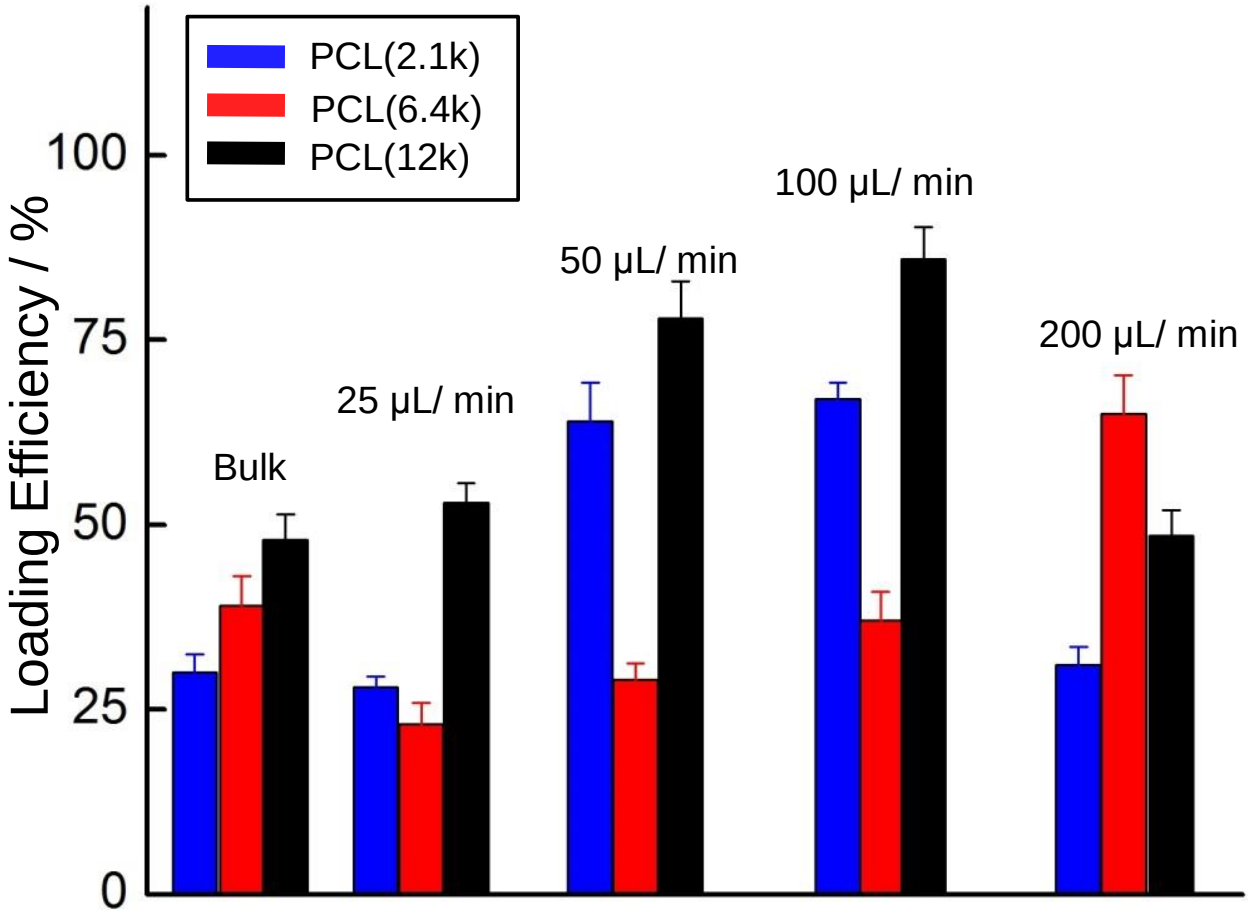

Figure 4.3 Effect of flow rate and water content on the loading efficiency of PAX-loaded PCL-*b*-PEO nanoparticles. Blue bars: nanoparticles prepared using the PCL(2.1k) composition; red bars: nanoparticles prepared the PCL(6.4k) composition; and, black bars: nanoparticles prepared using the PCL(12k) composition

increases as a function of increasing PCL block length. For the various microfluidic preparations (Figure 4.3, Q = 25 - 200 µL/min), the two extreme copolymer compositions increase with flow rate between Q = 25 - 100 µL/min and then decrease when flow rate is increased to Q = 200 µL/min. On the other hand, for the intermediate copolymer, PCL(6.4k), PAX-loading

efficiencies increase steadily with flow rate. We note that these trends in PAX loading efficiency (Figure 4.3) trend closely with PCL crystallinity (Figure 4.2) and morphology (Figure 4.1). For example, increasing PAX loading efficiency correlates with increasing PCL crystallinity and the formation of low internal curvature morphologies; furthermore, decreasing PAX loading efficiency correlates with decreasing PCL core crystallinity and the formation of mostly spherical PNPs.

The correlation between increasing core crystallinity and PAX loading efficiency as a function of increasing flow-rate is counterintuitive to what is expected. Increasing small molecule concentrations within semicrystalline block copolymer PNPs are expected to attenuate core crystallinity by disrupting copolymer chain packing, an effect similar to a plasticizer. An example of this effect is reported in Chapter 3, where an increasing crystallinity of the higher water content PNPs correlates to a lower DiI loading efficiency. Nevertheless, when PAX loading efficiency is analyzed in the context of both PNP core crystallinity and morphology (from TEM), the observed trends in loading efficiency tend to correlate with PNP morphology. For example, increasing flow rate results in higher PCL core crystallinity (Figure 4.2) which correlates with high aggregation number morphologies (cylinders; Figure 4.1 J and N); thus, promoting PAX loading efficiency, as observed in Chapter 2. Conversely, decreases in PCL core crystallinity correlates with lower aggregation number morphologies (spheres; Figure 4.1 E and O), resulting in lower PAX loading efficiencies. Therefore, these results suggest that PCL morphology influences PAX loading efficiency.

Effect of Flow-Rate and Polymer Composition on PAX Release Kinetics. Diffusional PAX release kinetics were investigated for the 15 formulations (three different block copolymers and five different flow rates) described previously (Figure 4.4). In general, without appropriate

statistical analysis it is possible that the PAX release data presented in Figure 4.4 shows no statistical change over the three different PCL PNP formulations self-assembled using microfluidics or under bulk conditions. Nevertheless, for the bulk assembly conditions there are two trends: 1. bulk formulations have faster PAX release than the on-chip formulations, consistent with results from chapter 2; and 2. PAX release slows as a function of increasing PCL block length (Figure 9.2, Appendix III). We speculate the first trend maybe a result of the superior mixing available on-chip, compared to bulk assembly methods; also observed in Chapter 2. The second trend is attributed to increasing PNP core crystallinity as a function of increasing PCL block length. For example, PCL crystallization increases for all three samples as PCL molecular weight increases (Figure 4.2). The increase in core crystallinity slows diffusional release kinetics of encapsulated PAX molecules by changing core viscosity. Changes in core viscosity affect the diffusion coefficient of the encapsulated PAX molecules; in general, as core crystallization increases there is a corresponding decrease in PAX diffusional release.[15,17,29,30]

For all microfluidic assembled formulations, diffusional PAX release slows monotonically as a function of increasing flow rate (Figure 9.2; Appendix III). In fact, for the PCL(12k) formulation, diffusional PAX release slows to a point where complete PAX release is not observed (Q = 100 and 200 μL/min; Figure 4.4 C). When considering PAX release kinetics for the different PCL block lengths, higher PCL molecular weight formulations have slower diffusional PAX release kinetics. An explanation for these trends may lie in PCL core crystallinity and is discussed next.

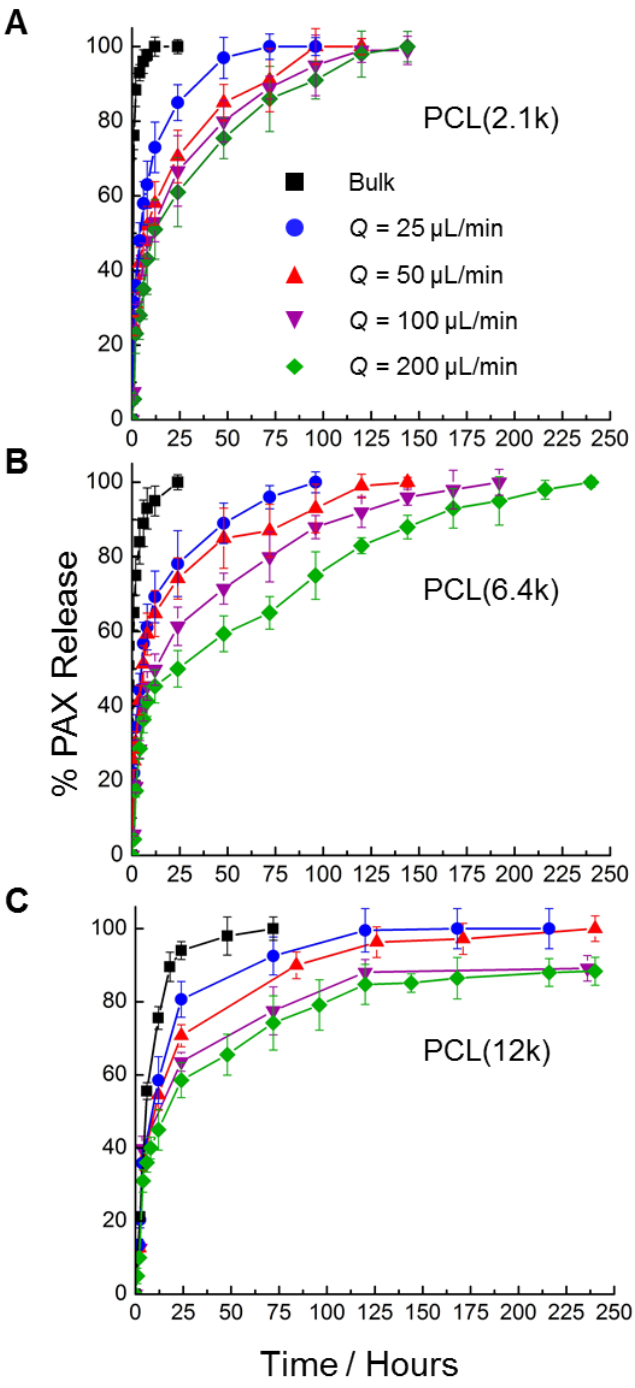

Figure 4.4 Effect of flow rate and water content on the release of PAX from PAX-loaded PCL-b-PEO nanoparticles. (A) Release profiles for nanoparticles prepared using the PCL(2.1k) composition and various flow rates. (B) Release profiles for nanoparticles using the PCL(6.4k) composition and various flow rates. (C) Release profiles for nanoparticles using the PCL(12k) composition and various flow rates. All release experiments were carried out at 37 °C in 1% PBS and albumin (45 g/L) as described in the text

Next we discuss the reported trends in PAX release for the microfluidic assembled formulations. For all compositions, core crystallinity increases as a function of increasing flow rate (Figure 4.2). As seen in Chapters 2 and 3, increasing core crystallization decreases diffusional PAX release by way of increasing core microviscosity.[11] Next we consider the PCL(12k) formulation where complete PAX release is not observed (Figure 4.4 C). PAX inclusion has also been observed previously, in Chapter 2. An explanation for this result may also lie in core crystallinity. For example, increasing core crystallization in the PCL(12k) formulation may lead to instances of crystalline PCL physically entrapping PAX molecules, restricting their release.

Effect of Initial Drug Loading Ratio on Multiscale Structure, PAX loading efficiency and Diffusional Release Kinetics. Next, we explored how initial drug loading ratio will influence PNP size and morphology. For this study we explored four different initial drug loading levels (r = 0.005, 0.001, 0.0005, and 0.0001), at constant copolymer composition (PCL(12k)) and flow-rate (Q = 50 μL/min). The TEM results are presented in Figure 4.5 along with DLS size distributions.

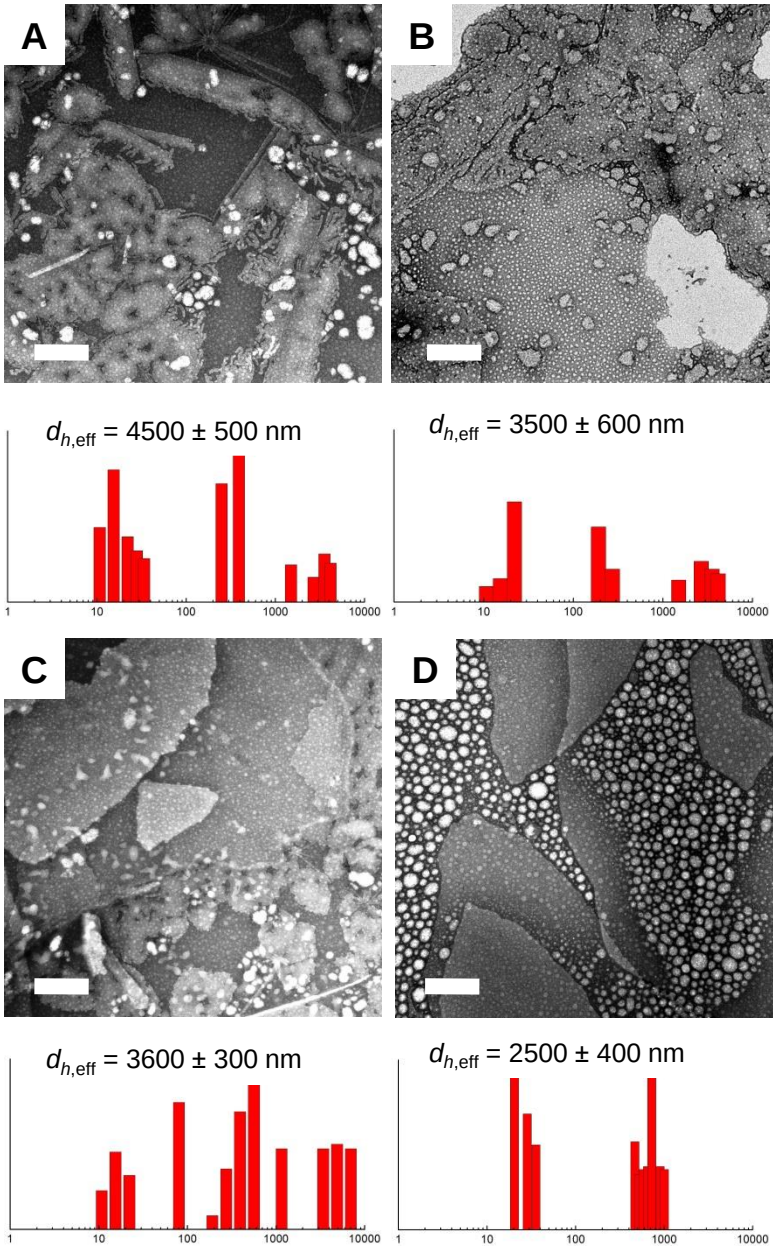

Figure 4.5 Effect of initial drug-to-copolymer ratio on morphology and hydrodynamic size of PAX-loaded PCL(12k) PNPs. Samples were prepared at Q = 50 μL/min and cwc + 5 wt %. (A) Representative TEM images of PNP samples prepared using r = 0.005; (B) Representative TEM images of PNP samples prepared using r = 0.001; (C) Representative TEM images of PNP samples prepared using r = 0.0005; and, (D) Representative TEM images of PNP samples prepared using r = 0.0001. TEM images were produced by negative staining with uranyl acetate. All scale bars are 200 nm. Below each TEM image is a representative size distribution obtained from CONTIN analysis of DLS autocorrelation functions, along with the mean effective hydrodynamic diameter determined from CUMULENT analysis.

Figure 4.5 (A-D) shows the formation of PAX-loaded PCL(12k) nanoparticles manufactured on-chip at Q = 50 μL/min. In general, all drug loading ratios yield spheres cylinders and lamellae. One exception to this trend is the r = 0.0001 (Figure 4.5 D) condition, where there are only spheres and lamellae. At this range of initial drug-to-copolymer ratio, the addition of small molecule cargo to the PCL(12k) nanoparticle core does not significantly influence nanocarrier size or morphology.

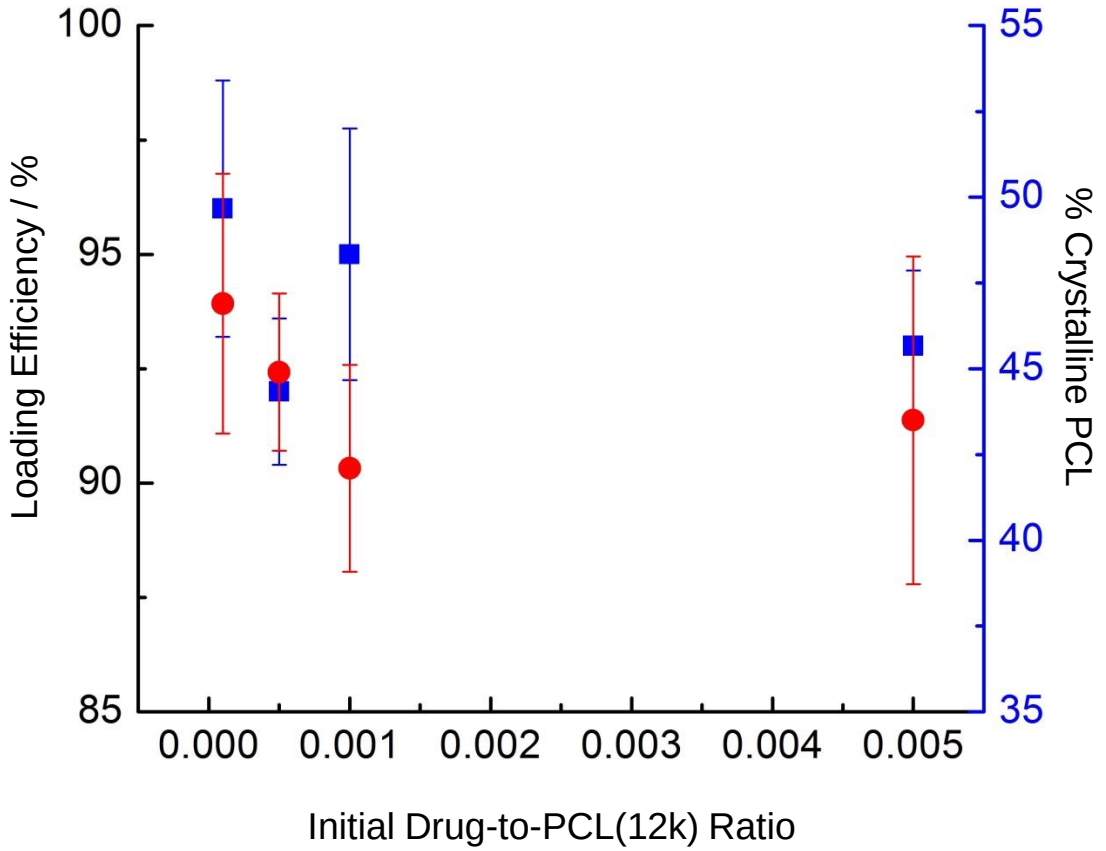

Figure 4.6 Effect of initial drug loading ratio on PAX-loaded PCL(12k) crystallinity (blue squares) and PAX loading efficiency (red circles). All samples were prepared using PCL(12k) copolymer compositions, at Q = 50 μL/min and cwc + 5 wt %.

We next present the core crystallization results for the various initial drug-to-copolymer ratio experiments (Figure 4.6). The results show a lack of core crystallinity dependence on initial drug loading ratio. Perhaps, at these initial drug loading ratios PNP core crystallization is not

influenced to a significant degree, as observed in Figure 4.6, where core crystallinity is between 40 and 50 %. Figure 4.6 also presents PAX loading efficiency results as a function of increasing initial drug-to-copolymer ratio. Loading efficiencies ranged from ~ 94% to 91%, and did not follow any trend with loading ratio.

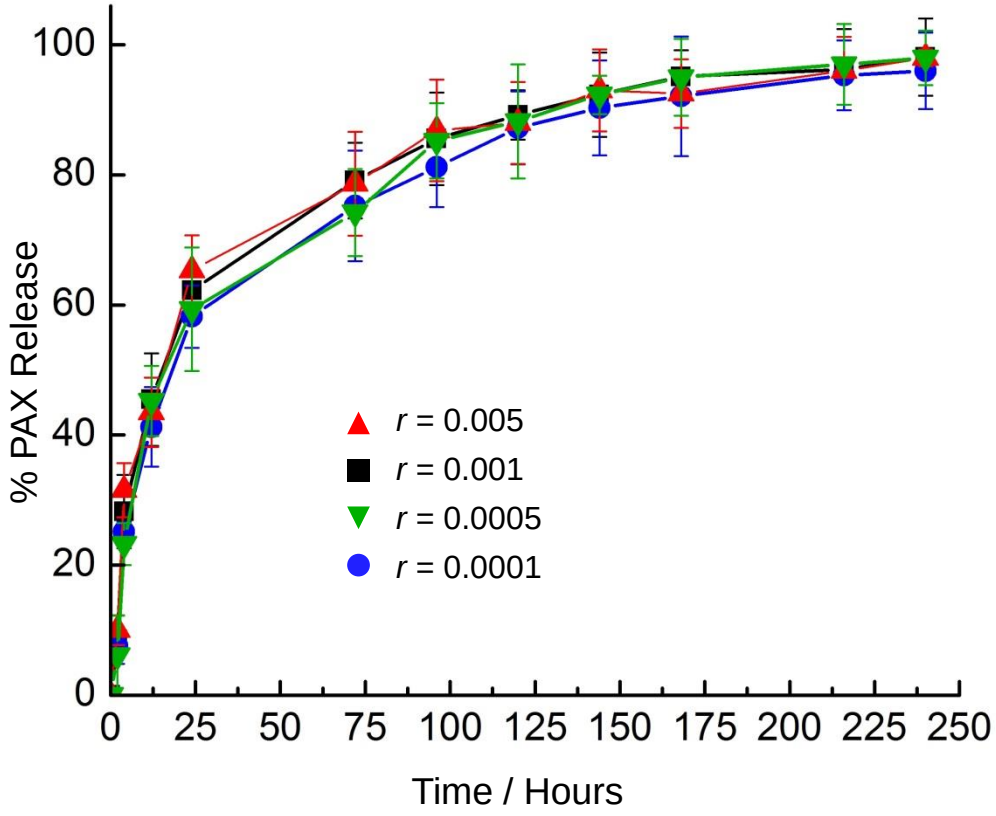

Figure 4.7 Effect of initial drug loading ratio on PAX-loaded PCL(12k) *in vitro* diffusional PAX release. All release experiments were carried out at 37 °C in 1% PBS and albumin (45 g/L) as described in the text

Next, Figure 4.7 presents diffusional PAX release results of the four initial drug loading ratio formulations. Complete release of PAX occurs within ~250 hours and all release profiles are similar with respect to loading ratio.

4.4 Conclusion

In this chapter, we use two-phase microfluidics to study the influence of flow-variable shear and various chemical parameters (copolymer block length and initial drug loading ratio) on PNP structural control. Then, we study the influence of PNP structure on PNP function by studying PAX loading efficiency and *in vitro* diffusional release kinetics.

First, we probed the effect of copolymer composition and flow rate on nanoparticle structure and function. Results indicated that formulations with higher molecular weight PCL blocks had a tendency to form nanoparticles of high aggregation number morphologies and higher core crystallinity. These changes to nanoparticle structure also influenced nanoparticle function. As formulations with longer PCL blocks had higher loading efficiencies and longer diffusional release profiles. Furthermore, we studied how increasing flow-rate influenced PNP morphology and core crystallinity through the mechanisms of flow-induced coalescence, breakup, and, crystallization. Changes in PNP morphology affected PAX loading efficiency and, increases in core crystallinity resulted in slowing diffusional PAX release. This study provided us with critical insight into how copolymer composition and flow-variable shear effectively combine chemical and mechanical handles, respectively, to influence PNP structure and function.

Next we studied the influence of initial drug loading ratio on microfluidic self-assembly of PAX-loaded PCL-*b*-PEO PNPs. Unfortunately, due to the low concentrations of PAX used, there was no significant influence of initial drug loading ratio on PNP structure and function.

In general, this chapter provides us with information that is applicable to the study in Chapter 5. For example, we learn that variations in PCL block length and flow rate will affect

PNP structure and function. For example, increasing both PCL block length and flow rate will increase PCL core crystallinity. Varying core crystallinity is an effective way to control diffusional PAX release. Furthermore, we learn that at low PAX loading ratio, flow-variable shear is the major factor influencing PNP structure and function. All of this information provides us with the necessary tools to study similar formulations at high PAX loading ratios; thus, enlarging our understanding of our microfluidic chip as a drug delivery formulation development platform.

4.5 References

(1) Zhang, Y.; Chan, H. F.; Leong, K. W. Advanced materials and processing for drug delivery: The past and the future. *Adv. Drug Deliv. Rev.* **2013**, 65, 104-120.

(2) Ahmad, Z.; Shah, A.; Siddiq, M.; Kraatz, H.-B. Polymeric PNPs as drug delivery vehicles. *RSC Advances* **2014**, 4, 17028-17038.

(3) Eetezadi, S.; Ekdawi, S. N.; Allen, C. The challenges facing block copolymer PNPs for cancer therapy: In vivo barriers and clinical translation. *Adv. Drug Deliv. Rev.* **2015**, 91, 7-22.

(4) Hickey, J. W.; Santos, J. L.; Williford, J. M.; Mao, H. Q. Control of polymeric nanoparticle size to improve therapeutic delivery. *J. Controlled Release* **2015**, 219, 536-547.

(5) Muller, R. H.; Mader, K.; Gohla, S. Solid lipid nanoparticles (SLN) for controlled drug delivery - a review of the state of the art. *Eur. J. Pharm. Biopharm.* **2000**, 50, 161-177.

(6) Mehnert, W.; Mader, K. Solid lipid nanoparticles - Production, characterization and applications. *Adv. Drug Deliv. Rev.* **2001**, 47, 165-196.

(7) Allen, T. M.; Cullis, P. R. Drug delivery systems: Entering the mainstream. Science 2004, 303, 1818-1822.

(8) Selvamuthukumar, S.; Velmurugan, R. Nanostructured Lipid Carriers: A potential drug carrier for cancer chemotherapy. *Lipids Health Dis*. **2012**, 11, 8.

(9) Andar, A. U.; Hood, R. R.; Vreeland, W. N.; Devoe, D. L.; Swaan, P. W. Microfluidic Preparation of Liposomes to Determine Particle Size Influence on Cellular Uptake *Mechanisms. Pharm. Res*. **2014**, 31, 401-413.

(10) Mai, Y. Y.; Eisenberg, A. Self-assembly of block copolymers. *Chem. Soc. Rev*. **2012**, 41, 5969-5985.

(11) Bains, A.; Cao, Y.; Moffitt, M. G. Multiscale Control of Hierarchical Structure in Crystalline Block Copolymer Nanoparticles Using Microfluidics. *Macromol. Rapid Commun*. **2015**

(12) Allen, C.; Maysinger, D.; Eisenberg, A. Nano-engineering block copolymer aggregates for drug delivery. *Colloids and Surfaces B: Biointerfaces* **1999**, 16, 3-27.

(13) Cuong, N.-V.; Li, Y.-L.; Hsieh, M.-F. Targeted delivery of doxorubicin to human breast cancers by folate-decorated star-shaped PEG-PCL PNP. *J. Mater. Chem.* **2012**, 22, 1006-1020.

(14) Wang, C.-W.; Sinton, D.; Moffitt, M. G. Flow-Directed Block Copolymer PNP Morphologies via Microfluidic Self-Assembly. *J. Am. Chem. Soc*. **2011**, 133, 18853-18864.

(15) Wang, C.-W.; Sinton, D.; Moffitt, M. G. *ACS Nano* **2013**, 7, 1424-1436.

(16) Xu, Z.; Yan, B.; Riordon, J.; Zhao, Y.; Sinton, D.; Moffitt, M. G. Microfluidic Synthesis of Photoresponsive Spool-Like Block Copolymer Nanoparticles: Flow-Directed Formation and Light-Triggered Dissociation. *Chem. Mater*. **2015**, 27, 8094-8104.

(17) Hoffman, J. D.; Miller, R. L. Kinetics of crystallization from the melt and chain folding in polyethylene fractions revisited: Theory and experiment. *Polymer* **1997**, 38, 3151-3212.

(18) Miyata, T.; Masuko, T. Crystallization behaviour of poly(L-lactide). *Polymer* **1998**, 39, 5515-5521.

(19) Garlotta, D. A literature review of poly(lactic acid). *J. Polym. Environ*. **2001**, 9, 63-84.

(20) Zen, A.; Saphiannikova, M.; Neher, D.; Grenzer, J.; Grigorian, S.; Pietsch, U.; Asawapirom, U.; Janietz, S.; Scherf, U.; Lieberwirth, I.; Wegner, G. Effect of molecular weight on the structure and crystallinity of poly(3-hexylthiophene). *Macromolecules* **2006**, 39, 2162-2171.

(21) Li, H. B.; Huneault, M. A. Effect of nucleation and plasticization on the crystallization of poly(lactic acid). *Polymer* **2007**, 48, 6855-6866.

(22) Liggins, R. T.; Burt, H. M. Paclitaxel loaded poly(L-lactic acid) microspheres: properties of microspheres made with low molecular weight polymers. *Int. J. Pharm*. **2001**, 222, 19-33.

(23) Liggins, R. T.; Burt, H. M. Paclitaxel loaded poly(l-lactic acid) (PLLA) microspheres: II. The effect of processing parameters on microsphere morphology and drug release kinetics. *Int. J. Pharm.* **2004**, 281, 103-106.

(24) Letchford, K.; Burt, H. A review of the formation and classification of amphiphilic block copolymer nanoparticulate structures: PNPs, nanospheres, nanocapsules and polymersomes. *Eur. J. Pharm. Biopharm*. **2007**, 65, 259-269.

(25) Letchford, K.; Liggins, R.; Wasan, K. M.; Burt, H. In vitro human plasma distribution of nanoparticulate paclitaxel is dependent on the physicochemical properties of poly(ethylene glycol)-*block*-poly(caprolactone) nanoparticles. *Eur. J. Pharm. Biopharm*. **2009**, 71, 196-206.

Chapter 5

Flow-Directed Structure and Cytotoxicity of Paclitaxel-Loaded Block Copolymer Nanoparticles Produced Using Microfluidics

5.1 Introduction

Biodegradable nanocarriers such as block copolymer or lipid-based nanoparticles can be used to increase the therapeutic efficacy of hydrophobic drugs while reducing their toxic side effects.[1-4] Block copolymer-based drug delivery nanoparticles offer a number of distinct advantages over their lipid-based counterparts, including increased morphological variability, robustness, and ease of functionalization.[5-9] In this dissertation we have used the semicrystalline and biodegradable block copolymer, poly(ε-caprolactone)-*block*-poly(ethylene oxide) (PCL-*b*-PEO), to study microfluidic drug delivery formulation development. Once this material undergoes self-assembly it forms polymeric nanoparticles (PNPs) that have structural hierarchy (multiscale structure), due to structural organization on the colloidal scale (nanoparticle size and morphology) and on the nanoscale (crystallization of the hydrophobic polymeric chains within the PNP core).[15,16,14,17-19] Control of PNP structure is critical for drug delivery applications because of their complex influence on *in vivo* nanocarrier function.[15,16,14,17-19]

Two-phase gas-liquid segmented microfluidic reactors provide a unique nanocarrier self-assembly environment that combines traditional chemical parameters with the microfluidic control handle of flow-variable shear. In this unique class of microfluidic chip, on-chip shear is maximized in the corners of the gas-liquid plugs, and has been previously used by our group to control structural hierarchy of self-assembled PCL-*b*-PEO PNPs.[20-25] In Chapter 2, we first explored the influence of water content and flow rate on the structural properties of drugless PCL-*b*-PEO PNPs. On-chip assembly resulted in PNPs with reproducible morphologies that were

varied by simply adjusting flow rate. We then used microfluidic assembly for paclitaxel (PAX) loaded PNPs and demonstrated the same reproducible variability of PNP structure (size, morphology, internal core crystallinity) and function (PAX loading efficiency and *in vitro* diffusional release kinetics). In Chapter 3, we used a surrogate dye (DiI) to explore how chemical parameters (water content) in conjunction with the microfluidic control handle of flow-variable shear influence dye-loaded PNP structure and function. These studies demonstrated the ability of our two-phase microfluidic chip to quickly and efficiently screen multiple chemical parameters for drug delivery formulation development. Similar to chapter 2, dye-loaded PCL-*b*-PEO PNP structure and function were reproducibly varied by simply changing flow rate during self-assembly. We also explored how release media composition and temperature affect diffusional release kinetics of the encapsulated DiI. For example, DiI diffusional release was faster when release experiments were conducted at 37 °C compared to room temperature. As well, the addition of phosphate buffered saline and albumin into the dialysate increased DiI release kinetics relative to release media composed of pure water.

In Chapter 4, we replaced the surrogate dye with PAX and screened the influence of chemical parameters (initial drug-to-copolymer ratio and copolymer composition) on on-chip assembly of PAX-loaded PCL-*b*-PEO PNPs. The PAX loading ratios investigated in this chapter are equal to or lower than the ratios utilized in chapter 2. An outcome for this chapter was the insight into how low initial drug loading ratios ($r < 0.01$) have a marginal influence on PNP structure and function. The results of this chapter setup our investigation into on-chip assembly of PAX-loaded PNPs with therapeutically relevant drug loading ratios ($r >> 0.01$).

In this chapter, we provide a systematic investigation of various chemical parameters (copolymer composition and initial drug loading ratio) influencing on-chip assembly of PAX-loaded PCL-*b*-PEO PNPs. A critical aspect of this chapter is the use of initial drug loading ratios that are at least an order of magnitude higher than what has been used in previous chapters. Higher initial drug loading ratios allow for drug encapsulation levels that pertinent to therapeutic applications. In this chapter we also explore how microfluidic-preparation of our PAX-loaded PNPs influences PNP cytotoxicity by using MCF-7 (human breast adenocarcinoma) cells. Cell line studies are important because they provide information on how drug loaded PNPs may behave *in vivo*. Furthermore, cell line studies provide insight into whether or not microfluidic-tuned PNP structure is effective in influencing PNP function within living biological environments. In the context of this dissertation, cell line and *in vivo* studies further progress our microfluidic chips from a proof-of-concept control handle on PNP structure and function towards a viable formulation development platform.

5.2 Experimental

5.2.1 Materials

Three different poly(ε-caprolactone)-*block*-poly(ethylene oxide) (PCL-*b*-PEO) copolymers with constant PEO block length and variable PCL block lengths were purchased from Advanced Polymer Inc. and used as received: PCL_{12k}-*b*-PEO_{5k}; $PCL_{6.4k}$-*b*-PEO_{5k}; $PCL_{2.1k}$-*b*-PEO_{5k}, where numbers in subscripts refer to number-average molecular weights of the respective blocks; these three copolymers are referred to simply as PCL(12k), PCL(6.4k) and PCL(2.1k) elsewhere in the chapter. *N*,*N*-dimethylformamide (DMF) (Aldrich, 99.9+%, HPLC

grade, H_2O < 0.03%), paclitaxel (PAX, Polymed Therapeutics, Inc.), methyl *tert*-butyl ether (Sigma-Aldrich) and bovine serum albumin (Sigma Aldrich), were used as received without further purification. The MCF-7 (human adenocarcinoma breast cancer) cell line was obtained as a generous gift from the BC Cancer agency. The CellTiter-Blue Cell Viability Assay kit (Promega) was used according to the manufacturer's instructions. Antiproliferative assays were conducted using pre-sterilized 96-well flat-bottomed plates from BD Falcon.

All quantitative stock solutions of PCL-*b*-PEO in DMF or PCL-*b*-PEO and PAX in DMF were prepared gravimetrically by accurately weighing the solid(s) into clean glass vials followed by gravimetric addition of a known quantity of DMF; all stock solutions were equilibrated overnight with stirring before further use.

5.2.2 Critical Water Content Determination

Static light scattering (SLS) measurements were carried out to accurately determine the critical water content (cwc) of 0.33 wt % DMF solutions of PCL-*b*-PEO, which was the initial condition for all self-assembly experiments in this study. SLS measurements were carried out using a Brookhaven Instruments photon correlation spectrometer equipped with a BI-200SM goniometer, a BI-9000AT digital autocorrelator, and a Melles Griot He-Ne Laser (633 nm) with a maximum power output of 75 mW.

A 1.0 wt % stock solution of PCL-*b*-PEO in DMF was filtered through a Teflon syringe membrane filter with a nominal pore size of 0.45 μm (VWR) into precleaned scintillation vials. The filtered stock was then diluted to 0.33 wt % by gravimetric addition of the required quantity of DMF. To the resulting ~6 g of solution, deionized water was added in successive 0.03-0.06 g quantities via a microsyringe equipped with two membrane filters (VWR) with nominal pore size

of 0.20 μm connected in series. After each addition of water, the solution was agitated using a vortexer to aid in mixing. The solution was then allowed to equilibrate for 15 min before measuring the scattered light intensity. All measurements were carried out at a scattering angle of 90° and a temperature of 23 °C. From the resulting plot of scattered light intensity versus weight percentage of added water, the cwc was determined from the intercept of linear fits to the baseline and the region of the plot in which scattered light intensity increased sharply (above the cwc). Determinations of cwc were carried out three times from the same stock solution and the mean value and standard deviation of the three measurements were used to calculate the reported cwc and experimental error. The cwc for the PCL(12k) sample in DMF is = 5.5 ± 0.4 wt %; the cwc for the PCL(6.4k) sample in DMF is = 6.3 ± 0.2 wt %; and, the cwc for the PCL(2.1k) sample in DMF is = 13.1 ± 0.2 wt %.

5.2.3 Microfluidic Chip Fabrication

Negative masters were fabricated on high quality silicon wafers (Silicon Quest International, Santa Clara, CA) using the negative photoresist SU-8 100 (Microchem Inc.). Immediately prior to use, the wafers were heated on a hot plate at 200 °C for 20 minutes to remove moisture. A 150 μm-thick SU-8 film was spin-coated onto the silicon and then heated to 95 °C for 60 minutes to remove residual SU-8 solvent. A photomask was then placed over the SU-8 film and exposed to UV light for 180 s. Then, the UV-treated film was heated at 95 °C for 20 min before submersion in SU-8 developer (Microchem) until all unexposed photoresist was removed.

Microfluidics chips were fabricated from poly(dimethylsiloxane) (PDMS) using a SYLGARD 184 silicon elastomer kit (Dow Corning, Midland, MI). For chips used in the

preparation of PAX-loaded PNPs, an elastomer base-to-curing agent ratio of 10:1 was employed as recommended by the kit. However, improved adhesion between the channel and substrate PDMS layers was later found when base-to-curing agent ratios were adjusted to 7:1 and 20:1 for the two layers, respectively, and these ratios were employed for the PAX-encapsulation experiments described the text. For fabrication of all PDMS chips, the elastomer and curing agent were mixed together and degassed in a vacuum chamber. The degassed PDMS was then poured over the negative master in a Petri dish and further degassed until all remaining air bubbles were removed. The PDMS was then heated at 85 °C for ~60 min until cured. The microfluidic chip was then peeled off of the negative master and holes were punched through its reservoirs to allow for the insertion of tubing. A thin PDMS film (substrate layer) was also formed on a glass slide by spin-coating and was permanently bonded to the base of the microfluidic reactor (channel layer) after both components were exposed to oxygen plasma for 60 s. The reactor has a set channel depth of 150 μm and consists of a sinusoidal mixing channel 100 μm wide and 18 mm in length and a sinusoidal processing channel 200 μm wide and 740 mm in length.

For further stabilization of the bubble generation process, an external resistor chip was used between the Ar gas tank and the microfluidic chip. The resistor chips served as high pressure drop systems to efficiently dampen the pressure fluctuations caused by the Ar gas tank and the bubble generation process. The total pressure drop in the external resistor chip was at least one order of magnitude higher than the pressure drop in the reaction channel. The resistor chip channels were 1000 mm long, 150 μm deep and 400 μm wide.

5.2.4 Flow Delivery and Control

Pressure-driven flow of liquids to the reactor inlet was provided using 1 mL gastight syringes (Hamilton, Reno, NV) mounted on syringe pumps (Harvard Apparatus, Holliston, MA). The microchip was connected to the liquid syringes via 1/16th-inch (OD) Teflon tubing (Scientific Products and Equipment, ON). Gas flow was introduced to the microchip via an Ar tank regulator and a downstream regulator (Johnston Controls) for fine adjustments. The microchip was connected to the downstream regulator through a 1/16th-inch (OD) / 100-μm (ID) Teflon tube (Upchurch Scientific, Oak Harbor, WA). The liquid flow rate (Q_{liq}) was programmed via the syringe pumps and the gas flow rate (Q_{gas}) was fine-tuned via the downstream pressure regulator in order to dial in the nominal total flow rates described in the main text. Due to the compressible nature of the gas and the high gas/liquid interfacial tension, discrepancies arise between the nominal (programmed) and actual values of Q_{gas}, Q_{gas}/Q_{liq}, and the total flow rate (Q_{total}). Therefore, actual gas flow rates were calculated from the frequency of bubble formation and the average volume of gas bubbles, determined from image analysis of the mean lengths of liquid and gas plugs, L_{liq} and L_{gas}, respectively, under a given set of flow conditions. This method of flow calculation has been previously employed in the context of gas-liquid segmented flow in the microfluidic device.[20] For all experiments, the relative gas-to-liquid flow ratio, Q_{gas}/Q_{liq} ~1 and all actual Q_{total} values are within 10% of nominal values reported in the main text.

Visualization of the gas bubbles and liquid plugs within the microfluidic reactor was achieved using an upright optical microscope (Omax) with a 10x-objective lens. Images were captured using a 2.07 megapixel PupilCam (Ken-A-Vision) and mean lengths of liquid and gas plugs were determined from the images using image analysis software (ImageJ).

5.2.5 Microfluidic Preparation of PAX-Loaded PCL-*b*-PEO PNPs

Various PAX-loaded PCL-*b*-PEO nanoparticle samples were prepared by combing three fluid streams at equal flow rate to form gas-segmented liquid plugs within the reactor: (1) a DMF solution containing 1 wt % PCL(12k), PCL (6.4k), or PCL(2.1k) with codissolved PAX in a drug : copolymer ratio (w : w) of r = 0.1, 0.25, 0.5, or 0.6; (2) a separator stream containing DMF only; and (3) a DMF solution containing deionized water at concentrations of 16.5 , 18.9 or 39.3 wt % for PCL(12k), PCL(6.4k), and PCL(2.1k) samples, respectively. In all cases, combination of the three liquid streams yielded steady-state on-chip concentrations of 0.33 wt % copolymer and cwc + 5 wt % deionized water.

The PAX-loaded nanoparticle samples were collected from the reactor into vials containing a 10x-excess volume of deionized water, followed by 12 h dialysis against deionized water (with changing of water every hour for the first 4 h of dialysis) to remove residual DMF and unencapsulated PAX. The resulting aqueous dispersions of PAX-loaded nanoparticles were analyzed by TEM, XRD, and also used for studies of PAX loading efficiencies and release kinetics, as described in the corresponding sections below. All samples were prepared in triplicate under the specified chemical and flow conditions.

5.2.6 Transmission Electron Microscopy

Transmission electron microscopy (TEM) was performed using a JEOL JEM-1400 TEM, operating at an accelerating voltage of 65 kV and equipped with a Gatan Orius SC1000 CCD camera. TEM images were obtained by depositing diluted dispersions (~0.03 wt %

copolymer) consisting of PAX-loaded PCL-*b*-PEO nanoparticles in water onto carbon-coated 300 mesh copper TEM grids as described below.

To improve contrast, uranyl acetate was used to negatively stain the PCL-*b*-PEO nanoparticles. Uranyl acetate selectively binds to the PEO coronal chains, providing reverse contrast for the PCL cores, which appear white in TEM images of stained samples. For reverse staining experiments, nanoparticle dispersions were mixed with 1 wt % aqueous solution of uranyl acetate in a 1:1 ratio (v/v) and one drop of the resulting mixture was deposited onto a TEM grid. Excess liquid was immediately removed using lens paper, followed by drying of remaining liquid under ambient conditions.

Due to the high electron density of uranyl acetate, negative staining generally impedes visualization of internal lumen of vesicle structures, such that vesicles and spheres cannot be readily distinguished from stained samples. Therefore, all samples revealing aggregates of spherical shape in negative contrast TEM images were also imaged without staining. In unstained images, contrast is provided by high density PCL crystallites which appear dark relative to both the background and the internal lumen of vesicles, such that vesicles appear hollow in unstained images and so can be differentiated from spheres. We find that one complication of imaging PCL-*b*-PEO nanoparticles without staining is that upon drying under ambient conditions, deposited dispersions form large crystallites of PEO which obscure identification of micellar PCL cores. To avoid this problem, micellar dispersions deposited without reverse staining were freeze-dried on TEM grids using the following method. First, one drop of the micellar dispersion was deposited onto a TEM grid and excess liquid was immediately removed using lens paper. The remaining liquid was then vitrified by submerging the TEM grid into liquid ethane. The resulting vitrified sample was then freeze-dried under

vacuum. As discussed below, the morphological identification of some aggregates required the evaluation of their heights. For these experiments, Pt/Pd shadowing of unstained aggregates following freeze-drying on the grid was carried out at a shadowing angle of 45°.

For each set of conditions, reported prominent morphologies and mean dimensions from TEM of nanoparticles with loaded PAX (Table 5.1 and Table 5.2) were determined from TEM analysis of three separate preparations starting with three individually-prepared stock solutions. For each sample preparation and TEM grid deposition method (unstained, stained, and shadowed), at least 2-3 TEM images taken in different regions of the grid were evaluated. Prominent morphologies for each condition were assigned based on the following definitions with associated evaluation methods in brackets. Spheres were defined as aggregates with circular projections (TEM with staining) but without internal lumen (TEM without staining). Vesicles were defined as aggregates with circular projections (TEM with staining) with internal lumen (TEM without staining). Cylinders were defined as high aspect-ratio filaments of approximately regular width (TEM with staining). Lamellae were defined as irregularly-shaped aggregates (TEM with staining) with heights significantly smaller than their lateral dimensions (TEM with shadowing); from cases where aggregate shadowing was carried out, lamellae heights were determined to be 10 nm. For each preparation, mean dimensions were determined from ~400 particles; therefore, for each of the mean dimensions in Table 1, N = 400 × 3 preparations = ~1200, such that the reported errors reflect reproducibility of the preparation method. Mean sphere diameters and cylinder widths were determined exclusively from TEM images with staining. Averaging and statistical analysis of dimensions from TEM images was conducted using Image J software.

5.2.7 Dynamic Light Scattering

Effective hydrodynamic diameters of DiI-loaded PCL-*b*-PEO nanoparticles were determined using dynamic light scattering (DLS). DLS measurements were carried out using a Brookhaven Instruments photon correlation spectrometer equipped with a BI-200SM goniometer, a BI-9000AT digital autocorrelator, and a Melles Griot He-Ne Laser (633 nm) with a maximum power output of 75 mW. All DLS measurements of DiI-loaded nanoparticles were performed in pure water and an experimental temperature of 23˚C and at a scattering angle of 90˚.

After overnight dialysis against deionized water to remove residual DMF and unencapsulated DiI, the DiI-loaded nanoparticles were transferred to pre-cleaned scintillation vials then diluted 5× using deionized water, filtered through two nylon syringe filters in series with nominal pore sizes of 0.2 m (National Scientific Company) to give a final copolymer concentration of ~0.07 mg/mL. For each nanoparticle preparation, mean effective hydrodynamic sizes were determined from three measurements of the autocorrelation function using cumulent analysis. Mean effective hydrodynamic diameters were determined from three separate data collections corresponding to one individually-prepared stock solution, such that reported errors reflect the error in data collection.

5.2.8 X-Ray Diffraction

X-ray diffraction measurements were performed on a Rigaku Miniflex diffractometer with a Cr source (kR radiation, λ = 2.2890 Å) operating at 30 kV and 15 mA with a resolution of

0.05° (2θ) and a scan speed of 1°/min. X-ray diffraction profiles were collected for 2θ ranging from 10-80 degrees.

For XRD sample preparation, water was removed from suspensions of DiI-loaded nanoparticles by rotory evaporation at 25 °C until solid films were obtained. The resulting films were then scraped as a powder into the XRD specimen holder with no subsequent drying step to remove residual solvent. We note that this preparation method will significantly increase the crystallinity of coronal PEO blocks relative to their colloidal state, as removal of water from the nanoparticle coronae will allow initially-solubilized PEO chains to pack together. However, since the hydrophobic cores will contain no water in the purely aqueous suspensions, we do not expect the crystallinity of the core-forming PCL blocks to be strongly affected when water is removed by rotory evaporation. Therefore, our XRD experiments should provide a reasonable probe of nanoparticle core crystallinity in the colloidal state.

Peak deconvolution of XRD data was done using Origin Pro Version 8.1. Two characteristic reflections for each of crystalline PCL and crystalline PEO were identified from the literature and these were used to fix the positions of four Lorentzian peak contributions to the fit;[29,24] another small Lorentzian peak contribution was used to account for a small shoulder on the more intense PCL peak in order to obtain a good fit (Figure 8.3). Thus, XRD data were fit to a sum of 6 Lorentzian functions: 3 peaks assigned to crystalline PCL (2θ = 32.5, 32.7, and 35.7), 2 peaks assigned to crystalline PEO (2θ = 29.2 , 35.4), and 1 peak (no fixed position) assigned to incoherent scattering from amorphous copolymer (amorphous halo). Areal peak contributions from the three components (crystalline PCL, crystalline PEO, and amorphous copolymer) were then determined by integration and percentages of crystalline PCL and PEO were calculated using:

$$\% \textit{ Crystalline } \text{PCL} = A_{\text{PCL}}/A_{\text{total,}} \text{ and } \% \textit{ Crystalline } \text{PEO} = A_{\text{PEO}}/A_{\text{total}},$$

$$\text{where } A_{\text{total}} = A_{\text{PCL}} + A_{\text{PEO}} + A_{\text{amorph.}}$$

5.2.9 PAX Loading Efficiency Determination

To determine PAX loading efficiencies, PAX-loaded PNPs were first dialyzed against pure water to remove residual DMF and then centrifuged at 12,000 g to remove any precipitate. Then an aliquot of solution was removed and in acetonitrile (ACN): First, water was removed from a known mass (~1 g) of an aqueous dispersion of PAX-loaded nanoparticles of known copolymer concentration by rotary evaporation at 25 °C; 2. Then a known amount (~0.5 g) of ACN was added to break up the PAX-loaded nanoparticles by stirring in ACN for 4 h. PAX quantification was conducted using high performance liquid chromotography-mass spectrometry (HPLC-MS, Ultimate 3000, Thermo Scientific) with a C18 column (Phenomenex Luna 5u C18) and a mobile phase composition of 65/35 acetonitrile/water (v/v) and 1 vol % formic acid using the diode array detector (DAD). Sample injection volumes were 50 μL and the HPLC-MS flow rate was set to 1 mL/min. For loading efficiency determinations, PAX solution concentrations were sufficiently high such that they could be detected and quantified using the diode array detector (DAD) by monitoring the elution of PAX at a characteristic absorption wavelength of 227 nm. A calibration curve for the DAD was generated by analysis of 5 stock solutions containing different known PAX concentrations in ACN. Quantities of PAX in the various dissolved PNP solutions were determined and loading efficiencies calculated for each sample using the following expression:

$$loading\ efficiency\ (\%) = \frac{PAX\ in\ micelles\ (g)}{total\ PAX\ used\ (g)} \times 100\%$$

Reported loading efficiencies are averages determined from triplicate nanoparticle preparations under the specified conditions. Initial drug-to-copolymer ratio refers to the PAX to PCL-*b*-PEO ratio before self-assembly, loading efficiency refers to the amount of PAX encapsulated against the initial quantity of PAX used, and PAX loading level is the product of the initial drug-to-copolymer ratio and PAX loading efficiency

5.2.10 *In Vitro* PAX Release Kinetics

Experiments were carried out to monitor the in vitro release of PAX from PAX-loaded nanoparticles using HPLC-MS (see previous section for instrument specifications). In a typical experiment, ~10 g of aqueous dispersion of PAX-loaded nanoparticles were transferred to a 10 mL-dialysis bag (SpectrumLabs, MWCO 100 kDa) which was placed in a 4 L-beaker of the release medium, consisting of ~2.5 L of a 1% phosphate buffer saline (PBS, pH = 7.4) solution containing albumin (Sigma Aldrich) at a concentration of 45 g/L; throughout release experiments, the release medium was constantly stirred using magnetic stirring and maintained at physiological temperature (37 °C) in an incubator. At each predetermined time, an aliquot of known mass (~1 g) was removed from the dialysis bag to which a known mass (~150 mg) of a deuterated PAX internal standard (d5-PAX, ~1 mg/mL, Toronto Research Chemicals) in ACN was added. A liquid-liquid extraction was conducted using methyl tert-butyl ether (Sigma Aldrich). The top organic liquid phase containing PAX and internal standard was decanted from the lower aqueous phase containing albumin. The methyl tert-butyl ether was then removed by rotary evaporation at 25 °C then a known quantity of ACN (0.1-0.5 g depending on release time) was added. The resulting solution was injected into the HPLC-MS and PAX and d5-PAX were detected and quantified using the MS detector by single ion monitoring (SIM) of the m/z = 286

and m/z = 291 peaks, respectively. Separate calibration curves for SIM detection of PAX and the internal standard were generated by analysis of five known stock solutions of both analytes. The internal standard (d_5-PAX) was used to determine the efficiency of each liquid-liquid PAX extraction, which was found to vary from 60-80%. These extraction efficiencies were used to calculate PAX concentrations in each aliquot before liquid-liquid extraction from PAX concentrations determined by HPLC-MS. From determined masses of PAX in aliquots obtained at different release times, percentages of PAX released were calculated relative to the determined mass of nanoparticle-encapsulated PAX at the $t = 0$ release time. Reported release percentages at each release time are averages determined from triplicate nanoparticle preparations under the specified conditions. Although release kinetics in such in vitro experiments have been shown to be very different from in vivo pharmakinetics,5 they provide useful information on drug diffusion and nanoparticle breakup that may contribute to drug release in pharmaceutical applications.

In general, for the *in vitro* release experiments there was no detection of PAX degradation products by the MS detector. On the other hand, when monitoring for the elution of PAX at the characteristic absorbance wavelength of 227 nm, samples with PAX diffusional release times less than ten days had no observable PAX degradation (Figure 9.3A; Appendix III); however, PAX release experiments with diffusional release times greater than ten days had one extra peak appear on the LCMS trace at ~ 5.5 minutes (Figure 9.3B; Appendix III). The peak at ~ 5.5 minutes (Figure 9.3B; Appendix III) indicates degradation products of PAX; however, since the magnitude of this peak is much lower than the main peak at ~ 5 minutes, the secondary peak at 5.5 minutes was not considered in the concentration calculations.

5.2.11 Cell-Culture and Antiproliferation Assay

MCF-7 cells were grown in Dulbecco's Modified Eagle's Medium (DMEM) supplemented with 10% fetal bovine serum (FBS) in a 75 cm^2 culture flask and maintained at 37 °C with 5% CO_2 in a tissue culture incubator.

MCF-7 cells were grown in 75 cm^2 tissue culture flasks to ~ 95% confluence, then were trypsinized, collected and pelleted by centrifugation (3 minutes at 16000 g). The cell pellet was then resuspended in DMEM media and the cell concentration was determined using a hemocytometer. After the initial cell concentration was determined the suspension was diluted to 1.0 x 10^5 cells/mL. Next, a multichannel pipet was used to fill a 96 well plate with 100 µL/ well of the diluted cell suspension. The cell loaded plates were then incubated for 24 h at 37 °C under an atmosphere of 5% CO_2. After 24 hours, 6.5 µL samples of PAX-loaded PCL-*b*-PEO PNPs were dissolved in 643.5 µL of DMEM media to obtain a working PAX concentration of 2 ppm. Serial dilutions were conducted to generate a range of different concentrations for analysis (1, 0.308, 0.095, 0.029, 0.0090, 0.0028, 8.5 x 10^{-4}, and 2.6 x 10^{-4} ppm PAX). The treated cells were incubated for 48, 72 and 96 hours at 37 °C under a 5% CO_2 atmosphere. In an effort to determine cell viability, 20 µL of CellTiter-Blue was added to each well after the predetermined incubation time was complete. After the addition of the CellTiter-Blue the 96 well plates were incubated for 4 hours (5% CO_2, 37 °C) and then fluorescence (λ_{ex} = 560 nm; λ_{em} = 590 nm emission) readings were recorded on a 96-well plate reader. Percent growth inhibition (GI) was calculated for each well, based upon the following formula:

$$\% GI = 100 \times \frac{(S - B_o)}{(B_t - B_o)}$$

Where S is the sample reading, B_t is the average reading for the PNP treated population of cells, and B_0 is the average reading of untreated population of cells at the beginning of the experiment.

Percent growth inhibition (GI_{50}) was calculated for these samples instead of the inhibition concentration (IC_{50}) because of the high levels of expression of the P-glycoprotein in MCF-7 cells. P-glycoprotein is a protein that aids in the removal of foreign substances from within cells. Due to this possible mechanism in our MCF-7 cancer cell line, we were not able to obtain IC_{50} values for all of our formulations; thus, we calculated GI_{50} values of our PAX-loaded PNP formulations used to treat the MCF-7 cells.

5.3 Results and Discussion

Effect of Copolymer Composition on the Multiscale Structure and Loading Efficiency of Microfluidic-Prepared PAX-Loaded PNPs. First, we explored the influence of copolymer composition on PAX-loaded PNPs prepared in the microfluidic device at two flow rates of Q = 100 and 200 μL/min. For this set of experiments, we prepared PNPs from three copolymers: PCL(12k), PCL(6.4k) and PCL(2.1k). The initial drug-to-copolymer ratio was held constant at r = 0.1. The size and morphology results are presented in Figure 5.1 and summarized in Table 5.1.

Table 5.1 Morphologies[a] Mean Dimensions[b] and PAX Loading Efficiencies for PAX-loaded PCL-*b*-PEO Nanoparticles Prepared in the Segmented Microfluidic Reactor using Various Flow Rates and Copolymer Compositions.

Polymer Composition	Q (μL/min)	r	Morphology	$d_{h,eff}$ (nm)	Core Dimensions (nm)	χ_{PCL} (%)	Loading Efficiency (%)	Loading Level
PCL(2.1k)	100	0.1	S, RC, L	1700 ± 200	S(15 ± 4) RC(38 ± 6)	4 ± 1	8 ± 2	0.8 ± 0.2
	200	0.1	V, S, L	1500 ± 300	S(9 ± 3)	7 ± 2	26 ± 4	2.6 ± 0.4
PCL(6.4k)	100	0.1	S, C, L	1900 ± 300	S(14 ± 3) C(11 ± 2)	11 ± 2	9 ± 3	0.9 ± 0.4
	200	0.1	S, C, L	3800 ± 500	S(14±1) C(10 ± 1)	16 ± 4	28 ± 4	3 ± 0.4
PCL(12k)	100	0.1	S, L	1700 ± 400	S(17 ± 3)	18 ± 3	36 ± 8	3.6 ± 0.8
	200	0.1	V, S, C, L	2300 ± 300	S(22 ± 5) C(13 ± 2)	26 ± 5	26 ± 4	2.7 ± 0.4

a) Prominent morphologies are indicated as S (spheres), C (cylinders or filomicelles), RC (rigid cylinders), V (vesicles), and L (lamellae).

b) Numbers refer to mean sphere diameters and cylinder widths. Reported errors are standard deviations of mean values determined for three replicate preparations.

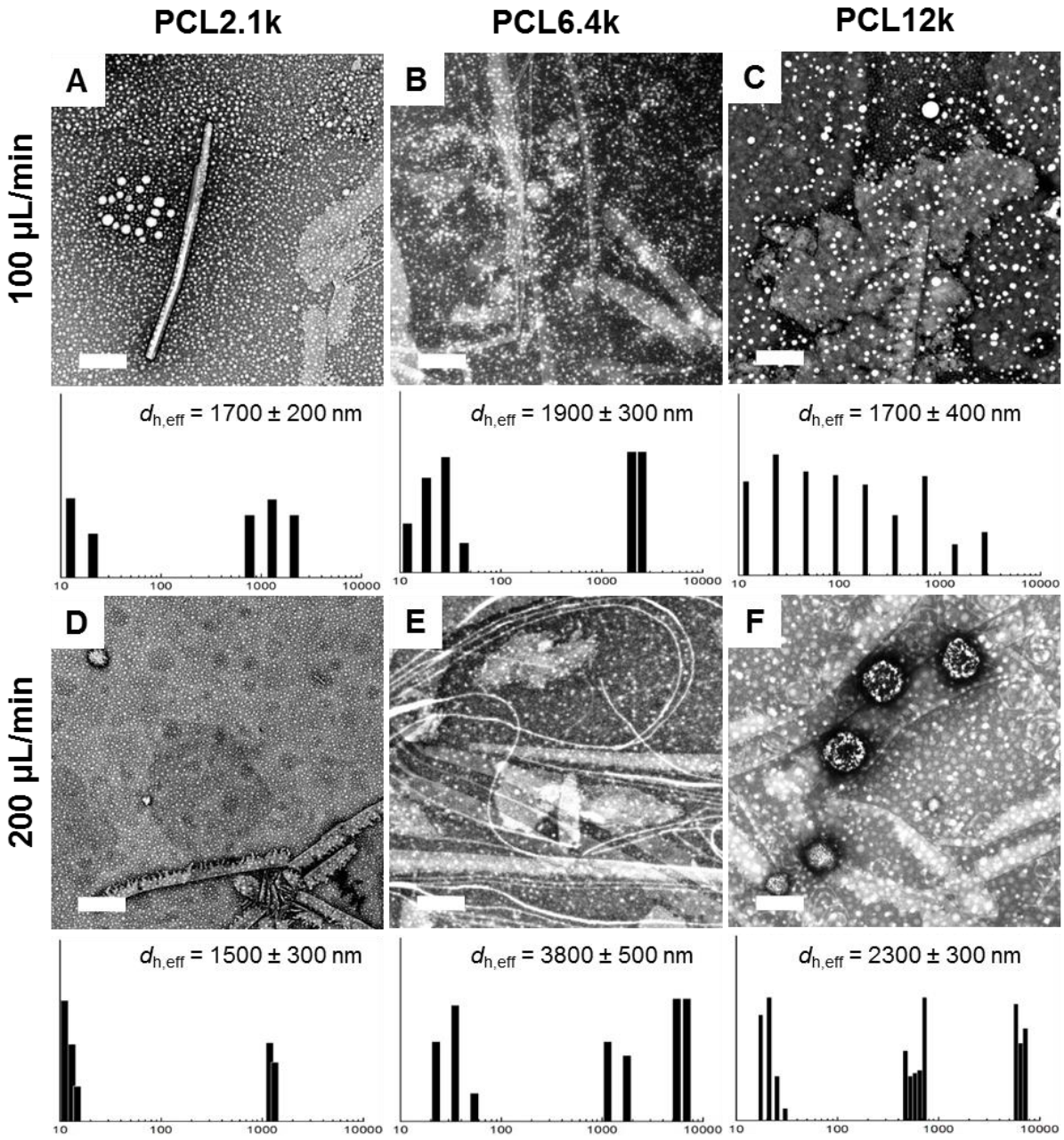

Figure 5.1 Effect of flow rate and copolymer composition on morphology and hydrodynamic size of PAX-loaded PCL-*b*-PEO nanoparticles. TEM images were produced by negative staining with uranyl acetate. All scale bars are 200 nm. Below each TEM image is a representative size distribution obtained from CONTIN analysis of DLS autocorrelation functions, along with the mean effective hydrodynamic diameter determined from CUMULENT analysis.

In Figure 5.1, the *Q* = 100 μL/min self-assembly condition (Figure 5.1 A – C) has no discernible trend in PNP size and morphology. All three formulations consist of spheres and lamellae; with the PCL(2.1k) and PCL(6.4k) compositions also yielding relatively few numbers of cylindrical PNPs. On the other hand, the *Q* = 200 μL/min condition (

Figure 5.1 D – F) has a general trend of increasing PCL block length with numbers of low core curvature PNPs.

To understand the effect of copolymer composition on PNP size and morphology (Figure 5.1 D – F), we consider the influence of PCL block length and core crystallinity on PNP structure. With respect to copolymer composition, we have previously reported on increasing PCL block length correlating with high aggregation numbers. For example, in Chapter 4 increasing PCL block length correlated with the formation of cylindrical and lamellar morphologies (Figure 4.1 A, F and K). The trend of high aggregation numbers correlating with increasing PCL block length is also observed in Figure 5.1 D – F; as, cylinders and vesicles are dominant morphologies in the PCL(6.4k) and PCL(12k) compositions, respectively. Next we consider the effect of PCL core crystallinity on PNP size and morphology. The correlation between morphology trending towards low core curvature structures with increasing PCL core crystallinity has also been reported previously, in this dissertation. For example, in Chapter 2 we reported that increasing PCL core crystallinity resulted in the formation of cylindrical and lamellar structures. This trend was also observed in Chapter 3, where increasing PCL core crystallinity correlated with the formation of cylindrical and lamellar morphologies. For the *Q* = 200 μL/min (Figure 5.1 D – F) condition, the formation of low core curvature morphologies trends with increases in both core crystallinity (Table 5.1) and PCL block length. Therefore, we

attribute the formation of cylinders and vesicles in Figure 5.1 E and F to increasing core crystallinity and PCL block length.

Next we report PCL core crystallinity results for the Q = 100 and 200 μL/min conditions (Table 5.1). For these set of results, there are two main factors influencing PCL core crystallinity: copolymer composition and flow rate. First, we discuss the effect of PCL block length on PCL core crystallinity (Table 5.1). In general, PCL core crystallization increases as a function of increasing PCL block length. A similar trend was previously reported in Chapter 4; where increasing PCL molecular weight correlated with increasing PCL core crystallinity. In general, PCL molecular weight is expected to increase PCL core crystallization.[13,14]

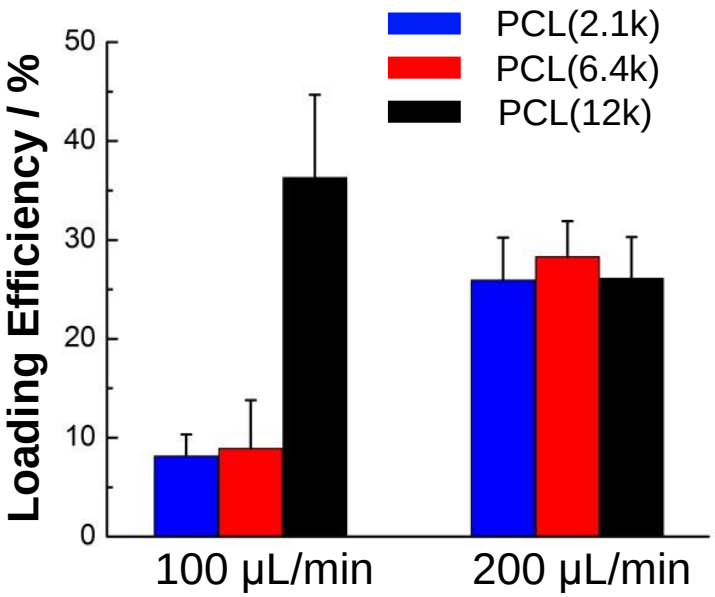

Figure 5.2 Effect of flow rate and copolymer composition on the loading efficiency of PAX-loaded PCL-*b*-PEO nanoparticles. Blue bars: PAX-loaded PNPs prepared using the PCL(2.1k) copolymer composition; red bars: PAX-loaded PNPs prepared using the PCL(6.4k) copolymer composition; and, black bars: PAX-loaded PNPs prepared using the PCL(12k) copolymer composition. Error bars are standard deviations of triplicate runs.

Now we report the effect of increasing flow rate on PCL core crystallinity (Table 5.1). Increasing core crystallization with increasing flow rate was reported in both Chapters 2 and 3. Increasing flow rate is expected to increase core crystallinity as a result of flow-induced crystallization; a mechanism that has been observed and explained previously.[24]

Figure 5.2 presents PAX loading efficiency results for three PCL copolymer compositions. For this study, we used one initial drug-to-copolymer ratio, r = 0.1; two flow rates, Q = 100 and 200 µL/min; and, three copolymer compositions. For these set of data, PAX loading efficiencies for the Q = 100 µL/min formulation increase with increasing PCL block length. As for the Q = 200 µL/min, PAX loading efficiencies slightly increase and then decrease with increasing PCL block length.

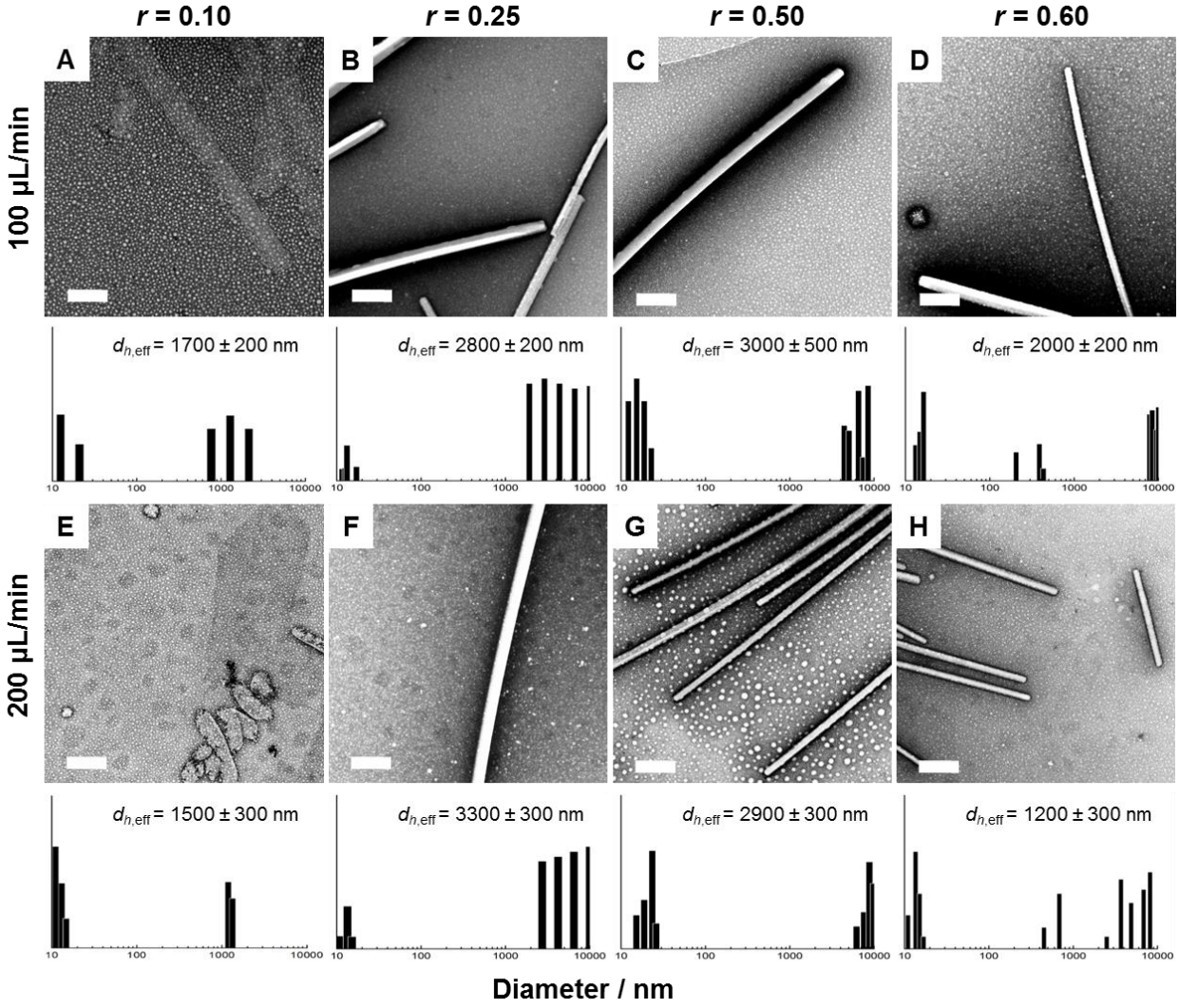

Figure 5.3 Effect of flow rate and initial drug-to-copolymer ratio on morphology and hydrodynamic size of PAX-loaded PCL(2.1k) PNPs. TEM images were produced by negative staining with uranyl acetate. All scale bars are 200 nm. Below each TEM image is a representative size distribution obtained from CONTIN analysis of DLS autocorrelation functions, along with the mean effective hydrodynamic diameter determined from CUMULENT analysis.

Effect of Drug-to-Copolymer Ratio and Flow Rate on the Multiscale Structure and Loading Efficiency of Microfluidic-Prepared PAX-Loaded PNPs. To probe the effect of drug loading ratio and flow rate on PAX-loaded PNPs, formulations were prepared at four initial drug loading ratios (r = 0.10, 0.25, 0.50, and 0.60); two flow rates (Q = 100 and 200 μL/min); and two copolymer compositions (PCL(2.1k) and PCL(6.4k)). The PCL(12k) copolymer was not included in this study due to its tendency to cause microchannel blockages during self-assembly at higher PAX loading ratios. As well, we note that the r = 0.1, Q = 200 μL/min cases for both PCL(2.1k) and PCL(6.4k) were discussed in the previous section but are included here for the sake of completeness. The results discussed in this section are summarized in Table 5.2 and presented in Figure 5.3 and Figure 5.4.

Figure 5.3 shows representative TEM images and DLS size distributions of the PCL(2.1k) copolymer composition. In general, PNP morphology does not change drastically with increasing r, as seven of the eight samples consist of: spheres, and rigid cylinders. On the other hand, the r = 0.1 Q = 200 μL/min condition (Figure 5.3 E) consists of spheres, lamellae and vesicles. The cylinders that are observed in this sample are especially interesting because they do not share the same structural properties as the cylinders (filoPNPs) that we have reported in our earlier reports.[20,23,24] For example, the cylinders observed in Figure 5.3 are considerably shorter than the previously reported cylinders, and are particularly rigid along their lateral axis. Thus, to distinguish these cylinders from the previously reported cylinders we term these cylinders: rigid cylinders (RCs).

Table 5.2 Morphologies[a] Mean Dimensions[b] and PAX Loading Efficiencies for PAX-loaded PCL-*b*-PEO Nanoparticles Prepared in the Segmented Microfluidic Reactor using Various Flow Rates and Copolymer Compositions.

Polymer Composition	Q (μL/min)	r	Morphology	$d_{h,eff}$ (nm)	Core Dimensions (nm)	χ_{PCL} (%)	Loading Efficiency (%)	Loading Level
PCL(2.1k)	100	0.25	S, RC	2800 ± 200	S(13 ± 2) RC(46 ± 7)	3 ± 1	13 ± 2	3 ± 0.6
	200	0.25	S, RC	3300 ± 300	S(18 ± 4) RC(58 ± 4)	15 ± 2	28 ± 5	7 ± 1
PCL(2.1k)	100	0.5	S, RC	3000 ± 500	S(10 ± 1) RC(49 ± 6)	0	15 ± 3	8 ± 0.8
	200	0.5	S, RC	2900 ± 300	S(9 ± 1) RC(36 ± 6)	12 ± 3	22 ± 6	11 ± 2
PCL(2.1k)	100	0.6	V, S RC	2000 ± 200	S(11 ± 2) RC(38 ± 5)	0	11 ± 5	7 ± 1
	200	0.6	S, RC	1200 ± 300	S(10 ± 1) RC(35 ± 7)	14 ± 3	16 ± 6	10 ± 1
PCL(6.4k)	100	0.25	S, C, RC, L	4300 ± 500	S(14 ± 2) C(10 ± 1) RC(35 ± 6)	10 ± 2	19 ± 3	5 ± 0.8
	200	0.25	V, S, C, RC, L	2500 ± 300	S(14 ± 2) C(9 ± 2) RC(29 ± 4)	23 ± 4	8 ± 2	2 ± 0.6
PCL(6.4k)	100	0.5	S, RC,L	2800 ± 600	S(9 ± 1) RC(20 ± 3)	16 ± 3	3 ± 0.8	1.5 ± 0.2
	200	0.5	V, S, C, L	3000 ± 200	S(12 ± 2) C(10 ± 1)	28 ± 2	4 ± 0.7	1.9 ± 0.2
PCL(6.4k)	100	0.6	S	80 ± 10	S(17 ± 3)	7 ± 2	15 ± 7	9 ± 2
	200	0.6	S, C, L	3500 ± 300	S(13 ± 2) C(9 ± 1)	18 ± 4	3 ± 1	1.8 ± 0.3

a) Prominent morphologies are indicated as S (spheres), C (cylinders or filomicelles), RC (rigid cylinders), V (vesicles), and L (lamellae).

b) Numbers refer to mean sphere diameters and cylinder widths. Reported errors are standard deviations of mean values determined for three replicate preparations.

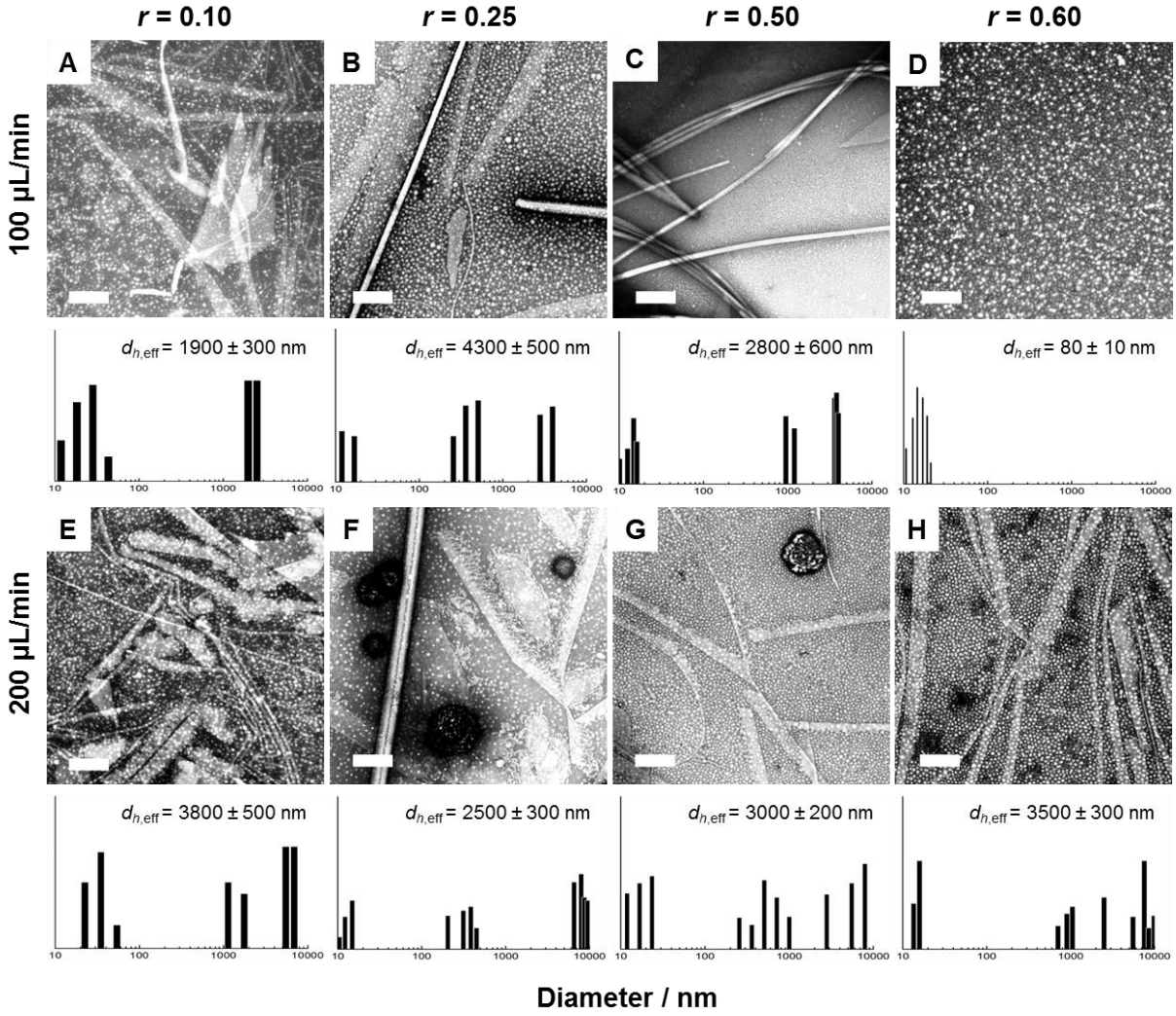

Figure 5.4 Effect of flow rate and initial drug-to-copolymer ratio on morphology and hydrodynamic size of PAX-loaded PCL(6.4k) PNPs. TEM images were produced by negative staining with uranyl acetate. All scale bars are 200 nm. Below each TEM image is a representative size distribution obtained from CONTIN analysis of DLS autocorrelation functions, along with the mean effective hydrodynamic diameter determined from CUMULENT analysis.

Figure 5.4 shows representative TEM images and DLS size distributions of the PCL(6.4k) copolymer composition. In general, with increasing *r* all samples consist of low core curvature morphologies. Nevertheless, there is one exception: Figure 5.4 D, where only spherical nanoparticles are present. To understand this change in morphology, we consider the effect of

core crystallinity on PNP multiscale structure. PCL core crystallinity stays relatively stable for the first three drug loading conditions (Figure 5.4 A – C; $r < 0.6$), and then decreases for the r = 0.6 condition (Figure 5.5; blue triangles). This change in core crystallinity trends well with PNP morphology, as low core curvature morphologies (Figure 5.4 A – C) are replaced with pure spheres when core crystallization decreases (Figure 5.4 D). Furthermore, to explain the appearance of vesicles in the Q = 200 μL/min condition (Figure 5.4 F and G) we also consider PCL core crystallinity. PCL core crystallinity for these two samples spikes relative to the r = 0.1 and 0.6 sample (Figure 5.5; green triangles). PNP cores have a tendency to crystallize with hydrophobic copolymer chains aligned perpendicular to the solvent-core interface. Crystallite packing within PNP cores drives the formation of low-curvature structures, such as the vesicles, observed in the r = 0.25 and 0.5 conditions.[30-32] Therefore, we attribute the appearance of vesicles for the r = 0.25 and 0.5 conditions (Figure 5.4 F and G) to increased PCL core crystallinity.

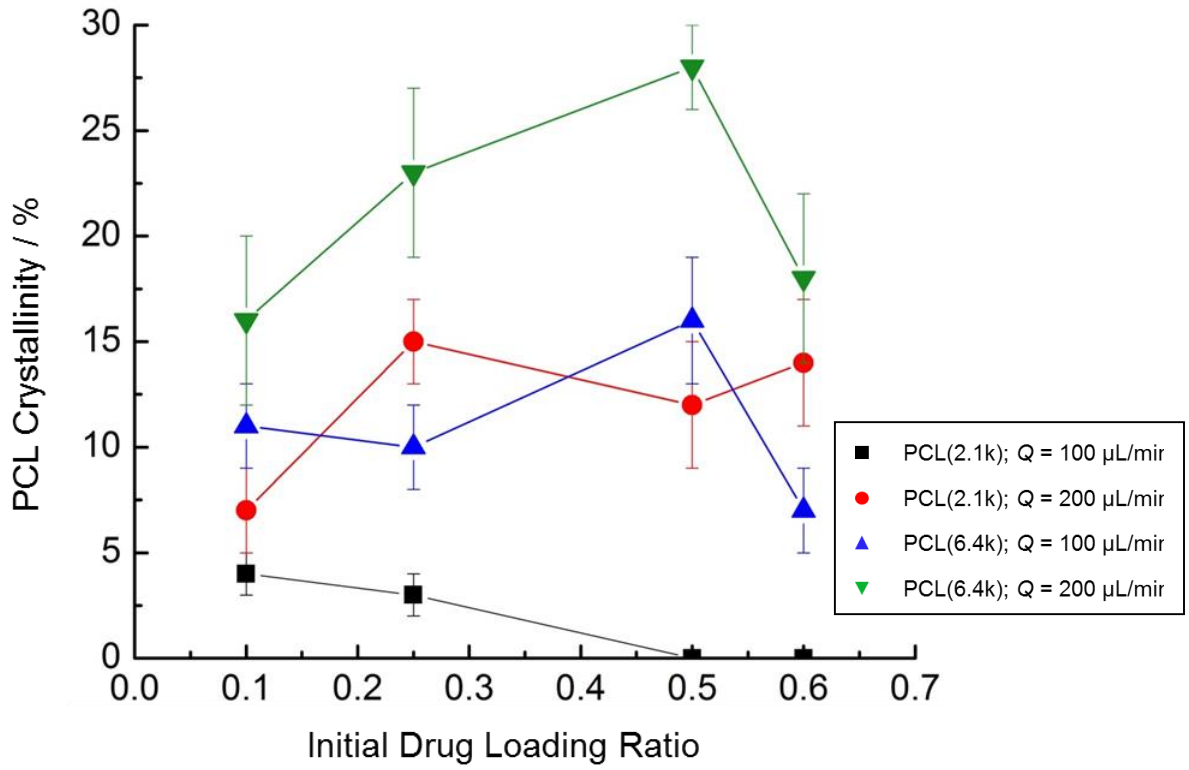

Figure 5.5 Effect of initial drug loading ratio on PCL core crystallinity. Black squares: PCL(2.1k) composition assembled on-chip at Q = 100 µL/min; red circles: PCL(2.1k) composition assembled on-chip at Q = 200 µL/min; blue triangles: PCL(6.4k) composition assembled on-chip at Q = 100 µL/min; and, green triangles: PCL(6.4k) composition assembled on-chip at Q = 200 µL/min. Error bars are standard deviations of triplicate runs.

Figure 5.4 presents core crystallinity results for the PCL(2.1k) and PCL(6.4k) formulations. For these set of results core crystallinity follows three distinct trends: 1. core crystallization increases as a function of increasing PCL block length; 2. core crystallinity increases as a function of increasing flow rate; and, 3. core crystallization is attenuated by increasing PAX loading levels.

Next we discuss the trends in PCL core crystallinity (Figure 5.5). The first trend of increasing core crystallinity with increasing PCL block length can be explained by the increase in PCL molecular weight. In general, increasing PCL molecular weight correlates with

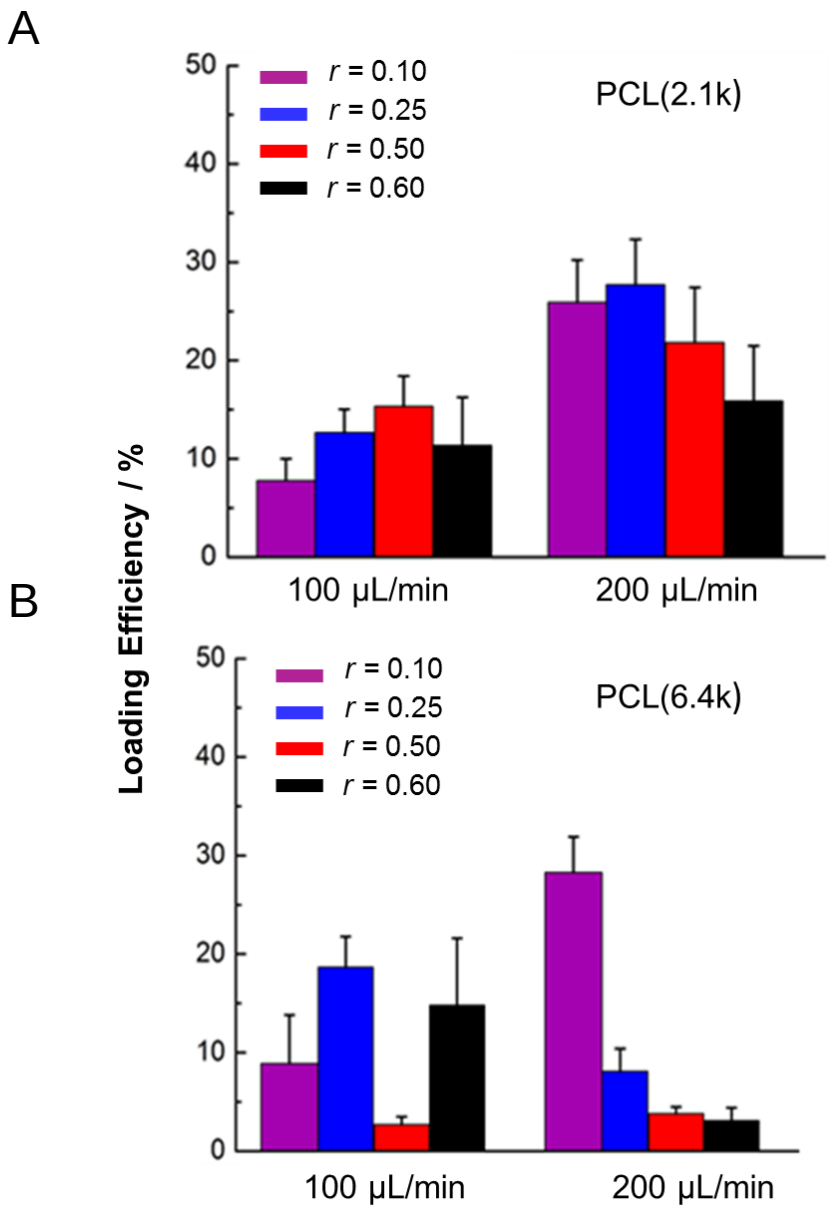

Figure 5.6 Effect of flow rate, copolymer composition, and initial drug loading ratio on the loading efficiency of PAX-loaded PCL-*b*-PEO PNPs. Error bars are standard deviations of triplicate runs.

increasing PCL core crystallinity.[13,14] With respect to the second trend, for similar copolymer compositions, core crystallization is higher for formulations assembled at higher flow rate (Figure 5.5). This trend is attributed to flow-induced crystallization. Examples of flow-induced crystallization have been observed previously in this chapter (Table 5.1) and Chapters 2 and 3. As for the third trend, formulations with higher PAX loading levels have relatively lower core

crystallization. For example, for the PCL(6.4k) formulation where Q = 100 μL/min, increasing PAX loading levels correlate with decreasing core crystallization (Figure 5.5, Table 5.2) .These observations are a result of increasing PAX efficiency attenuating core crystallinity through PAX molecules disrupting copolymer chain packing, similar to the effect of a plasticizer.

Next we will consider the effect of flow rate, copolymer composition, and initial drug-to-copolymer ratio on PAX loading efficiency. Figure 5.5 presents PAX loading efficiency results for the PCL(6.4k) and PCL(2.1k) formulations. In general, loading efficiency increases and then decreases as a function of increasing r; one exception to this trend is the PCL(6.4k) Q = 200 μL/min formulation, where PAX-loading efficiency decreases as a function of increasing r.

To understand these results in PAX loading efficiency we consider PCL core crystallinity. In general, increasing PAX loading efficiency correlates with decreasing PCL core crystallinity. For example, for the PCL(6.4k) Q = 200 μL/min formulation (Figure 5.6), as PCL core crystallinity increases (Figure 5.5; green triangles), PAX loading efficiency decreases (Figure 5.6 B). This trend is also observed in the PCL(2.1k) formulations. For example, for the PCL(2.1k) Q = 100 μL/min formulation (Figure 5.6 A), as PAX loading efficiency increases, PCL core crystallinity decreases (Figure 5.5; black squares). As described earlier, PAX molecules act as plasticizers within the PCL core, attenuating core crystallinity. This result is contrary to the result observed in Chapter 4, where increasing PAX loading efficiency did not negatively influence PCL core crystallinity. We speculate, the higher drug loading ratios presented in this chapter disrupt PCL chain packing to a significant degree; causing a decrease in PCL core crystallinity with increasing PAX loading efficiency.

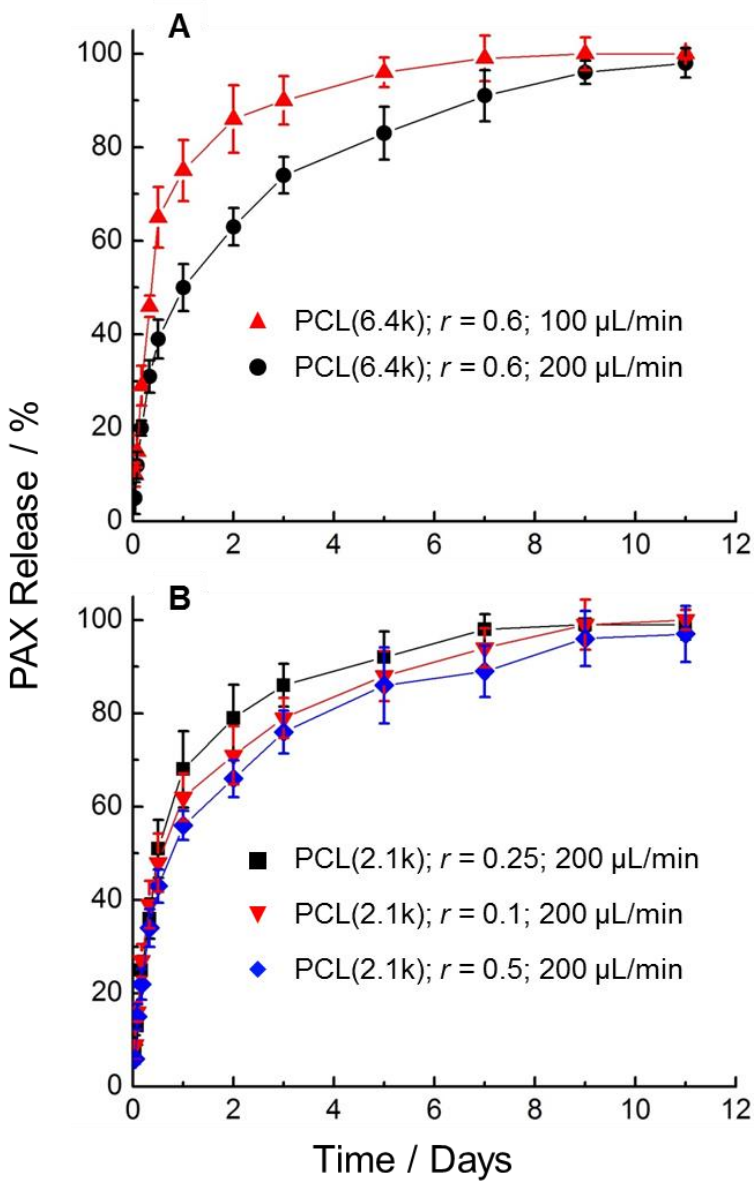

Figure 5.7 Effect of flow-rate, copolymer composition, and initial drug-to-copolymer ratio on the release of PAX from PAX-loaded PCL-*b*-PEO PNPs. (A) Release profiles for nanoparticles prepared using the PCL(6.4k) composition, with r = 0.6, and various flow rates. (B) Release profiles for nanoparticles prepared using the PCL(2.1k) composition, with r = 0.10, 0.25, and 0.5, and a flow-rate of 200µL/min. All release experiments were carried out into 1 % PBS and albumin (45 g/L) at 37 °C as described in the text. Error bars are standard deviations of triplicate runs.

***In Vitro* PAX Release and Cytotoxicity of Selected PAX-Loaded PNPs.** *In vitro* PAX release kinetics and cytotoxicity studies were conducted for five selected formulations discussed in the previous sections: three PCL(2.1k) formulations: Q = 200 μL/min and r = 0.10, 0.25 and 0.50; and two PCL(6.4k) formulations: r = 0.6, Q = 100 and 200 μL/min. The results of in vitro release kinetics are presented in Figure 5.6 and summarized in Table 5.3. The results for the cytotoxicity studies are presented in Figure 5.7 and also summarized in Table 5.3.

Figures 5.7 A and B report the *in vitro* PAX diffusional release profiles for the PCL(6.4k) and PCL(2.1k) formulations, respectively. In general, the PCL(6.4k) and PCL(2.1k) formulations exhibited complete diffusional PAX release within ~ 10 days. For the two PCL(6.4k) formulations, there was a general slowing of diffusional PAX release with increasing flow rate (Figure 5.7 A). The PCL(2.1k) formulations yield a general trend of slowing diffusional PAX release kinetics in the order of r = 0.25, 0.1 and finally 0.5 (Figure 5.7 B).

Next, we discuss the trends in *in vitro* diffusional PAX release, for the PCL(6.4k) formulation. The observed slowing in diffusional PAX release correlates well with increasing core crystallinity. For example, the PCL(6.4k) Q = 100 μL/min (Figure 5.7 A) formulation has a relatively quick PAX release which is correlated with relatively low PCL core crystallinity (Figure 5.5; blue triangles). Next, for the PCL(6.4k) Q = 200 μL/min formulation (Figure 5.7 A), the observed relatively slow diffusional PAX release is correlated with a relatively high PCL core crystallinity (Figure 5.5; green triangles). As discussed in previous chapters, increasing core crystallinity will increase the microviscosity of the nanoparticle core, leading to slower diffusion of encapsulated molecules and correspondingly slower release kinetics.[10,11,14,24]

We now discuss PAX release trends for the PCL(2.1k) formulation (Figure 5.6B). Without appropriate statistical analysis it is possible that the PAX release data presented in

Figure 5.6B shows no statistical change over the three different PCL(2.1k) PNP formulations. Nevertheless, unlike the PCL(6.4k) formulations, decreasing PAX diffusional release rates do not correlate with increasing core crystallinity (Figure 5.5; red circles). In fact, as a function of slowing diffusional PAX release, core crystallinity decreases and then increases. This result is an unexpected result. If core crystallinity was the major factor influencing PAX diffusional release, we would expect PCL crystallinity to increase with slowing diffusional release. Next we consider PNP core volume to understand the trend of slowing PAX diffusional release. The PCL(2.1k) formulations yield decreasing core dimensions (Table 5.3) with decreasing PAX release rate. This result is also counterintuitive to what is expected. Decreasing core dimensions should yield

faster diffusional release rates; because, of the shorter diffusional path lengths associated with smaller core dimensions. We speculate that PCL-*b*-PEO PNP hydrolytic degradation plays a major role in PAX release for this condition. We have previously explored the influence of PCL hydrolytic degradation in Chapters 2 and 3. Hydrolytic degradation is an alternative pathway, to diffusion, for PAX release from PCL-*b*-PEO PNPs.

Next we turn our attention to the PAX encapsulated PCL-*b*-PEO PNP cytotoxicity study (Figure 5.7). PAX antiproliferation activity was studied for the same five samples discussed above. The PNP samples were used to treat MCF-7 (human breast adenocarcinoma) cell lines for three time periods: 48, 72 and, 96 hours. Two control experiments exploring the potency of

Table 5.3 PCL Core Crystallinity, *In Vitro* Release τ – Half-Times, and Growth Inhibition$_{50}$ PAX Concentrations for Various PAX-loaded PCL-*b*-PEO PNP Formulations

Polymer Composition	Q (μL/min)	r	Morphology	$d_{h,eff}$ (nm)	χ_{PCL}	$\tau_{1/2}$ (hours)	Incubation Time (hours)	GI_{50} (x 10^3 ppm)
PCL(6.4k)	100	0.6	S	80 ± 10	7 ± 2	14	48	1.5 ± 0.4
							72	4.0 ± 1.0
							96	11 ± 6
PCL(6.4k)	200	0.6	S, C, L	3500 ± 300	18 ± 4	24	48	0.20 ± 0.06
							72	6.0 ± 0.8
							96	3.1 ± 0.7
PCL(2.1k)	200	0.1	V, S, L	1500 ± 300	7 ± 2	12	48	0.8 ± 0.1
							72	1.2 ± 0.4
							96	15 ± 3
PCL(2.1k)	200	0.25	S, RC	3300 ± 300	15 ± 2	10	48	0.30 ± 0.04
							72	1.6 ± 0.4
							96	3.6 ± 0.8
PCL(2.1k)	200	0.5	S, RC	2900 ± 300	12 ± 3	20	48	> 1
							72	1.0 ± 0.1
							96	0.9 ± 0.1
Free PAX							48	0.2 ± 0.05
							72	0.3 ± 0.08
							96	0.3 ± 0.08

empty PCL-*b*-PEO nanoparticles and unencapsulated PAX (free PAX) were carried out. The control experiment with empty PNPs yielded no significant cytotoxic response for all three time points; whereas, the free PAX study resulted in high antiproliferation activity for all three time points.

First, we report cytotoxicity results for the two PCL(6.4k) formulations (Figure 5.7 A). In general, both formulations have decreasing cytotoxicity with increasing incubation time. The Q = 100 μL/min condition (Figure 5.8; red bar) generally has a greater cytotoxic response compared to its Q = 200 μL/min counterpart (Figure 5.8; black bar).

Now we consider the cytotoxicity results for the three PCL(2.1k) formulations (Figure 5.7B). In general, the two low loading ratio formulations (r = 0.1 and 0.25) yield increasing GI_{50} PAX concentrations (Figure 5.8B, black and red bars), with increasing incubation time. On the other hand, the r = 0.50 formulation did not register 50% growth inhibition for the 48 hour experiment; nevertheless, after 48 hours the formulation yields high cytotoxicity with increasing incubation time.

Next, we discuss the cytotoxicity results for the two control experiments. The control study using drugless PNPs had an expected result. Empty PCL(6.4k) PNPs are expected to have a low cytotoxic response because, PCL-*b*-PEO is not toxic to cells. Next, the free PAX study also had an expected cytotoxic response (Figure 5.8). Administering PAX to cancer cells without PNPs ensures a high concentration of PAX is always readily available for metabolism by cells; resulting in high cytotoxicity.

Next we discuss the PAX-loaded PNP cytotoxicity results (Figure 5.8). When considering antiproliferation activity there are two mechanisms of PAX uptake into human epithelial cells: 1. PNP diffusional PAX release; 2. hydrolytic degradation of the nanoparticle;

and, 3. endocytosis of PAX encapsluated PNPs.[5,7,13,17,32-35] For cell lines such as MCF-7, endocytosis is limited to particles < 200 nm in diameter.[36-40] If we consider the PCL(6.4k) samples, the Q = 100 μL/min condition was composed of pure spheres (Figure 5.4 D) and the Q = 200 μL/min condition was composed of spheres, cylinders and lamellae (Figure 5.4 H). Both samples have different trends in cytotoxicity (Figure 5.8). For the Q = 100 μL/min samples, the spherical PNPs are < 200 nm (Figure 5.4 D; Table 5.2); therefore, they may be able to administer PAX through both diffusional release and endocytosis. On the other hand, the Q = 200 μL/min (Figure 5.4 H) formulation will have morphologies that can administer PAX either through diffusional release and endocytosis (spherical PNPs), or only through diffusional release (cylinders and lamellae). Therefore, when considering the reported trends in PAX-loaded PNP cytotoxicity (Figure 5.8), the polydisperse nature of the PAX-loaded PNP morphologies renders it difficult to elucidate the exact mechanisms responsible for PAX uptake and MCF-7 cytotoxicity.

In the context of this dissertation, the difficulties in understanding the mechanisms of PAX uptake into our breast cancer cell lines fails to address whether or not microfluidic-tuned PNP structure is effective in biological environments. To solve this problem, further experiments need to be conducted where only pure PNP morphologies are assembled, and their core crystallinity is adjusted using flow rate; therefore, systematically studying the influence microfluidic-tuned PNP structure on PNP function within living cells. Also, currently there are ANOVA statistical tests of our cytotoxicity data (Figure 5.8) and further cytotoxicity studies that are being conducted in our lab.

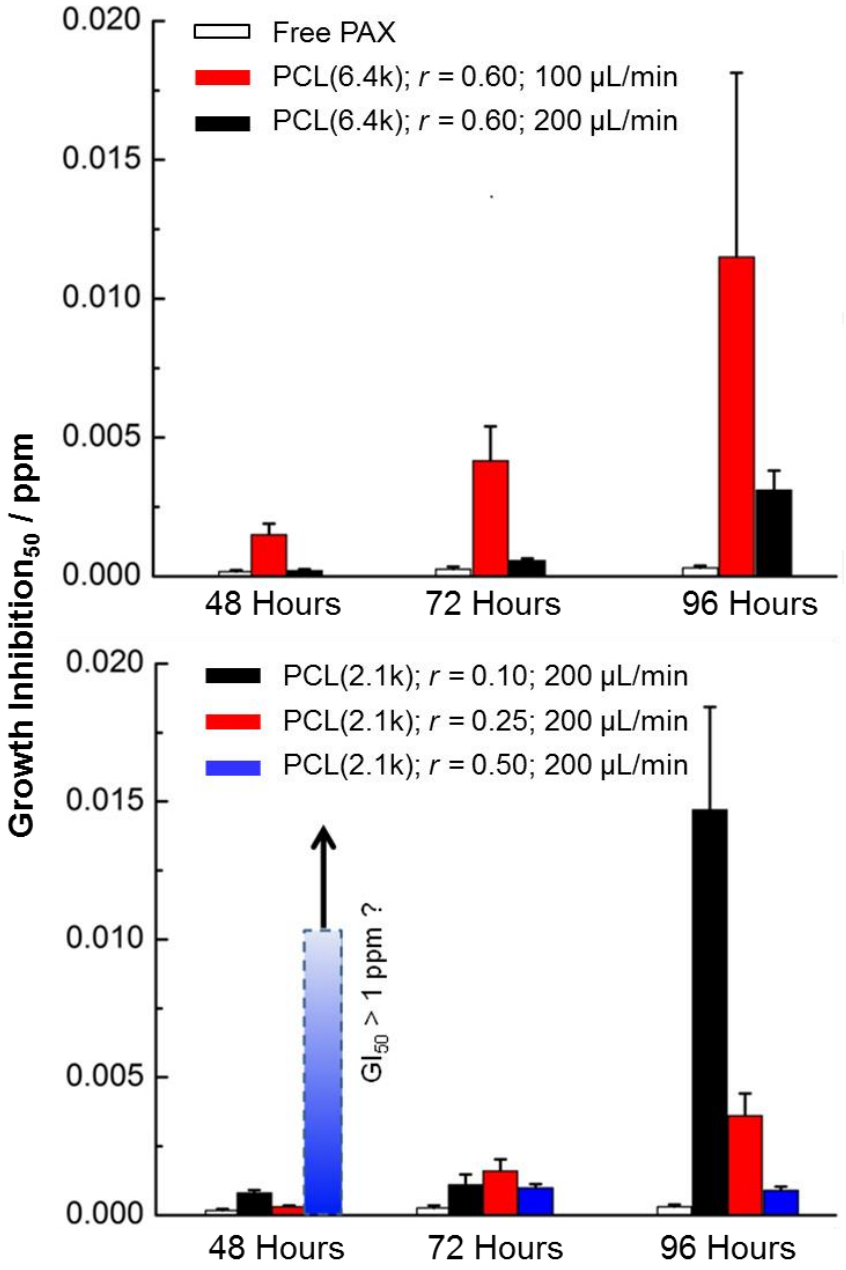

Figure 5.8 Effect of copolymer composition, flow-rate, and initial drug-to-copolymer loading ratio of PAX-loaded PCL-*b*-PEO PNPs on Growth Inhibition of MCF-7 breast cancer cells. The dashed column in B represents a sample which did not register a GI_{50} reading within the tested PAX concentrations.

5.4 Conclusion

In this chapter we investigated the influence of flow rate, copolymer composition and initial drug loading ratio on PCL-*b*-PEO PNP structure and function. An important difference in this chapter compared to the others is the high PAX loading ratios ($r > 0.1$) that were utilized.

We first explored the effect of flow rate and copolymer composition on PAX-loaded PCL-*b*-PEO structure. Results indicated a strong dependence of PNP size and morphology on flow rate and core crystallinity. Next, we explored the effect of initial drug loading ratio and flow rate on PCL(2.1k) and PCL(6.4k) based PAX-loaded PNP structure and function. Results indicated that core crystallinity was a major factor influencing PNP morphology and PAX loading efficiency. For example, formulations with high core crystallinity correlated with low curvature morphologies and relatively lower PAX loading efficiencies. These results enlarge our understanding of how copolymer composition, initial drug loading ratio and flow-induced factors such as: coalescence, breakup and crystallization; influence PNP structure and function at high drug loading ratios.

We also explored the effect of flow rate, initial drug loading ratio and copolymer composition on PAX-loaded PCL(2.1k) and PCL(6.4k) PNP *in vitro* diffusional PAX release and cytotoxicity. Results indicated a strong effect of flow rate and an indiscernible effect of initial drug loading ratio on diffusional PAX release. As for the cytotoxicity studies, due to the polydisperse nature of the PAX-loaded PNP morphologies, it was difficult to elucidate the exact influence of microfluidic-preparation on PNP cytotoxicity. Therefore, further studies need to be conducted where we only use PNPs with pure morphologies for cytotoxicity experiments.

In general, this study enlarges our understanding of microfluidic-preparation of PAX loaded PNPs using high drug loading ratios ($r > 0.1$). For example, we better understand the

effect of PCL block length and flow rate on PNP structure and function in the context of high PAX loading ratios. A critical difference between this chapter and Chapter 4 is that at high loading ratios PCL crystallinity is a major factor driving PNP structure and function; whereas, in Chapter 4 PCL block length and flow rate were major factors influencing PNP structure and function. The results of this study set the stage for further microfluidic studies focusing on PNP cytotoxicity. Future cytotoxicity studies should focus on microfluidic-preparation of PNPs with pure morphologies. Due to the complex nature of the interactions between PNPs and cancer cells, formulations consisting of pure morphologies would allow for the narrowing of possible factors influencing PNP function in the context of cell line studies; therefore, increasing our understanding of microfluidic control on PNP cytotoxic response. In future cytotoxicity studies, if we can use microfluidics to successfully vary and understand PNP cytotoxic response; we can then apply our microfluidic platform for the assembly of PNPs for *in vivo* studies.

5.5 References

(1) Zhang, Y.; Chan, H. F.; Leong, K. W. Advanced materials and processing for drug delivery: The past and the future. *Adv. Drug Deliv. Rev.* **2013**, *65*, 104-120.

(2) Ahmad, Z.; Shah, A.; Siddiq, M.; Kraatz, H.-B. Polymeric PNPs as drug delivery vehicles. *RSC Advances* **2014**, *4*, 17028-17038.

(3) Eetezadi, S.; Ekdawi, S. N.; Allen, C. The challenges facing block copolymer PNPs for cancer therapy: In vivo barriers and clinical translation. *Adv. Drug Deliv. Rev.* **2015**, *91*, 7-22.

(4) Hickey, J. W.; Santos, J. L.; Williford, J. M.; Mao, H. Q. Control of polymeric nanoparticle size to improve therapeutic delivery. *J. Controlled Release* **2015**, *219*, 536-547.

(5) Kataoka, K.; Harada, A.; Nagasaki, Y. Block copolymer PNPs for drug delivery: design, characterization and biological significance. *Adv. Drug Deliv. Rev.* **2001**, *47*, 113-131.

(6) O'Reilly, R. K.; Hawker, C. J.; Wooley, K. L. Cross-linked block copolymer PNPs: functional nanostructures of great potential and versatility. *Chem. Soc. Rev.* **2006**, *35*, 1068-1083.

(7) Sutton, D.; Nasongkla, N.; Blanco, E.; Gao, J. M. Functionalized micellar systems for cancer targeted drug delivery. *Pharm. Res.* **2007**, *24*, 1029-1046.

(8) Elsabahy, M.; Wooley, K. L. Design of polymeric nanoparticles for biomedical delivery applications. *Chem. Soc. Rev.* **2012**, *41*, 2545-2561.

(9) Mai, Y. Y.; Eisenberg, A. Self-assembly of block copolymers. *Chem. Soc. Rev.* **2012**, *41*, 5969-5985.

(10) Liggins, R. T.; Burt, H. M. Paclitaxel loaded poly(L-lactic acid) microspheres: properties of microspheres made with low molecular weight polymers. *Int. J. Pharm.* **2001**, *222*, 19-33.

(11) Liggins, R. T.; Burt, H. M. Paclitaxel loaded poly(l-lactic acid) (PLLA) microspheres: II. The effect of processing parameters on microsphere morphology and drug release kinetics. *Int. J. Pharm.* **2004**, *281*, 103-106.

(12) Aliabadi, H. M.; Brocks, D. R.; Mahdipoor, P.; Lavasanifar, A. A novel use of an in vitro method to predict the in vivo stability of block copolymer based nano-containers. *J. Controlled Release* **2007**, *122*, 63-70.

(13) Letchford, K.; Burt, H. A review of the formation and classification of amphiphilic block copolymer nanoparticulate structures: PNPs, nanospheres, nanocapsules and polymersomes. *Eur. J. Pharm. Biopharm.* **2007**, *65*, 259-269.

(14) Letchford, K.; Liggins, R.; Wasan, K. M.; Burt, H. In vitro human plasma distribution of nanoparticulate paclitaxel is dependent on the physicochemical properties of poly(ethylene glycol)-*block*-poly(caprolactone) nanoparticles. *Eur. J. Pharm. Biopharm.* **2009**, *71*, 196-206.

(15) Cai, S.; Vijayan, K.; Cheng, D.; Lima, E.; Discher, D. E. PNPs of Different Morphologies—Advantages of Worm-like FiloPNPs of PEO-PCL in Paclitaxel Delivery. *Pharm. Res.* **2007**, *24*, 2099-2109.

(16) Geng, Y. D., P.; Cai, S.; Tsai, R.; Tewari, M.; Minko, T.; Discher, D.E. Shape effects of filaments versus spherical particles in flow and drug delivery. *Nat. Nanotechnol.* **2007**, *2*, 249-255.

(17) Venkataraman, S.; Hedrick, J. L.; Ong, Z. Y.; Yang, C.; Ee, P. L. R.; Hammond, P. T.; Yang, Y. Y. The effects of polymeric nanostructure shape on drug delivery. *Adv. Drug Deliv. Rev.* **2011**, *63*, 1228-1246.

(18) Glover, A. L.; Nikles, S. M.; Nikles, J. A.; Brazel, C. S.; Nikles, D. E. Polymer PNPs with Crystalline Cores for Thermally Triggered Release. *Langmuir* **2012**, *28*, 10653-10660.

(19) Oltra, N. S.; Swift, J.; Mahmud, A.; Rajagopal, K.; Loverde, S. M.; Discher, D. E. FiloPNPs in nanomedicine - from flexible, fragmentable, and ligand-targetable drug carrier designs to combination therapy for brain tumors. *J. Mater. Chem. B.* **2013**, *1*, 5177-5185.

(20) Wang, C.-W.; Sinton, D.; Moffitt, M. G. Flow-Directed Block Copolymer PNP Morphologies via Microfluidic Self-Assembly. *J. Am. Chem. Soc.* **2011**, *133*, 18853-18864.

(21) Wang, C.-W.; Bains, A.; Sinton, D.; Moffitt, M. G. Flow-Directed Assembly of Block Copolymer Vesicles in the Lab-on-a-Chip. *Langmuir* **2012**, *28*, 15756-15761.

(22) Wang, C.-W.; Bains, A.; Sinton, D.; Moffitt, M. G. Flow-Directed Loading of Block Copolymer PNPs with Hydrophobic Probes in a Gas–Liquid Microreactor. *Langmuir* **2013**, *29*, 8385-8394.

(23) Wang, C.-W.; Sinton, D.; Moffitt, M. G. *ACS Nano* **2013**, *7*, 1424-1436.

(24) Bains, A.; Cao, Y.; Moffitt, M. G. Multiscale Control of Hierarchical Structure in Crystalline Block Copolymer Nanoparticles Using Microfluidics. *Macromol. Rapid Commun.* **2015**, n/a-n/a.

(25) Xu, Z.; Yan, B.; Riordon, J.; Zhao, Y.; Sinton, D.; Moffitt, M. G. Microfluidic Synthesis of Photoresponsive Spool-Like Block Copolymer Nanoparticles: Flow-Directed Formation and Light-Triggered Dissociation. *Chem. Mater.* **2015**, *27*, 8094-8104.

(26) Kong, F.; Zhang, X.; Hai, M. T. Microfluidics Fabrication of Monodisperse Biocompatible Phospholipid Vesicles for Encapsulation and Delivery of Hydrophilic Drug or Active Compound. *Langmuir* **2014**, *30*, 3905-3912.

(27) Lim, J.-M.; Swami, A.; Gilson, L. M.; Chopra, S.; Choi, S.; Wu, J.; Langer, R.; Karnik, R.; Farokhzad, O. C. Ultra-High Throughput Synthesis of Nanoparticles with Homogeneous Size Distribution Using a Coaxial Turbulent Jet Mixer. *ACS Nano* **2014**, *8*, 6056-6065.

(28) Wang, W.; Zhang, M. J.; Chu, L. Y. Functional Polymeric Microparticles Engineered from Controllable Microfluidic Emulsions. *Acc. Chem. Res.* **2014**, *47*, 373-384.

(29) Cuong, N.-V.; Li, Y.-L.; Hsieh, M.-F. Targeted delivery of doxorubicin to human breast cancers by folate-decorated star-shaped PEG-PCL PNP. *J. Mater. Chem.* **2012**, *22*, 1006-1020.

(30) Massey, J.; Power, K. N.; Manners, I.; Winnik, M. A. Self-assembly of a novel organometallic-inorganic block copolymer in solution and the solid state: Nonintrusive observation of novel wormlike poly(ferrocenyldimethylsilane)-*b*-poly(dimethylsiloxane) PNPs. *J. Am. Chem. Soc.* **1998**, *120*, 9533-9540.

(31) Massey, J. A.; Temple, K.; Cao, L.; Rharbi, Y.; Raez, J.; Winnik, M. A.; Manners, I. Self-assembly of organometallic block copolymers: The role of crystallinity of the core-forming polyferrocene block in the micellar morphologies formed by poly(ferrocenylsilane-*b*-dimethylsiloxane) in n-alkane solvents. *J. Am. Chem. Soc.* **2000**, *122*, 11577-11584.

(32) Wang, X.; Guerin, G.; Wang, H.; Wang, Y.; Manners, I.; Winnik, M. A. Cylindrical Block Copolymer PNPs and Co-PNPs of Controlled Length and Architecture. *Science* **2007**, *317*, 644-647.

(33) Rejman, J.; Oberle, V.; Zuhorn, IS.; Hoekstra, D. Size-dependent internalization of particles via the pathways of clathrin-and caveolae-mediated endocytosis. *Biochem. J.* **2004**, 377, 159-169

(34) Xintao, S.; Hua, A.; Nasongkla, N.; Saejeong, K.; Jinming, G. Micellar carriers based on block copolymers of poly(ε-caprolactone) and poly(ethylene glycol) for doxorubicin delivery. *J. Controlled Release.* **2004**, 98, 415-426

(35) Hu, Y.; Xie, JW.; Tong, YW,; Wang, CH. Effect of PEG conformation and particle size on the cellualr uptake effiency of nanoparticles with the HepG2 cells. *J. Controlled Release.* **2007**, 118, 7-17

(36) Ehrlich, M. Endocytosis by random initiation and stablization of clartrin-coated pits. *Cell*. 2004 118, 591-605

(37) Cureton, D.K.; Massol, R.H.; Saffarian, S.; Kirchhausen, T.L. Vesicular stomatitis virus enters cells through vesicles incompletley coated with clarthrin that depend upon actin for internalization. *PLoS Pathog*. **2009**, 5, e1000394

(38) Dhonukshe, P. Clarthrin-mediated constitutive endocytosis of PIN auxin efflux carriers in Arabidopsis. *Curr. Biol.* **2007**, 17, 520-527

(39) Smazynska-de Rooji, I. A role for the dynamin-like protein Vps1 during endocytosis of yeast. *J. Cell Sci.* **2010**, 123, 3496-3506

(40) Bretscher, M.S.; Thomson, J.N.; Pearse, B.M. Coated pits act as moleuclar filters. *Proc. Natl Acad. Sci.* **1980**, 77, 4156-4159

Chapter 6
Conclusions and Future Directions

6.1 Conclusion

In this dissertation we presented a two-phase microfluidic platform for the controlled synthesis of block copolymer based drug delivery nanoparticles. Microfluidics provides the added advantage, over their conventional self-assembly counterparts, of fast and efficient screening of various parameters influencing PNP structure and function. We use two-phase microfluidics to demonstrate the influence of flow-variable shear, along with other chemical parameters (copolymer composition, water content, and, initial drug loading ratio), on structure and function of drug-loaded biocompatible, semicrystalline polymeric nanoparticles (PNPs). The effect of high shear on block copolymer self-assembly has been investigated previously in our group;[1,2] however, for this dissertation we move away from a model system and investigates a medically relevant formulation. The formulation investigated in this dissertation is poly(ε-caprolactone)-*b*-poly(ethylene oxide) (PCL-*b*-PEO) nanoparticles with the encapsulated hydrophobic chemotherapeutic agent, paclitaxel (PAX). We use PCL-b-PEO as our polymer material for PNP development because of its biocompatible, semicrystalline nature, and its established use in drug delivery formulations.[4,5] Also, we use the anticancer drug, PAX, because, it is a well-known drug that has been used in many commercially available formulations, and, it has a high affinity for PCL. The following paragraphs are organized by themes covered in this dissertation.

One aspect of microfluidic drug delivery formulation development we tested in this dissertation is the influence of flow-variable shear on PNP size, and morphology. In Chapter 2, we studied the influence of flow-variable shear on the structure of drugless and PAX-loaded PCL-*b*-PEO nanoparticles. In this study we were able to reproducibly vary PCL-b-PEO size and morphology (with and without encapsulated PAX), simply by adjusting flow rate. One critical

piece of information we learned from this study is the influence of flow-variable shear in fine-tuning PNP morphology. In Chapter 3, we demonstrated the influence of flow-variable shear on DiI-loaded PCL-b-PEO PNPs; resulting in the manufacture of low curvature structures with increasing flow rate. This study helped us understand the applicability of two-phase microfluidics in controlling PNP structure with different encapsulated lipophilic molecules. In Chapter 5, we applied flow-variable shear to control PAX-loaded PNP size and morphology in the context of high drug loading ratios ($r > 0.1$). A key outcome for this study was, the ability of our microfluidic chip to reproducibly vary PCL-*b*-PEO size and morphology, simply by changing flow rate; however, with high concentrations of drug, we found that core crystallinity was a major driving force for PNP size and morphology.

Next, we explored the influence of flow rate on PCL core crystallinity. In Chapter 2, we were able to demonstrate the linear trend in PCL core crystallinity with increasing flow rate for drugless and PAX encapsulated PCL-*b*-PEO PNPs. For this study we postulated that flow-induced crystallization was a major factor in increasing core crystallinity with increasing flow rate. We then tested this hypothesis again in Chapter 3, by studying the dependence of core crystallinity on flow rate for DiI-loaded PCL-b-PEO PNPs. In this study we discovered the same linear trend of core crystallization with increasing flow rate. Furthermore, in Chapter 3, we also studied the influence of water concentration (chemical parameter), in conjunction with flow rate, on PCL core crystallinity. In general, higher water contents led to higher PCL core crystallinity when compared to lower water contents; a critical outcome for this chapter was that flow-induced crystallization was still a major factor influencing PCL core crystallinity even when self-assembly was conducted under different chemical environments. In Chapter 5, we studied the influence of flow-variable shear on PCL core crystallinity in the context of high drug load ratios.

A critical outcome for this chapter was that at high drug loading ratios, PAX encapsulation within the PCL core attenuated core crystallinity. Even though we were still able to reproducibly vary core crystallinity with flow rate, increasing PAX encapsulation levels had a major attenuation effect on core crystallinity; therefore, the previously observed linear trend in core crystallinity with increasing flow rate (Chapter 2 – 4) was not observed in Chapter 5. A critical outcome of this study was that with high loading ratios, PAX molecules had a greater influence on disrupting PCL core crystallinity than at low loading ratios (Chapters 2 and 4).

In this dissertation, we also explored how drug loading level and copolymer block composition influence PNP structure (size, morphology and core crystallinity) for microfluidic-prepared PAX-loaded PCL-*b*-PEO PNPs. In Chapter 4, we explored how varying PCL block length in conjunction with flow rate influenced PAX-loaded PNP size, morphology and crystallinity. In general, we found that higher molecular weight PCL blocks had a tendency to form high aggregation number morphologies (cylinders and lamellae) with associated high core crystallinity. On the other hand, we found that if we self-assembled our nanoparticles under high enough flow rates, we could tune PNP morphologies towards spheres. A prime example of this control was demonstrated using the PCL(12k) formulation, where low flow rates resulted in spheres, cylinders and lamellae and high core crystallinity (Q < 200 μL/min); however, when we increased flow rate to Q = 200 μL/min, we were able to tune nanoparticle morphology towards spherical morphologies with lower core crystallinity. Key outcomes for this chapter were the understanding of how PCL block length and flow rate can be used in conjunction to provide chemical and mechanical handles, respectively, for fine-tuning PNP structural properties. In Chapter 5, we explored how copolymer composition and flow rate influence PAX-loaded PNP structure in the context of high drug loading ratios. We found that at high drug loading ratios,

PCL core crystallinity was the major driving force for PNP size and morphology. In general, higher flow rates and longer PCL blocks resulted in PNPs with high core crystallinity; however, drops in crystallinity correlated with the formation of low aggregation number morphologies (spheres), and increases in crystallinity correlated with the formation of high aggregation number morphologies. The results in this chapter demonstrated, that an effective way to control PNP structure at high flow rates is through control of PNP core crystallinity.

Next we will discuss the influence of PNP structure on small molecule loading efficiency. In general, in the regime of low loading levels ($r \leq 0.01$), PNP morphology and flow rate were the major factors influencing small molecule loading efficiencies. For example, in Chapter 2 increasing flow rate resulted in the production of high aggregation number morphologies which correlated with high PAX loading efficiencies. Furthermore, in Chapter 3, we report a similar trend in loading efficiency as to what was observed in Chapter 2. Increasing flow rate resulted in the production of high aggregation number morphologies which resulted in higher DiI loading efficiencies. Again, this trend was observed in Chapter 4, where the presence of cylinders and lamellae were correlated to high PAX loading efficiency and spherical PNPs correlated with low PAX loading efficiencies. On the other hand, in Chapter 5, we found that core crystallinity was the major factor driving PAX loading efficiency. For example, increases in core crystallinity correlated with low PAX loading efficiency and low core crystallinity correlated with high PAX loading efficiency. Nevertheless, in this chapter we were able to achieve PAX loading efficiencies that are on par with what has been recently observed in literature for microfluidic-prepared formulations. For example, we were able to achieve PAX loading efficiencies of up to 22% with associated initial drug loading ratios of $r = 0.5$.

In this dissertation we also explored how PNP structure influences diffusional release and cytotoxicity. In general, increasing core crystallinity correlated with slowing diffusional release of encapsulated small molecule cargo. For example, in Chapter 2, we report that increasing core crystallinity correlates with slowing PAX diffusional release. Furthermore, in Chapter 3 we report a similar result; increasing core crystallinity was an effective tool in slowing diffusional DiI release. This trend also held for Chapters 4 and 5, as increasing core crystallization generally correlated with slowing diffusional PAX release. In general, diffusional PAX release studies enlarged our understanding on how core crystallinity influences PAX diffusional release. As for the cytotoxicity studies, this dissertation takes a good first step in exploring how microfluidics can be used to vary the cytotoxic response of PAX-loaded PNPs. In Chapter 5, we found that we were able to vary cytotoxic response of microfluidic-prepared PAX-loaded PNPs by adjusting flow rate; however, due to the complex interactions between our PNPs and the MCF-7 cancer cell line, further studies need to be conducted to accurately elucidate the exact influence of flow-variable shear, and copolymer composition on cytotoxicity.

6.2 Future Directions

An important future step in developing this PAX-loaded PCL-*b*-PEO formulation is animal studies. *In vivo* studies are an important next step because they will provide information on whether flow rate is a viable control mechanism (through flow-induced particle coalescence, breakup and crystallization) for formulation development with *in vivo* applications[3-5]. A challenge that needs to be overcome before these experiments can proceed is the polydisperse composition of morphologies present in our current formulations. Large nanoparticles, such as lamellae, would not be suitable for *in vivo* experiments because they will be filtered out by the

reticuloendothelial system[6]**.** One way to overcome this problem is to is to use flow rate to tune PNP structure towards pure morphologies. The studies in this dissertation lay the ground work for these future studies, as we have a greater understanding of how flow rate in conjunction with various chemical parameters (copolymer compositon, water concentration, and intial drug loading ratio) influence PNP size, morphology and core crystallinity. Furthermore, another way to work around this problem is to conduct post self-assembly workup procedures, where aggregates of different morphologies are filtered by size. Size filtration of particles will ensure that formulations are composed of pure morphologies.

Increasing throughput for our current microfluidic system is another avenue of research that needs to be investigated. With the current PDMS material, the fastest on-chip flow rates possible are ~ 400 μL/min. If we run this current version of our chip at maximum rate for 24 hours, we can only collect ~2 g of PNPs. Other groups, such as Langer *et al*[7,8] have been able to utilize single phase systems with high throughput, collecting ~3 kg of sample per day. A drawback of high flow rates, for our current PDMS chips, is the increase in pressure within the microchannel walls which delaminates the chip. To obtain competitive throughput, one solution would be to switch materials from PDMS to glass. Glass microchips would allow for higher pressures within the microchannels, increasing throughput. A drawback to using glass is the need for clean room facilities to etch and fabricate the microchips. Clean rooms are not always readily available and are more costly to operate than a traditional lab. Another way to increase throughput is through utilizing multiple microfluidic chips setup in parallel. Many groups have worked on this strategy, as it provides an easy way to scale up throughput while maintaining high reproducibility.[9]

In general, this dissertation provides a glimpse into two-phase microfludicis as a platform for formulation development. We were able to demonstrate that microfluidics allows for the fast and efficient screening of multiple parameters (flow rate, copolymer composition and initial drug loading ratio) influencing PNP structure and function. We systematically explored the influence of flow rate, copolymer composition and initial drug loading ratio on PCL-*b*-PEO structure and function. Viable future directions for this work include further cytotoxicity studies, to garner a greater understanding on how microfluidic-prepared PNPs interact with live biological environments; eventually culminating in animal studies and perhaps future clinical trials.

6.3 References

(1) Wang, C.-W.; Sinton, D.; Moffitt, M. G. Flow-Directed Block Copolymer PNP Morphologies via Microfluidic Self-Assembly. *J. Am. Chem. Soc.* **2011**, *133*, 18853-18864.

(2) Wang, C.-W.; Bains, A.; Sinton, D.; Moffitt, M. G. Flow-Directed Loading of Block Copolymer PNPs with Hydrophobic Probes in a Gas–Liquid Microreactor. *Langmuir* **2013**, *29*, 8385-8394.

(3) Zhang, Y.; Chan, H. F.; Leong, K. W. Advanced materials and processing for drug delivery: The past and the future. *Adv. Drug Deliv. Rev.* **2013**, *65*, 104-120.

(4) Ahmad, Z.; Shah, A.; Siddiq, M.; Kraatz, H.-B. Polymeric PNPs as drug delivery vehicles. *RSC Advances* **2014**, *4*, 17028-17038.

(5) Hickey, J. W.; Santos, J. L.; Williford, J. M.; Mao, H. Q. Control of polymeric nanoparticle size to improve therapeutic delivery. *J. Controlled Release* **2015**, *219*, 536-547.

(6) Eetezadi, S.; Ekdawi, S. N.; Allen, C. The challenges facing block copolymer PNPs for cancer therapy: In vivo barriers and clinical translation. *Adv. Drug Deliv. Rev.* **2015**, *91*, 7-22.

(7) Karnik, R.; Gu, F.; Basto, P.; Cannizzaro, C.; Dean, L.; Kyei-Manu, W.; Langer, R.; Farokhzad, O. C. Microfluidic platform for controlled synthesis of polymeric nanoparticles. *Nano Lett.* **2008**, *8*, 2906-2912.

(8) Lim, J.-M.; Swami, A.; Gilson, L. M.; Chopra, S.; Choi, S.; Wu, J.; Langer, R.; Karnik, R.; Farokhzad, O. C. Ultra-High Throughput Synthesis of Nanoparticles with Homogeneous Size Distribution Using a Coaxial Turbulent Jet Mixer. *ACS Nano* **2014**, *8*, 6056-6065.

(9) Vladisavljevic, G. T.; Khalid, N.; Neves, M. A. Industrial lab-on-a-chip: Design, applications and scale-up for drug discovery and delivery. *Adv. Drug Deliv. Rev.* **2013**, 65, 1626-1663

Appendix I

Table 7.1 Morphologies[a] and Mean Dimensions[b] for PCL-*b*-PEO Nanoparticles Prepared in the Segmented Microfluidic Reactor at Various Water Contents and Flow Rates.

Water Content (cwc + *x* wt %)	5 µL/min	25 µL/min	50 µL/min	100 µL/min
2	S (39 ± 8 nm) + C (19 ± 1 nm) + L	V (11 ± 4 nm)	S (31 ± 5 nm)	S (27 ± 3 nm) + C (26 ± 10 nm)
5	S (20 ± 2 nm)	V (32 ± 10)	S (40 ± 7 nm) + C (25 ± 6 nm) + L	C (19 ± 3 nm) + L
10	S (22 ± 2 nm)	S (32 ± 1 nm) + C (17 ± 1 nm) + L	V (5 ± 1 nm)	S (28 ± 1 nm)

a) Prominent morphologies are indicated as S (spheres), C (cylinders or filoPNPs), L (lamellae) and V (vesicles or polymersomes).

b) Numbers in brackets refer to the following characteristic mean dimensions for various morphologies: spheres (diameters) and cylinders (widths), and vesicles (wall thicknesses). Experimental errors are standard deviations of mean values determined for three replicate preparations.

bulk	25 µL/min	50 µL/min	100 µL/min
S (57 ± 12 nm) + L	S (33 ± 6 nm) + L	S (38 ± 6 nm) + C (20 ± 1 nm)	S (28 ± 1 nm) + C (17 ± 1 nm) + L

Table 7.2 Morphologies[a] and Mean Dimensions[b] for PAX-loaded PCL-*b*-PEO Nanoparticles Prepared by the Bulk Method and in the Segmented Microfluidic Reactor at cwc + 5 wt % and Various Flow Rates.

a) Prominent morphologies are indicated as S (spheres), C (cylinders or filoPNPs), and L (lamellae).

b) Numbers in brackets to the following characteristic mean dimensions for various morphologies: spheres (diameters) and cylinders (widths). Experimental errors are standard deviations of mean values determined for three replicate preparations.

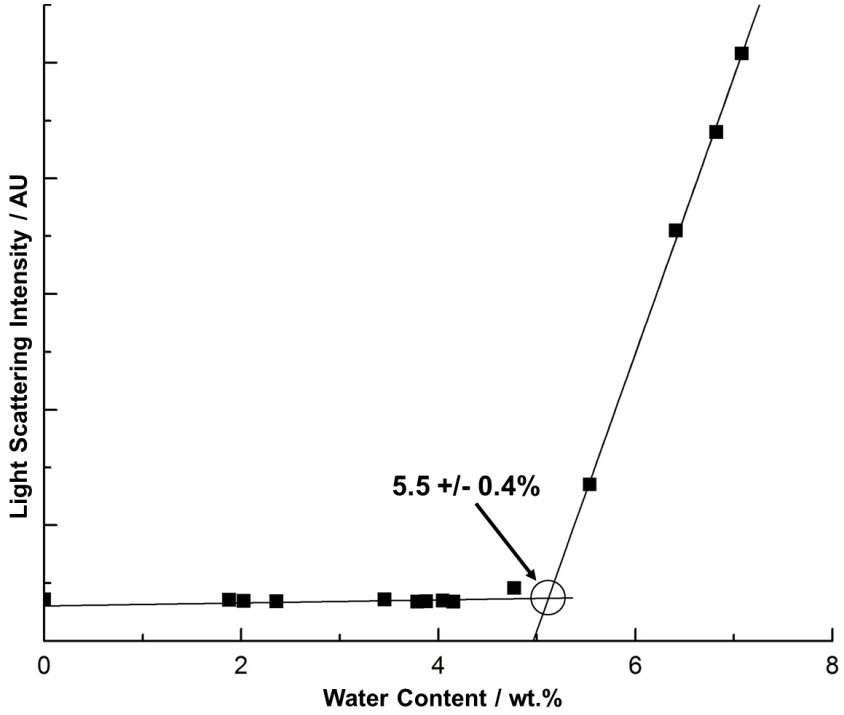

Figure 7.1 Critical water concentration (cwc) determination of 0.33 wt % PCl-*b*-PEO in DMF using the static light scattering method. The cwc determined from the above data is 5.5 ± 0.4 wt % as shown.

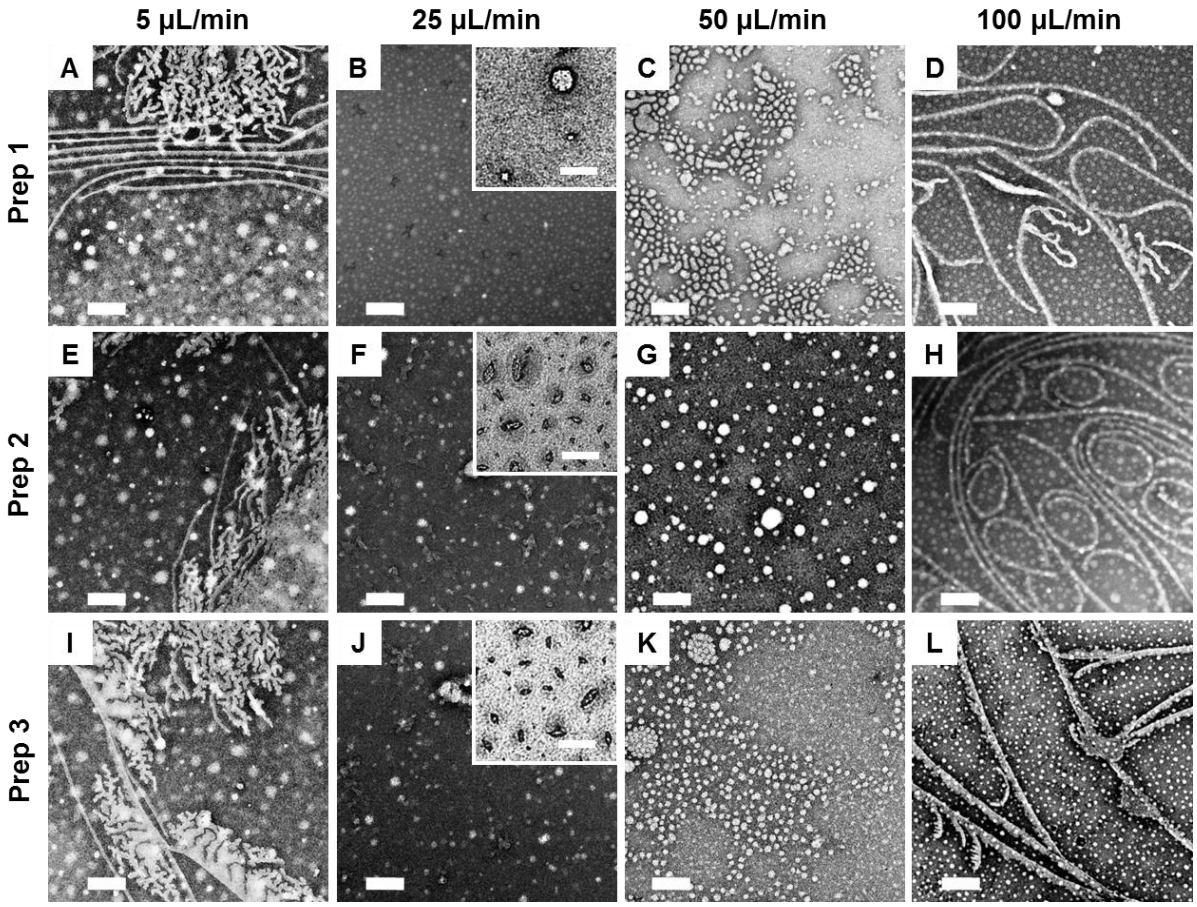

Figure 7.2 TEM images demonstrating reproducibility of flow-directed PCL-*b*-PEO morphologies over three replicate on-chip preparations at a water content of cwc + 2 wt % and various flow rates. Insets are unstained images allowing visualization of the internal lumen of vesicles. Scale bars are 200 nm in the main images and 100 nm in the insets.

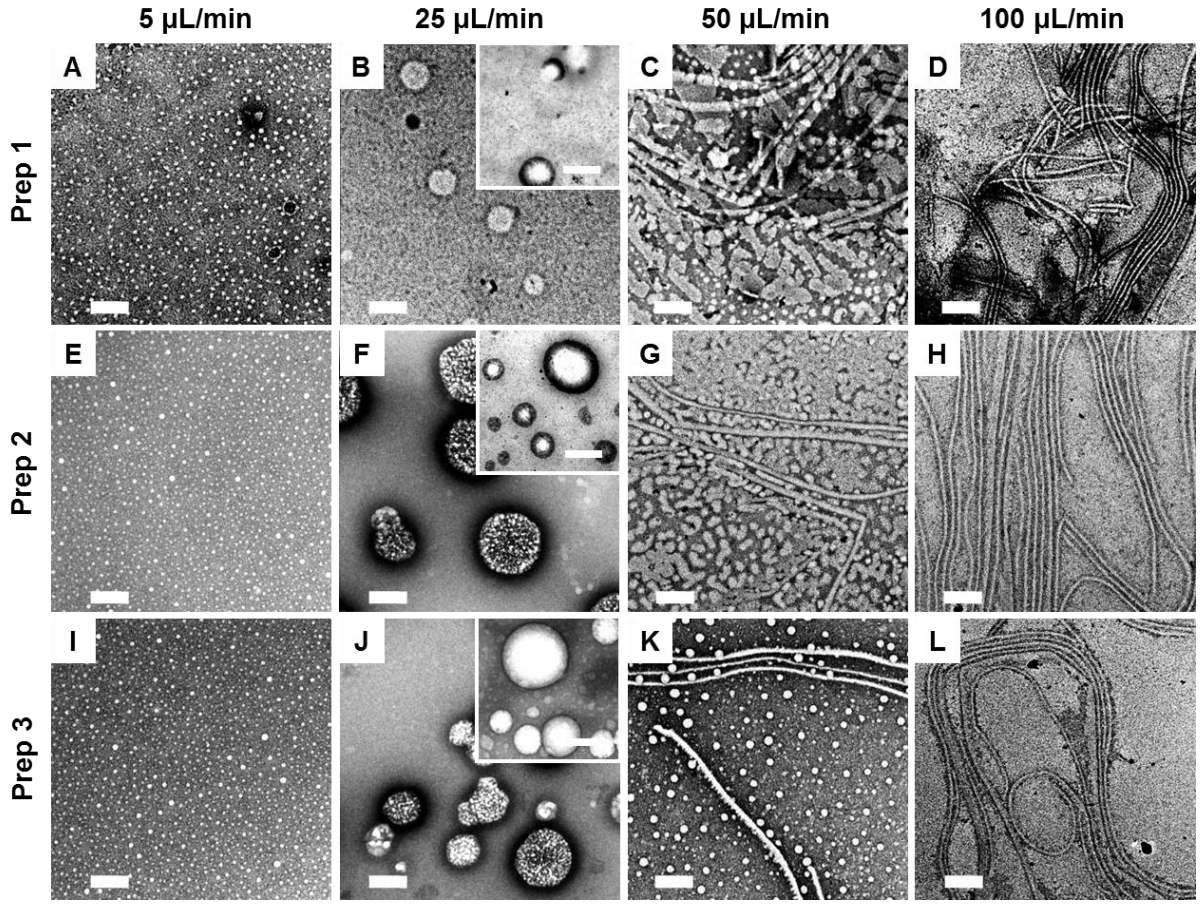

Figure 7.3 TEM images demonstrating reproducibility of flow-directed PCL-*b*-PEO morphologies over three replicate on-chip preparations at a water content of cwc + 5 wt % and various flow rates. Insets are unstained images allowing visualization of the internal lumen of vesicles. Scale bars are 200 nm in the main images and 100 nm in the insets.

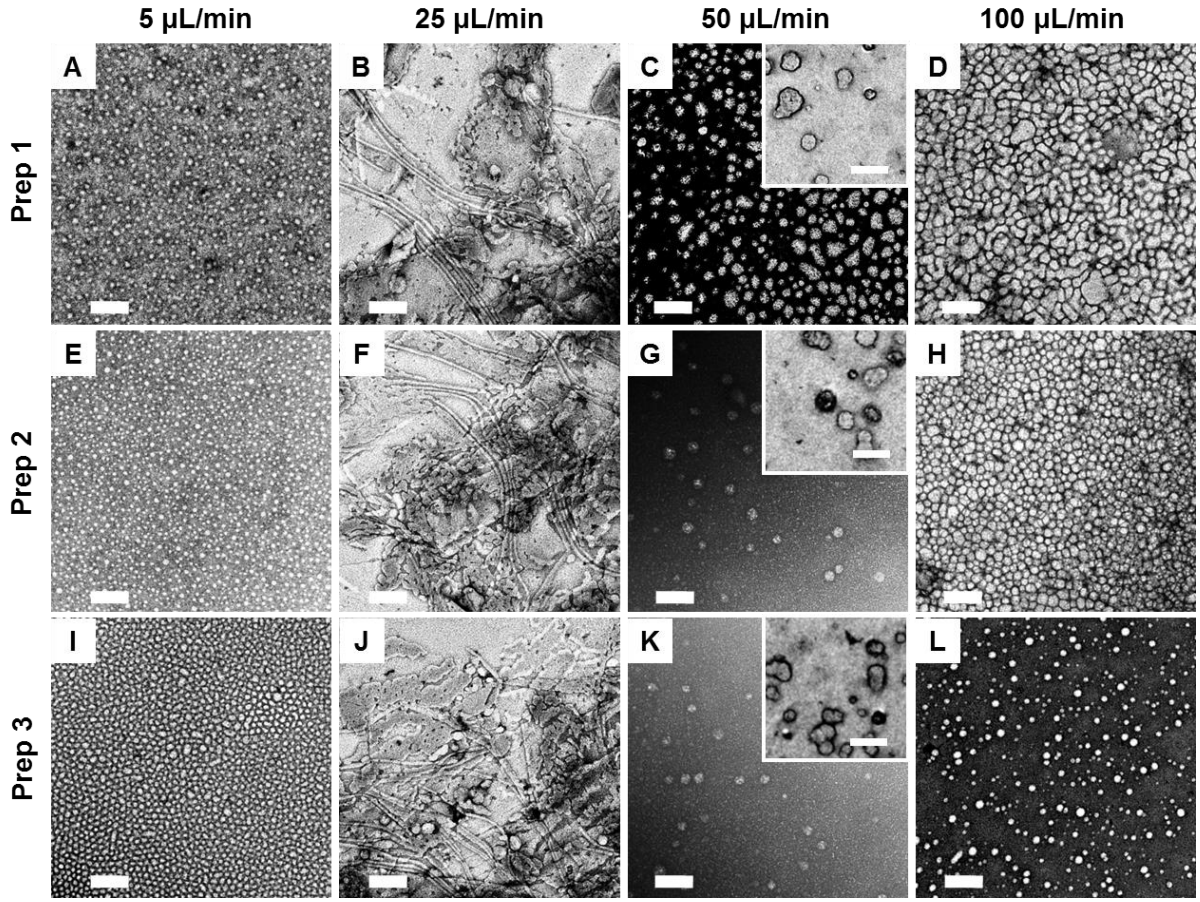

Figure 7.4 TEM images demonstrating reproducibility of flow-directed PCL-*b*-PEO morphologies over three replicate on-chip preparations at a water content of cwc + 10 wt % and various flow rates. Insets are unstained images allowing visualization of the internal lumen of vesicles. Scale bars are 200 nm in the main images and 100 nm in the insets.

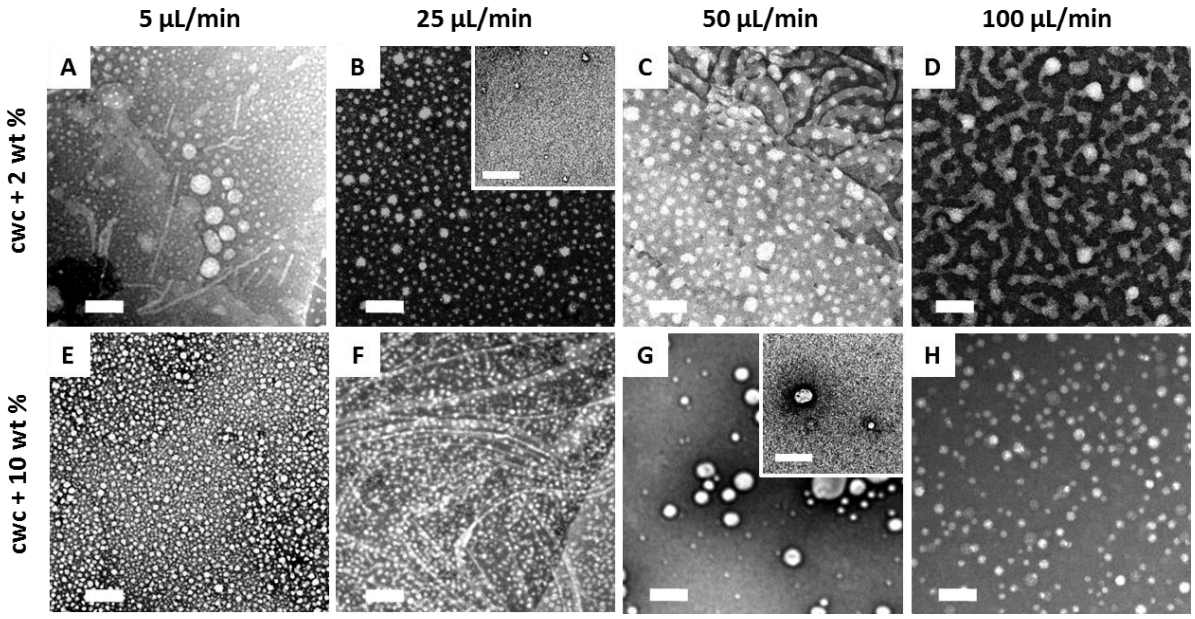

Figure 7.5 TEM images demonstrating stability of on-chip prepared PCL-*b*-PEO nanoparticles at two different water contents (cwc + 2 wt % and cwc + 10 wt %) and various flow rates. Following collection from the chip, the nanoparticles were stored for 24 h under quiescent conditions at 4° C. Insets are unstained images allowing visualization of the internal lumen of vesicles. Scale bars are 200 nm in the main images and 100 nm in the insets.

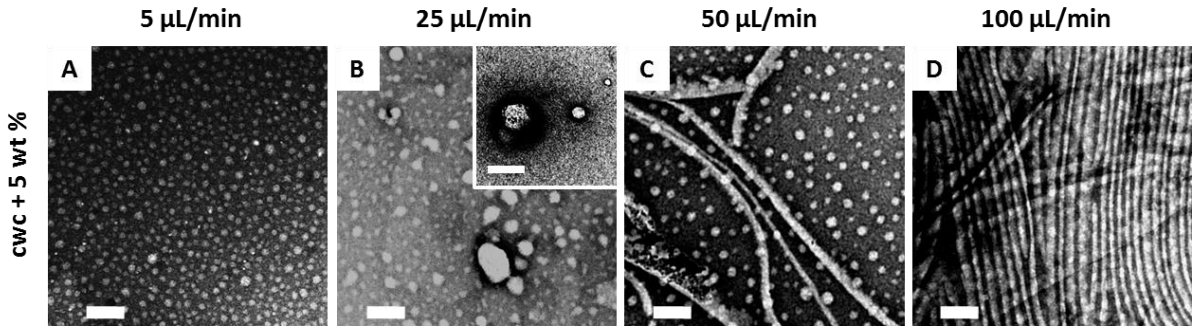

Figure 7.6 TEM images demonstrating long-term stability of on-chip prepared PCL-*b*-PEO nanoparticles at cwc + 5 wt % and various flow rates. Following collection from the chip, the nanoparticles were stored for 4 weeks under quiescent conditions at 4° C. Insets are unstained images allowing visualization of the internal lumen of vesicles. Scale bars are 200 nm in the main images and 100 nm in the inset.

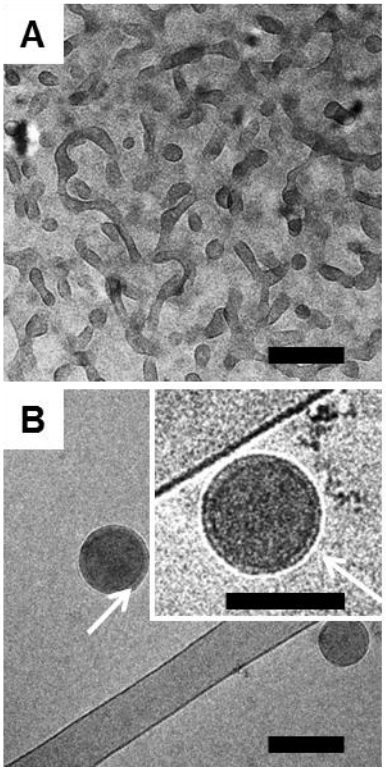

Figure 7.7 Cryo-TEM images of PCL- *b*- PEO nanoparticles formed on- chip at selected conditions, confirming corresponding morphologies identified from drop-cast samples with reverse staining: (A) cwc + 5 wt % at *Q* = 100 µL/min and (B) cwc + 10 wt % at *Q* = 50 µL/min. White arrows in (B) indicate thin walls of vesicles identified from contrast different between background and internal lumen; inset shows higher-magnification image of a single vesicle. All scale bars are 50 nm.

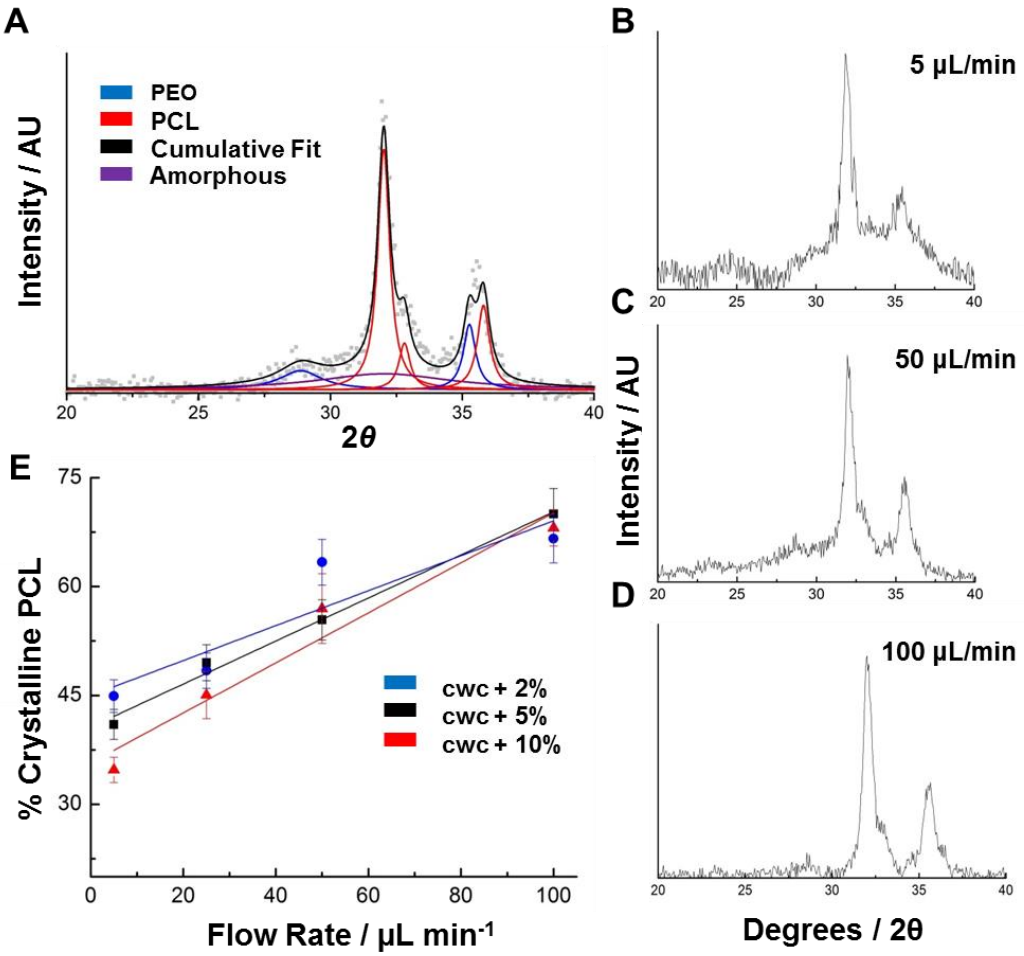

Figure 7.8 XRD and PCL crystallinity data for PCL-*b*-PEO nanoparticles prepared on-chip at various water contents and flow rates. (A) Example of a deconvoluted XRD profile in which raw data, best fit function, and PCL, PEO and amorphous Lorentzian contributions to the fit are shown. (B-D) raw XRD data for cwc + 10 wt % (water content featured in the main text) and three different flow rates, showing decrease in amorphous halo contribution with increase in flow rate. (E) Percentages of PCL crystallinity for various water contents and flow rates, including the cwc + 10 wt % conditions featured in the main text. Plots show linear increases in PCL crystallinity with flow rate for all water contents, with slope increasing as the water content increases.

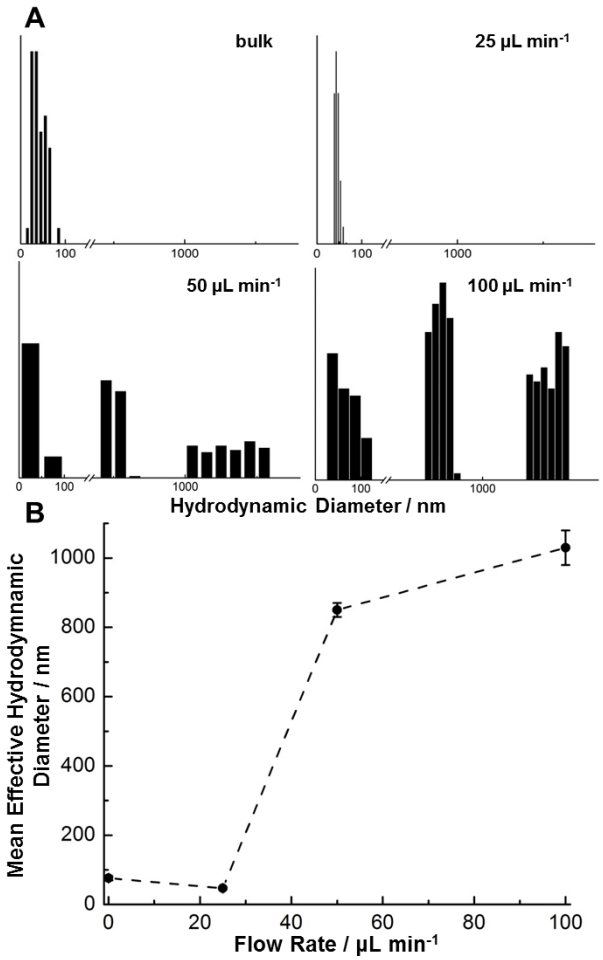

Figure 7.9 DLS size analysis for the PAX-loaded PCL-*b*-PEO nanoparticles corresponding to TEM data in Figure 4A. (A) Representative CONTIN distributions show single populations corresponding to pure spheres for bulk-prepared and on-chip Q = 25 µL/min cases with slower populations of diffusional modes (i.e. at higher $d_{h,eff}$) developing as flow rate increases (consistent with appearance of non-spherical nanoparticles in Figure 4A). (B) Mean effective hydrodynamic diameters, $\overline{\boldsymbol{d}_{h,eff}}$, determined from cumulent analysis of DLS autocorrelation functions as a function of flow rate ("zero flow" corresponds to the bulk-prepared sample). The errors on these values are standard deviations of three nanoparticle preparations under the same conditions. Dashed lines connecting data points are guides for the eye.

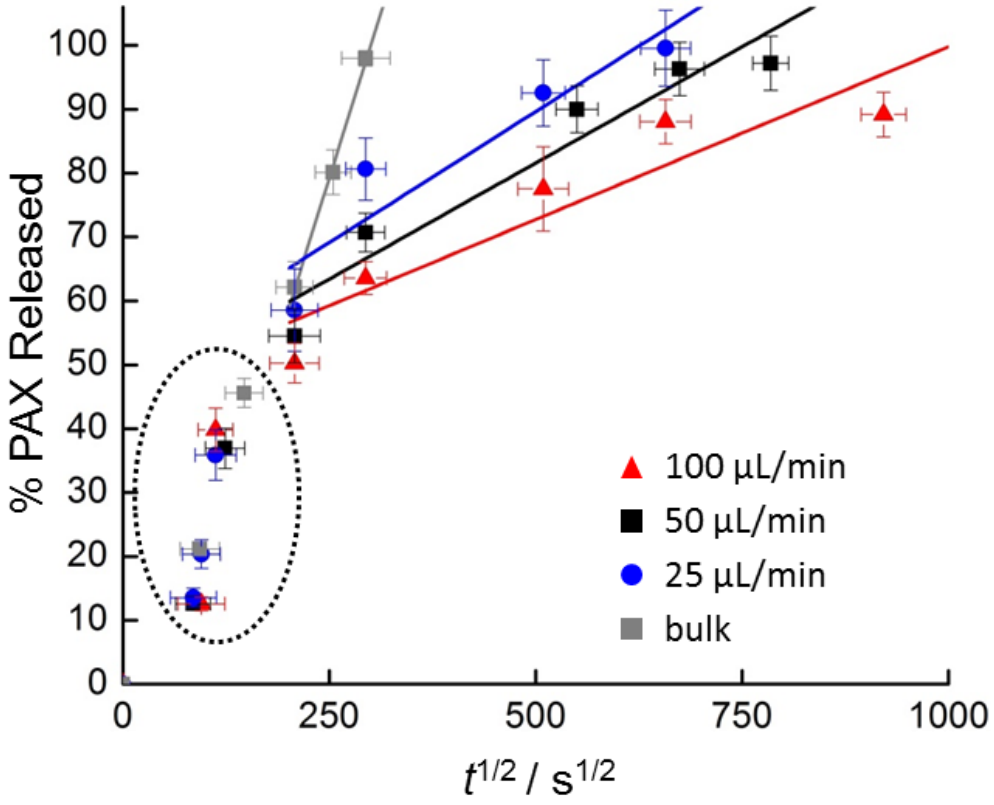

Figure 7.10 Release data for PAX loaded PCL-*b*-PEO nanoparticles plotted as *% PAX Released* vs. $t^{1/2}$. Data points t < 12 h (circled) show initial fast release; data points $t \geq 12$ h were fit to a diffusive release model *via* linear regression, with the resulting slopes increasing as: bulk-prepared > Q = 25 µL / min > Q = 50 µL / min > Q = 100 µL / min.

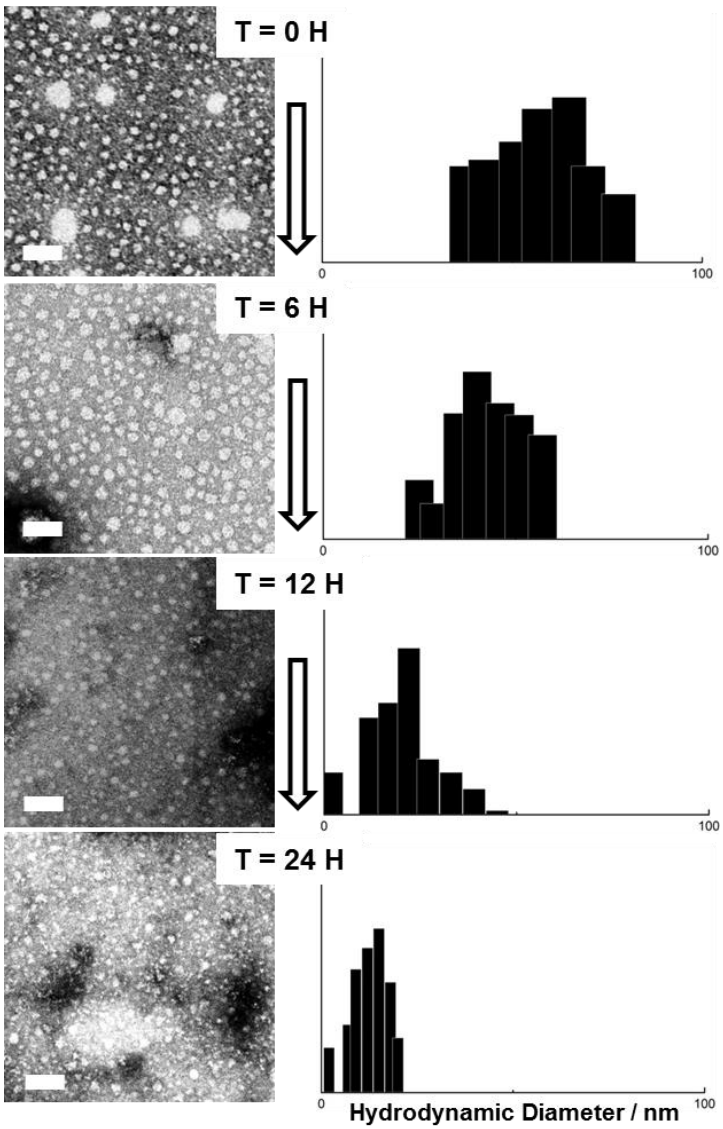

Figure 7.11 Hydrolytic degradation of bulk-prepared PAX-loaded PCL-*b*-PEO nanoparticles; TEM images and corresponding DLS hydrodynamic size distributions (CONTIN analysis) are shown for nanoparticles after various release times in PBS and albumin (pH = 7.4, 37 ° C). All scale bars are 200 nm.

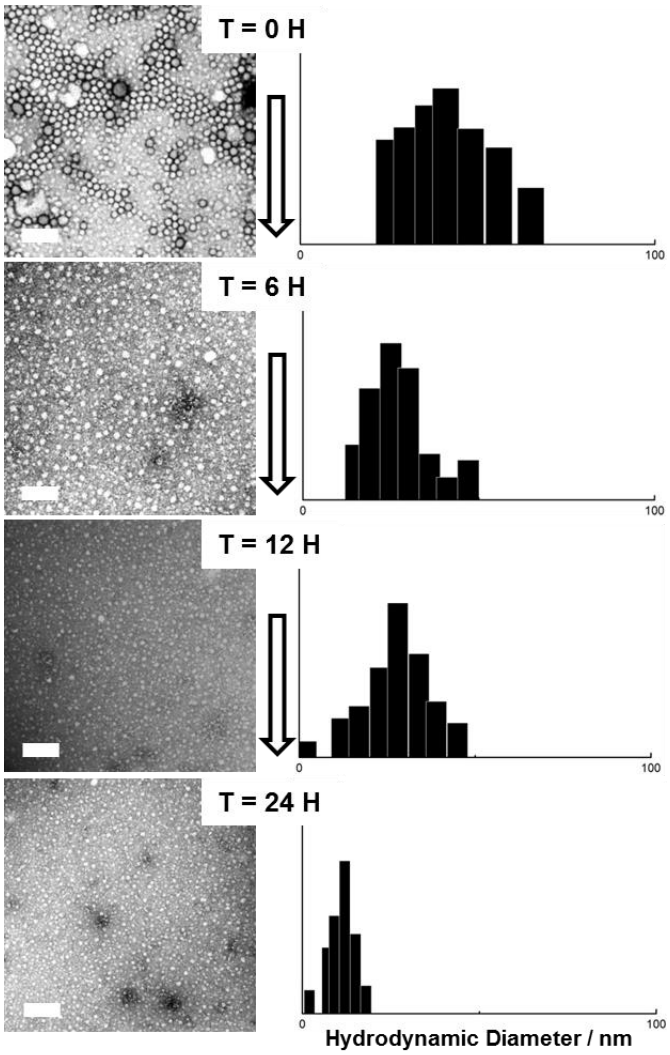

Figure 7.12 Hydrolytic degradation of PAX-loaded PCL-*b*-PEO nanoparticles formed on-chip at a water content of cwc + 5 wt % and Q = 25 μL/min; TEM images and corresponding DLS hydrodynamic size distributions (CONTIN analysis) are shown for nanoparticles after various release times in PBS and albumin (pH = 7.4, 37 ° C). All scale bars are 200 nm.

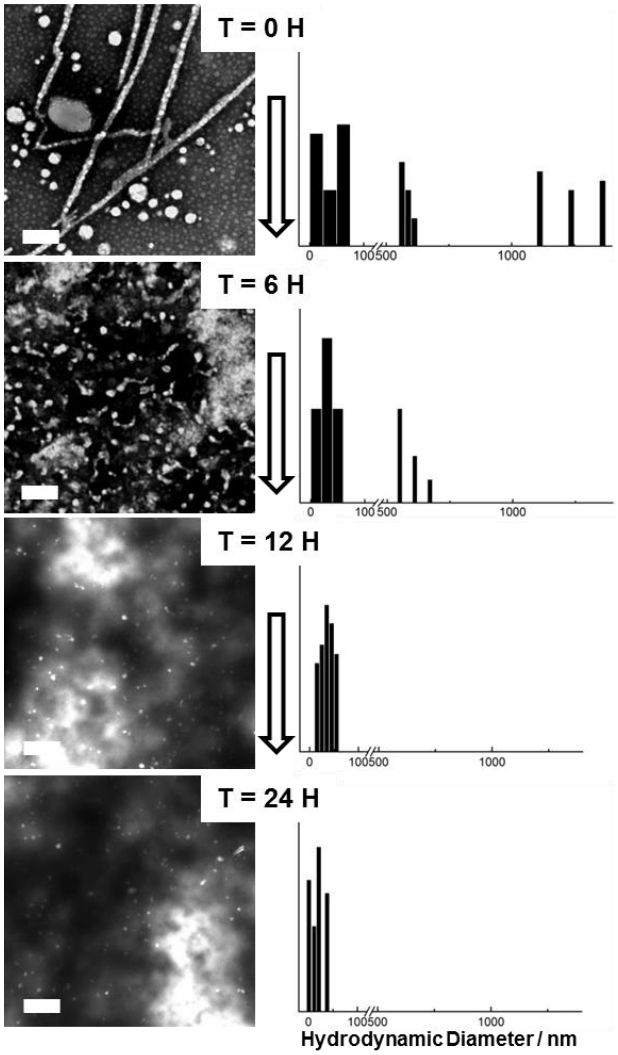

Figure 7.13 Hydrolytic degradation of PAX-loaded PCL-*b*-PEO nanoparticles formed on-chip at a water content of cwc + 5 wt % and Q = 50 µL/min; TEM images and corresponding DLS hydrodynamic size distributions (CONTIN analysis) are shown for nanoparticles after various release times in PBS and albumin (pH = 7.4, 37 ° C). All scale bars are 50 nm.

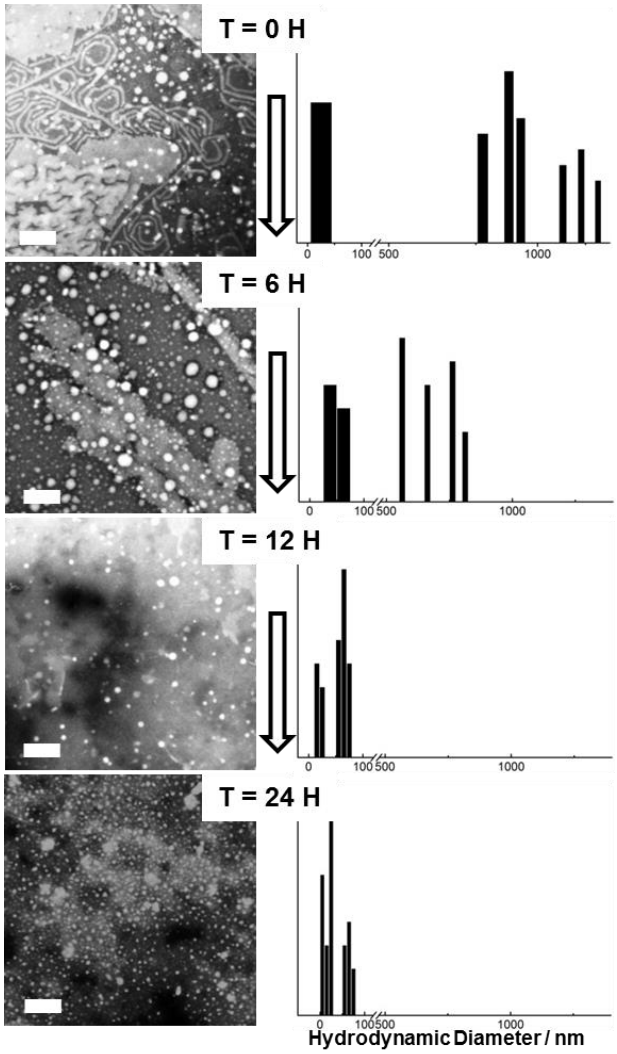

Figure 7.14 Hydrolytic degradation of PAX-loaded PCL-*b*-PEO nanoparticles formed on-chip at a water content of cwc + 5 wt % and Q = 100 µL/min; TEM images and corresponding DLS hydrodynamic size distributions (CONTIN analysis) are shown for nanoparticles after various release times in PBS and albumin (pH = 7.4, 37 ° C). All scale bars are 200 nm.

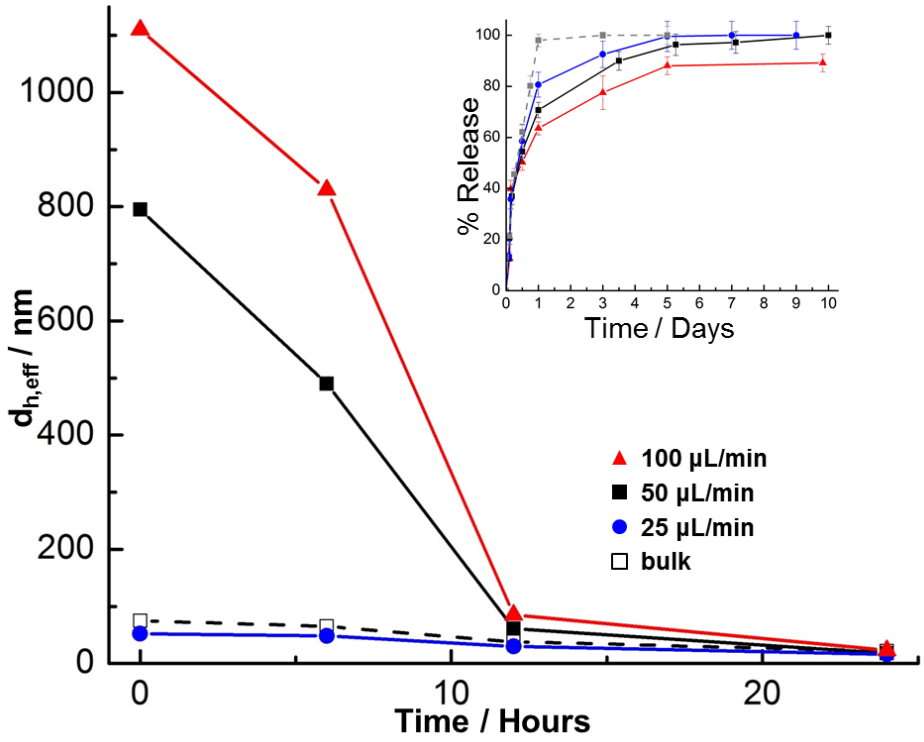

Figure 7.15 Hydrolytic degradation of PAX-loaded PCL-*b*-PEO nanoparticles formed on-chip at a water content of cwc + 5 wt % and various flow rates. The effective hydrodynamic sizes were obtained from cumulent analysis of the DLS autocorrelation function. Inset shows corresponding PAX release profiles from Figure 5B of the main text.

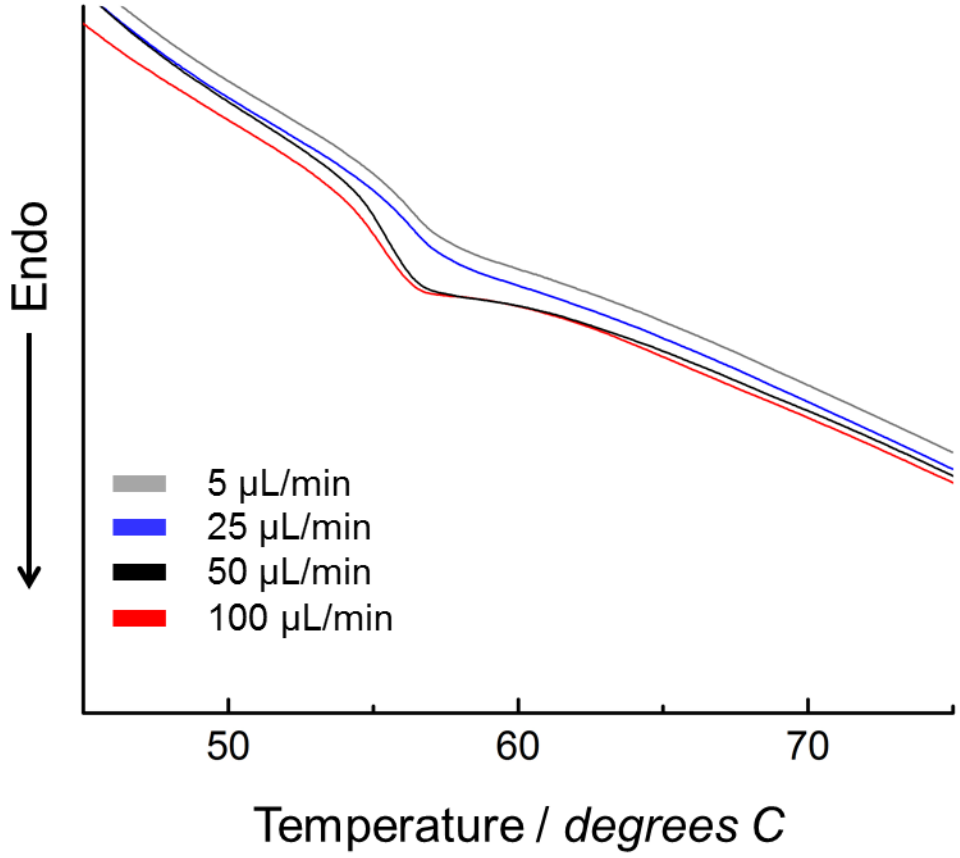

Figure 7.16 DSC data for cwc + 10 wt % PCL-*b*-PEO PNPs self-assembled using a microfluidic reactor.

Table 7.3 Actual Gas and Liquid Flow Rates for Various Preparations of PCL-*b*-PEO Nanoparticles Described in the Main Text.

Water Content, Nominal Flow Rate	L_{gas} (x 10^3m)	L_{liq} (x 10^3m)	Q_{gas} (µL/min)	Q_{liq} (µL/min)	Q_{gas}/Q_{liq}	Q_{total} (µL/min)
cwc + 2 wt %, 5 µL/min						
Prep #1	1.1	1.0	2.7	2.5	1.08	5.2
Prep #2	1.0	1.1	2.2	2.5	0.88	4.7
Prep #3	1.2	1.3	2.3	2.5	0.92	4.8
25 µL/min						
Prep #1	1.0	1.0	12.8	13.0	0.98	25.8
Prep #2	1.2	1.2	13.4	13.0	1.03	26.4
Prep #3	1.2	1.2	13.2	13.0	1.02	26.2
50 µL/min						
Prep #1	0.9	0.9	26.1	25.0	1.04	51.1
Prep #2	0.9	0.9	24.2	25.0	0.97	49.2
Prep #3	1.0	0.9	25.9	25.0	1.04	50.9
100 µL/min						
Prep #1	0.8	0.8	48.8	50.0	0.98	98.8
Prep #2	0.7	0.6	52.3	50.0	1.05	102.3
Prep #3	0.8	0.8	51.1	50.0	1.02	101.1
cwc + 5 wt %, 5 µL/min						
Prep #1	1.3	1.1	2.9	2.5	1.16	5.4
Prep #2	1.2	1.2	2.6	2.5	1.04	5.1
Prep #3	0.9	1.1	2.1	2.5	0.84	4.6
25 µL/min						
Prep #1	0.8	0.7	13.4	13.0	1.03	26.4
Prep #2	0.9	0.9	12.5	13.0	0.96	25.5
Prep #3	0.8	0.8	13.1	13.0	1.01	26.1
50 µL/min						
Prep #1	0.8	0.9	23.3	25.0	0.93	48.3
Prep #2	0.7	0.6	25.9	25.0	1.04	50.9
Prep #3	0.7	0.7	24.2	25.0	0.97	49.2
100 µL/min						
Prep #1	0.5	0.5	45.5	50.0	0.91	95.5
Prep #2	0.6	0.6	50.9	50.0	1.02	100.9
Prep #3	0.4	0.4	47.8	50.0	0.96	97.8

cwc + 10 wt %, 5 µL/min						
Prep #1	1.2	1.0	3.0	2.5	1.20	5.5
Prep #2	1.1	0.9	2.6	2.5	1.04	5.1
Prep #3	0.9	0.9	3.1	2.5	1.24	5.6
25 µL/min						
Prep #1	1.0	0.9	13.8	13.0	1.06	26.8
Prep #2	1.0	0.9	14.5	13.0	1.11	27.5
Prep #3	0.8	0.7	15.1	13.0	1.16	28.1
50 µL/min						
Prep #1	0.8	0.7	26.8	25.0	1.07	51.8
Prep #2	0.7	0.6	28.1	25.0	1.12	53.1
Prep #3	0.9	1.0	22.5	25.0	0.90	47.5
100 µL/min						
Prep #1	0.6	0.7	44.3	50.0	0.89	94.3
Prep #2	0.3	0.3	55.3	50.0	1.11	105.3
Prep #3	0.4	0.4	52.9	50.0	1.06	102.9

Table 7.4 Actual Gas and Liquid Flow Rates for Various Microfluidic Preparations of PAX-Loaded PCL-*b*-PEO Nanoparticles Described in the Main Text.

Nominal Flow Rate[a]	L_{gas} **(x 10^3m)**	L_{liq} **(x 10^3m)**	Q_{gas} **(µL/min)**	Q_{liq} **(µL/min)**	Q_{gas}/Q_{liq}	Q_{total} **(µL/min)**
25 µL/min						
Prep #1	0.8	0.8	13.4	13	1.03	26.4
Prep #2	0.8	0.9	11.2	13	0.86	24.2
Prep #3	0.7	0.6	15.1	13	1.16	28.1
50 µL/min						
Prep #1	1.1	1.0	26.3	25	1.05	51.3
Prep #2	1	0.9	27.1	25	1.08	52.1
Prep #3	1.3	1.4	23.2	25	0.93	48.2
100 µL/min						
Prep #1	0.7	0.7	26.1	25	1.04	51.1
Prep #2	0.8	0.8	24.2	25	0.97	49.2
Prep #3	0.8	0.8	25.9	25	1.04	50.9

a) The water content for all microfluidic preparations of PAX-loaded nanoparticles was cwc + 5 wt %.

Appendix-II

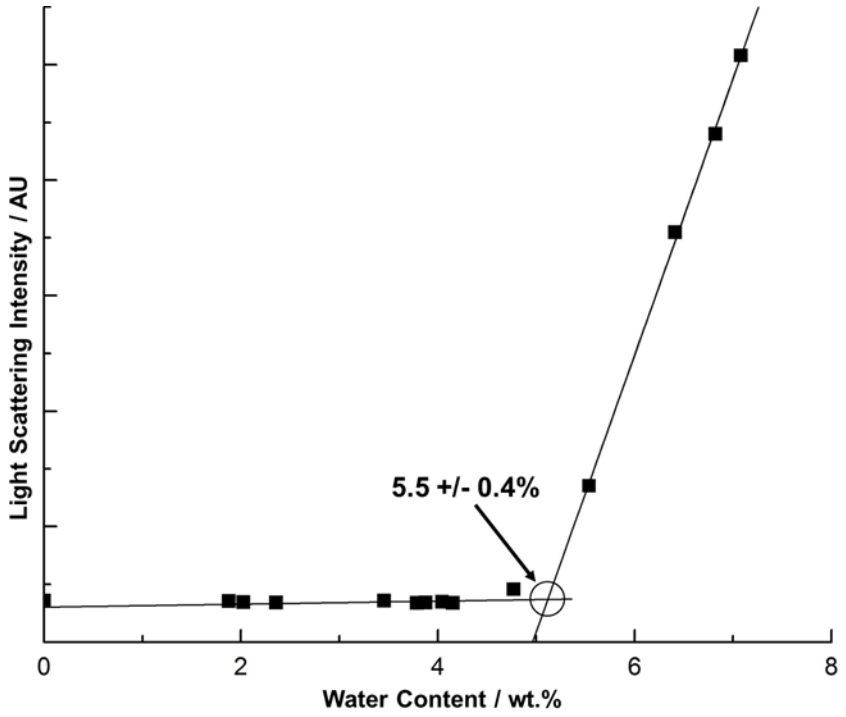

Figure 8.1 Critical water concentration (cwc) determination of 0.33 wt % PCl-*b*-PEO in DMF using the static light scattering method. The cwc determined from the above data is 5.5 ± 0.4 wt % as shown.

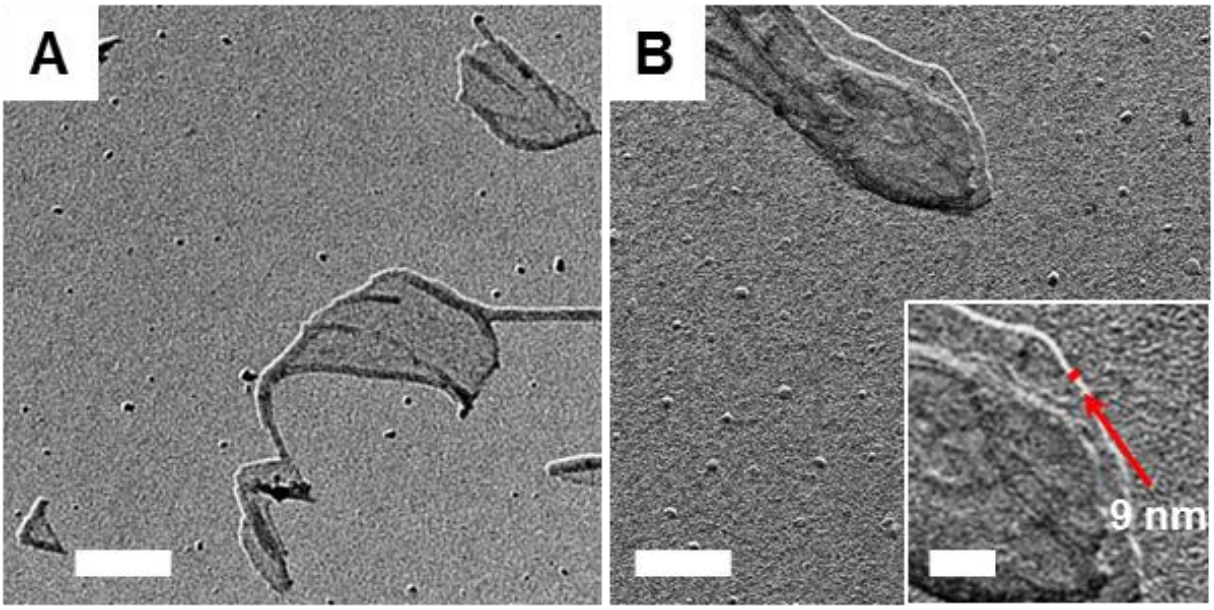

Figure 8.2 Representative TEM images of DiI-loaded PCL-*b*-PEO nanoparticles with Pt/Pd shadowing prepared at a flow rate of 50 µL/min and water contents of (A) cwc + 10 wt % and (B) and cwc + 75 wt %. Scale bars 200 nm in the main images and 50 nm in the inset.

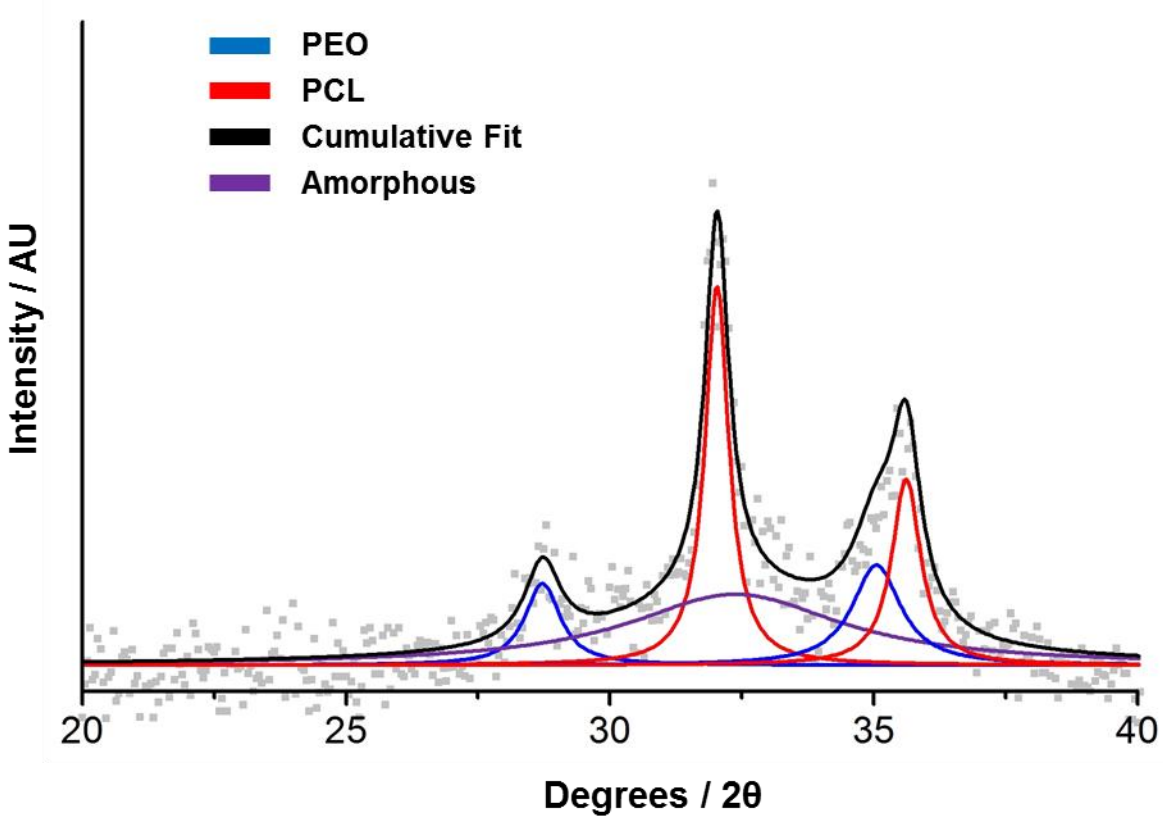

Figure 8.3 Representative XRD profile of a sample of DiI-loaded PCL-*b*-PEO nanoparticles, showing raw data, best fit function (black), and PCL (red), PEO (blue) and amorphous (purple) Lorentzian contributions to the fit. This sample was prepared at a flow rate of 25 µL/min and a water content of cwc + 75 wt %.

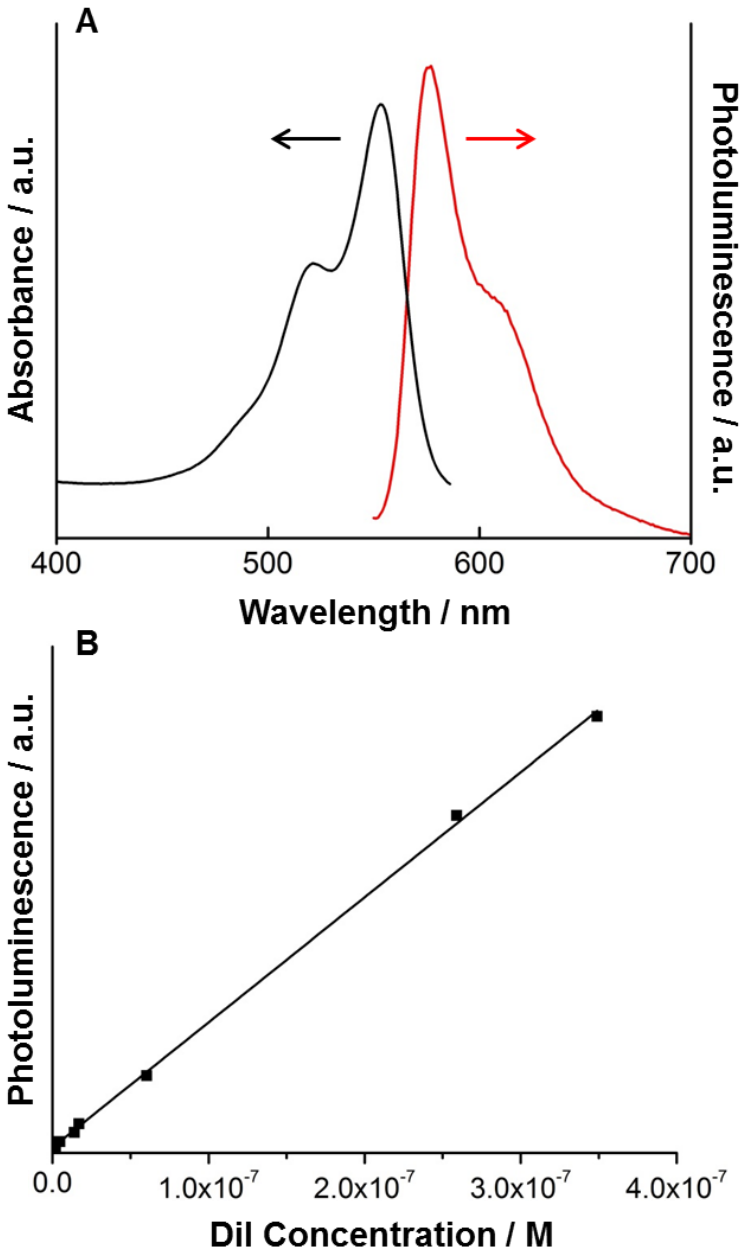

Figure 8.4 (A) Absorbance and photoluminescence (PL) emission spectra for DiI in DMF. (B) Intensity-concentration calibration curves for DiI obtained at excitation and emission wavelengths of λ_{ex} = 549 nm and λ_{em} = 565 nm.

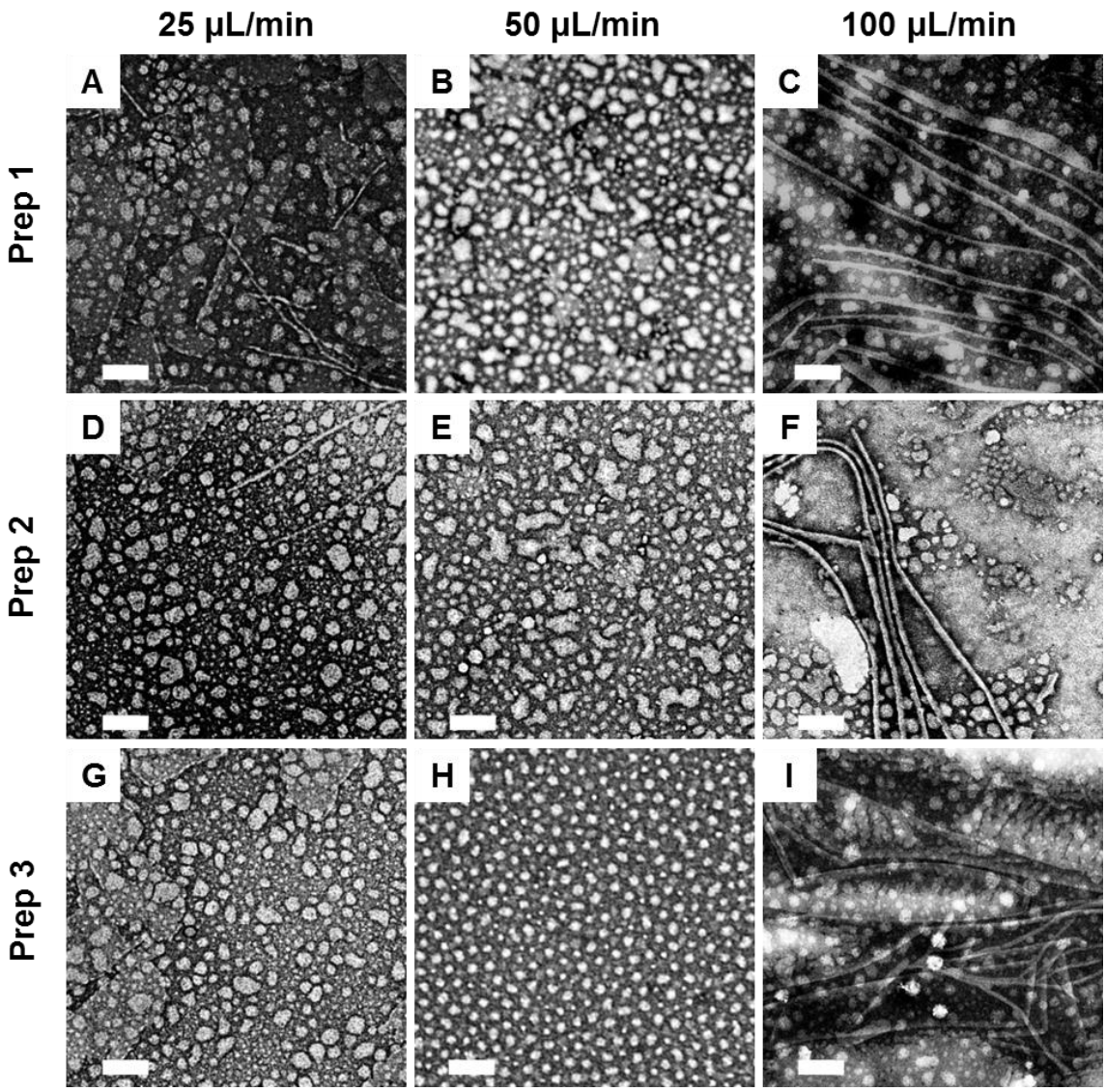

Figure 8.5 TEM images demonstrating reproducibility of DiI-loaded PCL- *b*- PEO nanoparticles over three replicate microfluidic preparations at a water content of cwc + 10 wt % and various flow rates. All scale bars are 200 nm.

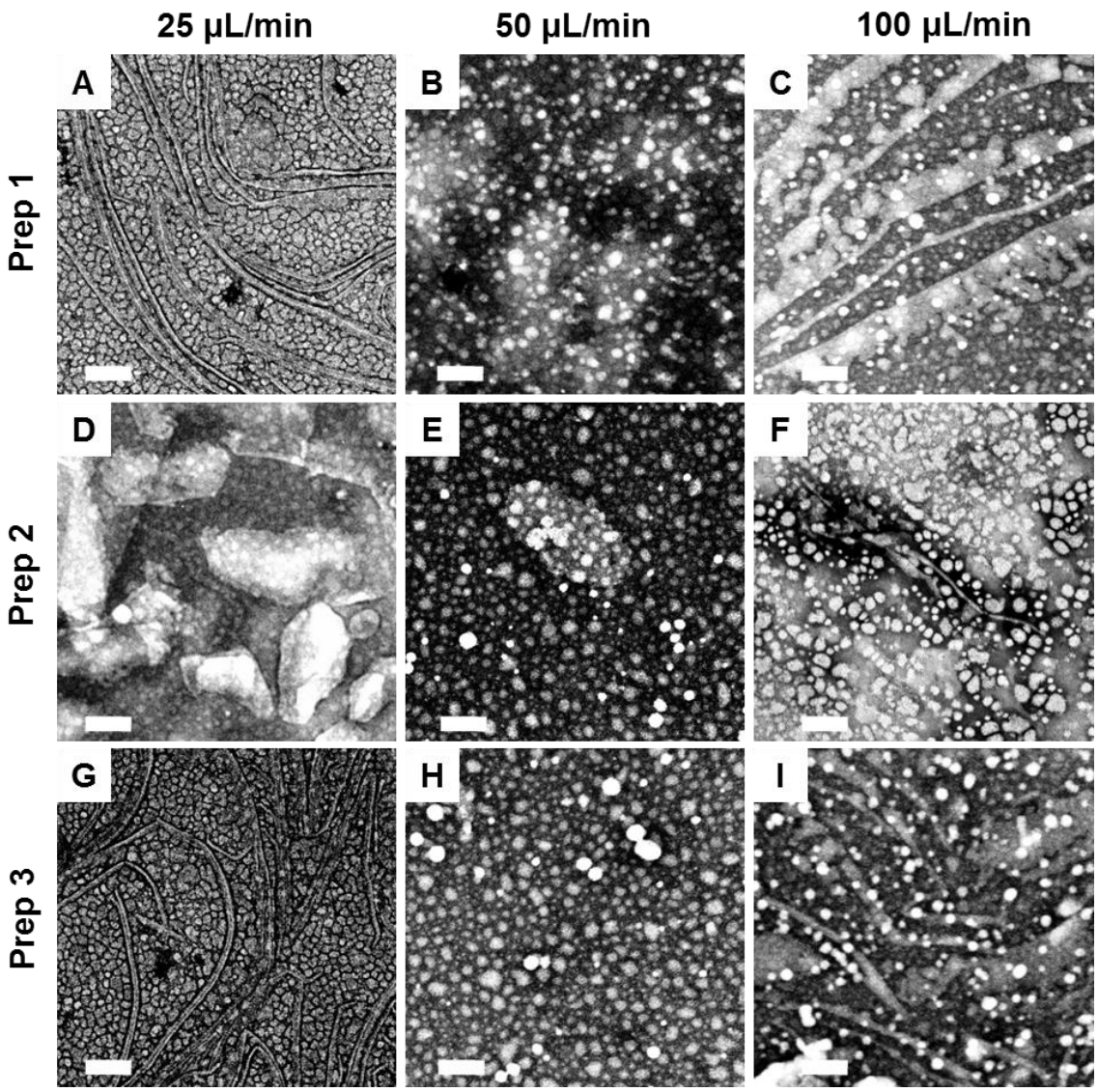

Figure 8.6 TEM images demonstrating reproducibility of DiI-loaded PCL- *b*- PEO nanoparticles over three replicate microfluidic preparations at a water content of cwc + 75 wt % and various flow rates. All scale bars are 200 nm.

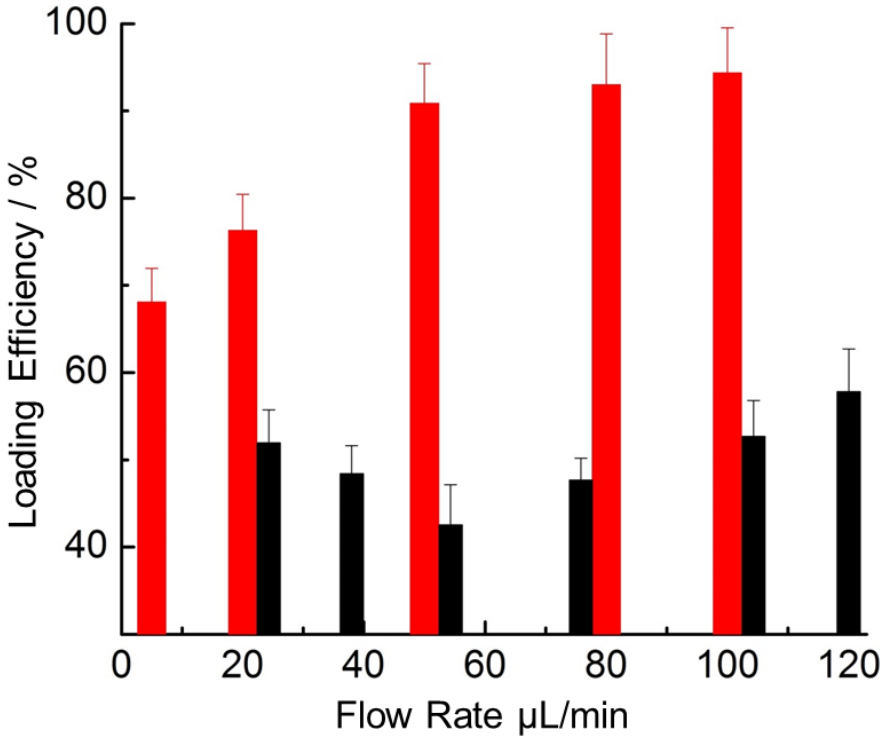

Figure 8.7 Loading efficiencies of DiI-loaded PCL-*b*-PEO nanoparticles prepared at various flow rates and two different contents: cwc + 10 wt % (red) and cwc + 75 wt % (black).

Table 8.1 Actual Gas and Liquid Flow Rates for Triplicate Microfluidic Preparations of DiI-Loaded PCL-*b*-PEO Nanoparticles Described in the Main Text.

Water Content, Nominal Flow Rate	L_{gas} ($\times 10^3$m)	L_{liq} ($\times 10^3$m)	Q_{gas} (μL/min)	Q_{liq} (μL/min)	Q_{gas}/Q_{liq}	Q_{total} (μL/min)
cwc + 10 wt %						
25 μL/min						
Prep #1	1.1	1.0	12.8	13.0	0.98	25.6
Prep #2	0.9	1.0	12.1	13.0	0.93	24.2
Prep #3	1.0	1.1	11.9	13.0	0.92	23.8
50 μL/min						
Prep #1	0.9	0.9	23.1	25.0	0.92	46.2
Prep #2	1.1	0.9	27.5	25.0	1.10	55.0
Prep #3	1.0	0.9	28.2	25.0	1.13	56.4
100 μL/min						
Prep #1	0.9	1.1	43.5	50.0	0.87	87.0
Prep #2	0.9	1.0	46.1	50.0	0.92	92.2
Prep #3	1.0	1.1	47.2	50.0	0.94	94.4
cwc + 75 wt %						
25 μL/min						
Prep #1	0.9	1.1	10.6	13.0	0.82	20.5
Prep #2	1.1	1.0	14.6	13.0	1.21	28.0
Prep #3	1.0	1.1	11.9	13.0	0.92	22.9
50 μL/min						
Prep #1	0.9	1.0	22.5	25.0	0.91	45.0
Prep #2	1.0	1.0	25.8	25.0	1.03	51.5
Prep #3	1.1	1.1	24.5	25.0	0.98	49.1
100 μL/min						
Prep #1	0.9	1.1	43.8	50.0	0.88	87.6
Prep #2	1.0	1.1	44.5	50.0	0.89	89.1
Prep #3	1.1	0.9	56.5	50.0	1.13	112.9

Appendix III

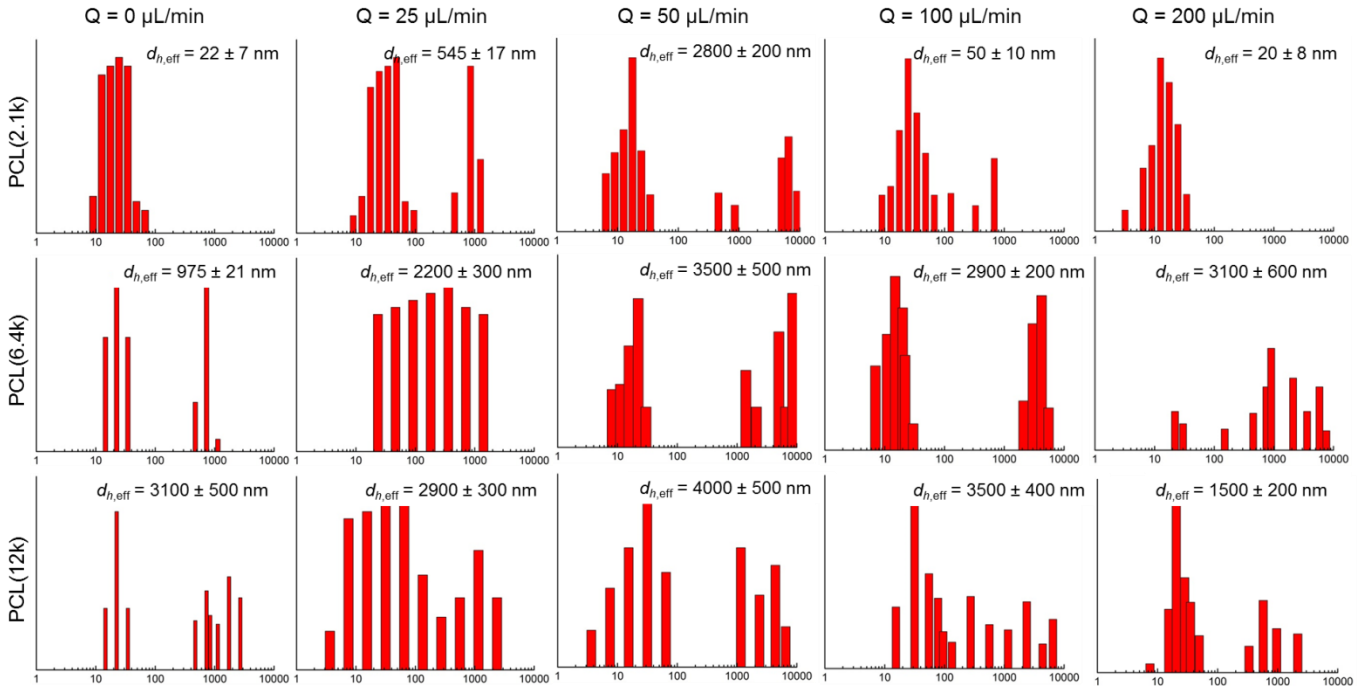

Figure 9.1 CUMULENT distributions and CONTIN effective hydrodynamic diameters for the formulations presented in Figure 4.1

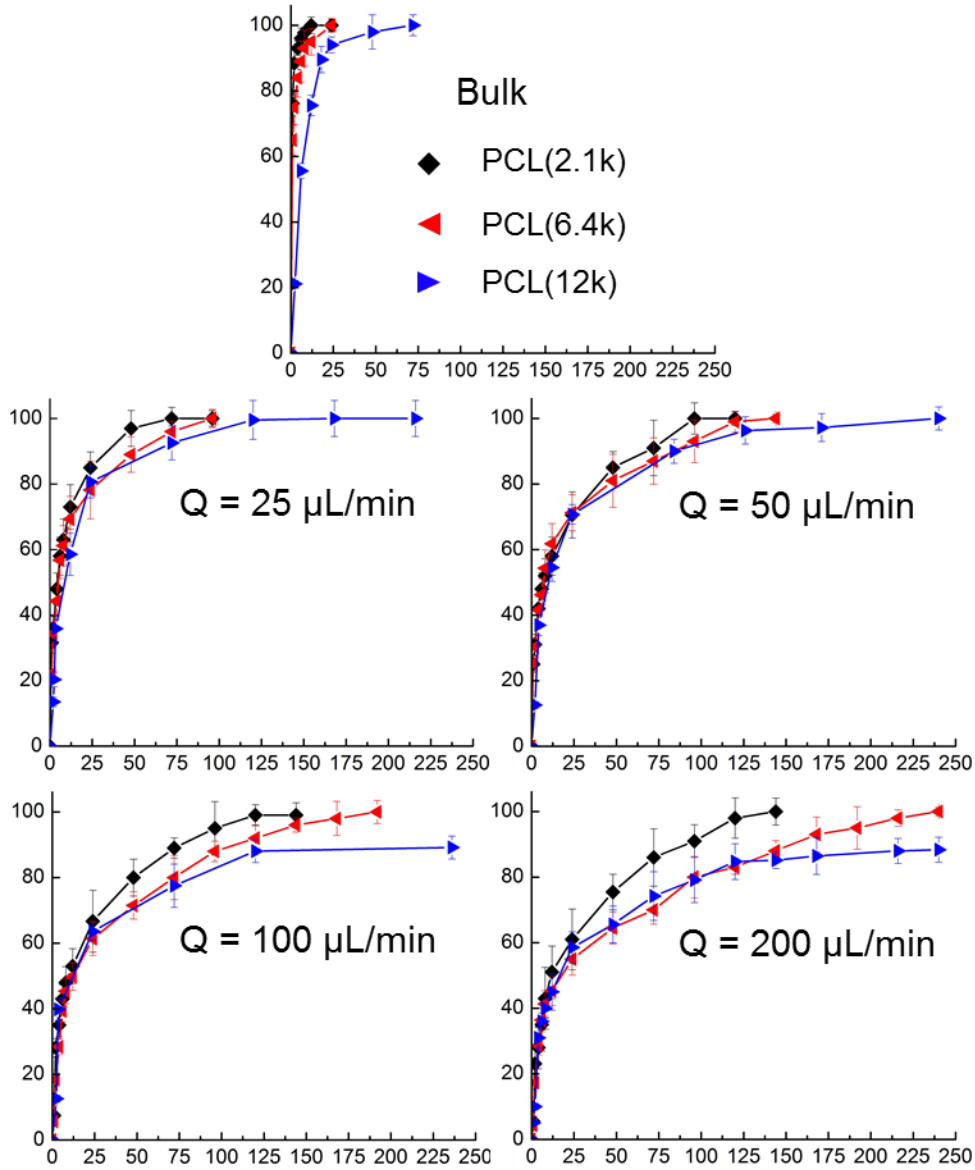

Figure 9.2 Effect of copolymer composition on PAX release from PAX-loaded PNPs self-assembled under bulk and various microfluidic conditions.

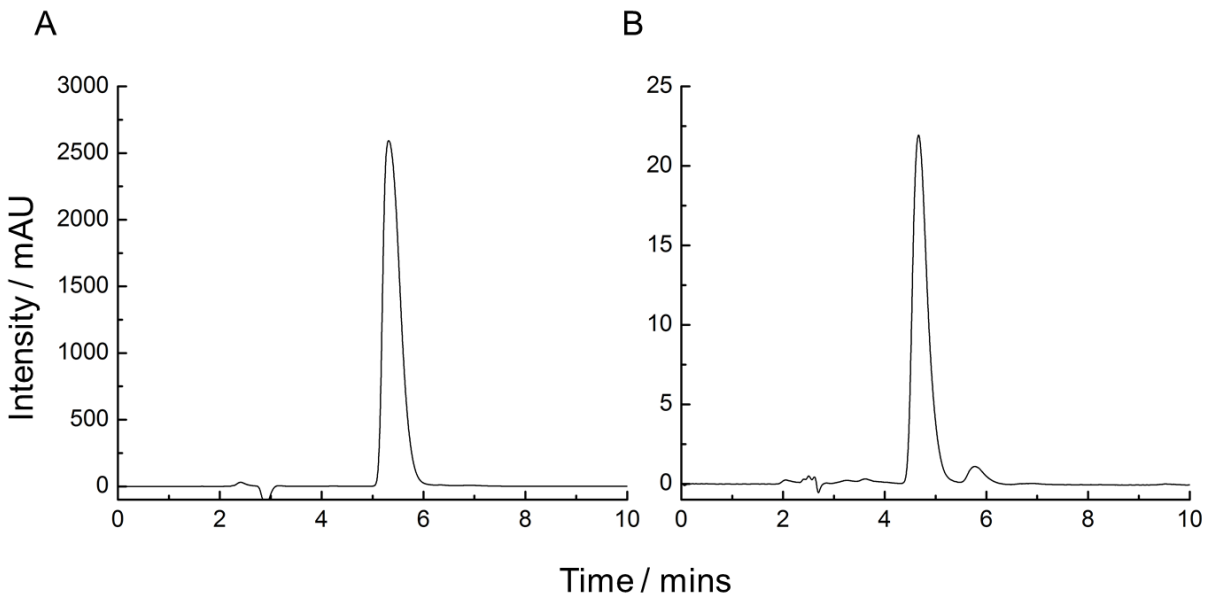

Figure 9.3 LCMS DAD traces of PAX diffusional release. A) Is a reproduced 24 hour diffusional PAX release LCMS trace, at the PAX characteristic absorbance wavelength of 227 nm. B) Is a reproduced 10 day diffusional PAX release LCMS trace, at the PAX characteristic absorbance wavelength of 227 nm.